Evaluation of Publicly Available Global Hydrologic Datasets to Improve Water Resources Management in Vietnam

A Dissertation
Presented to
the Faculty of the School of Engineering and Applied Sciences
at the University of Virginia

In Partial Fulfilment
of the requirements for the Degree
Doctor of Philosophy (Civil Engineering)
by Manh-Hung Le

April 2021

Abstract

Water resources management (WRM) is essential to sustainably improve prosperity in developing nations. WRM requires reliable estimates of key hydrometeorological variables to monitor changes in water availability. Thus, one of the biggest challenges in WRM at the national scale is accurate and timely observations of these variables from the ground networks (referred to as local datasets) that usually have low density. Without boundary restriction and global coverage, satellite-based and outputs from land surface models datasets (referred to as global datasets) are promising and can estimate these variables. However, there are several barriers to use global datasets in local WRM: (i) global datasets usually have large sizes and are not easy to handle, (ii) they often have coarse resolutions that are not suitable to local-scale WRM applications, and (iii) they have heterogeneous quality depending on climatic and geographic conditions. Therefore, large-scale validation of a global dataset is an area of research that requires more attention to provide practical insights about the usefulness of these assets over different regions. This dissertation aims to better understand the capacity of global datasets to support WRM in Vietnam–a tropical country that faces many water stresses in a warming climate and does not have a good observational network to monitor key hydrometeorological variables. Specifically, we examine satellite- and re-analysis- based precipitation products and satellite-based soil moisture products in hydrologic impact studies over a large number of catchments.

There are four key findings yielded from the four independent large-sample studies conducted within this dissertation. First, satellite-based precipitation products (e.g., TMPA; Tropical Rainfall Measurement Mission Multi-satellite Precipitation Analysis) accurately estimated rainfall in wet season compared to the dry season (rain gauge as a base reference) in the Red-Thai Binh River basin, the second largest river basin in Vietnam. The quality of TMPA datasets could be improved based on a climatology-topography-based linear-scaling approach, especially to reduce their bias. Second, high-spatial resolutions (at 1-km) of re-analysis dataset (e.g., MERRA-2; Modern-Era Retrospective analysis for Research and Applications version 2) could be useful to detect percentage drought areas as well as to quantify drought trends across Vietnam. This finding reveals the feasibility of using a model-based drought index in data-sparse areas to assess drought conditions, and for practical applications of advanced re-analysis products in WRM. Third, the Global Precipitation Mission (GPM) Integrated Multi-satellitE Retrievals for GPM (IMERG) final run version 6 (GPM IMERGv6) could be the input precipitation for a hydrological model (SWAT; Soil and Water Assessment Tool) to simulate streamflow. Also, the Climate Hazards group Infrared Precipitation with stations (CHIRPS) dataset demonstrates a relatively low bias and could benefit long-term water resources planning for droughts. These conclusions were based on a comprehensive hydrologic model study (a total of 54 simulated scenarios) across Vietnam basins. Fourth, remotely sensed soil moisture data assimilation in a hydrologic model streamflow simulation could increase the accuracy of streamflow simulation. The benefits of high-spatial resolution soil moisture (e.g., SMAP, Soil Moisture Active and Passive), at a spatial resolution of 1 km in the data assimilation framework, is outperformed by that data assimilation using SMAP at a spatial resolution of 9 km. This finding is based on an experiment using eight catchments with varying sizes and runoff patterns across contrasting climate zones in Vietnam. Overall, this dissertation is beneficial to water practitioners in developing nations, as a guide to decide whether publicly available global datasets are useful for local applications, and if so, which data sources would be the most suitable to consider.

Keywords: Earth Observations; Vietnam; SWAT; large samples; precipitation; soil moisture; drought

Approval Sheet

This dissertation is submitted in partial fulfilment of the requirements for the degree of
Doctor of Philosophy (Civil Engineering)

Manh-Hung Le

This dissertation has been read and approved by the Examining Committee:

James A. Smith

Julianne Quinn

Jonathan L. Goodall

Venkataraman Lakshmi

Robert E. Davis

John D. Bolten

Accepted for the School of Engineering and Applied Science

Jennifer L. West, Dean, School of Engineering and Applied Science

April 2022

To Hai, Nu, my family, and my country

Acknowledgements

I would like to express my gratitude to my wife, Nu, who endless supports me during my Ph.D. journey. Together with, we have a little Hai. Having him in our life is greatly joyful. Also, I want to say thanks to my parents and my brother for their continuous encouragement.

I am glad to know my lab mates in the research group– Arun, Sananda, Reyadh, Bin, Hyung, Chelsea, Prakrut, Runze, Robin, Gigi, Ben, and Jessica, and Duc. Their fruitful discussion in our regular group meetings and their friendships in our leisure time are valuable to keep my enthusiasm during my research time.

Acknowledgments are also given to several Vietnam collaborators – officials from National Central and Water Resources Planning and Investigation (NAWAPI), Dr. Hung Pham, Dr. Hong Do, Mr. Binh Nguyen, and Mrs. Thuy Nguyen. Their valuable support in discussion, guidance, encouragement, and data collection have shaped my research much better!

I also thank to committee members–Jim with an agreement to chair the committee, Julie with a genius math mindset, Jon with thoughtful suggestion in the field of hydrology, John for his soil moisture endeavor, and Bob with a quick agreement to join the committee members.

I specially thank to Venkat who brought me to the U.S. to have a four-year journey with him. His motivation keeps me being productive. His working attitude inspires me to work hard and be responsible. And his care helps me to overcome challenges and achieve many successes!

Finally, I greatly appreciate funding sponsors to provide financial aids for my research. They include NASA and ARO for my graduate research assistantship and Department of Engineering Systems and Environment, and Department of Applied Mathematics for my graduate teaching assistantship.

Charlottesville, April 7, 2022

Manh-Hung Le

Related publications and presentation

The following publications are planned for the research presented in this dissertation. The Ph.D. candidate name is in bold text and the supervisor is in *italic* text.

Chapter 2: **Le, H. M.**, Sutton, J. R., Bui, D. D., Bolten, J. D., & *Lakshmi, V*. (2018). Comparison and Bias Correction of TMPA Precipitation Products over the Lower Part of Red-Thai Binh River Basin of Vietnam. Remote Sensing, 10(10), 1582. https://doi.org/10.3390/rs10101582.

Chapter 3: **Le, M. H.**, Kim, H., Moon, H., Zhang, R., *Lakshmi, V*., & Nguyen, L.B (2020). Assessment of drought conditions over Vietnam using standardized precipitation evapotranspiration index, MERRA-2 re-analysis, and dynamic land cover. Journal of Hydrology: Regional Studies, 100767. https://doi.org/10.1016/j.ejrh.2020.100767.

Chapter 4: **Le, M. H.**, *Lakshmi, V*., Bolten, J., & Bui, D. D. (2020). Adequacy of Satellite-derived Precipitation Estimate for Hydrological modeling in Vietnam Basins. Journal of Hydrology, 124820. https://doi.org/10.1016/j.jhydrol.2020.124820.

Chapter 5: **Le, M.H.**, Nguyen Q.B., Pham, H.T., Patil, A., Do H.X., Ramsankaran R., Bolten, J. D., & *Lakshmi, V* (2022). Assimilation of SMAP products in streamflow simulations – Is spatial information more important than temporal information. Remote Sensing, 14(7), 1607. https://doi.org/10.3390/rs14071607.

This dissertation has resulted in the following presentations:

Le, M.H., & *Lakshmi, V* (2020). Long-short term memory (LSTM) neural network integrated with satellite datasets to simulate streamflow in transboundary river basins. In 2020 AGU Fall Meeting Abstracts, San Francisco CA, USA (Virtual Conference)

Le, M.H., & *Lakshmi, V* (2020). Integrating farmer interview data into SWAT+ model-a case study in Vietnamese Mekong Delta. In NexView Technical Meeting, Tempe AZ, USA

Le, M.H., & *Lakshmi, V* (2020). Assessment of eight satellite precipitation products for hydrological simulations in Vietnam. In 2020 GRAD Research Symposium, Engineering Systems and Environment, Charlottesville VA, USA

Le, M.H., *Lakshmi, V.,* Vo, Q.T., Hong, M.H., & Van, P.D.T. (2019). Assessment of hydrological processes in a polder of Mekong Delta using SWAT+ model. In 2019 AGU Fall Meeting Abstracts, San Francisco CA, USA

Le, H. M., *V. Lakshmi*, H. Q. Bui, & D. D. Bui (2018). Hydrological evaluation of TRMM and GPM Multi-satellite products for the data-scare regions, the upper Srepok River Basin of Vietnam. In 2018 AGU Fall Meeting Abstracts, Washington DC, USA

Table of contents

List of tables

List of figures

Chapter 1: Introduction

In developing nations, good water resources management (WRM) is fundamental to sustainably develop socio-economic, protecting public health, and ensuring food security and is thus a strategic key to reduce poverty. For instance, inadequate water supply and sanitation could cause economic losses of an estimated $260 billion per year in developing countries (Hulton, 2012). Under the water resources constraint scenario, China's overall economic growth rate can be dropped by 0.15% (Zhang et al., 2020). According to the World Economic Forum's 2015 Global Risk reports (Drzik et al., 2015), water crises are the most serious societal risk in the twenty-first century. If developing countries do not manage their water infrastructure and resources in a proper manner, they are likely not prepared for the complex challenges in the upcoming century and may lose the economic growth that has been achieved in the past decades (Borgomeo et al., 2018; García et al., 2016).

To inform WRM decision-making, it is essential to build a synthetic system to measure and monitor changes in water availability. This system requires reliable estimates of *key hydrometeorological variables such as streamflow, water level, groundwater, precipitation, soil moisture, actual evapotranspiration, potential evapotranspiration, snow and ice, and water quality* (Sheffield et al., 2018). Also, these variables have to be delivered in a timely fashion for the system to help the decision-makers in real-time. Commonly, these variables are collected from in-situ observation networks (referred to as *local datasets*). For example, rain gauge networks and stream gauge networks are essential sources to provide long-term records of precipitation and streamflow that are important to the design of flood control. Crop monitoring requires real-time water needs and soil moisture which can be provided by field crop sampling and soil moisture probes (García et al., 2016; Sheffield et al., 2018).

However, WRM-based local datasets systems confront risks that ground observation networks are substantially decreased. For example, one of the largest collected rain-gauge databases across the globe – the Global Precipitation Climatology Centre (GPCC) has experienced a reduction in available rain gauges. From 49,470 rain gauge stations in 1970, GPCC vs 7.0 database only has 30,000 in 2005 and about 10,000 by 2012 (Sun et al., 2018) and the reduction varied in different continents. Between 1990 and 2005, the available stations in GPCC vs 5.0 dataset were nearly constant over North America and Australia. On the other hand, significant drops in the number of gauges were observed in Europe (40% reduction as compared to the year 1990), Asia (60%), Africa (65%), and South America (85%) (Lorenz and Kunstmann, 2012). A decline in available rain gauges could seriously impact the ability to quantify changes in precipitation in the future. Similar declining trends for other in-situ measurements (e.g., stream gauges) have been also observed (Sheffield et al., 2018). The decline of such hydrometeorological networks is due to a lack of investment in infrastructures or human capacity to monitor (Sun et al., 2018), or restrictions in data-sharing policies (Du et al., 2020).

Moreover, it is challenging for the WRM-based local datasets systems in managing international transboundary river basins as a whole. Although there was evidence that water stress of downstream parts of a river system could be associated with the upstream water use (Munia et al., 2016; Munia et al., 2020), data sharing is a long-standing barrier to good WRM practice across transboundary river basins–a home of 40% of the total world population and accounting for 60% of global water flow (UN-Water, 2013; UNU-INWEH, 2013). Specifically, water resources managers in the downstream countries often have little information about changes in hydrometeorological conditions in the upstream countries (Munia et al., 2020). In cases when the upstream countries provide their ground observation datasets – for the downstream countries – the deliverables are usually not promptly to inform operational decisions. With insufficient spatial and timely ground monitoring networks, potential water stress could not be predicted, leading to numerous consequences including water-borne illnesses, water shortage, pollution, and ecosystem damage.

For the above-mentioned limitations of local datasets, the focus in recent years on WRM has shifted to global datasets that are publicly available. These global datasets include remote sensing (or earth observation, EO) and outputs from global land surface models, which can provide estimates of nearly all key hydrometeorological variables (Lettenmaier et al., 2015; McCabe et al., 2017). For example, precipitation within latitude from 60°S to 60°N could be estimated by Tropical Rainfall Measurement Mission (TRMM) Multi-Satellite Precipitation Analysis (TMPA; 3-hour, 0.25°, Huffman et al. (2007)) based on thermal infrared calibrated with precipitation radar and microwave data. TMPA's successor– the Global Precipitation Measurement Mission (GPM; Hou et al. (2014)) can distinguish rain and snow globally every half-hour at 10-km spatial resolution with GPM Microwave Imager and Dual-Frequency Precipitation Radar equipped in the GPM Core Observatory satellite and with support from several constellation satellites. For soil moisture, active and passive microwave sensors carried in satellites can observe radar backscatter or brightness temperature that can be converted to soil moisture retrievals at the 0-5 cm soil layer (Lakshmi, 2013; Njoku and Entekhabi, 1996). Several soil moisture products from active/passive microwave sensors include ASCAT (Advanced SCATterometer) (Bartalis et al., 2007), SMOS (Soil Moisture and Ocean Salinity) (Kerr et al., 2001), AMSR-E (Advanced Microwave Scanning Radiometer for the Earth Observing System onboard the Aqua satellite) (Kawanishi et al., 2003), and SMAP (Soil Moisture Active Passive) (Entekhabi et al., 2010). Meteo-hydrological variables (as states and fluxes that participate in processes happening at the Earth's surface) also can be obtained as outputs from Land Surface Models (LSMs). High-quality LSMs' datasets could provide useful information in predicting weather and investigating the water cycle from a global scale to a regional scale. Several LSMs datasets include Global Land Data Assimilation System (GLDAS, https://ldas.gsfc.nasa.gov/, Rodell et al. (2004)); Famine Early Warning Systems Network (FEWSNET) Land Data Assimilation System (FLDAS; https://ldas.gsfc.nasa.gov/fldas; McNally et al. (2017)); and ERA5-Land (https://www.ecmwf.int/en/era5-land; Muñoz-Sabater et al. (2021)).

Freely accessible global datasets are considered the new asset to effectively characterize water resources and help decision-makers in hydrologic impact analysis (Van Dijk and Renzullo, 2011), *due to their wealth of information*. For example, Goddard Earth Sciences Data and Information Services Center (GES DISC) is archiving approximately 150 million remotely sensed data files, or about 3,400 TBs of data (statistics on April 04, 2022). More importantly, these datasets can reveal much important information about water resources across the globe. For instance, the Gravity Recovery and Climate Experiment (GRACE) has been used to reveal considerable trends in freshwater resources across the globe and provide quantitative changes in freshwater resources at regional scales (Rodell et al., 2018). Without GRACE, several water scarce regions (e.g., north India, North China Plain, and the Middle East) could be predicted due to intensified human activities but the total water storage (TWS) depletion's magnitude at these hotspots regions was unknown due to sparse observational records or restricted data-access policies (Du et al., 2020). TRMM rainfall is useful in describing the spatio-temporal distribution of floods and landslides at the global scale (Hong et al., 2010), providing a better understanding of the characteristics and potential forecast of floods and rainfall-triggered landslides. In a regional study (Lower Mekong River basin), Mohammed et al. (2022) utilized various earth observation products to analyze the potential impacts of climate change on regional hydrology and water management. Pham et al. (2021) combined satellite observations for altimetry, land surface temperature, soil moisture, and rainfall to estimate daily water level in sparsely gauged catchments. In sub-Sahara, McNally et al. (2017)

proved the capability of the FLDAS dataset in monitoring drought conditions to cope with food security in the studied region. Based on different 16 experiments, Jung et al. (2017) suggested that water balance in the Upper Blue Nile basin can be represented by FLDAS and Catchment LSM version Fortuna 2.5 (CLSMF2.5).

Although the benefits of global datasets are promising, there are several concerns about their limitations and reliability. As the view from space, Earth observations (EO) indirectly measure hydro-metrological variables and have issues with their high-frequency sampling. For example, the averaged revisit time of TRMM Microwave Image (TMI) that provides quantitative rainfall information is approximately three hours. If between a TMI's revisit period, there is a rainfall event, this rainfall event will not be recorded from the TMI sensor. Some other satellites even have longer revisit time–3 days for SMAP soil moisture (Entekhabi et al., 2010) and 8 days for MODIS evapotranspiration (Justice et al., 1998; Vermote, 2015). Along with low-frequency sampling, missing spatial data is a common problem for microwave sensors, especially with the regions having a high degree of cloud coverage (Ahamed and Bolten, 2017; Mu et al., 2011). Satellite data quality is also heterogeneous across climatic and topographical conditions. For example, the global monthly rainfall quality index score of rainfall estimated from the GPM IMERG product indicated that large regions (except for the Eastern U.S., Europe, parts of India, parts of South Africa, and Thailand) have high uncertainties in rainfall estimates (Huffman et al., 2018). In these regions, adjustment of GPM IMERG product is suggested (Huffman et al., 2018). When using global datasets on hydrologic impact studies, inconsistent results have been discussed. As compared to the rain gauge driven hydrologic model, several studies indicated that satellite-based precipitation driven hydrologic models have poorly performed in streamflow simulations (Duan et al., 2018; Li et al., 2018; Nguyen et al., 2018); while other studies exhibited an opposite conclusion (considerably outperformed) (Ren et al., 2018; Luo et al., 2019). Based on simulation results from hydrologic models in more than 70,000 catchments worldwide, Beck et al. (2017b) highlighted the importance of selection of precipitation from global datasets in both research and operational applications.

Large-scale validation of global datasets is an area of research that requires more attention, and Vietnam is a compelling example due to the pressing demand for using global datasets to support the development and implementation of new WRM policies. The primary source of hydro-meteorological information to support WRM in Vietnam is still in-situ observations, although these local datasets have limited coverage in both time and space (NAWAPI, 2017b; NAWAPI, 2018). The averaged rain gauge network in Vietnam (about 400 km^2 per gauge) is far behind the standard of the World Meteorological Organization (WMO) (WMO, 1994), especially in the mountainous areas (100-250 km^2 per gauge). The density of the active stream gauge network in Vietnam has decreased more than twice during the past several decades (from ~ 1,900 km^2 per gauge to ~4,000 km^2 per gauge) and is also much lower than WMO's standard (1,000 km^2 per gauge for mountainous areas and 1,870 km^2 per gauge for low-land areas) (Tran Thanh Xuan et al., 2012). Additionally, WRM in Vietnam also faces the challenges of transboundary basins. Among the total areas of the Vietnam River basin (~ 1,100,000 km^2), seventy-two percent of areas and sixty percent of water resources are located outside of Vietnam territory (Nguyen and Bui, 2016; Tran, 2006). Looking at the two largest rivers in Vietnam – the Mekong River and the Red-Thai Binh River, these rivers only have 11% and 51% of total basin areas located in Vietnam, respectively (Tran, 2006).

The global datasets can be complementary to local datasets in quantifying water availability in such a sparse-ground hydro-meteorological network region as Vietnam but very few studies have investigated the usefulness and appropriateness of using these datasets in this region. Most of the studies in Vietnam have been conducted on a typical climate region or a river basin, such as the Srepok River basin (Nguyen et al., 2018), North Vietnam (Hiep et al., 2018; Nguyen, 2021), Ca River basin (Kha et al., 2020). In addition, studies that investigate a combination of multiple global datasets in improving hydrologic simulations are also rare. Ha et al. (2017) is perhaps one of the most notable studies that has taken this approach. The authors attempted to calibrate a hydrological model with multiple objectives using observed streamflow and remotely sensed products of evapotranspiration, and remotely sensed products of leaf area index over two catchments of the Day River Basin. It also found that no study in the Vietnam region has investigated the usefulness of assimilating remotely sensed products to inform the hydrological model – which is also a very promising approach to improve the efficiency of water prediction and forecasting. Low-spatial resolution of satellite-based precipitation products have been discussed as the main limitation on the usage of global datasets in hydrologic applications in several studies in Vietnam (Vu et al., 2018), however, no study attempts to assess high spatial resolutions of global datasets (at a spatial resolution smaller than 10km) in Vietnam region. Soil moisture content is an essential variable in the land surface hydrology model (Sheikh et al., 2009) and is proved as an important factor affecting drought conditions in Vietnam (Le et al., 2019c), but the capabilities of remotely sensed soil moisture product was not investigated for Vietnam's catchments.

This dissertation aims to fill these gaps through four studies that investigate different applications of global datasets in Vietnam. The purpose of these studies was to bring the global datasets closer to the scale of WRM applications that generally require information on water availability at a scale of several square kilometers to hundreds of square kilometers (Sheffield et al., 2018). The insights of this dissertation will be beneficial to water practitioners in developing nations, especially Vietnam, as guidance to decide whether publicly available datasets could be useful, and if so, which data sources would be the most suitable to consider.

The first study (Chapter 2) aims to understand error information of Tropical Rainfall Measurement Mission (TRMM) Multi-satellite Precipitation Analysis (TMPA) on spatio-temporal scale of the Red–Thai Binh River basin, the second largest river basin of Vietnam. Although the Red–Thai Binh River basin plays an essential role in Vietnam's economic and social development, a large proportional area of this basin does not have rain gauges due to complex topography to install instruments or cannot collect the rain gauge network (from upstream countries) due to limited data access. Therefore, it is challenging to estimate rainfall throughout the entire basin if we only use the ground networks. The first objective of this study is to compare two TMPA products (i.e., 3B42V7 and 3B42RT) with ground observation data over the lower part of the Red–Thai Binh River basin (where the ground data is available) to understand the errors of these two products. The second objective is to develop a linear-scaling bias correction using climate–topography indices for both datasets to better estimate rainfall using TMPA products at places where rain gauges are absent.

The second study (Chapter 3) focuses on the capability of a reanalysis product–The Modern-Era Retrospective Analysis for Research and Applications, version 2 (MERRA-2) in capturing drought conditions across Vietnam with different spatial resolutions. Specifically, this study aims to examine a hypothesis question that does high spatial resolution data have the advantages of capturing drought events and drought trends better than low spatial resolution data? The Standardized Precipitation Evapotranspiration Index (SPEI) derived from the MERRA-2 datasets was employed to estimate the drought percentage areas time series and these timeseries were validated with drought records from local authorities.

To further advance applications of satellite-based precipitation estimates in hydrologic modelling, the third study (Chapter 4) proposes a framework to examine eight satellite-based precipitation estimates products in an hydrologic model study. Specifically, these products were forced as precipitation inputs for the Soil and Water Assessment Tool (SWAT) model in simulating streamflow in six different catchments in Vietnam. The simulated streamflow was then compared to the observed streamflow and a good streamflow performance metric from the simulation could be a metric for the usefulness of the precipitation product forcing input. Also, a large number of catchments examined in this study enables us to draw a general conclusion about the suitability of satellite-based precipitation estimates products in hydrologic modelling.

To improve hydrologic model streamflow simulation, we conducted an experiment that assimilates remotely sensed soil moisture products into the top-soil layer (0-500 mm) during the soil water routing process of the hydrological SWAT model (Chapter 5). Eight catchments with different basin sizes, contrasting climate conditions, and varied runoff patterns have been selected to employ the experiment. Two satellite-based soil moisture products – 9km Soil moisture Active and Passive (SMAP) and its downscaled 1km SMAP are investigated to examine whether spatial–temporal resolution has a substantial impact on the performance of the hydrological model to simulate streamflow through a data assimilation framework.

Chapter 2: Comparison and Bias Correction of TMPA Precipitation Products over the Lower Part of Red–Thai Binh River Basin of Vietnam[1]

2.1. Introduction

Precipitation is the most crucial input variable enforced in water prediction models. Reliable precipitation is required for model calibration, forecast, and simulation (Brutsaert, 2005; Kumar and Lakshmi, 2018; Yilmaz et al., 2005). Gauge observation is the primary collection approach to obtain precipitation information (Kidd, 2001). However, gauge network is often sparse and nonexistent in many parts of the globe (Rana et al., 2015; Xie and Arkin, 1996). Moreover, it is often challenging to obtain gauge data, especially in developing countries and transboundary rivers, due to technical and administrative reasons (Gerlak et al., 2011; Plengsaeng et al., 2014; Viglione et al., 2010). In addition, gauge observations only provide point measurements of precipitation and cannot capture the full spatial variability. Space-based precipitation estimations, therefore, have great potential application to enhance the capacity of measuring this vital water cycle component (García et al., 2016; Sun et al., 2018).

Several satellite-derived datasets have been used in previous studies, such as the Tropical Rainfall Measurement Mission (TRMM) Multi-satellite Precipitation Analysis (TMPA) (Huffman et al., 2007), the Precipitation Estimation from Remotely Sensed Information using Artificial Neural Networks (PERSIANN) (Sorooshian et al., 2000), the Climate Hazards Group Infrared Precipitation with Stations (CHIRPS) (Funk et al., 2014), and National Oceanic and Atmospheric Administration/Climate Prediction Centre (NOAA/CPC) morphing technique (CMORPH) (Joyce et al., 2004) products. Among them, TPMA—the first space-borne product of the Earth Science Mission aimed at studying tropical and subtropical rainfall—has performed well in a wide range of applications, such as hydrological modeling (Adjei et al., 2015; Ha et al., 2018; Xue et al., 2013), drought monitoring (Sahoo et al., 2015; Zhang and Jia, 2013), and agronomy (Arvor et al., 2014; Cashion et al., 2005). TMPA products have also been evaluated as having better performance than other satellite-based rainfall products. For example, the TMPA 3B42V7 data is generally a better input in a distributed hydrological model compared to CMORPH and TMPA 3B42RT (real time) for multiple hydrological purposes, including annual water budgeting, monthly and daily streamflow simulation, and extreme flood modeling (Li et al., 2015). Similarity, Tong et al. (2014) showed that 3B42V7 was a better driving force of hydrological model for both monthly and daily streamflow simulation over the Tibetan Plateau compared to CMORPH, PERSIANN, and 3B42RT. Moazami et al. (2013) used six statistical indices and contingency table to evaluate 3B42V7, concluding it was a better estimation of daily precipitation than PERSIAN and 3B42RT over Iran. Simons et al. (2016) identified that monthly TMPA 3B43 rainfall product was the most suitable satellite dataset compared to CHIRPS and CMORPH over the Red River Basin of Vietnam.

[1] This chapter has been published as Le, H. M., Sutton, J. R., Bui, D. D., Bolten, J. D., & Lakshmi, V. (2018). Comparison and Bias Correction of TMPA Precipitation Products over the Lower Part of Red-Thai Binh River Basin of Vietnam. Remote Sensing, 10(10), 1582. https://doi.org/10.3390/rs10101582.

Table 2. 1 Rainfall station descriptions for the ground observation stations over Red–Thai Binh River Basin (March 2000–December 2016).

No	Station Name	Long. (°)	Lat. (°)	Elev. (m)	AR (mm/year)	SDR (mm/day)	NRD (day)
1	Baccan	105.82	22.13	241	1389	11.29	250
2	Bacninh	106.05	21.20	8	1537	13.27	248
3	Baolac	105.67	22.95	348	1201	9.91	263
4	Caobang	106.23	22.67	244	1417	11.5	251
5	Dienbien	103.02	21.40	487	1535	11.75	248
6	Hagiang	104.98	22.82	117	2333	17.15	222
7	Bavi	105.37	21.08	535	1791	14.61	234
8	Lang	105.85	21.02	17	1686	14.5	246
9	Phuxuyen	105.90	20.77	9	1516	13.16	272
10	Sontay	105.50	21.13	14	1600	13.27	244
11	Chilinh	106.38	21.07	1	1489	12.51	250
12	Haiduong	106.30	20.95	3	1530	13.6	249
13	Hoabinh	105.33	20.82	48	1861	14.69	239
14	Maichau	105.07	20.60	579	1859	18.79	251
15	Muongte	102.63	22.47	354	2433	17.1	229
16	Tamduong	103.15	22.05	303	2333	14.49	216
17	Chilang	106.57	21.65	124	1324	11.9	267
18	Langson	106.77	21.83	263	1315	11.55	253
19	Thatkhe	106.47	22.25	157	1484	12.33	243
20	Vanmich	106.37	22.10	238	1341	11.33	240
21	Laocai	103.95	22.50	152	1810	14.11	229
22	Ninhbinh	105.98	20.27	3	1725	15.16	242
23	Baichay	107.03	20.97	59	1898	17.93	246
24	Mongcai	107.97	21.52	7	2735	24.5	230
25	Tienyen	107.44	21.33	16	2139	19.04	231
26	Sonla	103.90	21.33	709	1364	10.96	252
27	Thainguyen	105.50	21.60	784	1760	15.02	238
28	Tuyenquang	105.20	21.82	29	1575	14.02	242
29	Yenbai	104.87	21.70	41	1796	14.97	222

Note: "AR" Annual Rainfall, "SDR" Standard Deviation of Rainfall, "NRD" No. of rain days

Differences between TMPA products and rain gauge observation analysis have been a cause of concern recently. Zad et al. (2018) pointed out that 3B42V7 tended to overestimate rainfall measurement by approximately 26.95% at Pahang River Basin of Malaysia and that 3B42V7 was likely to have a high accuracy of detecting rainfall events at high-altitude and mid-altitude areas compared to low-altitude regions. Kneis et al. (2014) analyzed that 3B42V7 and 3B42RT datasets were moderately correlated with their gauged-based counterpart at sub-basin level (4000 to 16,000 km^2) at the lower Mahanadi River Basin of India but that the 3B42V7 and 3B42RT data often do not reflect gauge observation at high-intensity level (>80 mm/day). The TMPA product is also likely to perform better on a monthly scale when compared to the ground data. Curtarelli et al. (2014) found that monthly 3B43 dataset had a great consistency (correlation coefficient >0.97) with ground observation data over the Itumbiara Reservoir drainage area in Central Brazil but that 3B43 tended to overestimate rainfall by 1.24%. Comparing monthly 3B43 dataset with 56 observations in Yangtze River Delta, Cao et al. (2018) also showed an inclination of 3B43 to overestimate monthly rainfall, with the bias ranging between −10% and 10% most of the study area; its correlation coefficient with observation was found to peak in March (0.96) and reach bottom in August (0.79). Although the TRMM satellite has not been operated since 2014, TMPA products are still being generated regardless (Huffman, 2016).

Following the highly successful TMPA, the Global Precipitation Measurement (GPM) mission was developed to continuously increase precipitation estimation over most of the globe (Huffman et al., 2018). A range of studies in many regions have demonstrated that GPM outperforms TMPA by having a better spatial resolution, coverage area, and lower systematic bias error (He et al., 2017; Kim et al., 2017; Xu et al., 2017). However, GPM has only been available for a short time (since 2014), while TMPA products date back to January 1998. In addition, GPM is just a slight improvement over TMPA products (Tan and Duan, 2017). Huffman et al. (2018) aim to extend the GPM data to the same length as the longest TMPA data. Therefore, assessments on TMPA products are of paramount importance to gain insights into their performance at various regions so that their algorithms can be improved and the next generation GPMs can be developed.

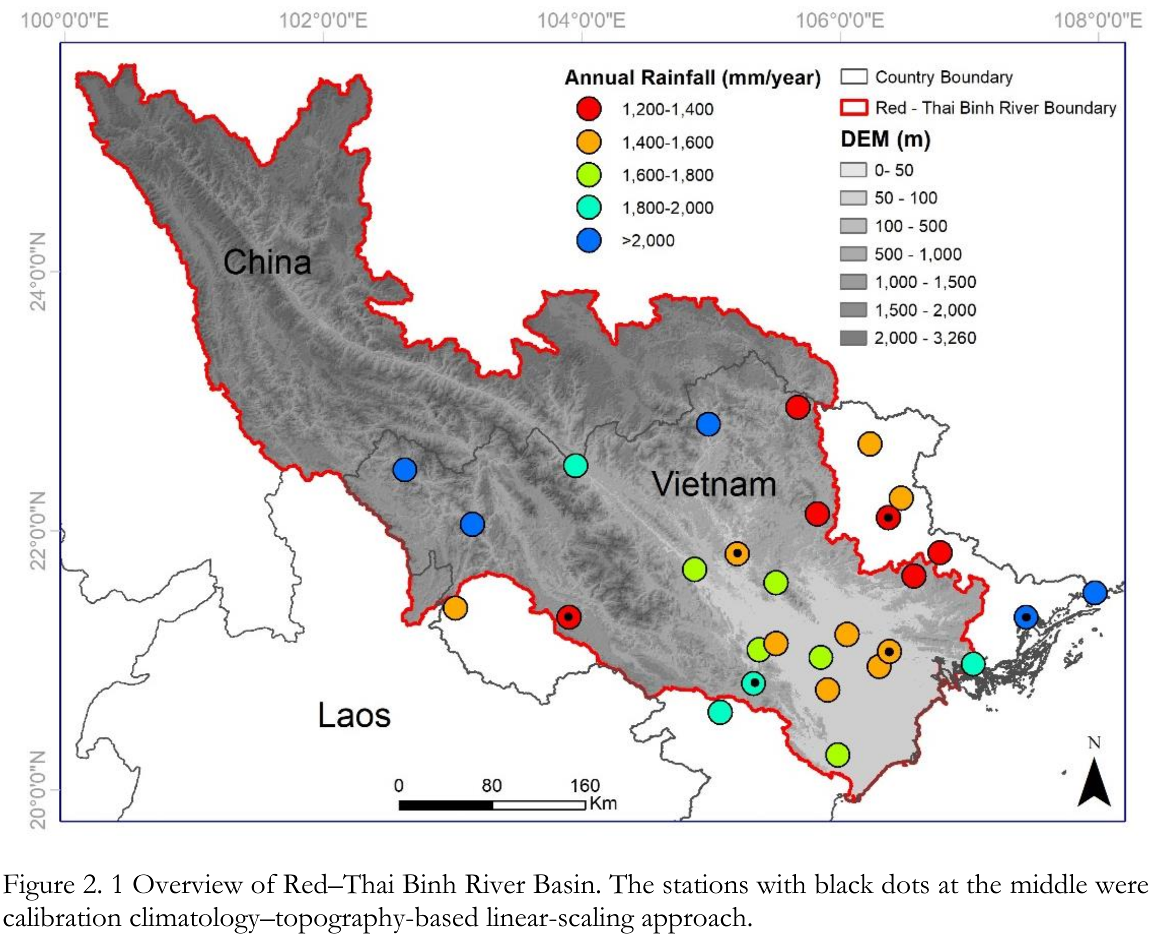

Figure 2. 1 Overview of Red–Thai Binh River Basin. The stations with black dots at the middle were used for calibration climatology–topography-based linear-scaling approach.

While there is a clear advantage of having a high temporal and spatial resolution using TMPA products, extra work is required because bias correction needs to be performed prior to application of any TMPA products in environmental, water resources, and ecological studies (Zad et al., 2018).

Climatology and topography are likely factors to induce errors in remote sensing retrievals (Khan et al., 2014). Consequently, their effects on the quality of TMPA products are inevitable. Based on the moderate inverse linear relationship between the monthly 3B43 bias and elevation, Hashemi et al. (2017) developed a linear model between 3B43 bias and elevation, especially for stations that have elevations above 1500 m above mean sea level in the U.S. The corrected monthly 3B43 product showed a significant improvement in the high elevation area. Thus, the empirical bias correction model using climatology and topography seems to be a potential investigation direction, although relatively little research has been conducted so far.

In Vietnam, ground observations provide poor spatial and temporal measurement of rainfall due to the lack of a dense network for rain gauge measurement. The average rain gauge network in Vietnam is around 400 km^2 per rain gauge, which is below the World Meteorological Organization standard (area per rainfall station of 100–250 km^2 for mountainous areas; area per rainfall station of 600–900 km^2 for lowland areas) (WMO, 1994). Moreover, the rain gauge distribution in Vietnam is uneven, with insufficient gauged stations at high elevation areas. According to the Vietnam Meteorological and Hydrological Administration, most rain gauge stations (75%) are concentrated at low elevation areas (<200 m), which only cover half of Vietnam's land (Dang Dinh Duc, 2017). With these perspectives, satellite-based precipitation is an indispensable alternative source of precipitation data for Vietnam. Preliminary studies on satellite-based precipitation products in the country have been conducted recently. However, these studies either focused on monthly rainfall (Poortinga et al., 2017; Simons et al., 2016) or used directly satellite-derived rainfall without bias correction analysis (Nguyen et al., 2018). Therefore, further research on satellite-based precipitation products is still of fundamental importance for the country.

This study selected the Red–Thai Binh River Basin—one of the largest river systems in Vietnam—as a case study. Although it plays an essential role in Vietnam's economic and social development, many parts of this basin do not have rainfall monitoring from ground, causing difficulties for basin rainfall estimation and water resources management. The first objective of this study was to compare the TMPA products 3B42V7 and 3B42RT with ground observation data over Red–Thai Binh River Basin in various aspects, such as calculating error statistics on a daily scale, monthly scale, dry and wet seasons, detecting rainfall events ability, and evaluating rainfall intensity. The second objective was to develop a linear-scaling bias correction model using climate–topography indices for both 3B42V7 and 3B42RT datasets. The results of the assessment and bias correction of TMPA precipitation products could help in supporting its potential application in hydrological modeling and drought monitoring in the studied region.

2.2. Materials

2.2.1. Study Area

The Red–Thai Binh River Basin is a transboundary river that flows through three countries—Vietnam, China, and Laos—with a total area of 169,000 km^2 (Figure 2. 1). The area of this in Vietnam is 88,680 km^2, which makes up 51.3% of the total area. In this study, due to the lack of observation data, description of water resource characteristics and evaluation results of TMPA 3B42V7 and TMPA 3B42RT data only focused on the Vietnamese part of the basin. There are two primary river systems in the Red–Thai Binh River. The Red River system originates in China and flows into Vietnam through three main tributaries—Da, Lo, and the Thao River—while the Thai Binh River system is entirely located in Vietnam. The Red–Thai Binh River belongs to a tropical climate with two distinct seasons: the wet season and the dry season. The total annual rainfall is approximately 1700 mm, with high rainfall amounts (>2000 mm) observed in the mountainous areas between the Vietnam and China border. The annual total flow of the Red–Thai Binh River is 131.4 billion m^3—the Chinese territory part generates 48.3 billion m^3, while the rest 83.1 billion m^3 is generated in the Vietnamese side (NAWAPI, 2017b). As the second largest river system in Vietnam, the Red–Thai Binh River is home to 29.1 million Vietnamese (2015 figure), making up for 22.6% of Vietnam's GDP (2010 figure) (General Statistics of Vietnam) (NAWAPI, 2017a).

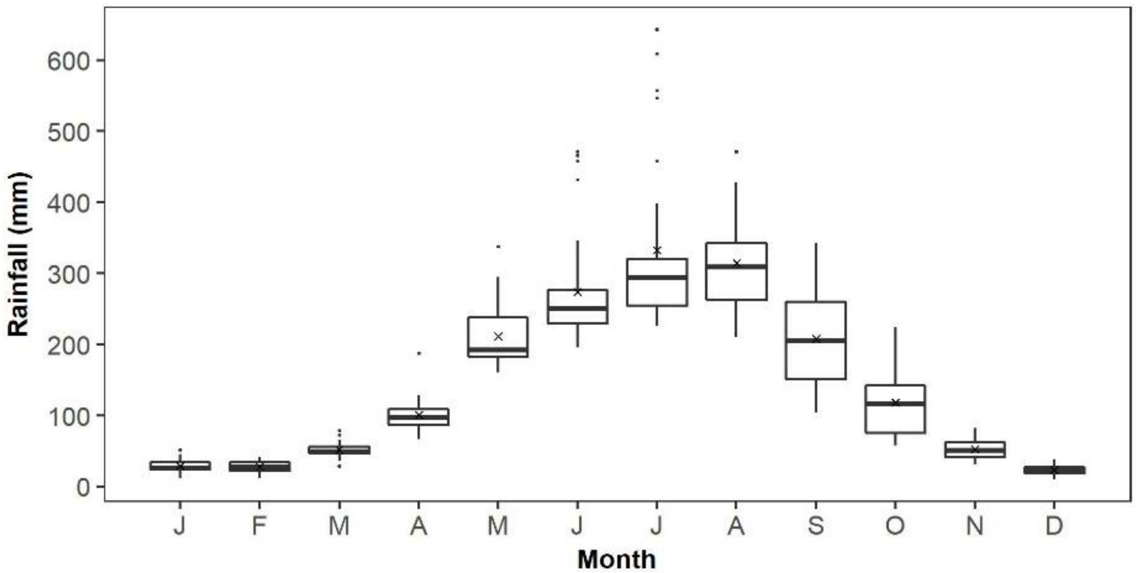

Figure 2. 2 Monthly rainfall distribution over Red–Thai Binh River Basin (March 2000–December 2016). Cross symbol indicates average monthly rainfall.

2.2.2. Data

2.2.2.1. Observation Data

Rainfall measurements from a total of 29 daily rainfall stations (March 2000 to December 2016) within or neighboring the basin were collected from the Vietnam Meteorological and Hydrological Administration. The distribution of rainfall stations is presented in Figure 2. 1, and their characteristics can be found in Table 2. 1. The stations were selected due to their reliable data and low missing values (5–10%).

In Vietnam, daily ground rainfall data is often collected twice per day at 7.00 a.m. UTC + 7 and 7.00 p.m. UTC + 7, and the daily accumulation is calculated as accumulated rainfall from 7.00 p.m. UTC + 7 to the same time next day (MONRE, 2012). Figure 2. 1 shows monthly rainfall distribution over Red–Thai Binh River Basin from gauge observation data. Wet season (May–October) has a high amount of rainfall, accounting for 85–90% of total annual rainfall. Very high amounts of rainfall are often observed during June, July, and August. During these periods, tropical storms often occur, with the accumulated rainfall reaching 200–600 mm within several days (NAWAPI, 2017a). During the dry season (November–April), the total amount of rainfall only accounts for 10–15% of total annual rainfall.

2.2.2.2. TMPA Products

The TRMM is a low Earth orbits (LEO) satellite with sensors used to analyze and understand the characteristics of precipitation. The satellite is equipped with various instruments, such as Precipitation Radar (PR), TRMM Microwave Imager (TMI), Visible and Infrared Scanner (VIRS), and Lightning Imaging Sensor (LIS) (Huffman et al., 2007). The spatial coverage of TRMM is mainly in tropical and subtropical zones (50°S to 50°N) from an altitude of 400 km. The TMPA products used in this study were TMPA 3B42V7 and its real-time version TMPA 3B42RT at 0.25° spatial resolution. Detailed description of 3B42V7 can be found in Reference (Huffman et al., 2007) and that of 3B42RT can be found in Reference (Huffman and Bolvin, 2013). The 3B42V7 dataset ranges from January 1998 to present, while the 3B42RT product ranges from March 2000 to present. However, for comparison purpose, a consistent data length was required and data was therefore collected from March 2000 to December 2016 for both TMPA 3B42V7 and TMPA 3B42RT. Both products were downloaded through NASA Goddard Space Flight Center (https://pmm.nasa.gov/data-access/downloads/trmm/). In order to match the satellite rainfall products with the daily precipitation gauge data, the 3-hourly 3B42 products were accumulated to daily values at 12.00 UTC (equivalent to 7.00 p.m. UTC + 7).

2.3. Method

The comparison of TMPA 3B42V7 and TMPA 3B42RT precipitation against the ground observation data involved the extraction of data time series of TMPA products at the corresponding locations of the 29 meteorological stations. As one TMPA pixel contained one rainfall station, a total of 29 TMPA pixels were extracted to form the time series corresponding to the ground observation data.

2.3.1. Error Metric Assessment

To compare rainfall values between TMPA products and ground observation data, widely accepted error metrics—correlation coefficient (CC), Nash–Sutcliffe efficiency (NSE), root mean square error (RMSE), and percent bias (PBIAS)—were used (Legates and McCabe, 1999; Moriasi et al., 2007). The formulas for the statistical metrics are presented as follows:

$$CC = \frac{\sum_{i=1}^{N}(OBS_i - \overline{OBS})(TMPA_i - \overline{TMPA})}{\sqrt{\sum_{i=1}^{N}(OBS_i - \overline{OBS})^2 \sum_{i=1}^{N}(TMPA_i - \overline{TMPA})^2}} \tag{2.1}$$

$$NSE = 1 - \frac{\sum_{i=1}^{N}(TMPA_i - OBS_i)^2}{\sum_{i=1}^{N}(OBS_i - \overline{OBS})^2} \tag{2.2}$$

$$RMSE = \sqrt{\frac{1}{N}\sum_{i=1}^{N}(TMPA_i - OBS_i)^2} \tag{2.3}$$

$$PBIAS = 100\,\frac{\sum_{i=1}^{N}(TMPA_i - OBS_i)}{\sum_{i=1}^{N} OBS_i} \tag{2.4}$$

where N is the total of samples, OBS_i and $TMPA_i$ represent the rainfall values for the ground observation data and the TMPA data, respectively, and $\overline{OBS}$ and $\overline{TMPA}$ represent the mean of the corresponding variables. CC ranges from −1 to 1, with strong positive correlation when the CC value is closer to 1 and strong negative correlation when the CC value is closer to –1. NSE varies between $-\infty$ to 1, indicating how well the plot of satellite product values and ground values fit the 1:1 line. A NSE value closer to 1 indicates a more perfect match between satellite product and ground data. RMSE is unit-based and would shed further light on the accuracy of the TMPA products. PBIAS measures the average tendency of the satellite values to be larger or smaller than the corresponding ground observations.

Table 2. 2 Contingency table to measure the correspondence between ground observation data and Tropical Rainfall Measurement Mission Multi-satellite Precipitation Analysis (TMPA) product concerning the threshold intensity of 0.6 mm/day of a point-to-point event (Wilks, 2006).

		Ground Observation	
		Yes	**No**
TMPA Product	Yes	Hit	False Alarm
	No	Miss	Correct Rejection

2.3.2. Detection Metric Assessment

The probability of detection (POD), false alarm ratio (FAR), the probability of false detection (POFD), and critical success index (CSI) were used to compare the occurrence and nonoccurrence of rainfall events between TMPA products and ground data (Schaefer, 1990; Xu et al., 2017; Zad et al., 2018). The POD was the ratio of the total number of rainfall events correctly detected by the TMPA products to the total number of actual rainfall events. The FAR evaluated the ratio of the number of rainfall falsely detected by the TMPA products to the total rainfall events estimated by the TMPA products. The POFD was a fraction of false events detected by the TMPA products versus the correct observations of no rainfall events by the TMPA products. The CSI, which is a function of POD and FAR, was the most accurate detection metric. The rainfall day threshold was set as 0.6 mm/day, which was defined as a threshold between no rainfall event and low rainfall event within 24 h based on long-term rainfall analysis over Vietnam (NCHMF, 2000). These detection metrics can be computed as follows:

$$POD = \frac{Hits}{Hits + Misses} \tag{2.5}$$

$$FAR = \frac{False\ Alarms}{Hits + False\ Alarms} \tag{2.6}$$

$$POFD = \frac{False\ Alarms}{False\ Alarms + Correct\ Rejections} \tag{2.7}$$

$$CSI = \frac{Hits}{Hits + False\ Alarms + Misses} \tag{2.8}$$

The Hit, Miss, False Alarm, and Correct Rejection are presented in a contingency table in Table 2. 2. The perfect scores of the POD and CSI are 1, while the perfect scores of the POFD and FAR are 0.

2.3.3. Rainfall Intensity Evaluation

To evaluate the rainfall intensity, we used probability density function (PDF) to classify the daily rainfall amounts into six categories based on Vietnam's regulation on rainfall classification (NCHMF, 2000): (1) 0 to 0.6 mm; (2) 0.6 to 6 mm; (3) 6 to 16 mm; (4) 16 to 50 mm; (5) 50 to 100 mm; (6) >100 mm. The PDF analysis has been previously applied for comparing satellite rainfall products and ground data in several studies (Tan and Duan, 2017; Xu et al., 2017).

2.3.4. Climate–Topography-Based Linear-Scaling (CTLS) Bias Correction Approach

The linear-scaling (LS) approach (Lenderink et al., 2007; Teutschbein and Seibert, 2012) was based on monthly correction factor, which was the ratio between long-term monthly mean data for ground observation and TMPA.

$$CF_m = \frac{\overline{OBS}_m}{\overline{TMPA}_m} \tag{2.9}$$

$$TMPA_{i,m}^{corrected} = TMPA_{i,m} \times CF_m \tag{2.10}$$

where CF_m is the monthly mean change factor at month m, $\overline{OBS}_m$ and $\overline{TMPA}_m$ represent the mean of ground observation and TMPA data at month *m*, respectively. $TMPA_{i,m}^{corrected}$ and $TMPA_{i,m}$ are the corrected TMPA data and original TMPA data at day i of month m, respectively. In this study, we developed a set of multiple linear models that predicted correction factors CF_m from climatology–topography characteristics. We acquired station information as longitude (LONG), latitude (LAT), elevation (ELEV), annual rainfall (AR), standard deviation of rainfall (SDR), and the number of rainfall day (NRD). The CF_m can be computed as follows:

$$CF_m = \alpha_{0m} + \alpha_{1m}LONG + \alpha_{2m}LAT + \alpha_{3m}ELEV + \alpha_{4m}AR + \alpha_{5m}SDR + \alpha_{6m}NRD \tag{2.11}$$

where $\alpha_{0m}, \alpha_{1m}, \alpha_{2m}, \alpha_{3m}, \alpha_{4m}, \alpha_{5m}, \alpha_{6m}$ are regression coefficients corresponding to correction factor at month *m*. In other words, we developed a set of 12 multiple linear models to estimate correction factors from climatology–topography data. In order to select the most suitable candidates for each multiple linear model, we analyzed the relationship between the correction factor and climatology–topography for a single month and selected the significant correlation candidates. We used 23 meteorological stations (80%) to develop the abovementioned multiple linear models and six meteorological stations (20%) to verify the models.

2.4. Results and Discussion

2.4.1. Comparison between TMPA Products and Ground Observation Data

2.4.1.1. Daily and Monthly Scale Assessment

Table 2. 3 presents the TMPA 3B42V7 and TMPA 3B42RT data in daily scale and monthly scale performance over the Red–Thai Binh River compared to the ground observation stations for 17 years (March 2000–December 2016). The results showed that daily rainfalls from both 3B42V7 and 3B42RT had very weak correlations with the ground observation data; the average of the CC and the average of NSE were 0.387 and −0.152 for 3B42V7 data and 0.304 and −0.521 for 3B42RT data, respectively.

The negative NSE values demonstrated that TMPA values were less accurate than the mean of observed data and were therefore very poor estimations.

Table 2. 3 Descriptive statistics for observation rain gauge and TMPA data in daily and monthly scale.

	n	TMPA 3B42V7						TMPA 3B42RT					
		Daily Scale			Monthly Scale			Daily Scale			Monthly Scale		
		Max	Min	Mean	Max	Min	Mean	Max	Min	Mean	Max	Min	Mean
CC	29	0.510	0.320	**0.387**	0.959	0.833	**0.896**	0.395	0.216	**0.304**	0.900	0.731	**0.842**
NSE	29	0.207	−0.507	**−0.152**	0.884	0.593	**0.765**	0.002	−0.968	**−0.521**	0.792	0.131	**0.480**
RMSE	29	21.7	11.4	**15.1**	111.6	36.2	**66.5**	24.5	13.7	**17.3**	143.6	76.4	**96.0**
PBIAS	29	33.2	−21.5	**3.2**	33.2	−21.5	**3.2**	38.5	−18.1	**14.8**	38.5	−18.1	**14.8**

Note: n is total number of stations. RMSE unit on a daily scale is mm/day. RMSE unit on a monthly scale is mm/month.

Table 2. 4 Descriptive statistics for daily and monthly observation rain gauge and those of TMPA data during the dry and wet seasons.

	n	TMPA 3B42V7						TMPA 3B42RT					
		Dry Season			Wet Season			Dry Season			Wet Season		
		Max	Min	Mean	Max	Min	Mean	Max	Min	Mean	Max	Min	Mean
Daily													
CC	29	0.487	0.289	**0.407**	0.494	0.264	**0.344**	0.423	0.196	**0.317**	0.364	0.141	**0.255**
NSE	29	−0.048	−0.884	**−0.325**	0.185	−0.601	**−0.201**	−0.076	−1.237	**−0.612**	−0.031	−1.107	**−0.598**
RMSE	29	8.8	5.8	**7.0**	29.1	14.7	**20.0**	10.2	6.4	**7.7**	32.8	17.9	**22.9**
PBIAS	29	18.9	−38.6	**−10.4**	37.2	−19.4	**6.1**	31.7	−47.3	**−14.1**	43.2	−13.3	**20.7**
Monthly													
CC	29	0.957	0.657	**0.827**	0.924	0.588	**0.796**	0.873	0.551	**0.718**	0.817	0.358	**0.691**
NSE	29	0.881	0.191	**0.586**	0.788	0.276	**0.566**	0.672	−0.381	**0.199**	0.618	−0.845	**0.009**
RMSE	29	44.9	16.8	**29.0**	152.8	48.0	**88.7**	57.1	26.7	**41.0**	198.3	100.6	**128.6**
PBIAS	29	18.9	−38.6	**−10.4**	37.2	−19.4	**6.1**	31.7	−47.3	**−14.1**	43.2	−13.3	**20.7**

Note: n is the total number of stations. RMSE unit on a daily scale is mm/day. RMSE unit on a monthly scale is mm/month.

The statistics metric for monthly scale showed a significant improvement for both 3B42V7 and 3B42RT compared to ground data (Table 2. 3). However, the PBIAS did not change from a daily to monthly scale. Monthly 3B42V7 and monthly 3B42RT had similar CC, with an average value of 0.896 and 0.842, respectively. However, monthly 3B42V7 data greatly outperformed monthly 3B42RT data regarding NSE, RMSE, and PBIAS. Average NSE of monthly 3B42V7 was 0.765 and no single station had a value smaller than 0.5, while average NSE of monthly 3B42RT was only 0.480. The monthly CC and NSE scores of 3B42V7 compared to ground data in this case study were very similar to the results of monthly 3B43 data compared to observations in the same basin (Simons et al., 2016). Average RMSE of monthly 3B42V7 was 66.5 mm/month, equivalent to 30% less than the figure of monthly 3B42RT. Average PBIAS of monthly 3B42V7 was approximately 5 times less than that of monthly 3B42RT, with values of 3.2% and 14.8% respectively. The positive of PBIAS also indicated that both TMPA products overestimated compared to ground observation data. This finding was consistent with the study at the Black Volta Basin of West African countries (Adjei et al., 2015) or Pahang River Basin of Malaysia (Zad et al., 2018), but it was contrary to the study in Iran (Alijanian et al., 2017). It should be mentioned that although belonging to the same South East Asia region, the

3B42V7 data over the Red–Thai Binh River Basin performed better than that for Malaysia's basin as the PBIAS of 3B42V7 for Malaysia's basin was up to 26.95% on average (Zad et al., 2018).

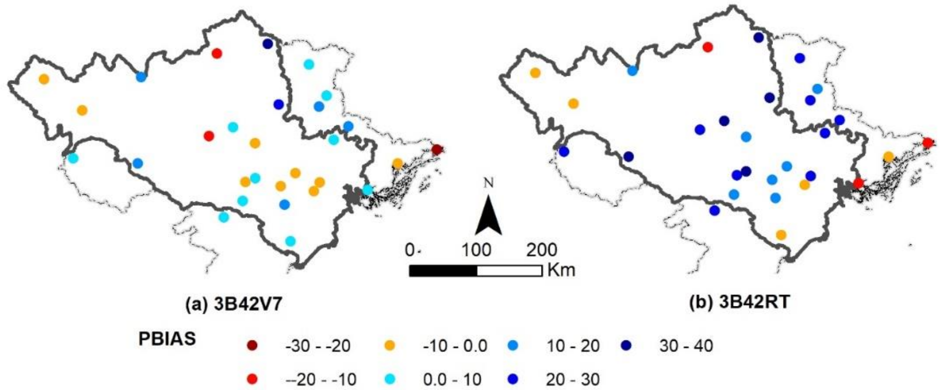

Figure 2. 3 Percentage bias (PBIAS) score's spatial performance of TMPA products (**a**) 3B42V7 and (**b**) 3B42RT against observation data on both daily and monthly scales from March 2000 to December 2016 over Red–Thai Binh River Basin. The grey line is the Red–Thai Binh River Basin boundary within the Vietnam territory.

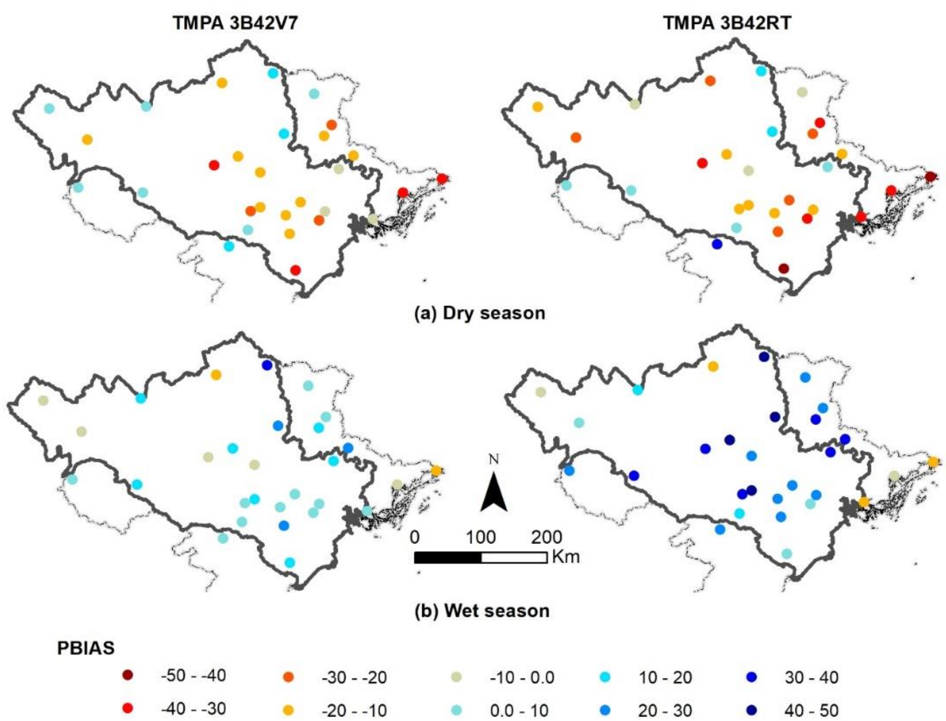

Figure 2. 4 PBIAS score's spatial performance of TMPA rainfall data against observation data during (**a**) the dry and (**b**) the wet season from March 2000 to December 2016 over the Red–Thai Binh River Basin. The grey line is the Red–Thai Binh River Basin boundary within Vietnam territory.

We calculated various error metrics—CC, NSE, RMSE, and PBIAS. However, for TMPA's spatial performance purpose, we only showed the spatial PBIAS score distribution. There were two reasons for this: (1) PBIAS is recommended in water resources planning projects because the overall difference between observed and estimated values is a criteria of paramount importance (NAWAPI, 2018); (2)

PBIAS is precisely aimed at defining a poor model performance and has immense variation between seasons (Gupta et al., 1999).

Looking at the PBIAS distribution, the PBIAS of 3B42V7 data mostly ranged within ±10%, while the PBIAS of 3B42RT data mostly fell in the range of 10–40% (Figure 2. 3). The poor performance of 3B42RT data was observed at the center of the Red–Thai Binh River Basin. Moderate performances for both TMPA products were found at the northwestern mountainous area between Vietnam and Chinese border as well as the northeast coastal area.

Figure 2. 5 Average rainfall detection measurement of TMPA 3B42V7 and TMPA 3B42RT over the Red–Thai Binh River Basin from March 2000 to December 2016.

2.4.1.2. Dry and Wet Season Assessment

Table 2. 4 presents the performances of both daily and monthly 3B42V7 and 3B42RT during the dry season (November–April) and wet season (May–October) over the Red–Thai Binh River Basin. Generally, 3B42V7 data was better than 3B42RT data in all statistical metrics compared to ground

stations, especially NSE, RMSE, and PBIAS. For example, monthly 3B42V7 had moderate NSE metric compared to ground observation, with averages of 0.586 and 0.566 in the dry season and wet season, respectively. In contrast, the figures of monthly 3B42RT were quite low, with 0.199 and 0.009, respectively. Interestingly, although RMSE of daily 3B42V7 during both dry and wet seasons were quite similar to those of daily 3B42RT, aggregation daily 3B42V7 to monthly was significantly less than monthly 3B42RT during both dry and wet seasons, with a reduction of approximately 30% for each. Regarding PBIAS, 3B42V7 and 3B42RT had almost the same bias during the dry season; however, in the wet season, 3B42V7 had significantly low PBIAS, with a value of 6.1% compared to 20.7% PBIAS of 3B42RT. In regard to the dry and wet seasons, although CC and NSE were slightly higher during the dry season than during the wet season, it was not clearly evident. On the other hand, RMSE during the dry season was observed to be much smaller than during the wet season. This can be explained as dry season receives a small amount of rainfall (10–15% of total annual rainfall), and its rainfall variation is not high as the fluctuation during the wet season.

Both TMPA products showed overall negative PBIAS values during the dry season and overall positive PBIAS values during the wet season, indicating overall underestimations during the dry season and overall overestimations during the wet season. 3B42V7 was observed to underestimate ground observation at 20 out of 29 stations, and this figure was 24 out of 29 stations for 3B42RT (Figure 2. 4). When we used scatter plot to compare monthly dry season of TMPA products and that of ground observation (data not shown), we found that TMPA products reported zero values in many months. The wrong no-rainfall reported by TMPA data was also found at Chindwin River Basin of Myanmar (Yuan et al., 2017). The underestimation of TMPA rainfall during the dry season was consistent with previous studies in Southwestern of China (Hu et al., 2014). On the other hand, during the wet season, 22 out of 29 stations experienced overestimations for 3B42V7 data and 24 out of 29 stations experienced overestimation for 3B42RT data. The northwest mountain region and the northeast coastal area were the only places where both TMPA products underestimated ground observation data during two seasons. The overestimation of rainfall during the wet season agreed with a case study in Malaysia (Zad et al., 2018) but was contrary to a study involving the southwestern region of China (Hu et al., 2014).

Although they had a generally positive PBIAS score, TMPA products seemed to underestimate large rainfall amounts. One possible explanation for this could be their spatial resolution. With a rather low 0.25° spatial resolution (approximately 25 km), rainfall observed in a grid was averaged over about 625 km^2. However, rainfall can vary dramatically even with a few kilometers, and the resolution of TMPA products are often unable to pick up these differences. If we consider the complexity of terrain, this variation can be harder to estimate. Additionally, many convective storms can have a rapid evolution that a satellite will often not be able to observe accurately (Ebert et al., 2007).

2.4.1.3. Rainfall Detection Assessment

The capacity of 3B42V7 and 3B42RT data regarding rainfall detection over the Red–Thai Binh River Basin from March 2000 to December 2016 is presented in Figure 2. 5. Generally, the detection capacity of daily TMPA products during the wet season was much better than during the dry season, and 3B42V7 data had slightly better score than 3B42RT data. This may be associated with the temporal resolution of TMPA data as short-duration rainfall events are a typical characteristic of the dry season. Indeed, with 3-hourly products, it is easy for TMPA to miss events lasting less than this figure. On the other hand, TRMM is meant to capture and estimate convective precipitation rather than other types because of its on-board sensors. In Vietnam, precipitation is generally associated with heavier storms and cloud coverage during the wet season (Nguyen et al., 2014), meaning the precipitation is more likely to be detected. In contrast, in the dry season, there will be much lighter rainfall with less cloud coverage and convection, meaning that it will be more difficult to detect (Ebert et al., 2007).

The POD for the whole daily TMPA data was stable over the years, with the average values of about 0.61 and 0.58 for 3B42V7 and 3B42RT, respectively. The POD scores for the daily time series in the wet season period were higher, with average values of 0.71 and 0.69 for 3B42V7 and 3B42RT, respectively. The POD scores of 3B42V7 and 3B42RT for the daily time series in the dry season period were typically low, with average values of 0.32 and 0.30, respectively. In the year 2012, the POD scores during the dry season were the lowest at about 0.2. The FAR of the daily time series and the daily values in wet season were moderate, with average values of 0.37 and 0.36 corresponding to 3B42V7 and 0.40 and 0.38 corresponding to 3B42RT. However, the FAR of the time series in the dry season was high, with an average of 43% of 3B42V7 rainfall prediction being wrong (FAR = 0.43). The wrong prediction of 3B42RT was even more than that of 3B42V7, with average FAR being 0.50. Interestingly, FAR scores of 3B42V7 and 3B42RT had great fluctuation over the years, reaching 0.6 and 0.62 in the year 2000, respectively, but the wrong prediction was reduced to only 0.30 for 3B42V7 and 0.42 for 3B42RT in the year 2014. The POD scores were moderate for both TMPA products, with average values of 0.15 and 0.16 for 3B42V7 and 3B42RT, respectively. The POD scores during the dry season were relatively low, with all years reporting values less than 0.1 for both TMPA products. During the wet season, POD scores were higher than those of the dry season, with a range of 0.2–0.3. The CSI scores showed that there was no single year during the study time where the CSI scores of both 3B42V7 and 3B42RT were over 0.5. During the wet season, the average CSI values were around 0.52 and 0.50 for 3B42V7 and 3B42RT, respectively. Regarding the dry season, the CSI were only about 0.24 and 0.21 for each TMPA product, and the lowest CSI scores in the dry season were observed in 2006 and 2012.

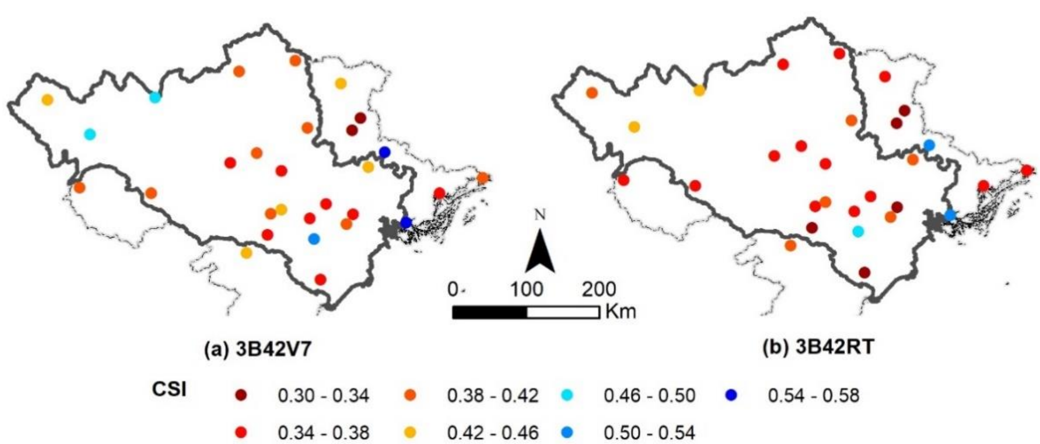

Figure 2. 6 Critical success index (CSI) score's spatial performance of TMPA rainfall data against observation data from March 2000 to December 2016 over the Red–Thai Binh River basin. The grey line is the Red–Thai Binh River Basin boundary within Vietnam territory.

As CSI combines different aspects of POD and FAR to give an overall assessment of TMPA performance, we used this metric to investigate the detection metric of TMPA products on the spatial scale (Figure 2. 6). The lowland central part of the basin experienced the worst CSI score, while the northwestern mountainous part of the basin had moderate CSI score (>0.5). The better detection capacity at high elevation region than the lower land area was consistent with the study in Malaysia's basin (Zad et al., 2018).

2.4.1.4. Rainfall Intensity Analysis

The rainfall frequency distributions of ground observations, 3B42V7, and 3B42RT over the Red–Thai Binh River Basin are presented in Figure 2. 7. Generally, rainfall intensity of both TMPA products followed the intensity of ground observations for the whole time series. Based on ground observation data, no rainfall (≤0.6 mm/day) accounted for 68.8% of total rainfall events, and 3B42V7 and 3B42RT data had similar figures. During the dry season, low rainfall intensity (0.6–6 mm/day) detected by TMPA datasets were relatively low (4.8% and 5.3% corresponding to 3B42V7 and 3B42RT) compared to the figure from ground measurement (13.1%). However, the no rainfall (≤0.6 mm/day) detected in the dry season was a different situation. The 3B42V7 estimated 86.4% of daily rainfall events during this season as no rainfall. Similarly, 88% of rainfall events during the dry season were considered as no rainfall events by 3B42RT. In contrast, the observations data only reported a figure of 79%. During the wet season, the no rainfall events by 3B42V7 and 3B42RT were relatively low (approximately 52% for both products), while the figure for observation data was nearly 60%. Regarding high rainfall events (50–100 mm/day) and heavy rainfall events (>100 mm/day), TMPA products had a high accuracy of detecting these, with the PDFs of both TMPA products almost the same as those of observation. The slight underestimation of low rainfall event (0.6–6 mm/day) was contrary to the overestimation conclusion of this rainfall intensity in a case study in Singapore (Tan and Duan, 2017).

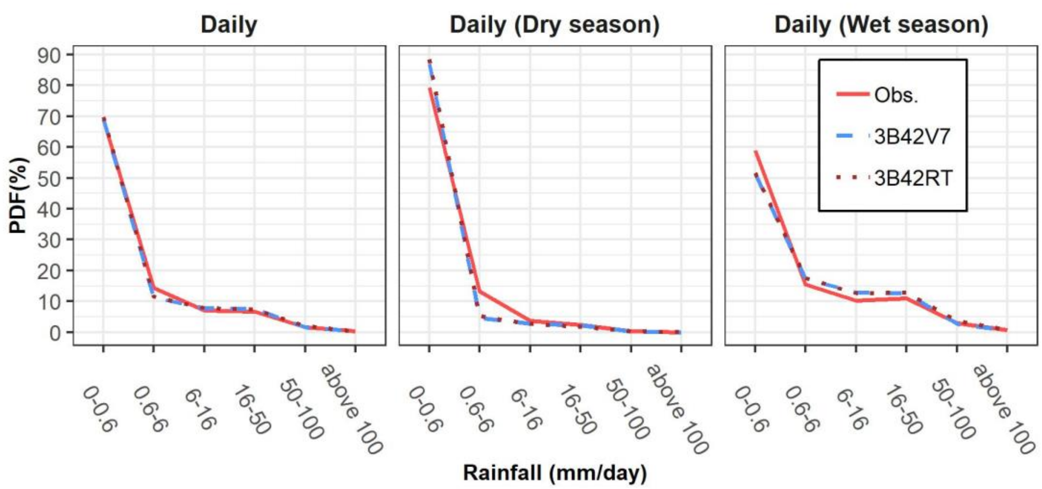

Figure 2. 7 Average probability density function (PDF) of ground observation, TMPA 3B42V7, and TMPA 3B42RT for rainfall in daily, daily (dry season), and daily (wet season) over the Red–Thai Binh River Basin from March 2000 to December 2016.

As no rainfall and low rainfall intensity during the dry season and wet season experience significant differences between ground observations and TMPA data, we exploited the differences by analyzing seasonal spatial low rainfall and light rainfall's intensity of TMPA products. PDF differences between each TMPA data and ground observation were calculated and are presented in Figure 2. 8. The 3B42V7 and 3B42RT data had similar characteristics, which overestimated no rainfall during the dry season (10–15%) and low rainfall intensity during the wet season (0–5%). On the other hand, the TMPA products underestimated no rainfall during the wet season (10–13%) and low rainfall intensity during the dry season (10–15%). It was noticed that the above characteristics occurred similarly for areas throughout the basin and were not specific to a typical region.

2.4.2. Development of Bias Correction Model Using Climatology–Topography Characteristics-Based Linear-Scaling (LS) Approach

2.4.2.1. Correlation Analysis between Climatology–Topography Characteristics and Correction Factors of LS Approach

In the LS approach, the correction factor is an important key to adjust satellite data closely to observation. Correction factors between TMPA products and observations were calculated for each month. In total, we had 12 group correction factors for 3B42V7 and 3B42RT data. Table 2. 5 and Table 2. 6 present the relationship between correction factors in each month with climatology–topography characteristics. Based on the significant levels of the correlation coefficient, we found that topographical characteristics (LONG, LAT, and ELEV) were often associated with correction factors during dry months (except for April), while climate characteristics (AR, SDR, and NRD) were often linked with correction factors during wet months. A larger correction factor indicates larger error between satellite data and observations. ELEV (elevation) had a significant inverse relationship with the correction factor, meaning satellite data at higher elevation areas probably had a smaller error with observations compared to lower areas. This result agreed with an observation in Iran that compared 3B43V7 with rain gauge over this country (Moazami et al., 2013). Similarly, LAT (latitude) also had significant negative relationship with the correction factor. This meant that the higher the latitude area, the smaller was the satellite error.

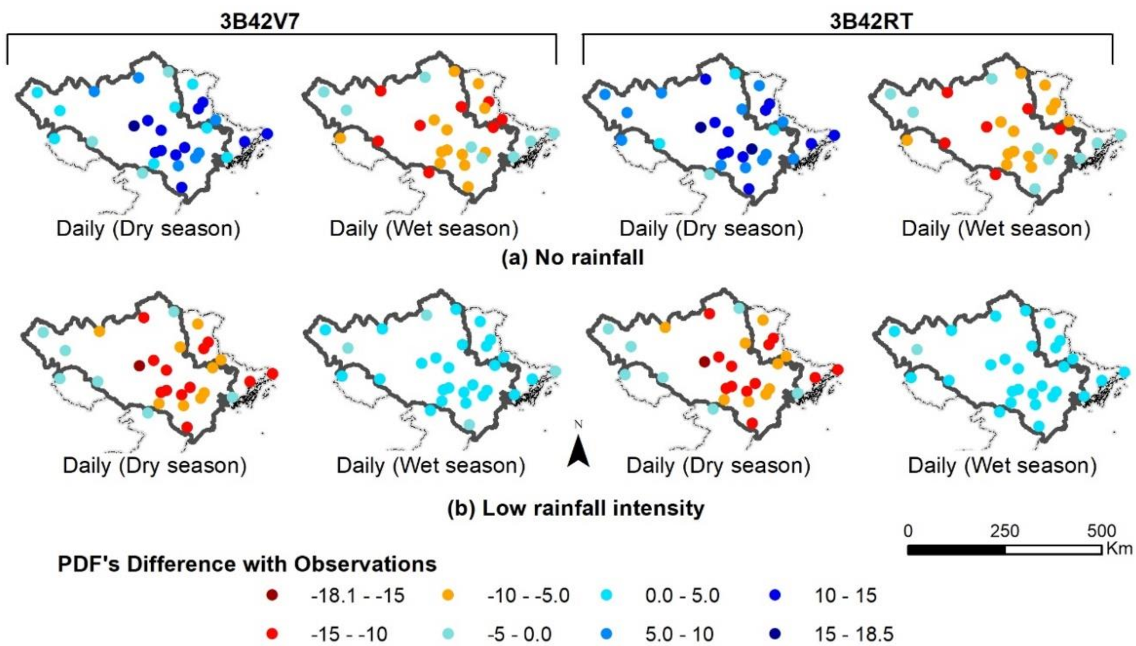

Figure 2. 8 Percentage difference of PDF between TMPA 3B42V7, TMPA 3B42RT, and observation at (**a**) no rainfall intensity (0–0.6 mm/day) and (**b**) low rainfall intensity (0.6–6 mm/day) over the Red–Thai Binh River Basin from March 2000 to December 2016.

The frequency occurrence of clouds can affect the accuracy of satellite rainfall estimation (Ochoa-Sánchez et al., 2014), and NRD (a number of the rainy days) is a variable that reflects this frequency.

As the number of rainy days had significant correlations with the correction factors with negative values, it seemed that the higher the number of rainy day stations, the more error of satellite-based rainfall there were. In addition, from Tables 5 and 6, AR (annual rainfall rate) and SDR (standard deviation of rainfall) had significant positive correlations with the correction factors. This means the higher the rainfall rate area, the higher was the correction factor, implying a more substantial error. This feature was the same as previous literature (Almazroui, 2011). As a result, the correction factor for each month could be estimated from significant climatology–topography candidates.

Table 2. 5 Correlation coefficient between correction factors of TMPA 3B42V7 against climatology–topography characteristics.

	LONG	LAT	ELEV	AR	SDR	NRD
CF_1	**−0.46 ****	−0.32	−0.35	0.18	0.27	−0.21
CF_2	**0.47 ****	**−0.61 ****	**−0.48 ****	0.09	0.29	−0.02
CF_3	**0.43 ***	**−0.58 ****	**−0.42 ***	−0.03	0.11	0.07
CF_4	0.01	0.00	−0.11	**0.52 ****	**0.47 ***	**−0.57 ****
CF_5	0.01	0.07	−0.02	**0.66 ****	**0.56 ****	**−0.65 ****
CF_6	−0.04	0.02	−0.09	**0.63 ****	**0.45 ***	**−0.46 ***
CF_7	0.03	0.12	−0.08	**0.69 ****	**0.60 ****	**−0.44 ***
CF_8	0.06	−0.16	−0.34	**0.53 ****	**0.54 ****	**−0.50 ****
CF_9	−0.29	0.17	0.25	**0.52 ****	**0.50 ****	**−0.58 ****
CF_{10}	0.26	**−0.42 ***	**−0.40 ***	**0.58 ****	**0.68 ****	**−0.47 ***
CF_{11}	0.29	−0.05	**−0.47 ****	0.31	0.33	−0.32
CF_{12}	**0.39 ***	**−0.39 ***	**−0.41 ***	0.12	0.23	−0.17

*Note: * 0.05 significant level; ** 0.01 significant level*

Table 2. 6 Correlation coefficient between correction factors of TMPA 3B42RT against climatology–topography characteristics.

	LONG	LAT	ELEV	AR	SDR	NRD
CF_1	−0.02	**−0.50 ****	−0.10	0.29	0.28	−0.30
CF_2	**0.48 ****	**−0.69 ****	**−0.56 ****	−0.03	0.16	0.23
CF_3	0.25	**−0.55 ****	**−0.42 ***	−0.06	0.01	0.05
CF_4	−0.15	0.22	−0.16	**0.61 ****	**0.43 ***	**−0.57 ****
CF_5	−0.22	0.37	−0.03	**0.69 ****	**0.47 ***	**−0.59 ****
CF_6	−0.28	**0.44 ***	0.02	**0.68 ****	**0.39 ***	**−0.53 ****
CF_7	0.10	−0.13	−0.30	**0.61 ****	**0.56 ****	−0.18
CF_8	**0.48 ****	−0.30	**−0.52 ****	**0.58 ****	**0.74 ****	−0.23
CF_9	0.30	0.04	−0.03	**0.54 ****	**0.69 ****	−0.34
CF_{10}	0.19	**−0.42 ***	−0.34	**0.57 ****	**0.66 ****	−0.35
CF_{11}	**0.55 ****	−0.22	**−0.51 ****	**0.46 ***	**0.62 ****	−0.24
CF_{12}	**0.64 ****	−0.37	**−0.45 ***	0.23	**0.43 ***	−0.16

*Note: * 0.05 significant level; ** 0.01 significant level.*

2.4.2.2. Multiple Linear Model Development to Estimate Correction Factors

As climatology–topography characteristics have various units, before building the multiple linear regression models for correction factors, we made it dimensionless for all input climatology–

topography data by scaling them to a range [0.1, 0.9]. The multiple linear models for the correction factors of 3B42V7 and 3B42RT are presented in Table 2. 7 and Table 2. 8. All *p*-values were smaller than 0.5, indicating that sets of linear models using climatology–topography characteristics could well predict correction factors.

Table 2. 7 Multiple linear models to predict correction factors of TMPA 3B42V7 data.

Formulas	**CC**	***p*-Value**
$CF_1 = 1.004 * LONG + 0.947$	0.446	0.045
$CF_2 = 0.736 * LONG - 2.331 * LAT - 1.347 * ELEV + 3.256$	0.779	<0.001
$CF_3 = 0.242 * LONG - 1.298 * LAT - 0.735 * ELEV + 2.200$	0.768	<0.001
$CF_4 = 0.103 * AR + 0.134 * SDR - 0.262 * NRD + 0.921$	0.604	0.003
$CF_5 = 0.046 * AR + 0.218 * SDR - 0.404 * NRD + 1.068$	0.748	0.001
$CF_6 = 1.019 * AR - 0.528 * SDR + 0.116 * NRD + 0.662$	0.712	0.003
$CF_7 = 0.937 * AR - 0.170 * SDR + 0.140 * NRD + 0.615$	0.733	0.002
$CF_8 = -0.351 * AR + 0.544 * SDR - 0.393 * NRD + 1.093$	0.694	0.006
$CF_9 = -0.491 * AR + 0.636 * SDR - 0.563 * NRD + 1.182$	0.687	0.006
$CF_{10} = -0.286 * LAT - 0.291 * ELEV - 0.665 * AR + 0.965 * SDR - 0.678 * NRD + 1.488$	0.840	<0.001
$CF_{11} = -0.755 * ELEV + 1.373$	0.600	0.003
$CF_{12} = 0.437 * LONG - 1.422 * LAT - 1.202 * ELEV + 2.671$	0.564	0.038

Note: p-value shows significant level between predicted correction factors using multiple linear models and calculated correction factors.

Table 2. 8 Multiple linear models to predict correction factors of TMPA 3B42RT data.

Formulas	**CC**	***p*-Value**
$CF_1 = -1.537 * LAT + 2.582$	0.501	0.041
$CF_2 = 1.102 * LONG - 3.343 * LAT - 2.204 * ELEV + 4.038$	0.875	<0.001
$CF_3 = -2.871 * LAT - 2.045 * ELEV + 4.432$	0.748	0.001
$CF_4 = 1.041 * AR - 0.515 * SDR - 0.003 * NRD + 0.672$	0.720	0.003
$CF_5 = 1.197 * AR - 0.687 * SDR - 0.082 * NRD + 0.545$	0.761	<0.001
$CF_6 = 0.215 * LAT + 1.524 * AR - 0.909 * SDR + 0.386 * NRD + 0.147$	0.875	<0.001
$CF_7 = 0.605 * AR + 0.112 * SDR + 0.696$	0.608	0.002
$CF_8 = 0.196 * LONG - 0.241 * ELEV - 0.011 * AR + 0.580 * SDR + 0.676$	0.877	<0.001
$CF_9 = -0.311 * AR + 1.037 * SDR + 0.681$	0.712	0.003
$CF_{10} = -0.664 * AR + 0.429 * SDR + 0.587 * SD + 0.948$	0.674	0.007
$CF_{11} = 1.233 * LONG - 0.638 * ELEV + 0.720 * AR + 0.616 * SDR + 0.250$	0.838	<0.001
$CF_{12} = 2.233 * LONG - 0.978 * ELEV + 0.936 * SDR + 0.842$	0.729	0.002

Note: p-value shows significant level between predicted correction factors using multiple linear models and calculated correction factors.

2.4.2.3. Calibration and Validation of the CTLS Bias Correction Approach

Table 2. 9 compares the TMPA products before and after using the LS and CTLS approaches against the observations on a daily scale. Both calibration and validation data showed that LS and CTLS performed very well in reduction PBIAS scores but had moderate performances regarding NSE scores, slight improvements in RMSE scores, and almost no change in CC scores. Moreover, the linear-scaling model seemed to reduce errors better for 3B42RT data compared to that for 3B42V7 data. The reason for this may be that 3B42V7 data had already passed through the correction stage before the online public, meaning other bias correction approaches did not improve this product's

quality significantly. The good performances during calibration and validation stations of the CTLS approach indicated that empirical correction factors calculated by climatology and topography characteristics could be applied for the satellite-based data bias correction process throughout the Red–Thai Binh River Basin.

Table 2. 9 The average performance of calibration and validation for climatology–topography-based linear-scaling approach (CTLS) with TMPA 34B42V7 and TMPA 3B42RT on a daily scale.

	Before Bias Correction				**LS**				**CTLS**			
	CC	**NSE**	**RMSE**	**PBIAS**	**CC**	**NSE**	**RMSE**	**PBIAS**	**CC**	**NSE**	**RMSE**	**PBIAS**
3B42V7												
Calibration	0.389	−0.147	15.2	3.0	0.389	−0.130	15.2	1.1	0.389	−0.119	15.2	0.8
Validation	0.378	−0.175	14.8	4.0	0.375	−0.153	14.7	1.5	0.372	−0.165	14.8	1.7
3B42RT												
Calibration	0.303	−0.509	17.3	13.5	0.309	−0.299	16.3	−0.2	0.306	−0.342	16.6	2.2
Validation	0.307	−0.565	17.1	19.4	0.308	−0.299	15.8	0.8	0.300	−0.409	16.4	7.4

Regarding bias correction models on a monthly scale, similar results were observed as the daily scale, with a significant reduction in PBIAS scores after bias correction (Table 2. 10). Moreover, the NSE scores of corrected monthly 3B42RT improved profoundly compared to those before bias correction. Before applying bias correction, the average monthly NSE for calibration and validation stations for 3B42RT data were 0.488 and 0.447, respectively. After using the LS approach, these figures improved to 0.734 and 0.713, respectively. Also, the empirical CTLS approach had considerable monthly NSE improvement, with values of 0.677 and 0.642 corresponding to calibration and validation stations.

Table 2. 10 The average performance of calibration and validation for CTLS with TMPA 34B42V7 and TMPA 3B42RT on a monthly scale.

	Before Bias Correction				**LS**				**CTLS**			
	CC	**NSE**	**RMSE**	**PBIAS**	**CC**	**NSE**	**RMSE**	**PBIAS**	**CC**	**NSE**	**RMSE**	**PBIAS**
3B42V7												
Calibration	0.899	0.767	66.7	3.0	0.904	0.816	59.5	1.1	0.899	0.799	62.1	0.8
Validation	0.881	0.755	65.8	4.0	0.883	0.778	63.2	1.5	0.873	0.755	65.9	1.7
3B42RT												
Calibration	0.843	0.488	96.1	13.5	0.866	0.734	71.8	−0.2	0.850	0.677	78.8	2.2
Validation	0.838	0.447	95.9	19.4	0.854	0.713	71.3	0.8	0.831	0.642	79.3	7.4

Table 2. 11 presents the performance of TMPA products regarding the PBIAS score before and after bias correction using LS and CTLS during the dry and wet seasons. The wet season seemed to benefit from bias correction more than the dry season. Using the LS approach, PBIAS scores for both 3B42V7 and 3B42RT were equal to 0, while the figures for the dry season were up to 10%. With the CTLS approach, PBIAS scores during the wet season also observed a significant decrease, ranging from 0.07% to 4.55%. During the dry season, highly positive PBIAS scores (up to 24%) were observed, indicating a high overestimation of dry season after bias correction.

Table 2. 12 shows the CSI scores for TMPA products against observations before and after bias correction using LS and CTLS during daily, daily (dry season), and daily (wet season). Generally, there was no significant change in CSI scores after bias correction compared to before bias correction for both products and for both bias correction approaches. By analyzing the intensity metric before and after doing bias correction (data not shown), we also obtained the same results as that of detection

metric, i.e. after doing bias correction, there was no significant change in the intense rainfall for TMPA products.

2.5. Conclusions

TMPA products are recommended for wide use over the tropical and subtropical regions due to their high temporal–spatial resolution. Therefore, this study carried out a comparison and bias correction between TMPA 3B42V7 and TMPA 3B42RT data and 29 ground observations over the lower part of the Red–Thai Binh River Basin from March 2000 to December 2016.

Table 2. 11 The average PBIAS score's performance of calibration and validation for CTLS with TMPA 34B42V7 and TMPA 3B42RT during the dry and wet seasons.

	Before Bias Correction		**LS**		**CTLS**	
	Dry Season	**Wet Season**	**Dry Season**	**Wet Season**	**Dry Season**	**Wet Season**
3B42V7						
Calibration	−10.32	5.75	6.97	0.00	3.37	0.51
Validation	−10.92	19.29	9.63	0.00	12.67	0.07
3B42RT						
Calibration	−14.48	7.32	−0.58	0.00	5.59	1.71
Validation	−12.75	26.23	5.59	0.00	24.32	4.55

Based on various error metrics—CC, NSE, RMSE, and PBIAS—we compared 3B42V7 and 3B42RT against observations at different scales, including daily and monthly scales and dry and wet seasons. Our analysis showed that both products had relatively weak relationships with observations on a daily scale but this significantly improved on a monthly scale. Except for the CC score, 3B42V7 data was considerably better than 3B42RT data in the rest of the error metrics on a monthly scale. In addition, 3B42V7 data showed better performance than 3B42RT data during both dry and wet seasons, especially regarding NSE and PBIAS measurements. Both products showed overall underestimations during the dry season and overestimations during the wet season. Spatial analysis of the PBIAS score indicated significant bias of TMPA products at the lowland area of the Red–Thai Binh River Basin, while the northwestern mountainous area and the northeast coastal area had low PBIAS for both products.

Table 2. 12 Average CSI score's performance of calibration and validation for CTLS with TMPA 34B42V7 and TMPA 3B42RT for daily, daily (dry season), and daily (wet season).

	Before Bias Correction			**LS**			**CTLS**		
	Daily	**Daily**	**Daily**	**Daily**	**Daily**	**Daily**	**Daily**	**Daily**	**Daily**
3B42V7									
Calibration	0.450	0.258	0.531	0.449	0.259	0.529	0.448	0.259	0.529
Validation	0.429	0.225	0.519	0.428	0.225	0.516	0.428	0.226	0.518
3B42RT									
Calibration	0.422	0.226	0.505	0.422	0.226	0.505	0.422	0.226	0.505
Validation	0.402	0.202	0.492	0.402	0.205	0.492	0.402	0.206	0.492

The comparison between 3B42V7 and 3B42RT was also viewed from a different angle using detection metrics—POD, FAR, POFD, and CSI—against observations on daily time series, daily time series in the dry season, and daily time series in the wet season. In this case, the 3B42V7 showed a slightly better performance compared to 3B42RT for the metrics mentioned. Both products had better detection metrics in the wet season compared to the dry season. Spatial CSI score distribution showed that the lowland area of the central basin had the lowest score compared to other parts.

From the perspective of the assessment on rainfall intensity on daily time series for the dry and wet seasons, it was found out that 3B42RT performed the same as 3B42V7 data. Both products overestimated no rainfall (≤0.6 mm/day) during the dry season and underestimated rainfall intensity during the wet season. The overestimation and underestimation compromised the daily time series for the dry and wet seasons, meaning the frequency distributions of no rainfall events were almost the same for TMPA products and ground observations. On the other hand, TMPA products underestimated low rainfall intensity (0.6–6 mm/day) during the dry season and overestimated rainfall intensity during the wet season. The underestimation of low rainfall was more significant than the overestimation, resulting in a slightly lower rainfall estimation by TMPA products at the daily time series compared to observations.

In addition, we used the LS approach to do bias correction for 3B42V7 and 3B42RT products. In this approach, the correction factor is an important key to adjust satellite rainfall data closely to observations. We found that the correction factors of the LS approach were associated with climatology–topography characteristics. Therefore, a set of multiple linear regression models was developed to predict correction factors from climatology–topography characteristics for 3B42V7 and 3B42RT. After bias correction using LS and CTLS approaches, corrected TMPA products showed significant improvement compared to the results before bias correction, especially for the 3B42RT dataset with PBIAS and NSE scores. However, we found that both bias correction approaches did not improve the TMPA products significantly on other measurement scores.

In conclusion, 3B42V7 and 3B42RT data should be a good alternative source for a wide range of hydrological purposes on a monthly scale. The 3B42V7 data is also a good source for typical analysis of dry and wet seasons, although these datasets should be used with caution for daily scale purposes. The post-TMPA products after using climatology–topography characteristics are promising sources, especially for total water resource estimation.

The biggest advantage of the LS approach was to reduce PBIAS score; however, other error scores remained almost the same. Future studies may merge satellite-based and ground-based rainfall product to further improve rainfall product quality (Nerini et al., 2015). The finding of this paper gives an overview of the capacity of TMPA products in the lower part of the Red–Thai Binh River Basin regarding water resource application and provides a simple bias correction that can be used to improve the correctness of TMPA products. Additionally, the study is beneficial for regions, such as Vietnam, that are seeking alternative rainfall sources. The reason for this is that approximately 60% of Vietnam's water resources come from abroad, and hydro-climatology acquisition from upstream countries faces many challenges due to limited administration interaction (Tran Thanh Xuan et al., 2012).

Chapter 3: Assessment of drought conditions over Vietnam using standardized precipitation evapotranspiration index, MERRA-2 re-analysis, and dynamic land cover[2]

3.1. Introduction

The slowly evolving nature of drought and its multiple drivers contribute to the various definitions adopted for different purposes and diverse conclusions in identifying the trends under changing climate (Dai, 2011; Van Loon et al., 2016). While a global trend of drought over the last century remains debatable (Greve et al., 2014; Orlowsky and Seneviratne, 2013; Sheffield et al., 2012), some regions of the world have observed robust tendencies that droughts are becoming more frequent and severe. Drying trends were found in equatorial Africa (Diem et al., 2014; Kawase et al., 2010), South Asia (Krishnan et al., 2016), and the Mediterranean (Hoerling et al., 2012; Valdes-Abellan et al., 2017) in contrast to wetting trends in high latitude regions (Sheffield and Wood, 2008; Zhang et al., 2013). Notably, in recent years several extreme droughts have been observed—California (Ganguli and Ganguly, 2016; Mazdiyasni and AghaKouchak, 2015), Australia (Herold et al., 2016), China (Yuan et al., 2019), Europe (Miralles et al., 2019), and India (Sharma and Mujumdar, 2017). These droughts occurred concurrently with extreme heatwaves, causing severe socioeconomic and ecological damages and are likely to occur with increased frequency. Such possibly intensified impacts of drought, compounded by its intricate characteristics, demands a substantially improved quality of observations for proper monitoring and management in many regions of the world.

While impacts of varying temporal scales on the efficiency of drought indices are well-documented (Raziei et al., 2013; Zhu et al., 2016; Zuo et al., 2018), only a few studies have investigated the performances of drought indices at different spatial scales. Golian et al. (2019) found that the values of Critical Success Index (CSI) derived from products of Multi-Source Weighted-Ensemble Precipitation (MSWEP) at coarser resolution (0.5° and 1°) as significantly lower skill in drought detection for severe drought events compared to the CSI computed from the MSWEP data at 0.1°. Additionally, Raziei et al. (2013) demonstrated that the dependence of the spatial patterns of droughts on time scales increased when using higher spatial resolution data. In light of this, it seems that the drought indices computed from the high-resolution data have greater potential to accurately describe the spatial characteristics of drought conditions than those derived from coarser-resolution data. Previous studies have focused on drought indices based on the data sets with relatively coarser-resolution (e.g., larger than 10km), while the analyses that assess the performance of the drought indices at finer spatial resolutions (e.g., less than 10km) have seldom been studied.

Drought risk in agricultural regions is essential information; however, this information is currently limited by using static datasets. For example, when Rojas et al. (2011) and Winkler et al. (2017)

[2] This chapter has been published as Le, M. H., Kim, H., Moon, H., Zhang, R., Lakshmi, V., & Nguyen, L.B (2020). Assessment of drought conditions over Vietnam using standardized precipitation evapotranspiration index, MERRA-2 re-analysis, and dynamic land cover. Journal of Hydrology: Regional Studies, 100767. https://doi.org/10.1016/j.ejrh.2020.100767.

investigated agricultural areas affected by drought, they only used a typical year to represent land cover for the entire study period. However, land cover, especially for agricultural land, is subjected to change over time due to international trade, climate adaptation, urbanization, industrialization, food security and economic policies (Rutten et al., 2014). Therefore, in order to accurately evaluate drought conditions in agricultural locations, it is required to use a dynamic land cover database to reflect spatial changes in land cover over time. To the best of our knowledge, previous studies have not used dynamic land cover for drought assessment.

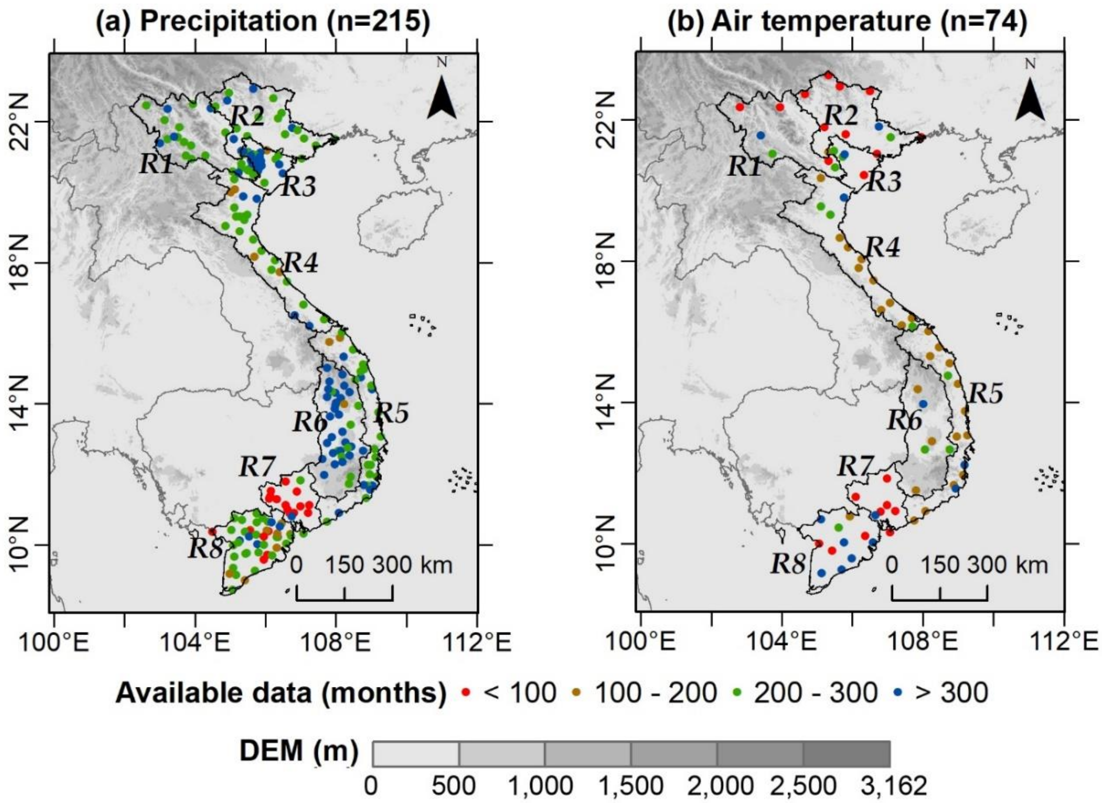

Figure 3. 1 Boundaries of eight sub-regions (R1-R8) in Vietnam and data lengths of in-situ precipitation and temperature stations.

In this study, we aim to examine three hypotheses, viz. — (1) Does high spatial resolution data detect drought trends better than low spatial resolution data? (2) Does high spatial resolution data have advantages of capturing drought events better than low spatial resolution data? (3) Does dynamic land cover provide better information on agricultural lands affected by drought over the years? We selected the country of Vietnam as a case study to test our hypotheses. Firstly, drought investigation is of paramount importance for Vietnam as this disaster ranked third among economic losses amongst natural hazards in the country (Nguyen and Shaw, 2011). Secondly, most of the studies which assessed droughts in Vietnam are either based on sparsely distributed in-situ observations (Le et al., 2019b; Vu-Thanh et al., 2014) or relatively coarse spatial resolution data (Vu and Mishra, 2016; Vu et al., 2018). Therefore, high spatial resolution drought datasets are unexplored in Vietnam. Moreover, we can obtain annual land cover information for Vietnam for the past 30 years from SERVIR-Mekong land use land cover portal. This land cover database could enable us to examine our third hypotheses mentioned above.

This study selected the Standardized Precipitation Evapotranspiration Index (SPEI) (Vicente-Serrano et al., 2010) to estimate drought conditions in Vietnam. This index is an appropriate drought index in examining changes in droughts under global warming (Le et al., 2019a; López-Moreno et al., 2013; Wang et al., 2018), and in representing different drought types such as meteorological, agricultural, hydrological, and socioeconomic droughts (Chen and Sun, 2015). We estimated the SPEI at three spatial resolutions (1-, 9- and 36-km) using precipitation and air temperature from the second Modern-Era Retrospective analysis for Research and Applications (MERRA-2). One of the main reasons that we chose MERRA-2 is that the data has been widely validated, showing good performance globally. Readers will find representative research at https://gmao.gsfc.nasa.gov/reanalysis/MERRA-2/pubs/. Furthermore, as MERRA-2 is open to the public and allows the downloading of near-real-time data, it has great potential for practical application in drought analysis. To investigate agricultural drought areas, we extracted agricultural land cover in each year from SERVIR-Mekong land use land cover database, and re-sampled the data to 1-, 9-, and 36-km. To explore the possible trends in a time series, we applied the Mann-Kendall test, which is commonly used to detect trends in hydro-meteorological time series (Joshi et al., 2019; Mondal et al., 2015; Velpuri and Senay, 2013).

This study is organized as follows. Section 3.2 introduces the Study Area. Section 3.3 presents the Datasets. Section 3.4 presents the Methodology. Results and Discussions, and Conclusions are presented in Section 3.5 and Section 3.6, respectively.

Table 3. 1 Descriptive statistics of precipitation and air temperature from MERRA-2 and in-situ data in eight sub-regions. The MERRA-2 data were extracted at the same in-situ locations.

Annual Precipitation	**In-situ**			**MERRA-2**		
	Max (mm)	Min (mm)	Mean (mm)	Max (mm)	Min (mm)	Mean (mm)
R1 (n = 25)	2,411	1,129	1,764	1,563	939	1,352
R2 (n = 18)	3,775	1,170	1,775	1,481	1,231	1,361
R3 (n = 25)	1,793	1,239	1,533	1,502	1,374	1,453
R4 (n = 24)	3,889	1,320	2,063	2,122	1,342	1,604
R5 (n = 27)	3,738	841	2,069	2,140	1,166	1,532
R6 (n = 36)	2,538	1,267	1,834	1,602	834	1,100
R7 (n = 16)	2,779	1,288	1,914	1,496	1,175	1,369
R8 (n = 44)	2,459	809	1,628	2,006	1,124	1,569
Annual Air Temperature	In-situ			MERRA-2		
	Max (°C)	Min (°C)	Mean (°C)	Max (°C)	Min (°C)	Mean (°C)
R1 (n = 6)	24.6	23.1	24.0	23.0	20.0	21.3
R2 (n = 10)	24.4	20.7	22.9	23.2	18.9	21.2
R3 (n = 5)	24.2	23.6	23.9	23.9	23.0	23.4
R4 (n = 14)	25.1	21.9	24.2	25.1	21.7	23.6
R5 (n = 15)	27.5	24.6	26.5	26.3	24.2	25.0
R6 (n = 6)	25.2	21.8	23.2	24.5	21.9	23.5
R7 (n = 7)	28.2	26.0	27.1	27.3	26.4	26.8
R8 (n = 11)	28.0	27.0	27.4	27.5	26.7	27.0

3.2. Study Area

Vietnam has a total area of 331,212 km^2, extending from 8.2°N – 23.5°N, 101.1°E – 110.3°E, and a home of more than 95 million people (In 2018 ranked 15th in global population). In order to assess drought condition in Vietnam, previous studies often divided it into seven sub-regions that are based on differences in climatic conditions (Le et al., 2019b; Vu et al., 2018). This study, however, divided Vietnam into eight sub-regions based on a sub-national administrative level. This allows for easy comparison with existing agricultural drought statistics. These eight sub-regions are Northwestern Region (R1); Northeastern Region (R2); Red River Delta (R3); North Central Region (R4), South Central Region (R5); Central Highlands (R6); Southeastern Region (R7); and the Mekong Delta (R8) (Figure 3. 1).

Table 3. 2 Mean elevation and Gini-Simpson index (Simpson, 1949) in eight sub-regions. The Gini-Simpson index is calculated to reflect heterogeneity of surface land for each sub-region. Higher Gini-Simpson index corresponds to greater variation in land surface.

Sub-region	R1	R2	R3	R4	R5	R6	R7	R8
Mean Elevation (m)	801.6	387.1	22.3	298	334.4	660.5	89.4	3.9
Gini-Simpson Index	0.939	0.92	0.451	0.926	0.933	0.914	0.897	0.015

3.3. Data Sets

3.3.1. Ground Observations

This study collected monthly data from 215 precipitation stations and 74 temperature stations from multiple sources, including Vietnam Meteorological and Hydrological Administration (VMHA), Mekong River Commission (MRC), and Japan International Cooperation Agency (JICA) (Figure 3. 1). All data has passed quality checks. We used these in-situ observations to compare with precipitation and air temperature from MERRA-2 datasets. Data availability at each station varied between 40 and 360 months (Figure 3. 1). Descriptive statistics of observed precipitation and air temperature in each sub-region can be found at Table 3. 1.

We obtained 1989-2014 data on agricultural land affected by drought for the R4 and R5 regions from the Vietnamese Ministry of Agriculture and Rural Development (MARD). The Decree No.01.2008/ND-CP on responsibilities, tasks, authorities and organization structure of MARD: *"Ministry of Agriculture and Rural Development is a state agency, carrying out tasks of state management on such fields as agriculture, forestry, salt industry, aquaculture, water resource and rural development in the country; of state management on public services and fields under the management of the Ministry"*. The MARD has its department located in each province through Vietnam. Officials from these departments conduct annual surveys on agricultural activities lands within their provinces to obtain statistical records on natural disasters and the development of these activities.

3.3.2. The Modern-Era Retrospective Analysis for Research and Applications, Version 2 (MERRA-2)

The Modern-Era Retrospective Analysis for Research and Applications, version 2 (MERRA-2), is the latest atmospheric reanalysis of the modern satellite era produced by NASA's Global Modeling and Assimilation Office (GMAO). The goals of MERRA-2 are to provide a regularly-gridded, homogeneous record of the global atmosphere, and to incorporate additional aspects of the climate system (Gelaro et al., 2017). The superior feature of MERRA-2 over its predecessor, MERRA, is that it assimilates several observation types and includes updates to the Goddard Earth Observing System (GEOS) model and analysis scheme; this allows it to provide a feasible ongoing climate analysis. MERRA-2 includes ground-based remotely sensed data and numerous satellite observations both before and after the introduction of NOAA-18 satellite in 2005. The complete set of input observations assimilated in MERRA-2 is summarized in Table 3. 1 in Gelaro et al. (2017) and detailed description of these data uses shown in McCarty et al. (2016). In this study, the bilinear transform was used to produce $0.01^{\circ} \times 0.01^{\circ}$ (~1-km), $0.09^{\circ} \times 0.09^{\circ}$ (~9-km), and $0.36^{\circ} \times 0.36^{\circ}$ (~36-km) spatial resolutions of MERRA-2-derived precipitation and air temperature forcing data using the Land surface Data Toolkit (LDT) (Kumar et al., 2006). For further information regarding LDT, please refer to Arsenault et al. (2018); and visit https://lis.gsfc.nasa.gov".

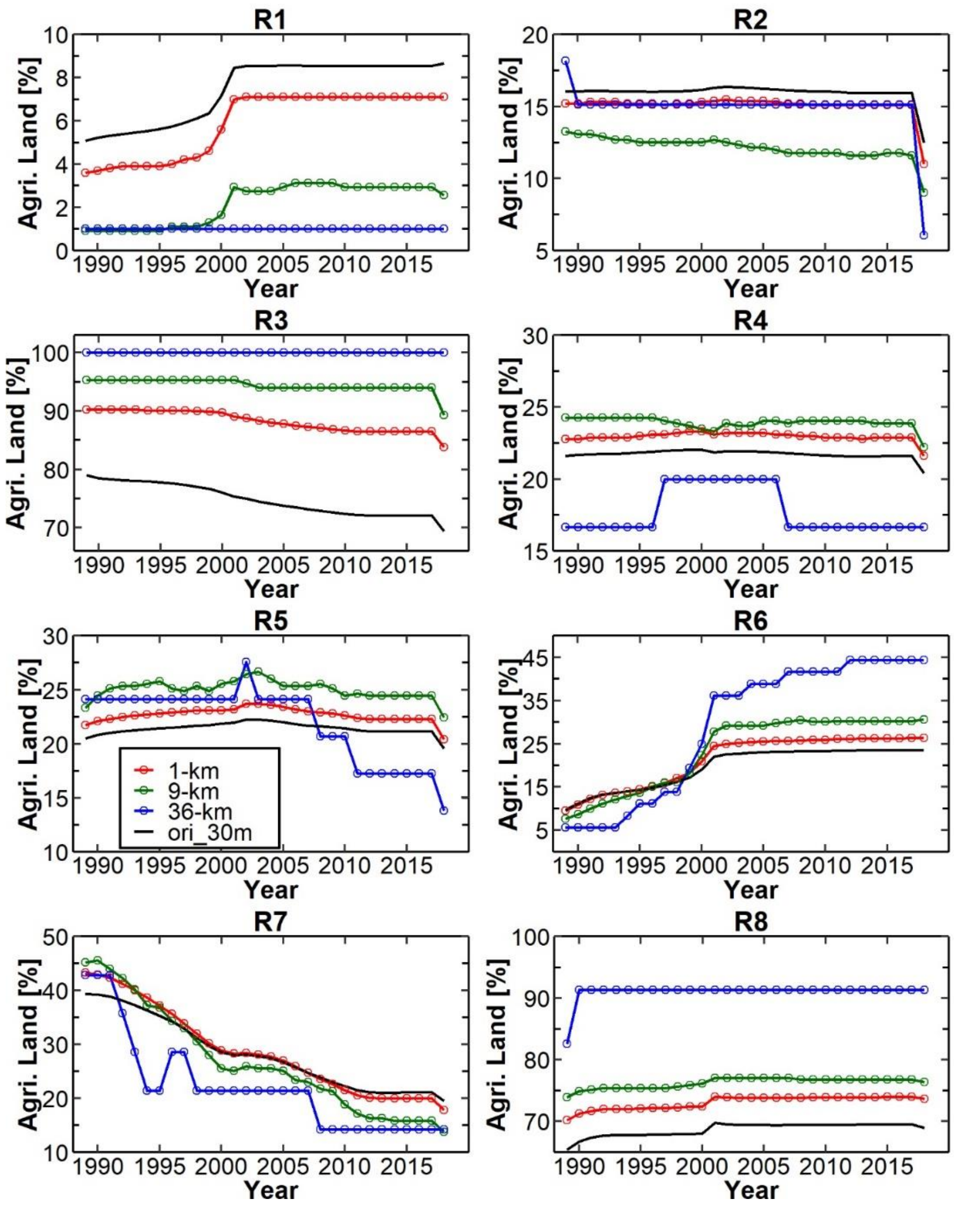

Figure 3. 2 Percentage of agricultural land based on different spatial resolutions in eight sub-regions during 1989-2018. The black line is the agricultural land area derived from the 30-m original land cover dataset.

3.3.3. Agricultural Land Cover Dataset

High resolution (30m) land cover data for Vietnam during 1989-2018 were obtained from the land-cover portal website maintained by SERVIR-Mekong (https://rlcms-servir.adpc.net/en/landcover/).

This system provides consistent land cover products at regular intervals, with quality control from multiple sources. Based on these yearly land cover data, we determined agricultural land areas (sum of croplands and rice paddies from SERVIR-Mekong's classification) and calculated the area percentage of drought on a monthly basis. This work enables us to precisely estimate drought areas for agricultural regions only and not for other land covers. Since we used MERRA-2 datasets with three different spatial resolutions (1-, 9-, and 36-km), the land cover datasets were also re-sampled from 30m to these corresponding resolutions.

The temporal percentage change of agricultural land in Vietnam at three spatial resolutions is given in Figure 3. 2. The R3 and R8 are two deltas corresponding to the two largest river basins in Vietnam - Red-Thai Binh River and Mekong River, respectively. Therefore, agricultural lands in these regions account for a large proportion of the total land over the years. For 30 years, agricultural land in R7 experienced a significant reduction while that land in R6 exhibited a considerable increase. Comparing agricultural land estimated from three spatial resolutions (1-, 9-, and 36-km), higher spatial resolution land cover datasets seem to have smoother inter-annual changes over 1989-2018, and to be closer with these figures of original land cover dataset (Figure 3. 2). Different agricultural land resolution datasets can result in a significant difference in percentage of total agricultural land. For example, in R8, the agricultural land was around 90% of the total land with a 36-km land cover dataset but 73% with the 1-km land cover dataset. The large inhomogeneous distribution of land cover is probably a result of the different agricultural land estimations given when we used different spatial resolutions. An example of agricultural land in R3 in different spatial resolutions is given in Appendix 1.

In short, the agricultural land in Vietnam exhibited a great variation in both temporal and spatial scales. Therefore, drought evaluation in agricultural land in Vietnam requires a rigorous information for a better estimate.

3.4. Methodology

3.4.1. Temporal Trend Analysis

The Mann-Kendall (MK) test was performed to analyze the trends of precipitation, temperature, and drought conditions. The MK test is a non-parametric test that statistically assesses the monotonic trends in data over time (Hirsch and Slack, 1984; Kendall, 1938; Mann, 1945). We selected this non-parametric test because our data sets are not normally distributed, and this test is distribution-free (Gocic and Trajkovic, 2014). For purpose of robustness, in the presence of autocorrelation time series which could affect trend interpretation results (Yue et al., 2002), we removed the serial correlation effect using the pre-whitening method before applying the MK test (Gocic and Trajkovic, 2014). Then, the Sen’s slope (Sen, 1968) was used to examine the magnitude of trends.

3.4.2. Characteristics of Drought Dynamics

From MERRA-2’s precipitation and air temperature for each grid cell, we calculated the SPEI throughout Vietnam, at three spatial resolutions - 1-, 9-, and 36-km. We employed three-parameter log-logistic distribution for fitting SPEI. A negative value of SPEI indicates that a particular value of the water-related variable is lower than the median of the total distribution. A drought event occurs when the SPEI value reaches -1 or lower. The water-related time series - SPEI requires a deficit between precipitation (P) and potential evapotranspiration (PET). We calculated PET from air temperature data based on the Thornthwaite method (Thornthwaite, 1948).

In the present study, we used a 3-month timescale, which was estimated by accumulating three consecutive months of P-ET. This 3-month timescale often reflects a shortage of water availability for agricultural uses (Svoboda et al., 2012).

Temporal drought characteristics were analyzed using drought frequency (F) and drought severity (S) (Le et al., 2019b). The details regarding these drought characteristics are the following Equation (1) and Equation (2).

$$F = \frac{\sum_{i=1}^{m} Du_i}{N} \times 100\% \tag{3.1}$$

Where Du_i is ith drought duration, which is the number of consecutive months in which the SPEI is below -1; m is the number of drought duration, N is the total months.

$$S = \sum_{i=1}^{Du} DI_i | DI_i < -1 \tag{3.2}$$

Where DI_i is SPEI at month *i*.

For assessing drought in space, we used a binary approach to represent drought state $Ds(t)$ at time step t for each grid cell as follows:

$$D_S(t) = \{1 \; if \; DI(t) \leq -1; \; 0 \; if \; DI(t) > -1 \tag{3.3}$$

Where $DI(t)$ is the value of drought index at time step t.

For a given region, the percentage drought area at time step t, $PDA(t)$ (%), is a ratio between total number cells in drought and the total number of cells in the region N_{total}.

$$PDA(t) = \frac{\sum_{i=1}^{N_{total}} D_S(t) | DI(t) \leq -1}{N_{total}} \times 100\% \tag{3.4}$$

We estimated three monthly percentage drought area (PDA) datasets. The first dataset is the percentage drought area for the entire region (hereafter referred to as PDA-E), which is equivalent to the total land area of a region. The second dataset is the percentage of drought area for agricultural land using static land cover (hereafter PDA-AS). N_{total} in the second case is equivalent to total agricultural land of 2005 which represents for the period 1989 and 2018. The cells in drought are counted for the agricultural land in the year of 2005. The third dataset is the percentage of drought area for agricultural land using dynamic land cover (hereafter PDA-AD). N_{total} in the third case is equivalent to total agricultural land of the year *i* (*i* =1989, 1990, …, 2018). The cells in drought are counted for the agricultural land each year. We compared these three estimated PDAs with record PDAs in R4 and R5 regions. Since the record PDAs datasets are only available annually, we averaged monthly PDAs from our estimations to an annual basis to have the same temporal time step as the actual data.

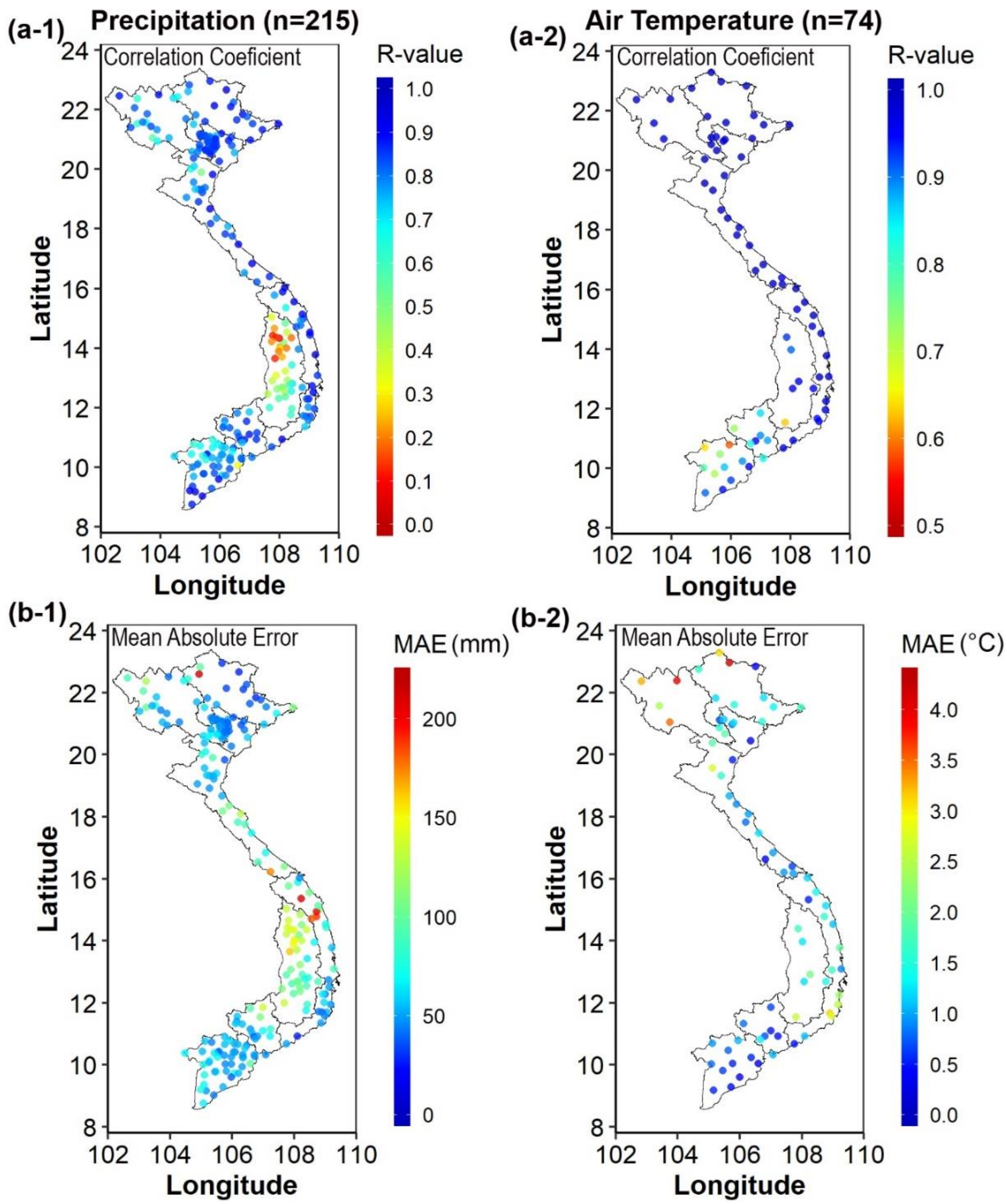

Figure 3. 3 (a) Correlation coefficient and (b) Mean absolute error between MERRA-2 datasets and observed precipitation (right) and observed air temperature (left).

3.5. Results and Discussion

3.5.1. Assessment on MERRA-2's Precipitation and Air Temperature in Vietnam

Over our region of interest, there is no prior research of validating MERRA-2 using in-situ measurement; therefore, we conducted a validation study before applying MERRA-2 data for drought analysis. To do that, we extract grid values of MERRA-2 to ground observation points using the nearest neighbor method. We used this method to preserve the values at different spatial resolutions. In total, for each precipitation and air temperature dataset, three comparisons were made between MERRA-2 datasets (1-, 9-, and 36-km) and in-situ measurements. Since the results were found similar in each spatial resolution of MERRA-2 product, this section only presents evaluation results of 1-km MERRA-2 in terms of correlation coefficient (R-value) and mean absolute error (MAE) (Figure 3. 3). The results of 9- and 36-km MERRA-2 can be found in Appendix 2.

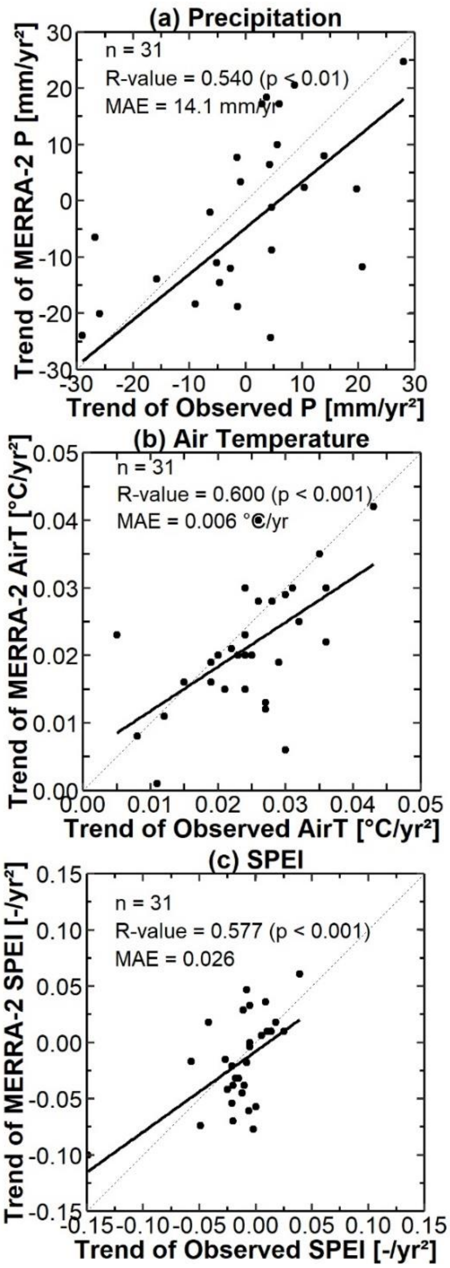

Figure 3. 4 Validation of the MERRA-2 dataset against observation in (a) comparison of MERRA-2 and observed precipitation Sen's slope, (b) comparison of MERRA-2 and observed air temperature Sen's slope , (c) comparison of MERRA-2 and observed SPEI Sen's slope .

Generally, precipitation from MERRA-2 exhibited a good agreement with the precipitation from in situ data, with median R-value of 0.809 (Figure 3. 3a). The MERRA-2 precipitation exhibited relatively poor correlation with in-situ dataset in Central Highlands (R6), specifically in its northern part. This can probably be attributed to a combination of a typical bimodal South Asian summer monsoon interacting with complex topography (Phan and Ngo-Duc, 2009; Tuan, 2019; Van Der Linden et al., 2016). The MERRA-2 precipitation product itself observed many outlier values in the R6 region (see Appendix 3). Note that the R1, R2, and R5 regions also have high Gini-Simpson Indices but their monsoon circulation is not as complex as that of the R6 region (Nguyen and Nguyen, 2004). With respect to air temperature, a very good relationship between MERRA-2 and in-situ data was found, with a median R-value of 0.977. Among sub-regions, only the North Mekong Delta (North R8) exhibited a moderate relationship (median R-value of 0.75).

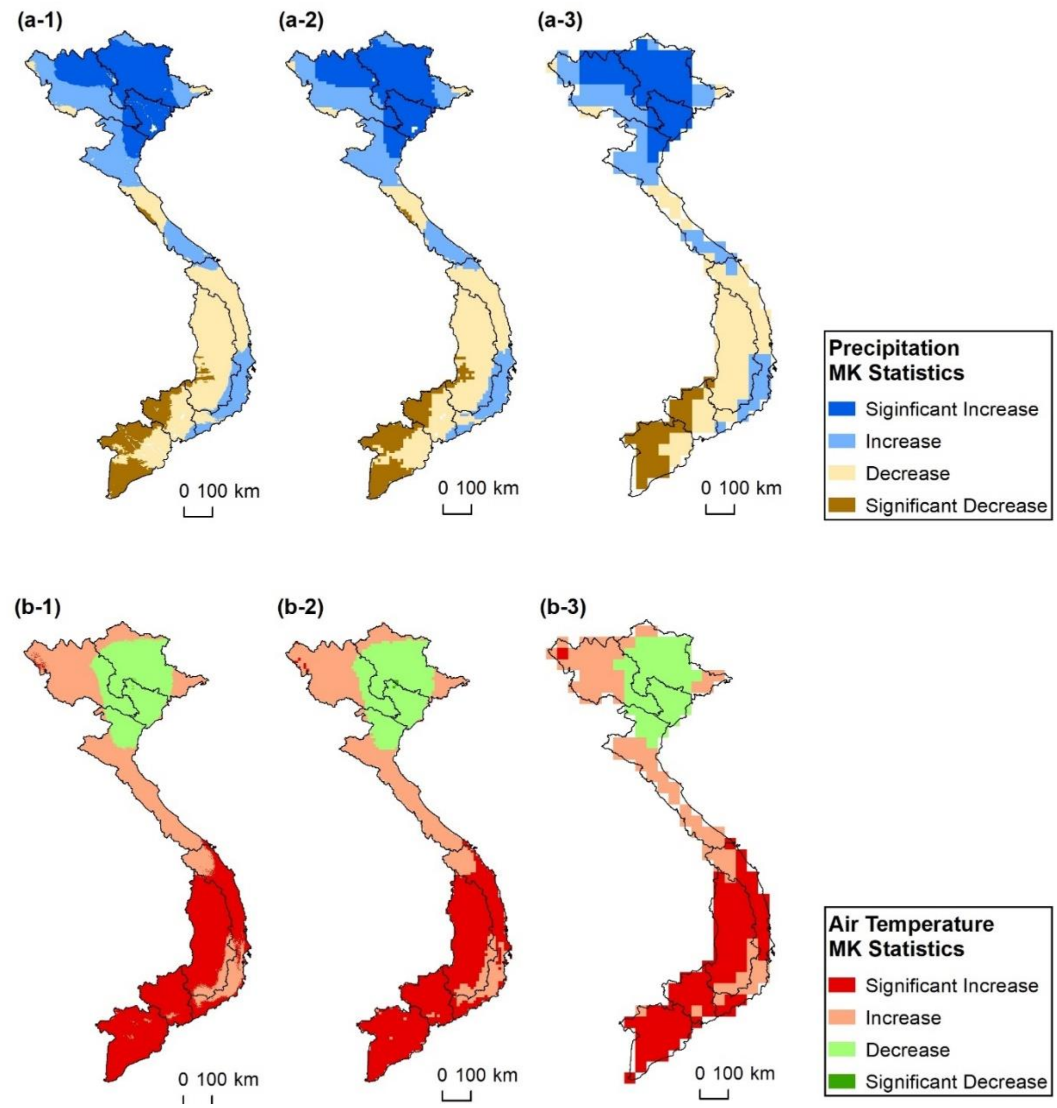

Figure 3. 5 MK Statistics test of precipitation (upper) and air temperature (lower) during 1989-2018 in Vietnam in different spatial resolutions (1-, 9-, 36-km).

The MAE values between precipitation and air temperature from MERRA-2 and these from in-situ data is given in Figure 3. 3b. The median MAE value of precipitation was 57.5 mm. High precipitation MAE values (>150 mm) were found at several stations in north R5 and in northwest R3 (Figure 3. 3(b-1)). These high values can probably be attributed to the typical local rainfall problem. The stations in these areas are located at the base of mountains (i.e., Truong Son mountains and Tay Con Linh mountains), meaning they receive the highest rainfall amounts in Vietnam (3,500 - 4,300 mm annually) due to orographic rainfall. With such typical very high rainfall observed, MERRA-2 often underestimates the rainfall during the rainy season. Previous studies also revealed large underestimation of satellite-based and re-analysis rainfall datasets in Central Vietnam where observed rainfall is extremely high (>3000 mm) (Le et al., 2020b). The median MAE values of MERRA-2's air temperature was 1.14°C (Figure 3. 3(b-2)). Except for R6, MERRA-2 dataset generally underestimated air temperature over Vietnam (Table 3. 1). This underestimation is similar to the results from re-analysis ERA-4.0 data (Phan and Ngo-Duc, 2009). It may be attributed to the lapse rate due to complex topography.

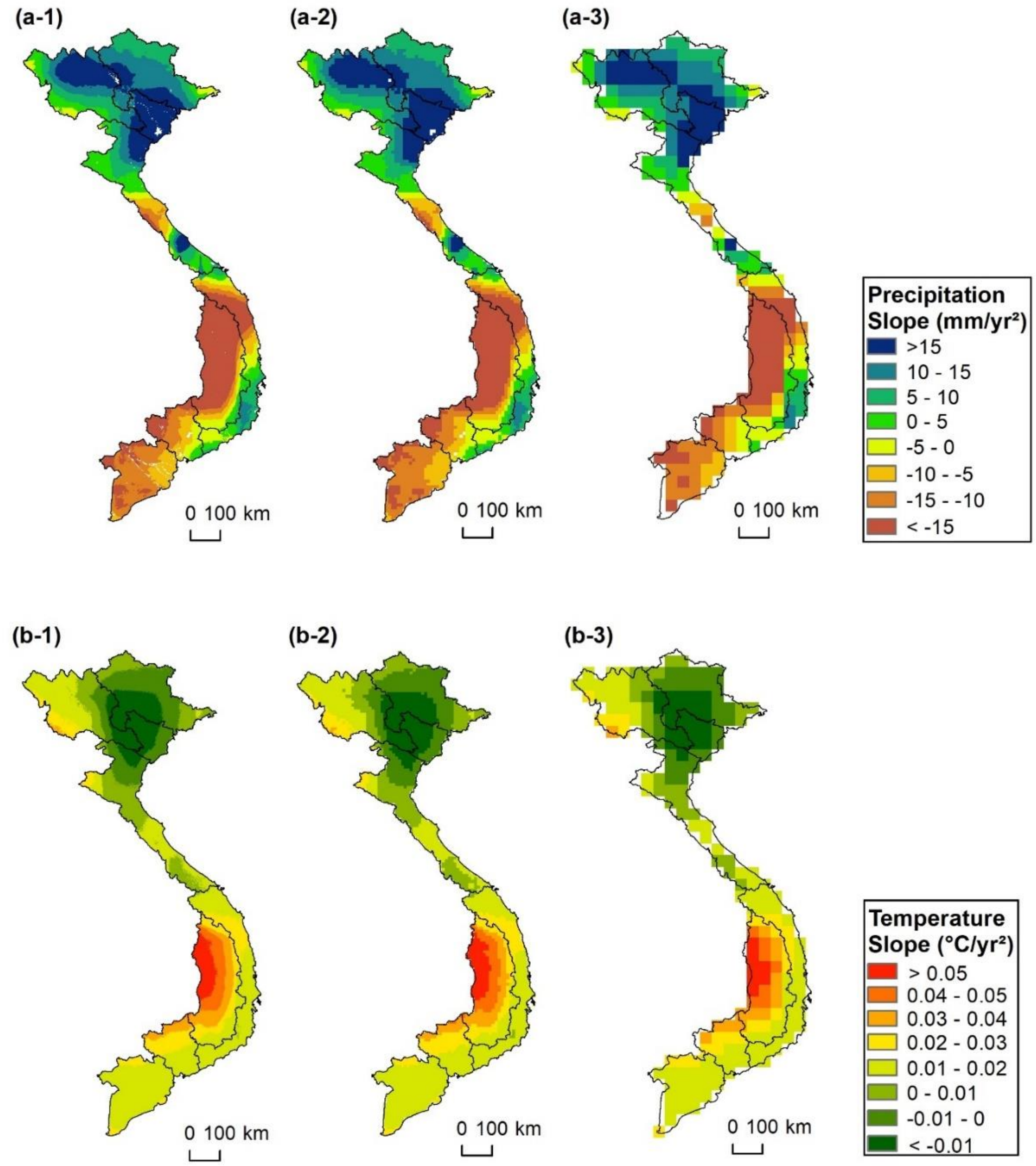

Figure 3. 6 Sen's slope of precipitation (upper) and air temperature (lower) during 1989-2018 in Vietnam in different spatial resolutions (1-, 9-, 36-km).

We further assessed MERRA-2 datasets in terms of trend estimation at 31 stations that have both precipitation and air temperature datasets longer than 15 years. A comparison between MERRA-2 and observed precipitation trend is given in Figure 3. 4a. The estimated annual precipitation trend from

MERRA-2 exhibited a reasonable agreement with observed values, with a correlation coefficient of 0.540 ($p < 0.01$). The estimated annual air temperature from MERRA-2 demonstrated a slightly better relationship with observed air temperature (R-value = 0.600, $p < 0.001$, Figure 3. 4b). The SPEI which were calculated from precipitation and air temperature at the same location, also exhibited a reasonable relationship between modelled and observed data (R-value 0.577, $p < 0.001$, Figure 3. 4c).

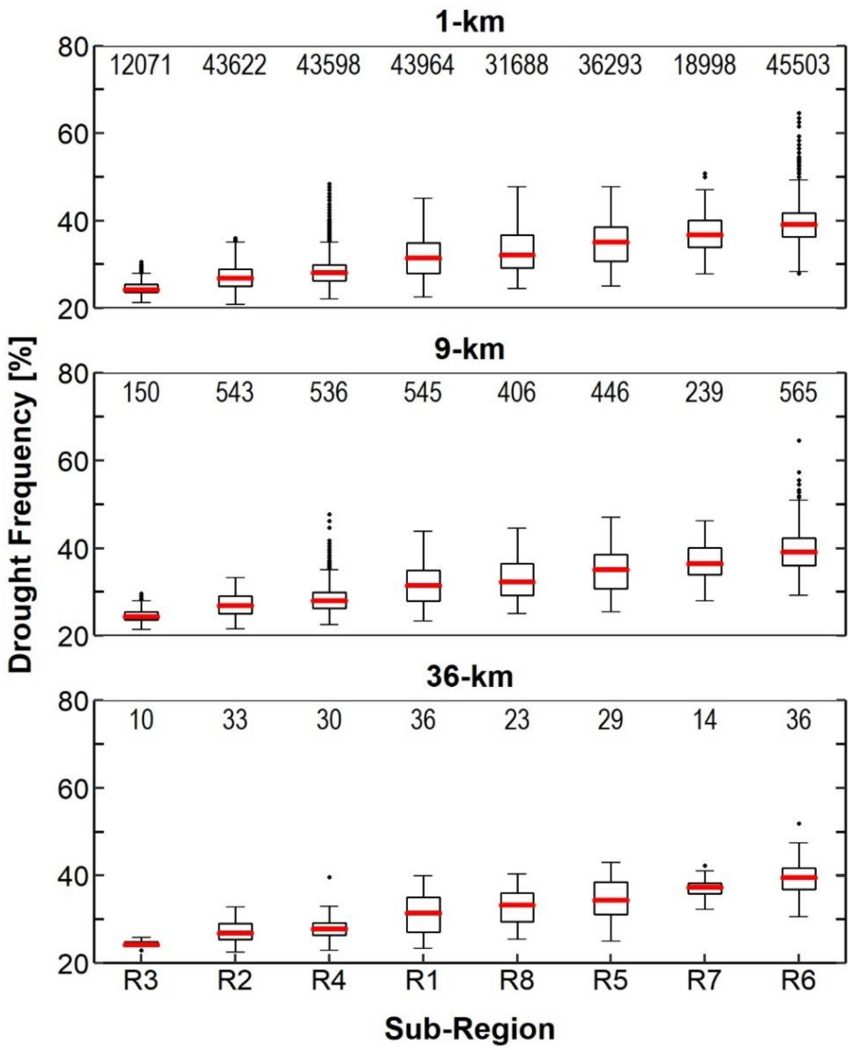

Figure 3. 7 Regionally averaged drought frequency estimated from SPEI in eight sub-regions of Vietnam in different spatial resolutions (1-, 9-, 36-km). Boxes represent the interquartile range, median, and outliers. The tops and bottoms of each box are the 10th and 90th percentiles of the data. The number on top of each box plot denotes sample sizes for each sub-region.

In short, the above results demonstrate that MERRA-2 is adequate to investigate climate change and drought characteristics in Vietnam. Therefore, in the next sections, we will utilize the advantages of the MERRA-2 dataset in characterizing precipitation, air temperature, and drought trends over 30 years in Vietnam.

3.5.2. Spatial-Temporal Assessment on Precipitation and Air Temperature Characteristics in Vietnam based on MERRA-2 Dataset

Thirty-year trends in annual precipitation and air temperature are given in Figure 3. 5 and Figure 3. 6. Most of the northern parts of Vietnam (R1, R2, and R3) exhibited an increasing trend in precipitation. On the contrary, annual precipitation trends in the south of R6, R7, and R8 declined during the study period. The most significant decreasing trend of annual precipitation can be observed partially in R6, and the northern portion of R5 and a similar decreasing trend over these regions have also been observed during the winter season (Vu and Mishra, 2016).

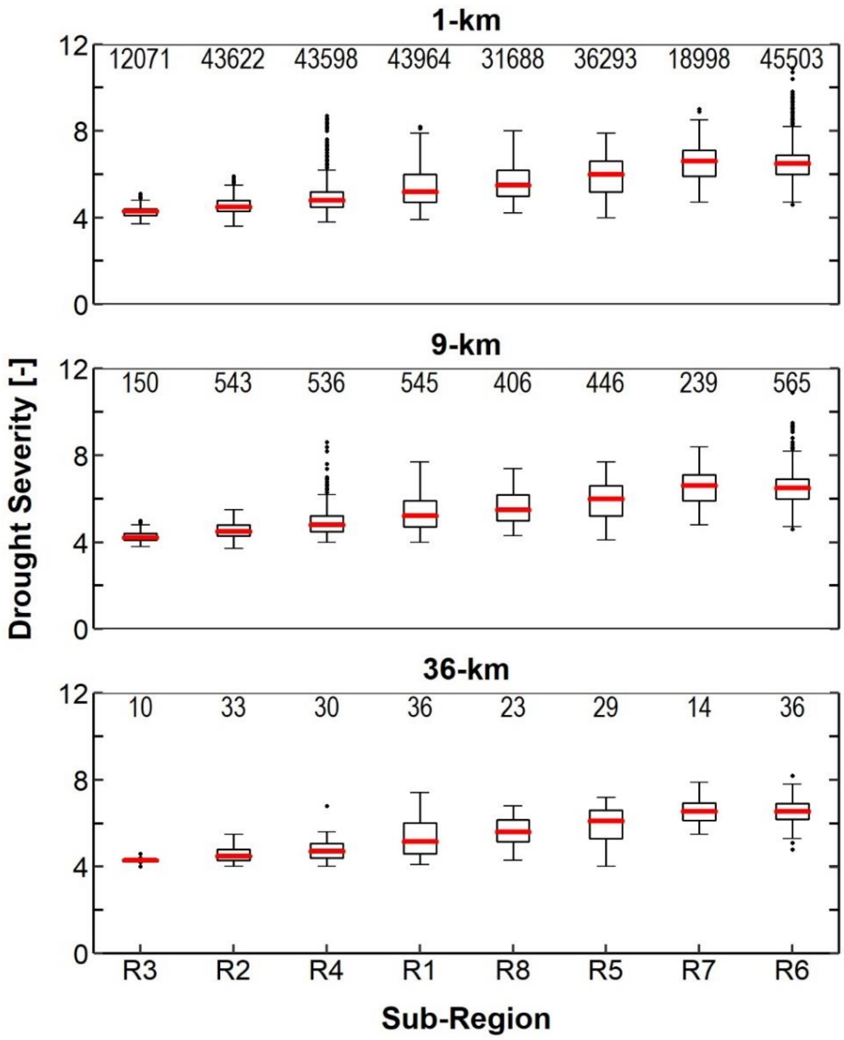

Figure 3. 8 Regionally averaged drought severity estimated from SPEI in eight sub-regions of Vietnam in different spatial resolutions (1-, 9-, 36-km). Boxes represent the interquartile range, median, and outliers. The tops and bottoms of each box are the 10th and 90th percentiles of the data. The number on top of each box plot denotes sample sizes for each sub-region.

Overall, the total areas with significant increasing trends in precipitation were 25.7%, 25.7%, and 26.5% in 1-, 9-, and 36-km resolutions, respectively. Significant decreasing trends in precipitation were also found in 11.4%, 11.8%, and 11.8% of the total area in 1-, 9-, and 36-km resolutions, respectively. Although different spatial resolutions of precipitation and air temperature MERRA-2 products showed similar spatial patterns, the 1-km product provided more detailed spatial variation in trends compared to the other two.

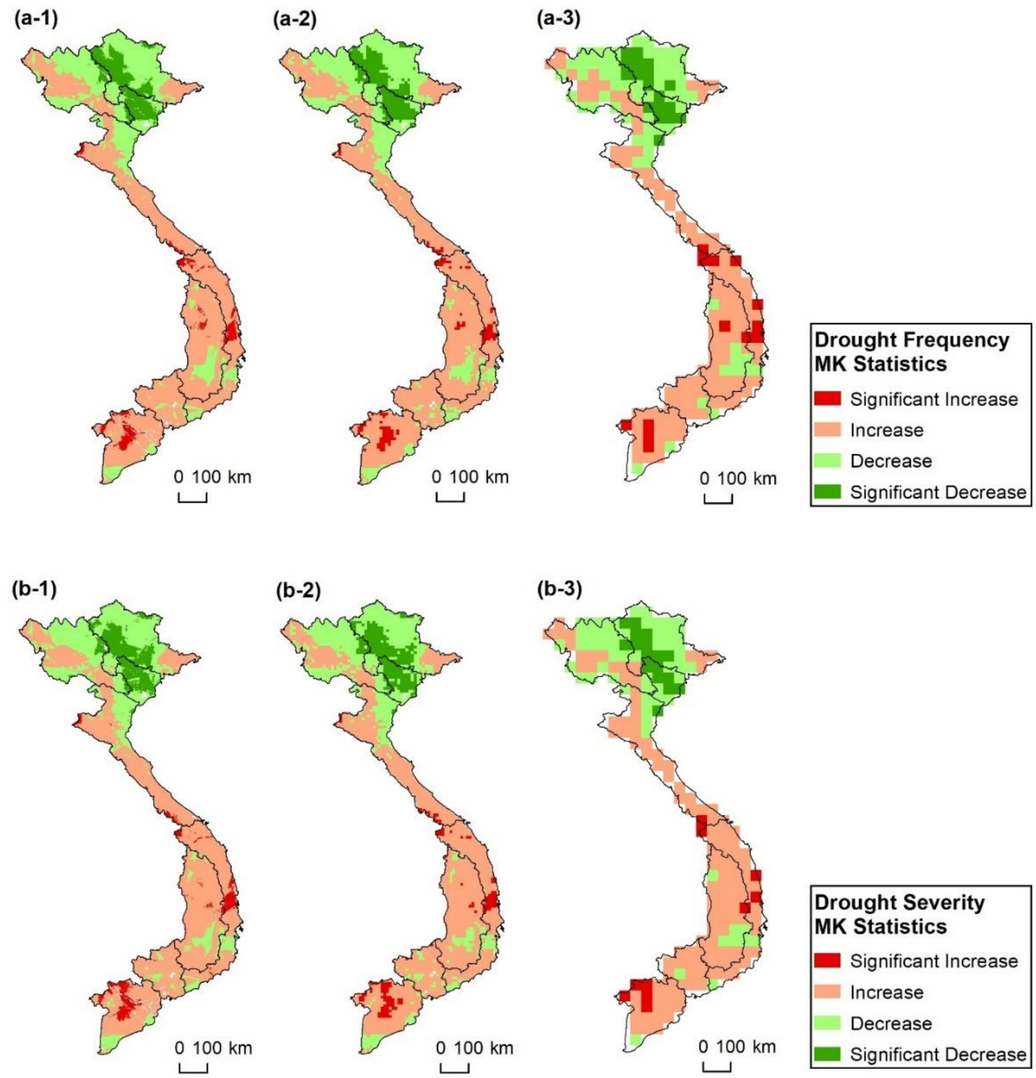

Figure 3. 9 MK Statistics of drought frequency (upper) and severity (lower) based on SPEI during 1989-2018 in Vietnam in different spatial resolutions (1-, 9-, 36-km).

In the past thirty years, the temperature in Vietnam went through a significant increase throughout the country, especially in the southern part (Figure 3. 5b, Figure 3. 6b). The highest increase rate was found in R6. The rapid increase of the temperature in southern Vietnam was also found in Nguyen et al. (2014). Our data show that 40.3%, 40.5%, and 40.2% of the total land area in Vietnam exhibited significant increasing trends based on 1-, 9-, and 36-km products, respectively. Again, the 1-km product could provide more variation details in temperature trends than the other two.

3.5.3. Spatial-Temporal Assessment on Drought Characteristics in Vietnam based on MERRA-2 Datasets

In this section, we assess drought characteristics and trends for the entire land in each sub-region of Vietnam. Figure 3. 7 and Figure 3. 8 show regionally averaged drought frequency and severity for

SPEI. Generally, regions with a higher frequency of drought show higher drought severity (in absolute values), inferring a possibly positive correlation between the two metrics of drought. The drought-prone areas were found in the R5, R6, R7 and R8 regions. The drought problems in R5, R6, and R8 were in line with observed records (Hoc, 2002; Ngo et al., 2020; Nguyen and Shaw, 2011). Interestingly, we detected high values in drought frequency and drought severity in R7. However, not many records of droughts were observed in this region by comparison with other regions.

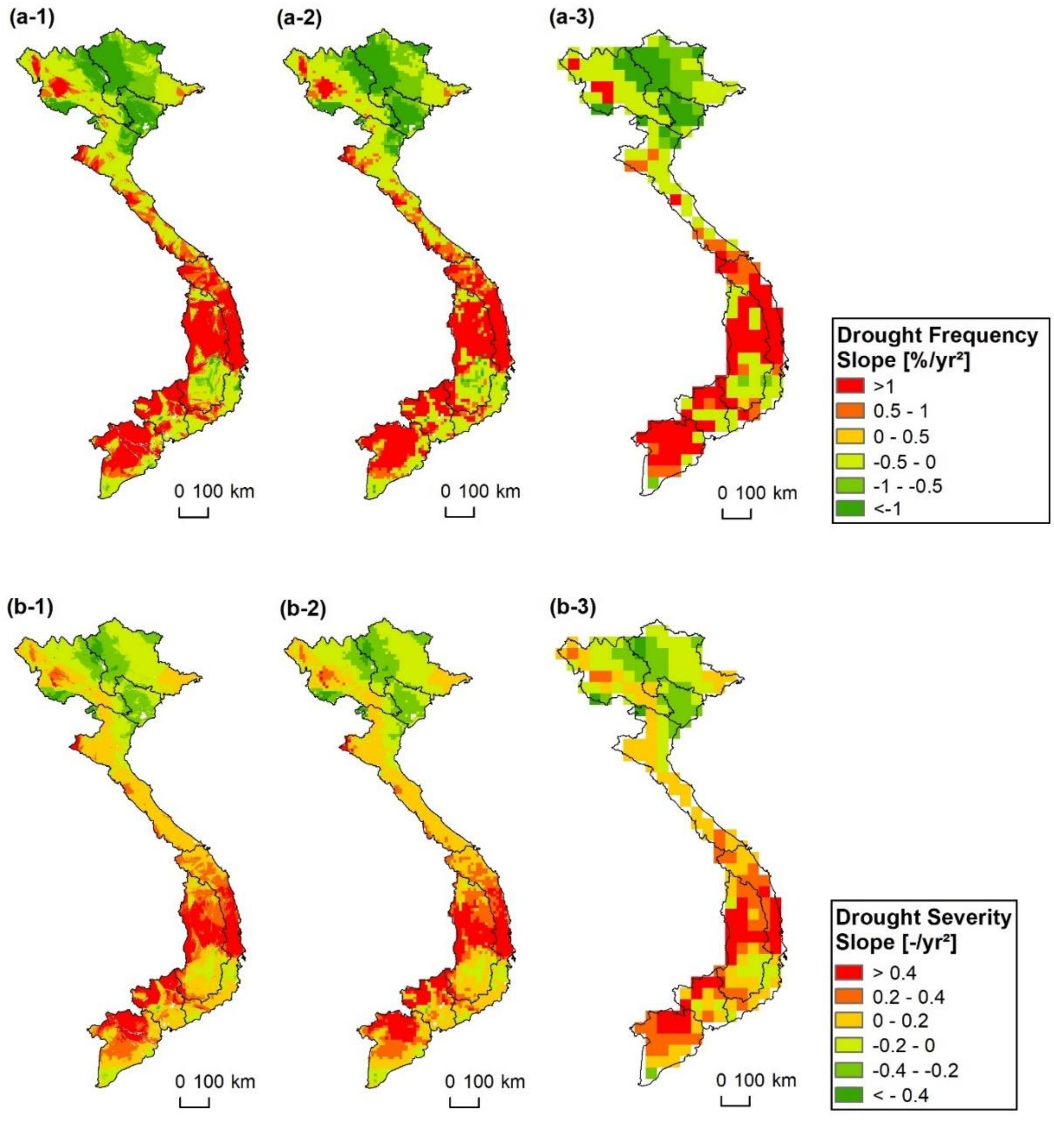

Figure 3. 10 Sen's slopes of drought frequency (upper) and severity (lower) based on SPEI during 1989-2018 in Vietnam in different spatial resolutions (1-, 9-, 36-km).

The reason that drought is less noticeable in R7 may be that this region primarily cultivates cash crops (e.g., pepper, coffee, rubber, and cashew) which require less water supply and perform good drought resilience. Therefore, unfavorable climate conditions may not significantly affect the productivity of these crops. Note that R4 only ranked sixth of eight regions in terms of drought frequency and severity; it exhibited many outliers, possibly caused by large variations in rainfall and air temperature in this region (see Appendix 3). Overall, the three spatial resolutions provided similar drought characteristics information; however, higher resolution datasets exhibited more spatial details in the variation of drought characteristics, demonstrating a higher number of outliers.

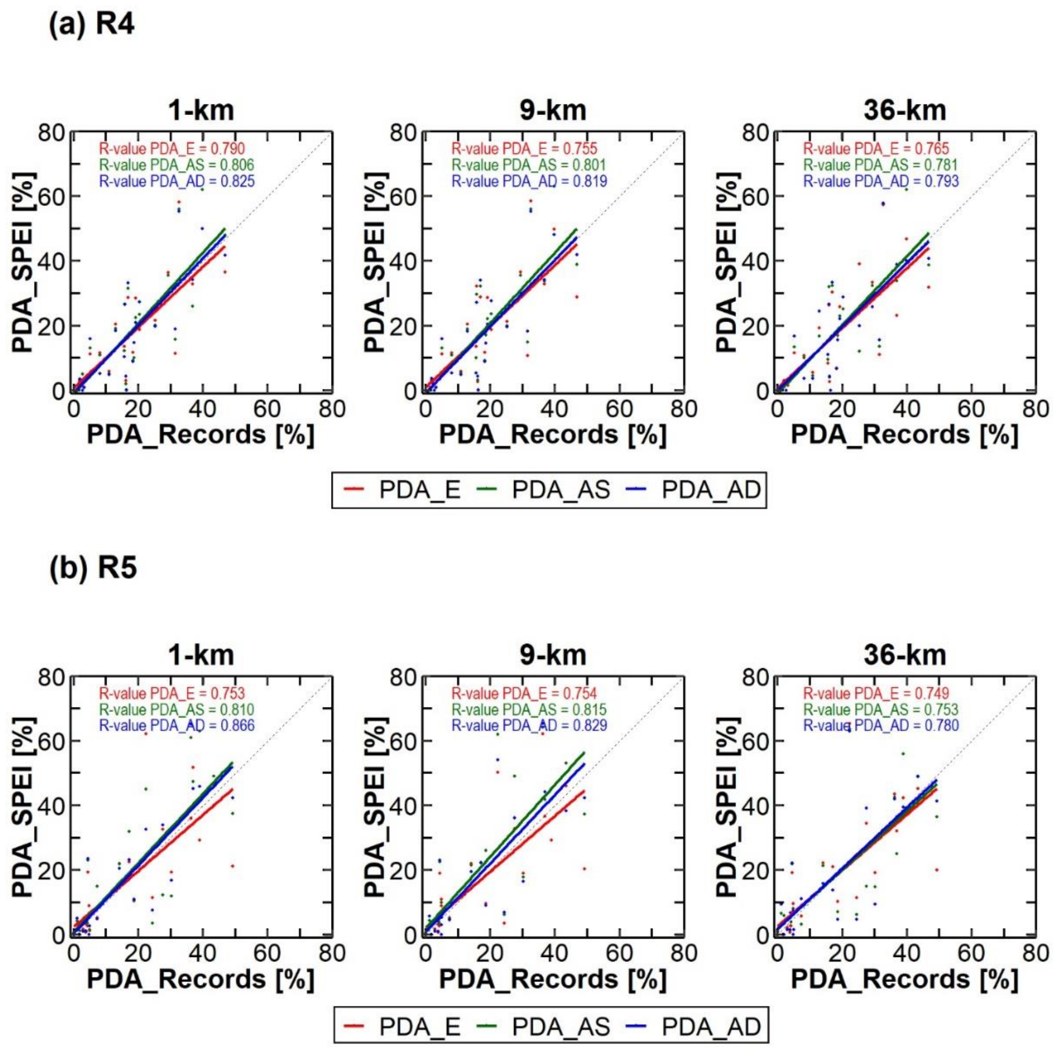

Figure 3. 11 Comparison of Percentage Drought Area (PDA) estimated from simulated SPEI and observed records in different spatial resolutions (1-, 9-, 36-km) in R4 and R5. The gray dash line denotes a 1-1 line. The bold lines in red, green, and blue are the regression lines between PDA based on SPEI and PDA based on observed records.

Trends of severity and frequency of droughts are presented in Figure 3. 9 and Figure 3. 10. Spatial patterns of these trends can roughly be characterized as having a north-south contrast, similar to the patterns found in the trends of precipitation and air temperature (Figure 3. 5 and Figure 3. 6). Both wetting in the northern region and drying in the southern region were found to be most significant based on SPEI. The increasing trend in drought frequency and severity in the southern part is more widespread, with the most significant areas ($p < 0.05$) found in the northern and central part of R8, which might reflect the prevalent decreasing trend of precipitation and the increasing trend of air temperature in the same region.

Table 3. 3 presents descriptive statistics of significant decreasing (increasing) trends in terms of drought frequency in different spatial resolutions during 1989-2018. The drought frequency exhibited

a significant reduction in R3 in 62.8%, 66.0%, and 60.0% of total land, based on 1-, 9-, and 36-km, respectively. On the contrary, significant increasing trends in drought frequency were found in the R5 and R8 regions. According to 1-, 9, and 36-km products, drought frequency significantly increased to 9.59%, 9.19%, and 10.69% of the total land in R5, respectively. These magnitudes for R8 regions were 13.40%, 13.55%, and 17.39% of total land, respectively.

Table 3. 3 Descriptive statistics of the Mann-Kendall test and Sen's slope for drought frequency in different spatial resolutions (1-, 9-, and 36-km) in eight sub-regions. Significant trends occur when p-value < 0.05.

Spatial	Description	R1	R2	R3	R4	R5	R6	R7	R8
1-km	n	43,964	43,622	12,071	43,598	36,293	45,503	18,998	31,688
	Sig. Decrease (% of total land)	5.47	27.23	62.80	0.15	-	-	-	-
	Sig. Increase (% of total land)	0.22	-	-	2.51	9.59	2.23	0.01	13.40
	Average Slope (%/year)	-0.28	-0.80	-1.11	0.21	1.14	1.66	1.82	1.42
9-km	n	545	543	150	536	446	565	239	406
	Sig. Decrease (% of total land)	6.06	28.55	66.00	0.19	-	-	-	-
	Sig. Increase (% of total land)	0.37	-	-	2.61	9.19	1.95	0.00	13.55
	Average Slope (%/year)	-0.27	-0.80	-1.12	0.21	1.15	1.69	1.82	1.41
36-km	n	36	33	10	30	29	36	14	23
	Sig. Decrease (% of total land)	5.56	27.27	60.00	-	-	-	-	-
	Sig. Increase (% of total land)	-	-	-	3.33	10.69	5.56	-	17.39
	Average Slope (%/year)	-0.24	-0.78	-1.05	0.00	1.01	1.91	1.71	1.70

Regarding drought severity (absolute values) during 1989-2018, descriptive statistics of significant decreasing (increasing) trends are given in Table 3. 4. A similar observation in drought severity compared to drought frequency, R3 exhibited the most decreasing trends in drought severity, while R5 and R8 experienced the most increasing trends. The proportion of land in decreasing (increasing) trends in drought severity were largely similar to these figures in drought frequency but averaged a difference of around 2%.

3.5.4. Comparison between PDA Estimated from SPEI and Actual Agricultural Record PDA

For each spatial resolution, when we compared PDA estimated from different land cover (PDA-E, PDA-AS, and PDA-AD), there was evidence that the PDA-AD exhibited better agreement with PDA from the data records Figure 3. 11 Comparison of Percentage Drought Area (PDA) estimated from simulated SPEI and observed records in different spatial resolutions (1-, 9-, 36-km) in R4 and R5. The gray dash line denotes a 1-1 line. The bold lines in red, green, and blue are the regression lines between PDA based on SPEI and PDA based on observed records.. First, the slopes from PDA-AD products were closer to the 1:1 line than these slopes from PDA-E and PDA-AS. Second, R-values between PDA-AD and PDA-observation were generally higher than R-values from others. Overall, a better estimation of percentage drought areas in agricultural lands based on SPEI was found at the higher-resolution dataset and in using dynamic land cover. Note that, using a constant land cover to estimate PDA also provided comparable results with using dynamic land cover. This validation has a limitation: we only examined PDA_AD in R4 and R5, which had no significant changes in agricultural land over the study period. However, they still provide the first identification of potential usefulness of using dynamic land cover (Figure 3. 11).

Table 3. 4 Same as Table 3. 3 but for drought severity (absolute value).

Spatial	Description	R1	R2	R3	R4	R5	R6	R7	R8
1-km	n	43,964	43,622	12,071	43,598	36,293	45,503	18,998	31,688
	Sig. Decrease (% of total land)	5.36	29.46	61.94	0.61	-	-	-	-
	Sig. Increase (% of total land)	0.00	-	-	2.77	9.00	1.40	0.27	16.13
	Average Slope (%/year)	-0.07	-0.15	-0.21	0.06	0.22	0.30	0.35	0.27
9-km	n	545	543	150	536	446	565	239	406
	Sig. Decrease (% of total land)	5.50	29.28	65.33	0.75	-	-	-	-
	Sig. Increase (% of total land)	0.00	-	-	2.99	8.74	1.59	0.84	16.26
	Average Slope (%/year)	-0.07	-0.15	-0.21	0.06	0.23	0.31	0.35	0.27
36-km	n	36	33	10	30	29	36	14	23
	Sig. Decrease (% of total land)	2.78	27.27	60.00	3.33	-	-	-	-
	Sig. Increase (% of total land)	-	-	-	3.33	10.34	2.78	-	21.74
	Average Slope (%/year)	-0.06	-0.15	-0.21	0.03	0.21	0.34	0.30	0.30

3.5.5. Assessing Spatio-Temporal Dynamics Drought from High-Resolution Data Sets

It is important to understand total agricultural land in drought in each month for the past 30 years 1989-2018. In the previous section, 1-km PDA-AD exhibited the best overall among others in terms of estimation of PDA in agricultural land in the R4 and R5 region. Therefore, we used this product to explore the historical agricultural lands in drought conditions over Vietnam during 1989-2018 (Figure 3. 12 and Figure 3. 13). Generally, droughts in agricultural land throughout sub-regions occurred every 1-2 years, which is in agreement with the conclusions of Hoc (2002). After 2010, the PDA was found less severe in north Vietnam (R1-3), but more severe in south Vietnam (R7-8). During extreme El Niño conditions (1998, 2002, 2005, 2010, and 2014-16), drought nearly occurred in all sub-regions, with PDA up to 100% in many months. It was also found that extreme drought conditions (high PDA in consecutive months) during El Niño years were more pronounced in sub-regions from R5 toward the south, reflecting the fact that these sub-regions are more sensitive to El Niño conditions. This finding is in agreement with previous studies (Le et al., 2019b). During 1989-2018, agricultural land in Northern Vietnam went through the long-lasting drought in 1989-1991. In R2 and R3 regions, nearly 100% of agricultural lands were in drought condition during May to December 1989 and May to December 1990. Note that the drought of 1989-1992 may not be directly linked to the El Niño event since the most recent El Niño condition during that time was 1987-1988 and was followed by a La Niña event from 1988-1989. Generally, El Niño conditions cause less rainfall and increased temperatures for Vietnam, while La Niña conditions bring more rainfall. Nguyen and Shaw (2011) also reported droughts in R2, R3 and R5 over the course of 1989-1991.

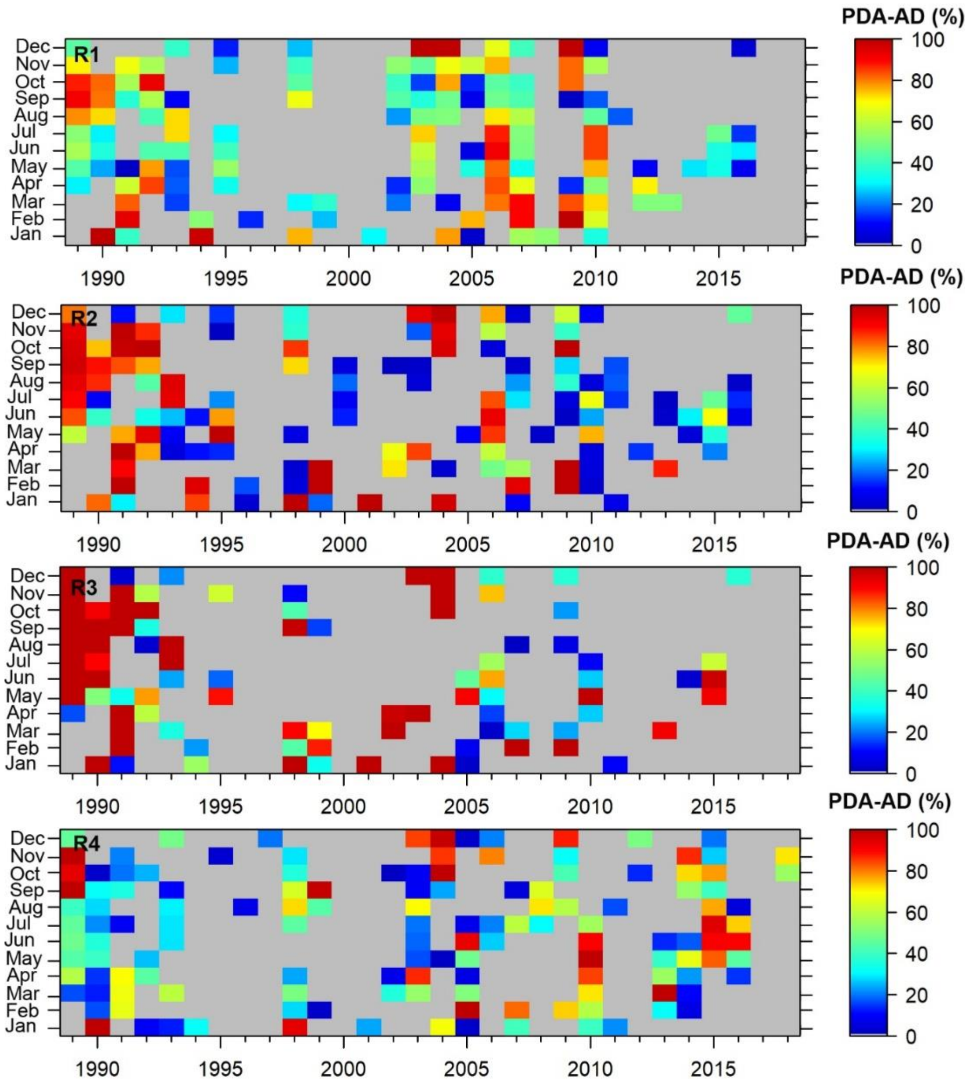

Figure 3. 12 Percentage drought area for agricultural land using dynamic land cover (PDA-AD) estimated from 1-km spatial resolution in R1, R2, R3, and R4 sub-region based on SPEI during 1989-2018. Gray color denotes no drought condition.

In Southern Vietnam, during the 30-year study period, the 2014-16 drought caused the worst conditions in agricultural regions in R6, R7, and R8. During summer – autumn – winter period (May-November) of 2014 and 2015, the PDA-AD were estimated at around 80-100% in R6. This situation is even worse for R7 and R8. Extreme drought conditions (PDA > 80%) were found in July – August 2013 for these both regions. Agricultural lands in drought conditions were continuously found from May to December (2014); May-December (2015), and January – April (2016). From 1-km PDA-AD, the end of 2014-16 historical drought seems to be at the end of April 2016 (lower PDA observed after that month). This is similar to the actual record as the reports in the losses due to drought for R6 and R8 were also estimated up to April 2016 (Ngo et al., 2020). Up to that month, total land losses due to 2014-16 drought and saline intrusion in R5, R6, and R8 were 242,215 ha paddy rice, 55,651 ha fruit trees, 104,106 ha perennial cash crops, and 4,641 ha aquaculture. More than 400,000 households (equivalent to 1.5 million people) were limited access to drinking water (Ngo et al., 2020).

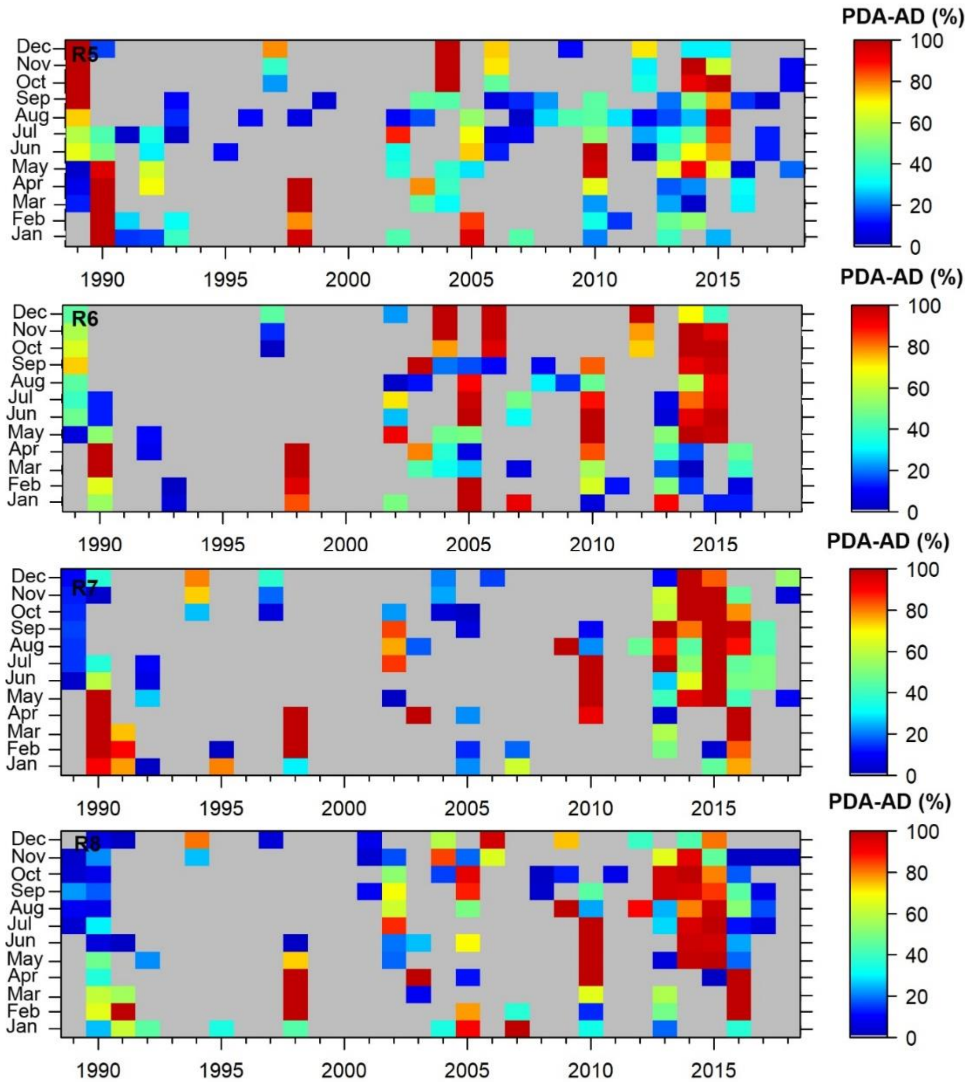

Figure 3. 13 Percentage drought area for agricultural land using dynamic land cover (PDA-AD) estimated from 1-km spatial resolution in R5, R6, R7, and R8 sub-region based on SPEI during 1989-2018. Gray color denotes no drought condition.

3.5.6. Limitations and Further Studies

Although the MERRA-2 dataset exhibited an overall reasonable relationship with ground observation, it somehow overestimates or underestimates dryness and wetness, as well as often underestimates precipitation and air temperature in Vietnam. Therefore, trend analysis in high error areas should be judged carefully (for example, northern R6 and northern R5). Regarding the validation of PDA from agricultural land, this study could only obtain drought records data in R4 and R5, thus limiting a comprehensive assessment of PDA estimated from SPEI and actual agricultural record PDA for the entire study region.

This study mainly explores drought conditions from a meteorological perspective, which is a combination between precipitation and potential evapotranspiration (i.e. calculated from air temperature). Future study could work on a combination of multi-drought impact factors – actual evapotranspiration, runoff, soil moisture, and soil temperature. For such poorly gauged conditions, land surface models could be a potential approach to obtain these hydrological variables listed above.

In this study, we focused on investigating the applicability of finer resolution disaggregated reanalysis data in drought analysis. It is worth noting that the original spatial resolution of MERRA-2 data is about 50-km, but we intentionally included only 36-km SPI results in this study because we plan a future comparison of the present research with satellite-based drought indices. Drought indices employing soil moisture data obtained from Soil Moisture Active Passive (SMAP) data will be 36-km because SMAP's original spatial resolution is 36-km (Entekhabi et al., 2010). In the planned future study, the results shown here will be compared with drought indices from satellite-based soil moisture data.

3.6. Conclusions

In this study, we investigated the ability of a high-resolution re-analysis dataset and dynamic land cover to capture drought conditions over data-sparse areas in Vietnam. The 3-month SPEI was calculated to assess drought trends and its spatio-temporal characteristics using three different spatial resolution datasets from the MERRA-2 datasets on a monthly time scale from 1989 to 2018.

By comparing with in-situ measurements, MERRA-2 exhibited an overall good relationship with these measurements (median R-value and MAE for precipitation: 0.809 and 57.5 mm, respectively; median R-value and MAE for air temperature: 0.977, and 1.14 °C, respectively). It suggests the adequacy of MERRA-2 for studies in Vietnam for drought analysis.

Regarding trend analysis, along with the observed significant trends in precipitation and air temperature, SPEI showed increasing (decreasing) trends in drought severity and frequency in the southern (northern) part of Vietnam. The significant increasing trends of these drought characteristics were found mostly in R5 and R8. The high spatial resolutions of MERRA-2 used in this study allowed us to identify the contrast in drought trends between the northern (wetting/decreasing) and southern (drying/increasing) parts of Vietnam, which are generally shown in coarser climate model simulations.

We designed an experiment which compared the percentage drought area (PDA) estimated based on different land use data sets with PDA from observed records. Overall, the results support the hypothesis that (1) Higher spatial resolution of drought indices, help to accurately characterize and monitor drought events, and (2) PDA using dynamic land cover scenarios results in better agreement with the observed records.

Over the 30-year study period, southern Vietnam underwent unfavorable climate conditions, exhibiting a reduction in rainfall and an increase in temperature which consequently increased the risk of drought frequency and severity. In this region of Vietnam, the 2014-16 drought seems to have produced the worst conditions in terms of temporal duration and spatial extent.

With the advent of higher spatial resolution data sets, specifically for soil moisture (Fang et al., 2018b; Kim and Lakshmi, 2018; Narayan and Lakshmi, 2008) add information to ecohydrology (Billah et al., 2015; Hong et al., 2007; Lakshmi et al., 2011) and help to understand the connectivity between hydrology, meteorology and ecology.

In conclusion, this study emphasizes the feasibility of drought analysis using re-analysis datasets in areas where observations are scarce. As we currently have a wide range of re-analysis datasets produced by different institutions, we expect more accurate global-scale drought monitoring with high-resolution model datasets to become possible in future studies.

Chapter 4: Adequacy of Satellite-derived Precipitation Estimate for Hydrological modelling in Vietnam Basins[3]

4.1. Introduction

The major uncertainties in hydrological modelling are associated with incorrect precipitation patterns over space (Sangati and Borga, 2009). Several studies indicated that a better representation of the spatial variability in precipitation could improve model performances (Emmanuel et al., 2012; Lobligeois et al., 2014; Zhao et al., 2013). Rain gauge-, radar-, and satellite-based products are popular methods to estimate precipitation across the globe. Rain gauges are the primary approach to obtain precipitation information, as they measure rainfall by directly on the ground and thus do not need transformation into any type of signal, nor need to be corrected (Kidd, 2001). However, rain gauge networks are often sparse, with irregular spatial coverage. In many parts of the world, they are non-existent (Mondal et al., 2018; Rana et al., 2015). Moreover, it is often challenging to obtain rain gauge data, especially in developing countries and transboundary river basins, for technical and administrative reasons (Gerlak et al., 2011; Plengsaeng et al., 2014).

Ground-based radar systems are useful and provide data with high temporal and spatial resolution. However, radar systems frequently have a limited spatial range (Michaelides et al., 2009), and are thus most useful for rapid events, typically in urban hydrology (Thorndahl et al., 2017). In addition, radar sensors are often not feasible in developing countries, due to high installment costs and complex maintenance demands. In an effort to cover large areas over long periods, regionally and globally, Satellite-derived Precipitation Estimate (SPE) products emerge as promising approaches to reflect the spatial pattern and temporal variability of rainfall. Several gridded SPE products have been developed over the last few decades, including PERSIANN (Precipitation Estimation from Remotely Sensed Information using Artificial Neural Networks) (Sorooshian et al., 2000); CMORPH (Climate Prediction Center(CPC) MORPHing technique) (Joyce et al., 2004); GSMaP (Global Satellite Mapping of Precipitation) (Ushio et al., 2009); TMPA (TRMM Multi-satellite Precipitation Analysis) (Huffman et al., 2007); and GPM (Global Precipitation Mission) (Hou et al., 2014). Moreover, several promising datasets incorporating gauge, satellite, and re-analysis observations, such as CHIRPS (Climate Hazards group InfraRed Precipitation with Station data) (Funk et al., 2015), and MSWEP (Multi-Source Weighted-Ensemble Precipitation) (Beck et al., 2017a), have also been released.

Many studies have shown that gauge-based hydrological models outperform SPE-based models, in terms of streamflow simulation (Duan et al., 2018; Li et al., 2018a; Nguyen et al., 2018). However, SPE-driven hydrological simulations exhibit better performance in simulating streamflow than rain gauge-driven hydrological simulations, for example, in the Luanhe River (Ren et al., 2018), and Lower Mekong River basins (Luo et al., 2019; Mohammed et al., 2018). This is likely associated with the low density of rain gauges and poor-quality of ground rainfall data. For example, a low rain gauge density was observed at the Upper Yangtze River Basin of China, where stations were located approximately

---

[3] This chapter has been published as Le, M. H., Lakshmi, V., Bolten, J., & Bui, D. D. (2020). Adequacy of Satellite-derived Precipitation Estimate for Hydrological modeling in Vietnam Basins. Journal of Hydrology, 124820. https://doi.org/10.1016/j.jhydrol.2020.124820.

every 30,000 km^2 (Liu et al., 2017). Also, Le and Pricope (2017) reported the case of the Nzioa Basin, Western Kenya, where rain gauge data was missing (30%-65% records). Interpolating that data resulted in a poorer performance than that of the Climate Forecast System Reanalysis (Saha et al., 2010) and the CHIRPS (Funk et al., 2015) datasets, in terms of streamflow simulation. Wang et al. (2016) indicated that satellite-based rainfall could be more suitable for driving distributed hydrologic models, particularly in basins with poor rain gauge conditions. The superiority of remote sensing in deriving precipitation products has become more pronounced as advanced algorithms have been developed. For example, the TMPA 3B42V7 has proven to be better, compared to its previous version TMPA 3B42V6 (Zhang et al., 2019). The increased spatial and temporal resolution of GPM IMERG follow the successes of TMPA (Hou et al., 2014), with an increase from 0.25° and 3 hours to 0.1° and half hour. Furthermore, a fine spatial scale of CHIRPS (0.05°, ~ 5 km) has been developed (Funk et al., 2015). These developments enable SPE to better characterize the spatial and temporal variability of precipitation.

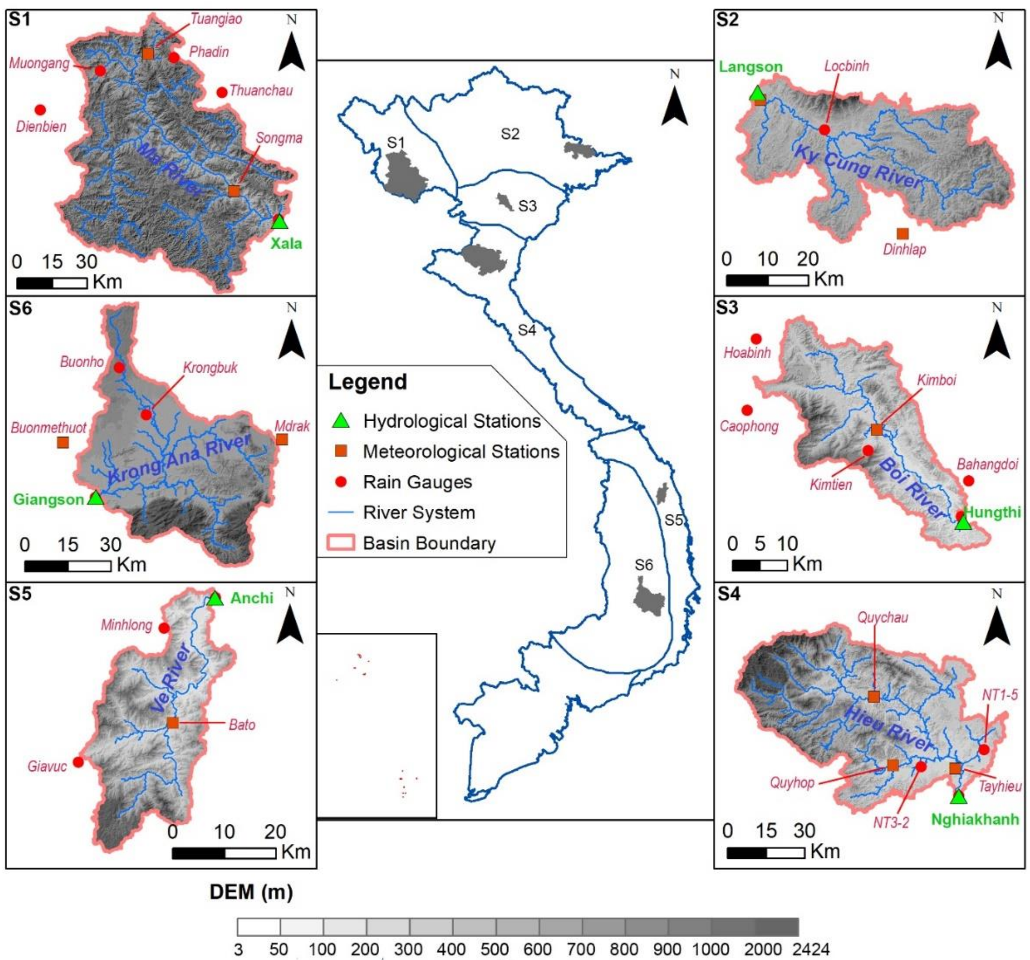

Figure 4. 1 Digital Elevation Model (DEM) and the distribution of hydrometeorological stations, at six basins, used in this study. S1 North West (XL basin of Ma River); S2 North East (LS basin of Kycung River); S3 North Delta (HT basin of Boi River); S4 North Central (NK basin of Hieu River); S5 South Central (AC basin of Ve River); and S6 Central Highland (GS basin of Krong Ana River).

Each of the SPE products contains various versions, often divided into two groups: gauge-adjusted (gauge-corrected SPE) and gauge-unadjusted (gauge-uncorrected SPE). Gauged-corrected SPE datasets use measured rain gauges or re-analysis data to adjust precipitation estimates at the locations of the gauges. Correction factors used at those rain gauge locations are then applied to the entire dataset, leading to a decrease or increase in rainfall estimates, so that the dataset fits the directly measured, more precise rain gauge data (Beck et al., 2018). However, the gauge networks used for corrections (e.g., GPCC-Global Precipitation Climatology Centre, CPC-Climate Prediction Center) were sparse in many areas, typical in developing countries. Therefore, rigorous comparisons between gauge-corrected SPE products and uncorrected SPE products should be performed, specifically in regions where few gauges are used for creating the adjusted SPE.

In this study, six SPE products were evaluated, including the gauge-corrected SPE products (i.e., GPM IMERGF-V6, TMPA 3B42V7, and CHIRPS V2.0) and the uncorrected SPE products (i.e., GPM IMERGE-V6, TMPA 3B42RT, and CHIRP V2.0), on various climate regions of Vietnam. A hydrological model assessment of the SPE was performed, using the SWAT (Soil Water Assessment Tool) hydrological model. This model has demonstrated strong capabilities in hydrologic assessment throughout Vietnam, in many studies (Ha et al., 2018; Vu et al., 2012; Vu et al., 2017). The primary goal of this study is to obtain insight into the performances between gauge-corrected and uncorrected SPE products in: 1) comparisons to the rain gauge data; and 2) simulations of the monthly stream flow. In this paper, Section 2 introduces the case study. Section 3 presents material and methods. Section 4 presents the results and discussions, and the conclusions are presented in Section 5.

4.2. Watersheds

In this study, six basins with areas ranging from 684 km^2 to 6042 km^2 were selected (Figure 4. 1), based on the following criteria. Firstly, headwater basins were selected, to reduce the impact of human activities on the flow regime. Secondly, each basin is located entirely within a single climatological region of Vietnam; it allows to thoroughly examine the performance of SPE datasets over Vietnam. These sub-climatological regions include North West (S1); North East (S2); North Delta (S3); North Central (S4); South Central (S5); and Central Highland (S6). These regions were classified based on the duration of the rainy season; the three heaviest rainfall months; differences in solar radiation; and temperature (Nguyen and Nguyen, 2004), and are widely accepted by the climatological community (Nguyen-Xuan et al., 2016; Phan and Ngo-Duc, 2009; Trinh-Tuan et al., 2019b). Annual precipitation across basins ranges from 1400-3800 mm. There is a seasonal variability in precipitation in each basin, with 70%-85% total rainfall during May-August (MJJA) or September-December (SOND). For example, in the rainy season, MJJA in the S1 region is highly influenced by the summer monsoon, whereas the S4 region is dominated by the winter monsoon (Nguyen-Le et al., 2015). The average elevations of selected basins are also diverse, ranging from 3 m to more than 2000 m above mean sea level.

4.3. Data and Methods

The chosen approach contains two steps: 1) an inter-comparison of SPE products with in-situ rain gauge data; and 2) an evaluation of a hydrological model for monthly streamflow simulation, driven by rain gauge precipitation measurements and SPE products. Below, we describe the data and methodology used for these two steps.

4.3.1. Ground hydro-meteorological data

The hydro-meteorological data used in this study were obtained from the Vietnam Meteorological and Hydrological Administration (VMHA) (http://kttvqg.gov.vn/) and National Central for Water

Resources Planning and Investigation (NAWAPI) (http://nawapi.gov.vn/). The data were recorded and have undergone quality control at regional meteorological and hydrological services before the post-processed version was delivered to the VMHA. This process depends on region and data types, which are varied from several days to several months (personal communication).

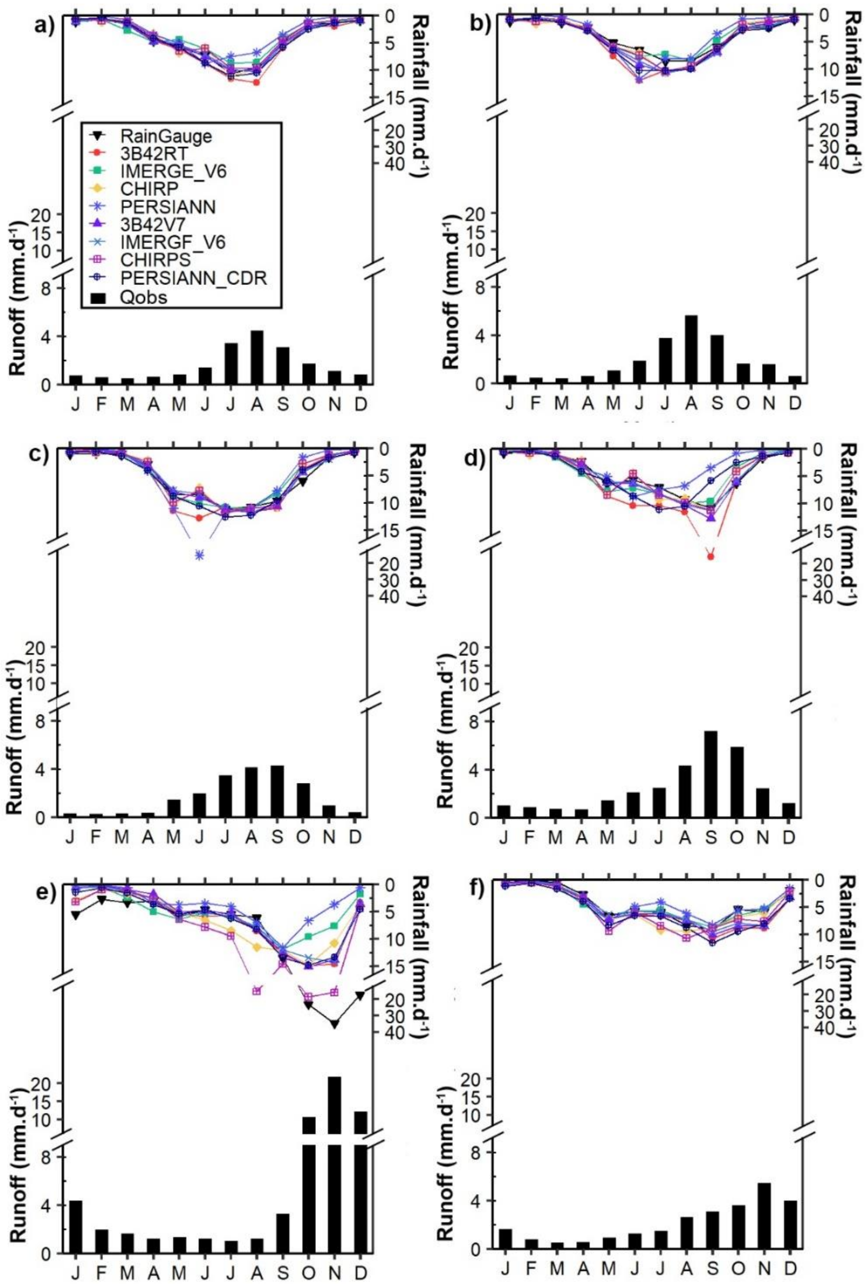

Figure 4. 2 The observed monthly average runoff and different precipitation datasets (rain gauge; 3B42RT; IMERGE-V6; CHIRP; 3B42V7; IMERGF-V6; and CHIRPS), at the river outlets of a) XL, b) LS, c) HT, d) NK, e) AC, and f) GS basins.

The daily 2002-2017 runoff data at six hydrological stations were collected corresponding to different climatological regions (Xala (XL) of Ma River; Langson (LS) of Kycung River; Hungthi (HT) of Boi River; Nghiakhanh (NK) of Hieu River; Anchi (AC) of Ve River; and Giangson (GS) of Krong Ana

River). The data quality of the streamflow was checked and assured with no gaps, during the given study period. Averaged monthly streamflow at different climate zones in Vietnam exhibits high variability in both time and space (Figure 4. 2). Examining Figure 4. 2 as we move from the northern part of Vietnam to the south, that is, from climate zone S1 to S6, we observe that the peak of the monthly runoff shifts from August (zones S1 and S2) to September (zones S3 and S4) to November (zones S5 and S6). We also observe that the AC (Ve River) basin of zone S5 has the largest runoff (by a factor of two as compared to the other river basins).

We collected daily 2000-2017 precipitation data from 31 rain gauge stations across six basins (see Appendix 4). There are several rain gauges in each of these basins, and their number ranges from three to seven. The average missing values across all rain gauges were approximately 1.0%. The long-term mean values were used to substitute for the missing data. The rain gauge data were tested for homogeneity, using the double mass curve to exclude systematic errors over time in the datasets. Annual rainfall at each station was compared with the average annual rainfall of surrounding stations to detect inconsistencies. The results indicated no significant difference between the two curves at all rain gauge stations, ensuring consistency through recorded precipitation.

Besides, at each basin, one to three air temperature datasets (minimum and maximum variables) were collected at meteorological stations, with the same duration as that of precipitation measured by the rain gauges. Since air temperature is less varied than precipitation, a small number of air temperature stations are adequate to represent temperature profiles throughout the basins.

In conclusion, the data from rain gauges used in this study serve two purposes: 1) as a benchmark to compare with the SPE datasets; and 2) together with air temperature data, as inputs to the SWAT hydrological model for the simulations of streamflow.

4.3.2. Satellite Precipitation Estimation (SPE) products

4.3.2.1. TMPA precipitation datasets

The Tropical Rainfall Measurement Mission (TRMM) Multi-satellite Precipitation Analysis (TMPA), launched in late 1997, is a collaboration between the National Aeronautics and Space Administration (NASA) and the Japan Aerospace Exploration Agency (JAXA). It is the first space mission to measure rainfall in tropical regions. The TRMM is a low-Earth orbit satellite, equipped with Precipitation Radar (PR); TRMM Microwave Imager (TMI); Visible and Infrared Scanner (VIRS); and Lighting Imaging Sensor (LIS) (Huffman et al., 2007). The two TMPA products used in this study are the near real-time version TMPA 3B42RT (hereafter 3B42RT); and an adjusted version, using monthly gauge precipitation, TMPA 3B42V7 (hereafter 3B42V7) (Huffman and Bolvin, 2013; Huffman et al., 2007). The three hours 0.25° grid TMPA products were accessed from NASA's Goddard Space Flight Center website (https://pmm.nasa.gov/data-access/downloads/trmm), then accumulated to a daily time step.

4.3.2.2. GPM IMERG precipitation datasets

The Global Precipitation Measurement (GPM) mission was developed as a continuation and improvement of the TRMM mission. The Integrated Multi-satellitE Retrievals for GPM (IMERG) product, is the Level 3 multi-satellite precipitation algorithm of GPM, which combines all of the microwave sensors in the constellation, and Infrared-based observations from geosynchronous satellites (Hou et al., 2014). The two latest products of GPM IMERG used in this study are GPM IMERG Early Run Version 6 (hereafter IMERGE-V6) and IMERG Final Run Version 6 (hereafter

IMERGF-V6). The half-hour 0.1° gridded GPM IMERG products were accessed from NASA's Goddard Space Flight Center website (https://pmm.nasa.gov/data-access/downloads/gpm), then accumulated to a daily time step.

Table 4. 1 Summary of Satellite Precipitation Estimation datasets used in this study, with spatial-temporal characteristics and used period.

Product Name	**Spatial coverage**	**Spatial resolution**	**Temporal coverage**	**Finest Temporal**	**Latency**	**Reference**
TMPA 3B42RT	50°N – 50°S	0.25°	2000 – present	Every three	Hours	Huffman et al. (2007)
GPM IMERGE-	65°N – 65°S	0.1°	2000 - present	Every half hour	Hours	Hou et al. (2014)
CHIRP V2.0	50°N – 50°S	0.05°	1981 - present	Daily	Days	Funk et al, 2015
PERSIANN	60°N – 60°S	0.25°	2000 - present	Hourly	Days	Sorooshian et al, 2000
TMPA 3B42V7	50°N – 50°S	0.25°	1998 – present	Every three	Months	Huffman and Bolvin,
GPM IMERGF-	65°N – 65°S	0.1°	2000 - present	Every half hour	Months	Hou et al., 2014
CHIRPS V2.0	50°N – 50°S	0.05°	1981 - present	Daily	Days	Funk et al, 2015
PERSIANN CDR	60°N – 60°S	0.25°	1983 - present	Daily	Months	Ashouri et al, 2015

4.3.2.3. CHIRPS precipitation datasets

University of California-Santa Barbara's Climate Hazards Group developed the Climate Hazards group Infrared Precipitation (CHIRP), and the Climate Hazards group Infrared Precipitation with Stations (CHIRPS) datasets, which each provides a more than 30 years quasi-global rainfall dataset. These products aim to support the United States Agency for International Development Famine Early Warning System Network (FEWS NET). The CHIRP dataset estimates rainfall from infrared cold cloud duration (CCD) regression, calibrated by 2000-2013 TMPA pentadal precipitation product (Funk et al., 2015). The gauge-corrected grid CHIRPS dataset uses rain gauge station observations from various datasets, mainly in the USA, Central America, South America, and sub-Saharan Africa (Funk et al., 2015). This study obtained the daily 0.05° grid CHIRP V2.0 (hereafter CHIRP) and CHIRPS V2.0 (hereafter CHIRPS) datasets from the Climate Hazards Group website (http://chg.geog.ucsb.edu/data/chirps/).

4.3.2.4. PERSIANN precipitation datasets

Precipitation Estimation from Remotely Sensed Information using Artificial Neural Networks (PERSIANN) is developed at the Center for Hydrometeorology and Remote Sensing (CHRS) at the University of California, Irvine. This product uses artificial neural networks (ANNs) to estimate rainfall rates from cloud-top temperature, measured by long wave infrared imagery at a spatial resolution of 0.25° (Sorooshian et al., 2000). The Precipitation Estimation from Remotely Sensed Information using Artificial Neural Networks-Climate Data Record (PERSIANN-CDR) is PERSIANN's adjusted version using Global Precipitation Climatology Project (GPCP) monthly product version 2.2. PERSIANN-CDR has a long-term data set with more than 30 years of data from 1983 to the near present. However, this dataset degrades the temporal resolution to daily scale (Ashouri et al., 2015; Nguyen et al., 2019). This study acquired the daily 0.25° gridded PERSIANN and PERSIANN-CDR datasets from CHRS portal website (https://chrsdata.eng.uci.edu/).

A summary of SPE is listed in Table 4. 1, and monthly rainfall distributions of SPE at each basin are presented in Figure 4. 2. The rainfall for the AC (Ve River) basin of Zone S5 is nearly two to three times of the other five river basins. This is reflected in the monthly runoff, which is twice as large in the AC (Ve River) basin, compared to the other five basins.

Table 4. 2 Performance metrics for precipitation comparison and hydrological model assessment.

	Statistic	**Equation**	**Optimal Value**	**Performance Evaluation Criteria**
Precipitation Performance Metrics	POD	$\frac{N_{11}}{N_{11}+N_{01}}$	1	
	FAR	$\frac{N_{10}}{N_{11}+N_{10}}$	0	
	CSI	$\frac{N_{11}}{N_{11}+N_{01}+N_{10}}$	1	
	CC	$\frac{\sum_{i=1}^{N}(RG_i-\overline{RG})(SPE_i-\overline{SPE})}{\sqrt{\sum_{i=1}^{N}(RG_i-\overline{RG})^2\sum_{i=1}^{N}(SPE_i-\overline{SPE})^2}}$	1	
	RB	$\frac{mean(SPE)}{mean(RG)}-1$	0	
	$RMSE$	$\sqrt{\frac{1}{N}\sum_{i=1}^{N}(SPE_i-RG_i)^2}$	0	
Streamflow Performance Metrics	NSE	$1-\frac{\sum_{i=1}^{N}(OBS_i-SIM_i)}{\sum_{i=1}^{N}(OBS_i-\overline{OBS})^2}$	1	VG: $NSE \geq 0.80$ G: $0.70 \leq NSE < 0.80$ S: $0.50 \leq NSE < 0.70$ NS: $NSE < 0.50$
	$PBIAS$	$1-\frac{\sum_{i=1}^{N}(OBS_i-SIM_i)}{\sum_{i=1}^{N}OBS_i}$	0	VG: $PBIAS \leq \pm 5$ G: $\pm 5 < PBIAS \leq \pm 10$ S: $\pm 10 < PBIAS \leq \pm 15$ NS: $PBIAS > \pm 15$

Note: N_{11} represents the precipitation observed by the rain gauge and satellite simultaneously. N_{10} represents the precipitation observed by the satellite, but not observed by the rain gauge. N_{01} is contrary to N_{10}. OBS_i is observed streamflow (m^3/s) at the i^{th} day or month, SIM_i is simulated streamflow (m^3/s) at the i^{th} day or month. $\overline{OBS}$ and $\overline{SIM}$ are average observed streamflow and average simulated streamflow, respectively. "VG" Very Good, "G" Good, "S" Satisfactory, "NS" Not Satisfactory.

4.3.3. SWAT Model and Setup

SWAT (Soil and Water Assessment Tool) is a physically based, semi-distributed, eco-hydrological model that operates at various time-steps (i.e., daily, monthly, yearly) to simulate the streamflow, sediment, and water quality of large complex river basins (Arnold et al., 1998). In the SWAT model, the smallest spatial unit is the Hydrologic Response Unit (HRU). Runoff is supposed to be predicted separately for each HRU, then routed to estimate the runoff for each sub-basin, as well as that of the entire basin. A detailed description of the SWAT model can be found in Neitsch et al. (2011).

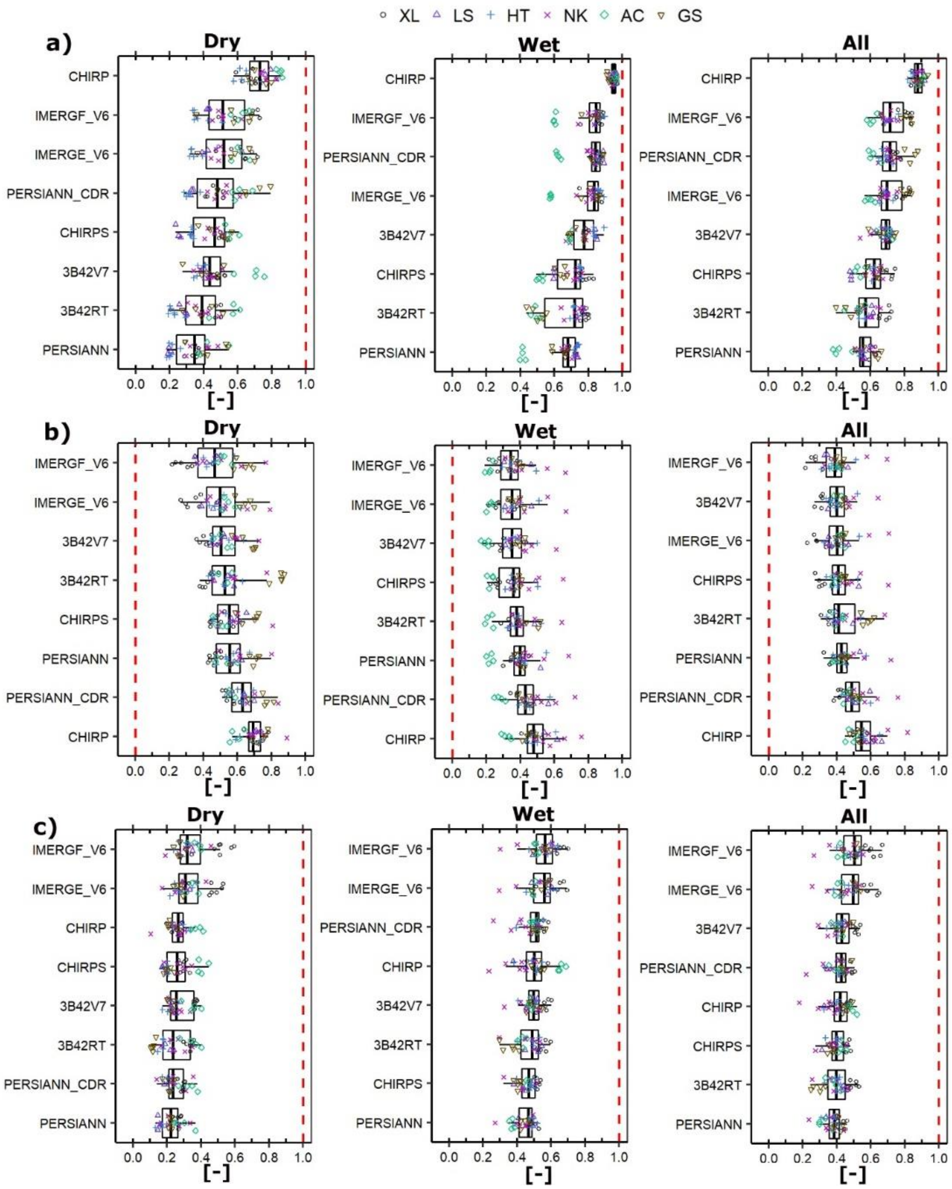

Figure 4. 3 Box plot of rainfall performance metrics a) POD, b) FAR, and c) CSI for six river basins. The red dash line indicates the optimal value.

Determining HRUs requires data on elevation, land use, and soil properties. The 30 m Shuttle Radar Topographic Mission Digital Elevation Model (SRTM DEM), was used to estimate slope and delineate the basin boundary; it was obtained from United States Geological Survey (USGS) Earth Explorer (https://earthexplorer.usgs.gov/). The basin boundaries delineated by SRTM DEM were validated, using a reference from the Vietnamese national basin database. The average error between areas delineated from the SRTM DEM and those from the database was 3%, indicating reliable basin boundaries from the SRTM DEM. The 30 m spatial resolution land-use map representing the year 2010, was obtained from the land use portal for Lower Mekong Basin, which was maintained by SERVIR-Mekong (https://rlcms-servir.adpc.net/en/landcover/). A soil map developed by the Vietnam National Institute for Soil and Fertilizers, at 1:1,000,000 scale (National Institute for Soils and Fertilizers, 2002), was used in this study, resampled from polygons to a 30 m raster file. To prepare associated information of soil properties required in SWAT, a soil database using soil water characteristics equations, following the work of Saxton and Rawls (2006), was created.

Table 4. 3 Median values of the performance metrics of six Satellite-derived Precipitation Estimation, based on daily rain gauge, during 2002 - 2017. For all the metrics, except for FAR and RMSE, larger values represent the better performance of SPE products. Values in bold represent the best score for each metric.

		3B42RT	**IMERGE _V6**	**CHIRP**	**PERSIAN N**	**3B42V7**	**IMERGF _V6**	**CHIRPS**	**PERSIANN _CDR**
POD	Dry	0.391	0.519	**0.732**	0.347	0.437	0.515	0.465	0.481
	Wet	0.722	0.835	**0.949**	0.680	0.778	0.846	0.725	0.843
	All	0.572	0.699	**0.878**	0.558	0.693	0.718	0.624	0.717
FAR	Dry	0.527	0.500	0.694	0.558	0.507	**0.467**	0.554	0.633
	Wet	0.380	0.352	0.480	0.400	0.354	**0.344**	0.362	0.431
	All	0.411	0.403	0.546	0.427	0.400	**0.391**	0.410	0.490
CSI	Dry	0.237	0.311	0.267	0.223	0.255	**0.322**	0.261	0.237
	Wet	0.491	0.563	0.503	0.468	0.498	**0.565**	0.470	0.513
	All	0.399	0.497	0.423	0.386	0.430	**0.505**	0.398	0.427
CC	Dry	0.315	0.497	0.302	0.245	0.430	**0.550**	0.341	0.302
	Wet	0.317	0.610	0.316	0.257	0.420	**0.635**	0.364	0.351
	All	0.358	0.605	0.362	0.296	0.472	**0.651**	0.394	0.389
RB	Dry	**-0.02**	0.06	-0.09	-0.41	-0.08	-0.04	**-0.02**	0.07
	Wet	0.18	-0.04	-0.01	0.01	0.07	0.05	**0.00**	0.17
	All	0.17	-0.03	**0.00**	-0.03	0.07	0.05	**0.00**	0.20
RMSE	Dry	9.20	6.60	6.30	7.30	6.80	**6.10**	6.30	7.50
	Wet	21.6	**15.4**	17.2	18.7	20.1	16.2	16.7	18.3
	All	16.5	12.4	13.2	15.0	15.4	**12.0**	13.0	14.4

Statistical descriptions of elevation, land use, and soil used for the SWAT input, are described in Appendix 5. Generally, evergreen forests, mixed forests, and orchards dominate land use, while Acrisols (ACf, ACu), Ferralsols (FRr), and Fluvisols (FLd) are the dominant soil types across basins. In this study, the watershed networks, sub-basins, and HRUs were generated by the QSWAT version 1.7 plug-in in Quantum Geographical Information System (QGIS) version 2.6.1 (Dile et al., 2016). Several advantages of these software systems have been observed, compared to the commonly used Arc SWAT plug-in on the ArcGIS software (Mohammed et al., 2018; Tuo et al., 2016). The advantages are that QSWAT and QGIS are open source software, and QSWAT has additional features such as merging small sub-basins and static, and dynamically visualizing the outputs.

A contributing area over a threshold of 25 km^2 was applied for all basins, resulting in ranges from 15 (HT) to 145 (XL) sub-basins. To create HRUs, the method of the filter by land use, soil, and slope was used, with a threshold of 10% percent of sub-basins chosen for each feature (see Appendix 5). Because solar radiation is not well-observed, we used the simple Hargreaves method (Hargreaves and Samani, 1982), which requires only air temperature data to calculate potential evapotranspiration. To simulate surface runoff processes, the SCS curve number (USDA Soil Conservation Service, 1972) and Variable Storage Routing method (Williams, 1969), were used. By changing precipitation input datasets, including rain gauges; 3B42RT; IMERGE-V6; CHIRP; 3B42V7; IMERGF-V6; and CHIRPS for the SWAT model, seven simulation scenarios were established for each basin to investigate the effects of different rainfall inputs on monthly streamflow simulation.

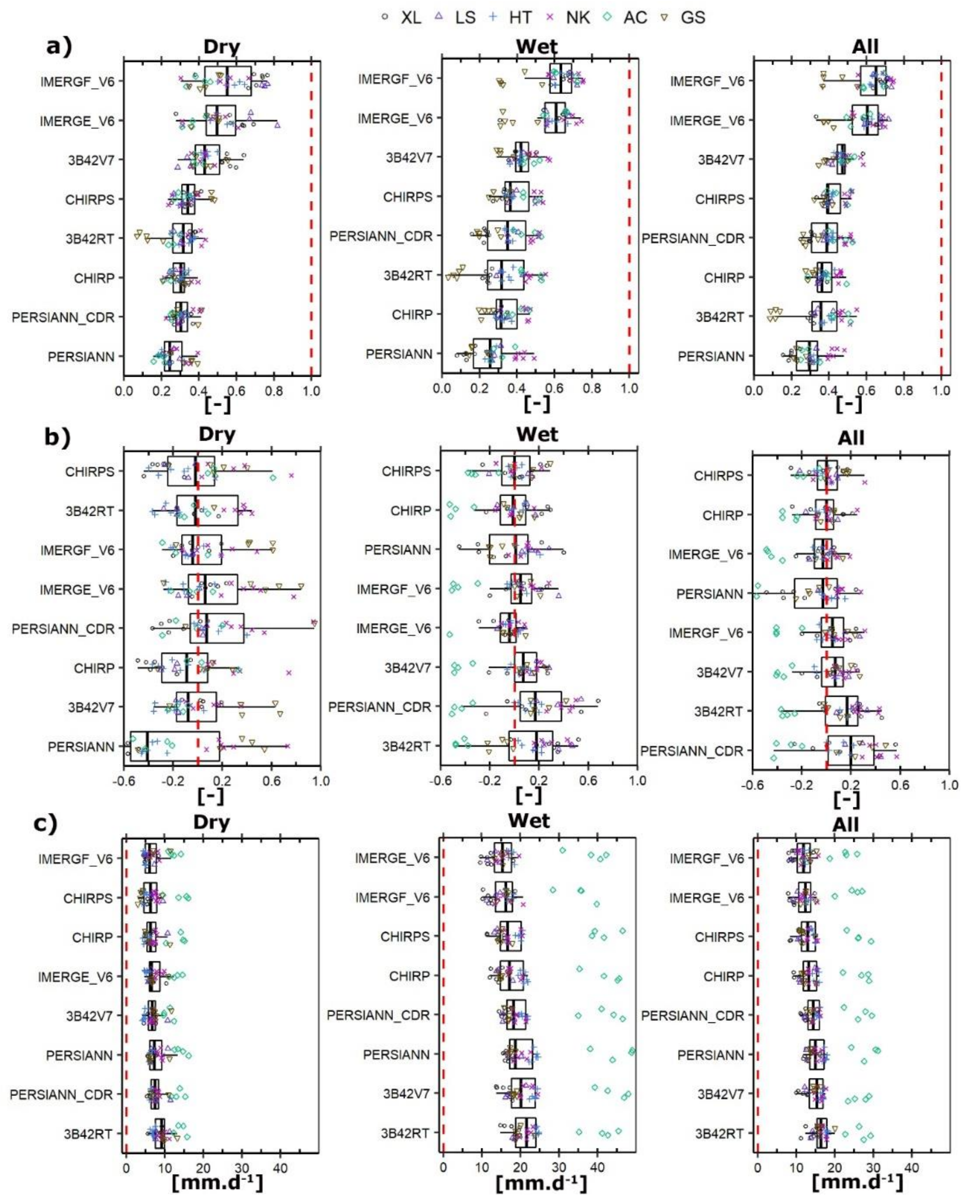

Figure 4. 4 Box plot of rainfall performance metrics a) CC, b) RB, and c) RMSE for six river basins. The red dash line indicates the optimal value.

This study ran the SWAT model on both daily and monthly time scale, selecting the first two years (2000-2001) as the warm-up period; the next eight years (2002-2009) as the calibration period; and the last eight years (2010-2017) as the validation period. The calibration procedure was performed separately for each precipitation dataset. The automatic calibration was performed for streamflow simulation based on the Sequential Uncertainty Fitting algorithm version 2 (SUFI-2) (Abbaspour et al., 2007), using the SWAT-CUP tool (Abbaspour et al., 2015). Fifteen sensitive parameters were identified and set up for the same initial range for all scenarios (see Appendix 6). For each scenario, a total of 1000 simulations were generated for the calibration process, using the Nash-Sutcliffe Efficiency (NSE, Nash and Sutcliffe (1970)) as the objective function.

4.3.4. Performance metrics

To compare SPE datasets and ground observations, we considered the following three performance metrics in terms of rainfall detection: 1) Probability of Detection (POD); 2) False Alarm Ratio (FAR); and 3) Critical Success Index (CSI). To evaluate the SPE datasets in terms of temporal dynamics, we considered the following three performance metrics: 1) Correlation Coefficient (CC); 2) Relative Bias (RB); and 3) Root Mean Square Error (RMSE). To evaluate hydrological model performance, we considered performance metrics, including Nash-Sutcliffe Efficiency (NSE) and Percentage Bias (PBIAS) (Moriasi et al., 2015). The POD provides the ratio of the total precipitation events, which SPE products detect among the actual precipitation events. The FAR evaluates the fraction of false rainfall events, detected by SPE products from the total rainfall events. The CSI, which is a function of POD and FAR, is the most balanced and accurate detection metric. The rainfall day threshold in this study was set as 0.6 mm.day^{-1} (NCHMF, 2000). The CC is a score of the similarity between the SPE products and ground observations, while the RB and RMSE demonstrate the bias and error of satellite estimates. The NSE indicates how well the observed streamflow and the simulated streamflow fits the 1:1 line. The PBIAS measures the average tendency of the simulated streamflow to be larger or smaller than its observed counterpart. The formulae and perfect scores for each performance metric are given in Table 4. 2.

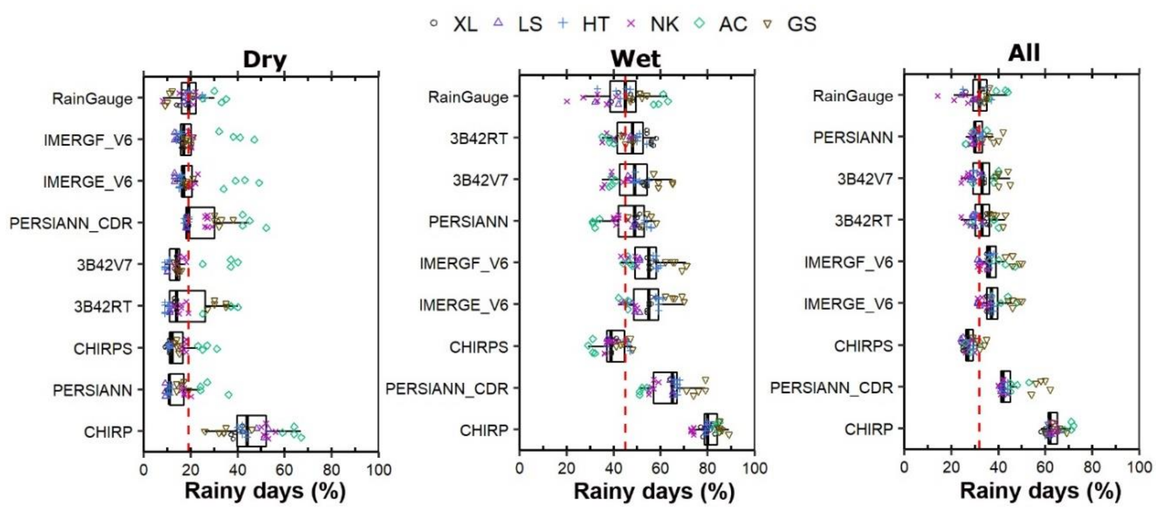

Figure 4. 5 Box plot of the number of rainy days retrieved from rain gauge and Satellite-derived Precipitation Estimation during the dry, the wet, and entire period. The red dash line indicates the median value from the rain gauge.

This study aims to assess the quality of SPE in seasonal water balance. Therefore, we used one-way Analysis of Variance (ANOVA) and Dunnett's Test (Ott and Longnecker, 2015), to compare mean values of SPE with that of the rain gauges. The one-way ANOVA test was first applied to determine whether significant differences exist between the means of rainfall datasets. If the difference was significant, Dunnett's test was used. By comparing each SPE dataset with a single control (rain gauge), it was possible to specify which SPE dataset was significantly different from that of the rain gauge.

4.4. Results and Discussion

4.4.1. Inter-comparison between rain gauges and Satellite Precipitation Estimate (SPE) datasets

To assess the statistical characteristics of SPE, the precipitation data from the eight SPE products (3B42RT, IMERGE-V6, CHIRP, PERSIANN, 3B42V7, IMERGF-V6, CHIRPS, and PERSIANN-CDR) were directly compared to the precipitation data from rain gauges in the six river basins. We matched precipitation values extracted from SPE's grids to the rain gauge locations. If there were more than one rain gauge located in a grid, we averaged values from those gauges before the comparison. As we examined the GPCC gauges in Vietnam, 27/31 (~90%) rain gauges in our study were not used in the generation of the GPCC product. Therefore, our comparisons between SPE datasets and rain gauges are considered as an independent evaluation.

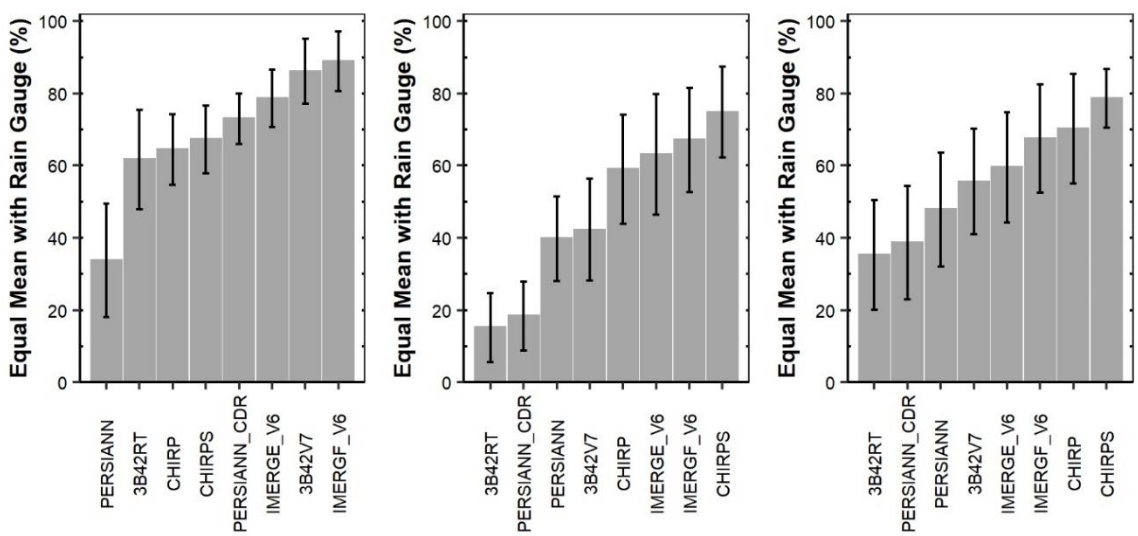

Figure 4. 6 Statistically equal mean between Satellite-derived Precipitation Estimation products and rain gauge, during the dry, the wet, and the entire period (2002-2017).

3.4.1.1. Detection metrics assessment

Regarding rainfall detection metrics, the gauge-corrected IMERGF-V6 exhibited the best overall performance for the entire period (median POD of 0.718-rank 2; median FAR of 0.391-rank 1; median CSI of 0.505-rank 1; see Figure 4. 3 and Table 4. 3).The second-best dataset for the entire period was IMERGE-V6 (median POD of 0.699-rank 4; median FAR of 0.403-rank 3; median CSI of 0.497-rank 2), reflecting the quality of the new IMERG retrieval algorithms on both real-time and research products (Huffman et al., 2014; Huffman et al., 2018). Note that uncorrected CHIRP obtained the highest POD score (median POD of 0.878), but the poorest FAR score (median FAR of 0.546), reflecting the imbalance of this rainfall retrieval algorithm. All SPE products exhibited better rainfall detection scores in the wet season than the dry season, which is in line with previous studies (Le et al., 2018; Li et al., 2019; Wang and Lu, 2016). The average median values during the dry season for POD, FAR, and CSI were 0.486, 0.555, and 0.264, respectively. The average median values during the wet season for POD, FAR, and CSI were 0.797, 0.388, and 0.509, respectively (see Figure 4. 3 and Table 4. 3). In conclusion, the newly released IMERG-V6 dataset outperformed other SPE datasets in terms of rainfall detection. The worst SPE performance was observed in the PERSIANN dataset.

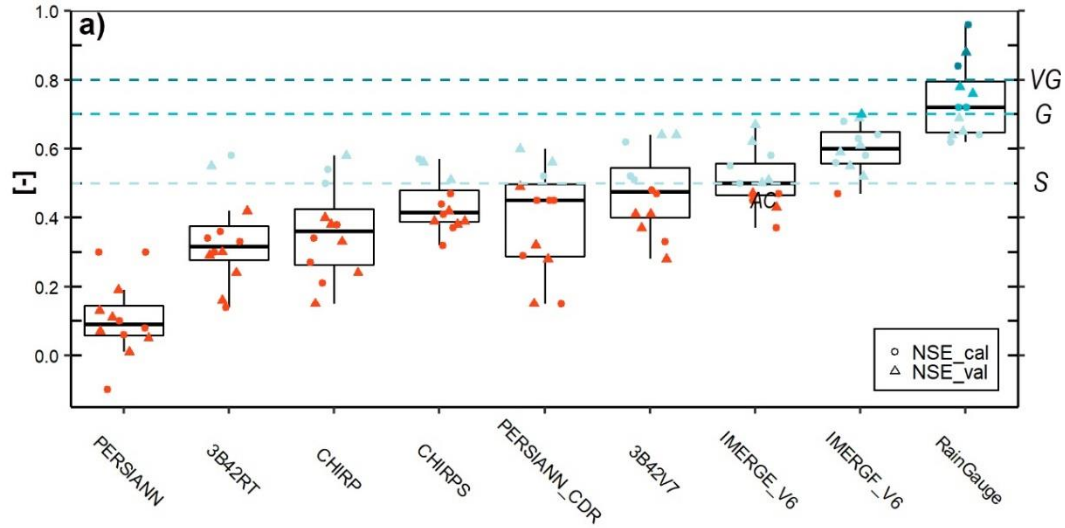

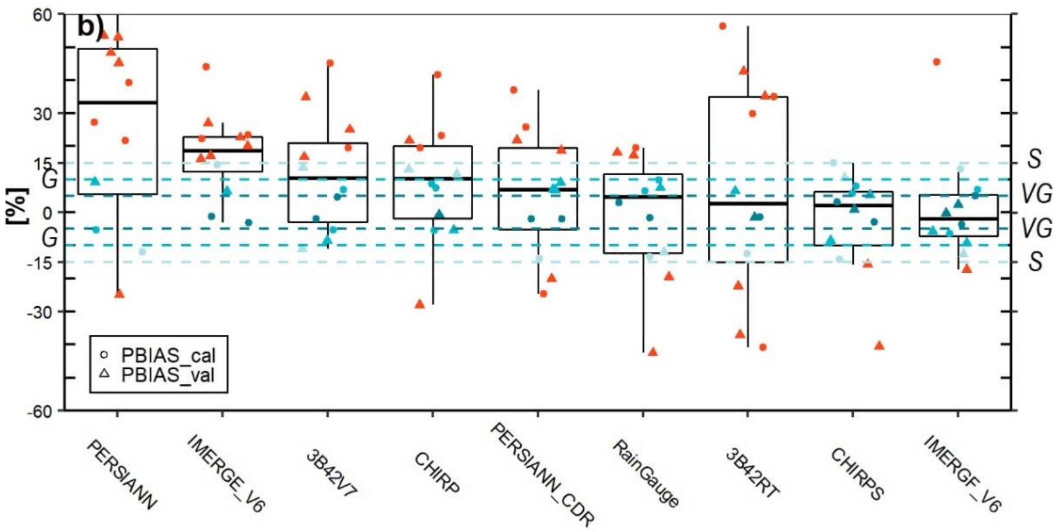

Figure 4. 7 Performance measures a) NSE, b) PBIAS of daily streamflow SWAT simulations, driven by different precipitation input datasets, at the six basins in Vietnam. Total samples in each boxplot are 12 (six calibration and six validation values). Boxes represent the interquartile range and median and outliers are lower or higher than the 10th or 90th percentile, respectively. The performance explanation: VG Very Good, G Good, S Satisfactory. The evaluation period: Cal. Calibration (2002-2009), Val. Validation (2010-2017).

3.4.1.2. Temporal dynamic metrics assessment

In the assessment of temporal dynamic metrics (see Figure 4. 4 and Table 4. 3), the best overall correlation coefficient for the entire period was demonstrated by IMERGF-V6 (median CC of 0.650), followed by IMERGE-V6 (median CC of 0.605). Other SPE datasets exhibited moderate CC scores, ranging from 0.296 to 0.472. The CHIRPS and its uncorrected CHIRP product exhibited the best overall RB scores for the entire period (median RB of 0.0 for each product), in line with Beck et al. (2018). These were followed by the IMERGE-V6 and IMERGF-V6 datasets, with moderate RB scores. The best overall RMSE score for the entire period was achieved by IMERGF-V6 (median RMSE of 12.0 mm. d^{-1}), followed by IMERGE-V6 and CHIRPS (median RMSE of 12.4 mm. d^{-1} and 13.0 mm. d^{-1}). Regarding seasonal assessment, the difference between the dry and wet seasons, in terms of temporal dynamic metrics, was not significant. The average median values during the dry season for CC and RB were 0.373 and -0.066, respectively. The average median values during the wet season for CC and RB were 0.409 and 0.054, respectively (see Figure 4. 4 and Table 4. 3). The average median value of RMSE during the dry season was 7.01 mm. d^{-1}, which was lower than the RMSE figure during the wet season (18.03 mm. d^{-1}). This reflects less variability in rainfall during the dry season, compared to the wet season. The AC basin (South Central), exhibited the largest negative RB and extremely high RMSE values of all SPE products. This is attributed to the greater spatial-temporal rainfall variation of this region (Trinh-Tuan et al., 2019a).

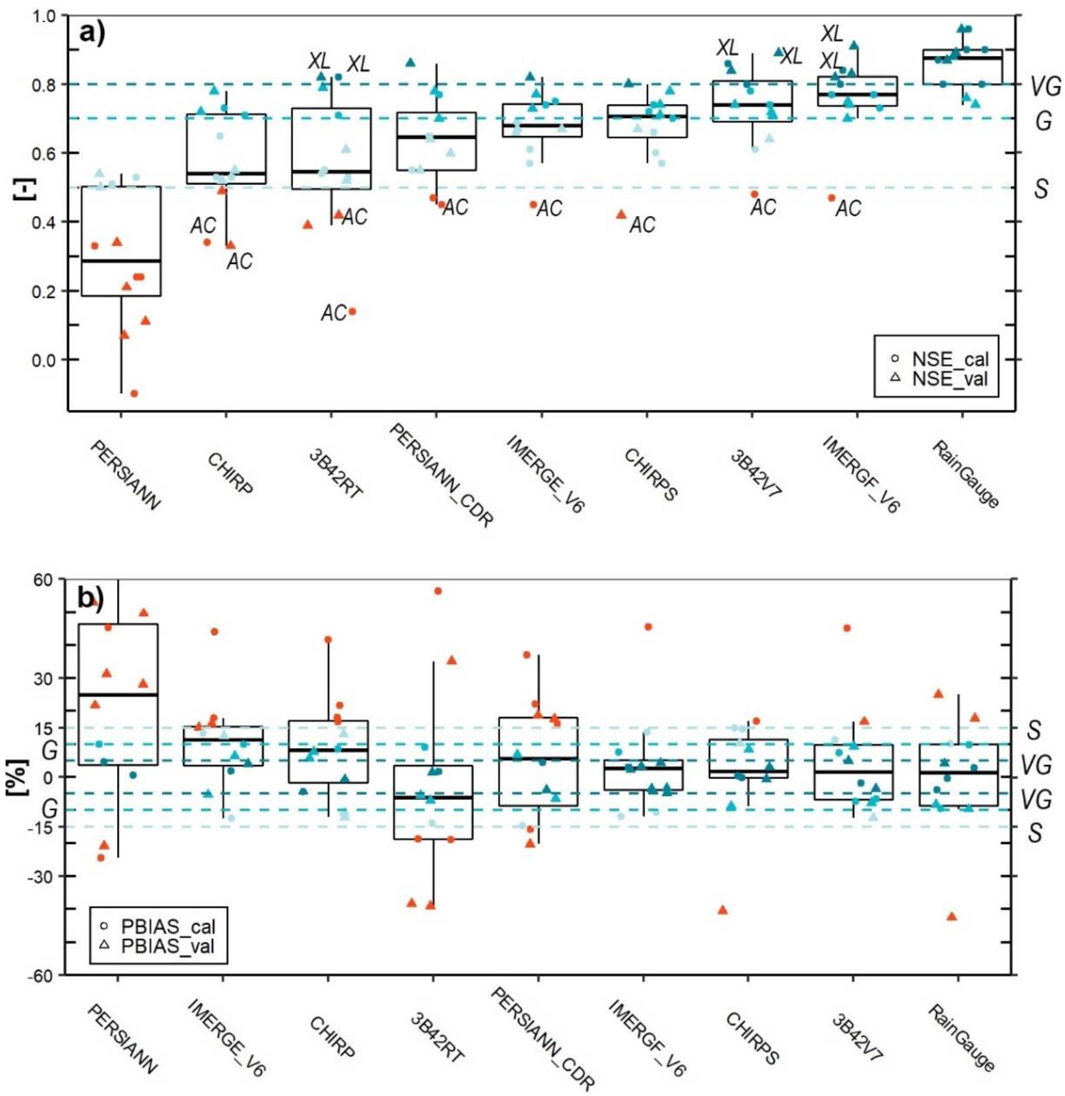

Figure 4. 8 Performance measures a) NSE, b) PBIAS of monthly streamflow SWAT simulations, driven by different precipitation input datasets, at the six basins in Vietnam. Total samples in each boxplot are 12 (six calibration and six validation values). Boxes represent the interquartile range and median and outliers are lower or higher than the 10th or 90th percentile, respectively. The performance explanation: VG Very Good, G Good, S Satisfactory. The evaluation period: Cal. Calibration (2002-2009), Val. Validation (2010-2017).

3.4.1.3. Rain-no rain detection assessment

Rain-no rain detection is an important aspect to assess the quality of SPE products. The 3B42V7 and 3B42RT exhibited the most similar figures in terms of the number of rainy days, compared to the observations from rain gauges, for the entire period (Figure 4. 5). Specifically, 32% of observations across six basins had rainfall events over the entire period; those figures from 3B42V7 and 3B42RT comprised 33% of the entire period. The rainy days detected by PERSIANN, CHIRPS, IMERGF-V6, IMERGE-V6, accounted for 30%, 27%, 36%, and 37% of the entire period, respectively. CHIRP exhibited a large overestimation of rainy days, as 62% of its entire period measured rainfall events, respectively reflecting the impact of intercept values in its algorithm (Funk et al., 2015). The gauge-corrected PERSIANN-CDR also highly overestimated the rainy days as these days accounted for 42% of its entire period. During the dry season, apart from CHIRP, all SPE datasets underestimated rainy days, reflecting the difficulty of SPE in terms of detecting short-term rainfall events. However, IMERG products exhibited significant improvement over the other SPE products. During 19% of the dry period, rain gauge data observed rainfall events, while those estimations from IMERGF-V6 and IMEGRE-V6 were only 2% less (17% of the dry period), suggesting frequently temporal rainfall sampling (every 30 minutes) could benefit in capturing short-term rainfall events. On the other hand, the IMERG retrieval algorithm highly overestimated rainfall events during the wet season, suggesting a re-evaluation for this algorithm during this period.

3.4.1.4. Mean annual rainfall assessment

Figure 4. 6 compares average 2002-2017 rainfall values annually, during the wet season, and the dry season, between rain gauge and SPE products. It was found that CHIRPS product exhibited the most statistically equal mean with rain gauges, among SPE products (78.6% agreeing cases during the entire period). The following SPE products, which demonstrated significantly similar means with those from rain gauges, were CHIRP, IMERGF-V6, IMERGE-V6 (overall agreement 70.2%, 67.5%, and 59.5%, respectively). This finding is in line with the low RB scores of CHIRPS and its uncorrected counterpart, previously described, reflecting that CHIRPS' retrieval algorithm is suitable for trend analysis and drought assessment. From another perspective, all SPE products achieved better agreement during the dry season, than the wet season. The worst mean estimation was observed at the PERSIANN dataset.

4.4.2. Hydrological simulation driven by different precipitation data inputs

4.4.2.1. Daily simulations

Figure 4. 7 represents the performance measures for daily streamflow SWAT simulation, driven by different precipitation datasets. For the NSE scores (Figure 4. 7a), rain gauge-driven simulations exhibited the best overall performance (median NSE of 0.720). Two SPE-based models had moderate performances in simulating daily streamflow. These are IMERGF-V6-driven simulations; IMERGE-V6-driven simulations, with median NSE scores of 0.600 and 0.500, respectively. Overall, based on the median NSE scores, the rain gauge-based models exhibited *Good* performances in a daily simulation; two SPE-based models (IMERF-V6 and IMERE-V6) demonstrated *Satisfactory* performances; while other SPEs driven simulations performed at *Unsatisfactory* levels (Moriasi et al., 2015).

The daily SPE-driven simulations performed better in terms of the PBIAS score (Figure 4. 7b.). The median PBIAS of IMERG-F-V6-driven simulations was -1.95%, followed by CHIRPS-driven simulations (2.05%); 3B42RT-driven simulations (2.50%); and rain gauge-driven simulations (4.65%). These performances were at *Very Good* levels (Moriasi et al., 2015). The daily simulation using rainfall inputs from PERSIANN-CDR exhibited at *Good* levels based on the PBIAS score (median PBIAS of -6.85%); the PBIAS scores of CHIRP-, and 3B42V7- driven simulations were at *Satisfactory* levels (median PBIAS of 10.10 and 10.25%, respectively). With the median PBIAS scores greater than 15%, IMERGE-V6-, and PERSIANN-driven simulations were at *Unsatisfactory* levels (Moriasi et al., 2015). Details of the daily simulation results can be found at Appendix 7.

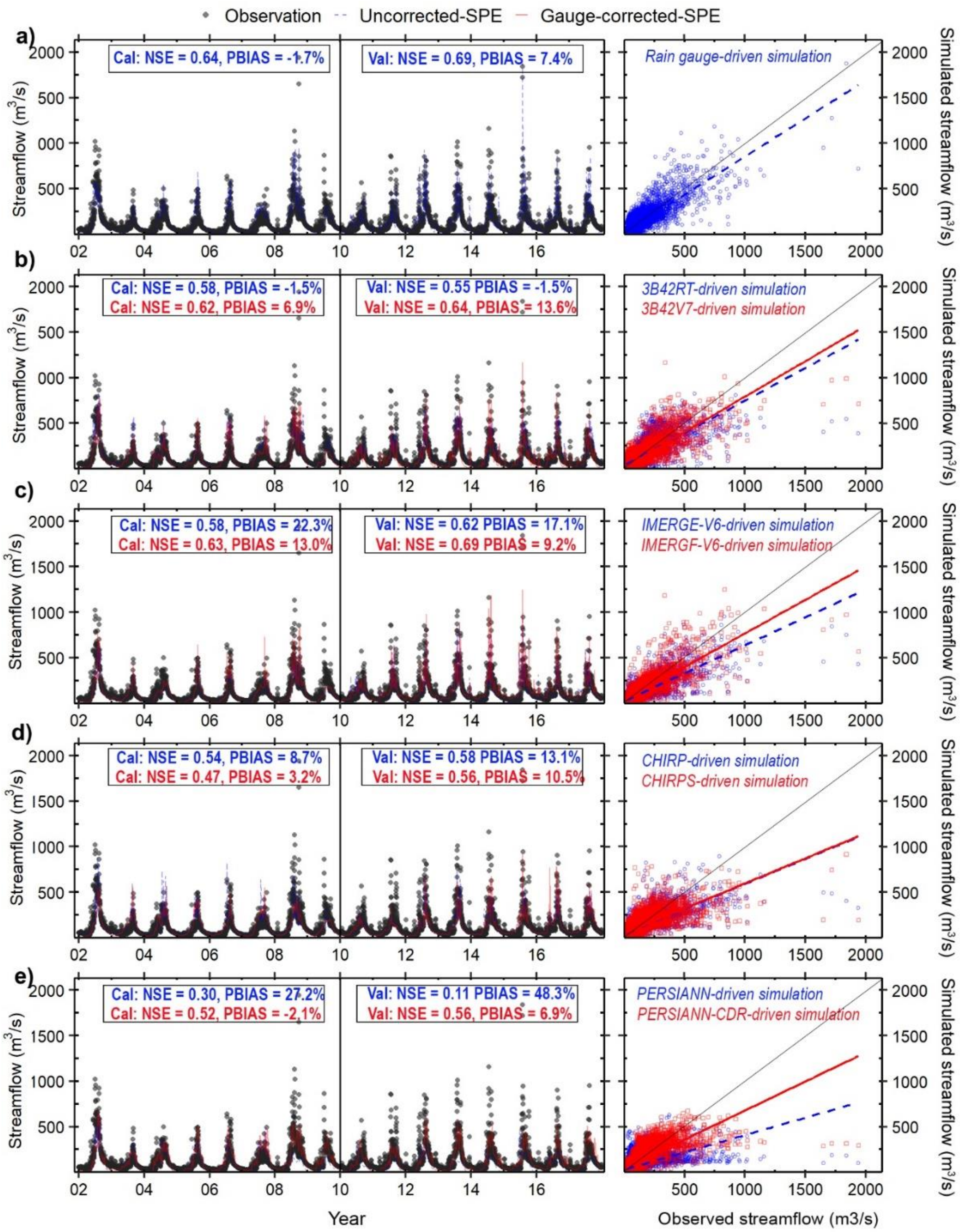

Figure 4. 9 Comparison between daily observed streamflow and simulated streamflow, driven by a) rain gauge; b) TMPA precipitation datasets; c) GPM IMERG precipitation datasets; d) CHIRPS precipitation datasets; and e) PERSIANN precipitation datasets, at the XL basin, during 2002 – 2017. The calibration period is 2002-2009; the validation period is 2010-2017. Apart from panel a), blue texts denote performances of uncorrected-SPE-driven simulations, while red texts denote

performances of gauge-corrected-SPE-driven simulations. In the scatter plot, dash blue line exhibits linear regression between simulated streamflow from uncorrected SPE-based model and observed streamflow. Red line exhibits linear regression between simulated streamflow from gauge-corrected SPE-based model and observed streamflow.

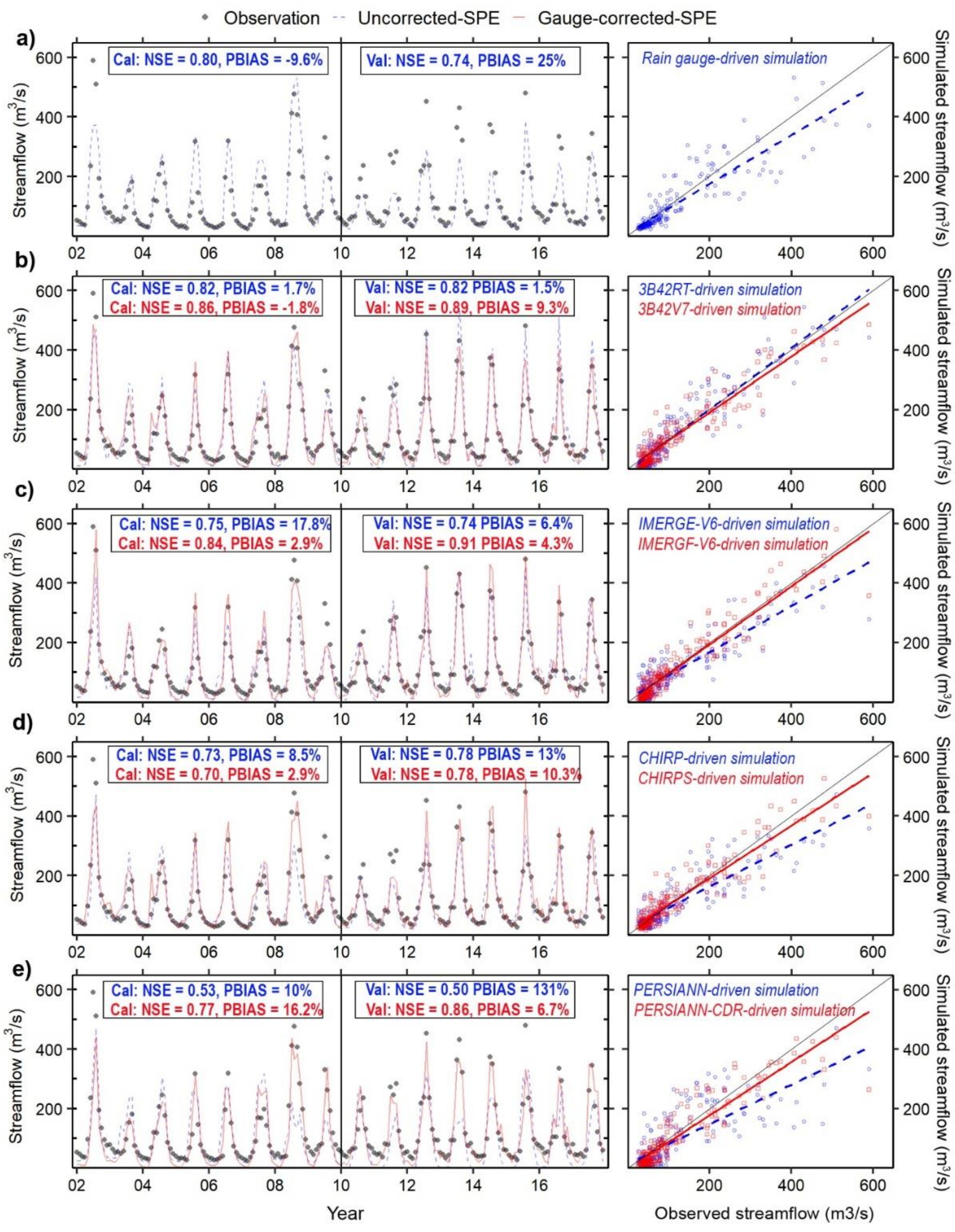

Figure 4. 10 Similar to Figure 4.9 but for monthly simulations.

3.4.2.2. Monthly simulations

Figure 8 presents the performance measures for monthly streamflow SWAT simulation, imposed with different precipitation datasets. Regarding the NSE scores (Figure 4. 8a), the best overall performance was gained by rain gauge-driven simulations (median NSE of 0.875). The gauge-corrected SPE-based models had comparable performances in simulating monthly streamflow. The median NSE values of IMERGF-V6-driven simulations; 3B42V7-driven simulations; CHIRPS-driven simulations, PERSIANN-CDR-driven simulations were 0.770, 0.740, 0.705, and 0.645, respectively. Apart from PERSIANN-driven simulations, the uncorrected SPE-based model produced monthly streamflow at moderate levels. The median NSE values of IMERGE-V6-driven simulations, 3B42RT-driven simulations; and CHIRP-driven simulations were 0.680, 0.545, and 0.540, respectively. Overall, based on the median NSE scores, the rain gauge-based models exhibited *Very Good* performances; the gauge-corrected SPE-based models demonstrated *Good* (IMERGF-V6, CHRIP, 3B42V7) and *Satisfactory* (PERSIANN-CDR) performances; and uncorrected SPE-based models performed at *Satisfactory* (IMERGE-V6, 3B42RT, CHIRP) and *Unsatisfactory* (PERSIANN) levels (Moriasi et al., 2015).

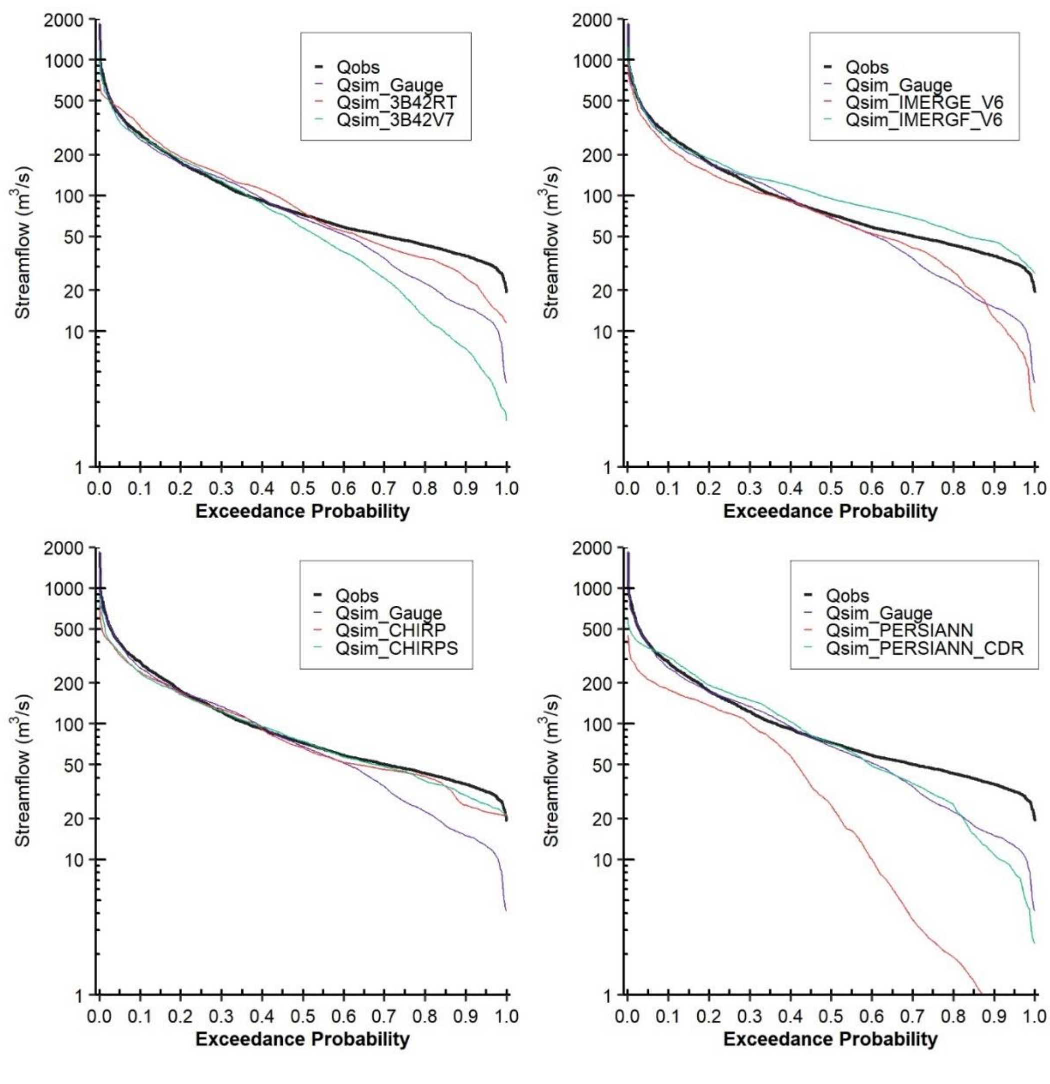

Figure 4. 11 Exceedance probability of the daily observed streamflow and simulated streamflow, driven by different precipitation inputs, at the XL basin, during the validation period (2010-2017). The logarithm was applied for the y-scale.

In terms of the PBIAS score (Figure 4. 8b), the median PBIAS of rain gauge-driven simulations was 1.25%, followed by 3B42V7-driven simulations (1.55%); CHIRPS-driven simulations (1.70%); and

IMERGF-V6-driven simulations (2.60%). These performances were at *Very Good* levels (Moriasi et al., 2015). The models using rainfall inputs from uncorrected 3B42RT and CHIRP datasets exhibited at *Good* levels (median PBIAS of -6.25% for 3B42RT and 8.10% for CHIRP); the PBIAS scores of IMERGE-V6 driven simulations were at *Satisfactory* levels (mean PBIAS of 11.2%). The median PBIAS of PERSIANN-driven simulations (24.95%) indicated that these simulations performed at *Unsatisfactory* level. Details of the monthly simulation results can be found at Appendix 8.

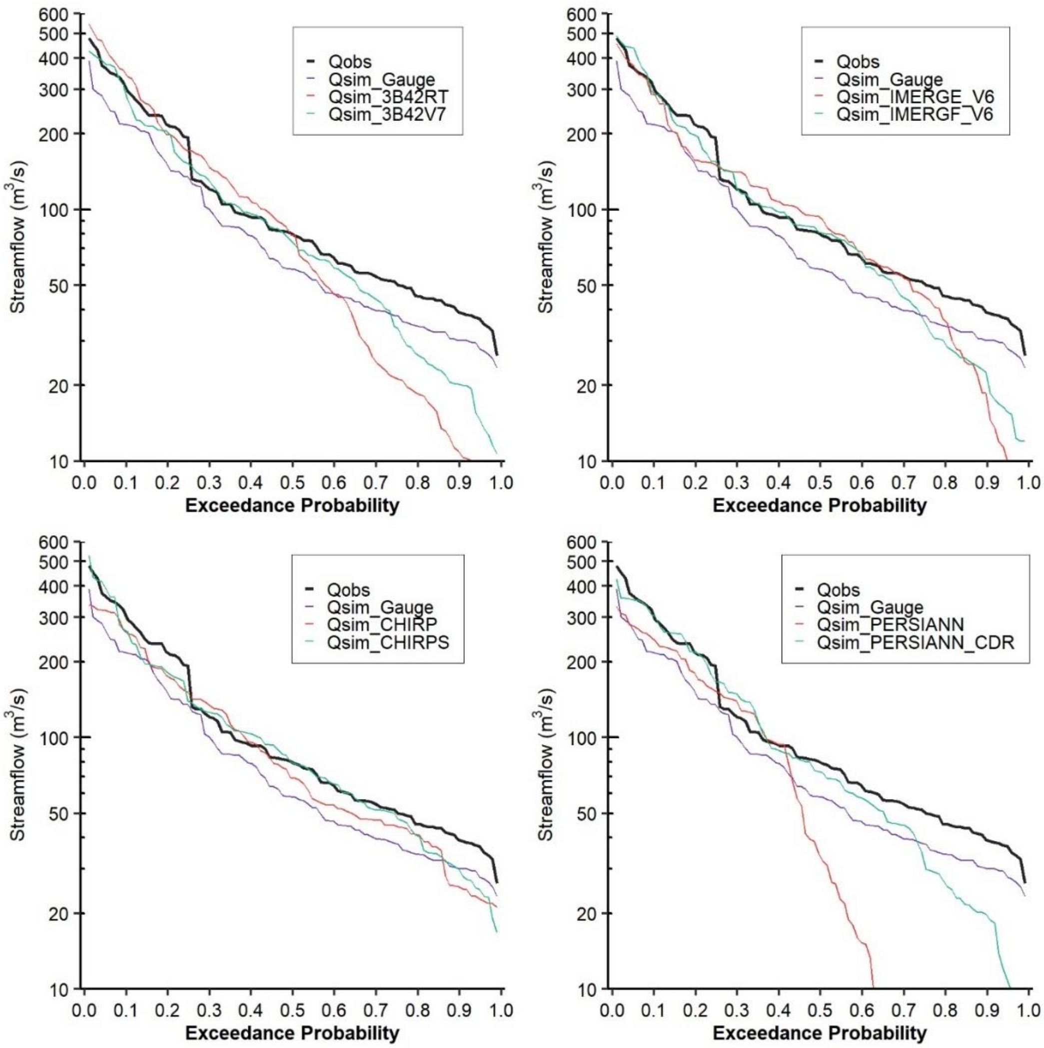

Figure 4. 12 Similar to Figure 4. 11 but for monthly dataset.

3.4.2.4. SPE-driven simulations in a large basin

Although rain gauge-driven simulations exhibited the best overall performance, compared to SPE datasets, the number of cases in which the PBIAS scores at *Unsatisfactory* level (|PBIAS| > 15%) from rain-gauge-driven simulations were high. These *Unsatisfactory* PBIAS scores were found at five and three cases in the daily time step and monthly time step, respectively. This reflects an insufficient estimation at the spatial scale from the rain gauge. On the other hand, the PBIAS's *Unsatisfactory* figures for the IMERGF-V6-based model were observed at two simulations (daily time step, Figure 4. 7b.) and one simulation (monthly time step, Figure 4. 8b) only. In daily streamflow simulations at the large XL basin, gauge-corrected SPE-driven simulations exhibited comparable in performance as rain gauge-driven simulations. The daily NSE scores of rain gauge-driven simulations during the calibration and validation period, at the XL basin, were 0.64 and 0.69, respectively (Figure 4. 9a.). Those figures from IMERGF-V6 were nearly similar, with the scores of 0.63 and 0.69, respectively (Figure 4. 9c). Interestingly, in monthly streamflow simulation at the XL basin, the SPE-based models were even slightly better than rain-gauge driven simulation. The daily NSE scores of rain gauge-driven simulations during the calibration and validation period, at the XL basin, were 0.80 and 0.74, respectively (Figure 4. 10a); those from the IMERGF-V6-driven simulations were 0.84 and 0.91, respectively (Figure 4. 10c). We also examined the exceedance probability of both daily and monthly streamflow, from observations and simulations driven by different precipitation datasets, at the XL basin (Figure 4. 11 and Figure 4. 12). Overall, the flow curves from simulated results followed the observation curves well, at low exceedance levels. At high exceedance level flow, the simulated curves began to look different from the observed curve. CHIRPS- and CHIRP-driven simulations produced better accurate curves than that from rain gauge-driven simulation, up to exceedance of around 85% flow for daily streamflow data and around 75% flow for monthly streamflow data, suggesting the capability of those products in terms of low-flow simulation.

Table 4. 4 The difference in median of precipitation and streamflow performance metrics between uncorrected and gauge-corrected SPE products. For all performance metrics, except for FAR, RMSE, and PBIAS, a positive value represents a better performance gauge-corrected version over its uncorrected version. The bold value indicates the gauge-corrected version worse than its uncorrected counterpart.

	Performances	3B42V7-3B42RT	IMERGF_V6-IMERGE_V6	CHIRPS-CHIRP	PERSIANN_CDR-PERSIANN
Precipitation Performance Metrics	POD	+0.121	+0.019	**-0.254**	+0.159
	FAR	-0.011	-0.012	-0.136	**+0.063**
	CSI	+0.031	+0.008	**-0.025**	+0.041
	CC	+0.114	+0.046	+0.032	+0.093
	RB	-0.1	+0.08	0.0	**+0.230**
	RMSE (mm. d^{-1})	-1.1	-0.4	-0.2	-0.6
Daily Streamflow Performance Metrics	NSE	+0.07	+0.12	+0.06	+0.24
	PBIAS (%)	-7.0	-7.6	-7.9	-18.7
Monthly Streamflow Performance Metrics	NSE	+0.20	+0.09	+0.17	+0.33
	PBIAS (%)	-4.7	-8.6	-6.4	-14.8

3.4.2.4. SPE-driven simulations in basin frequently affected by typhoon and tropical storm

Many poor scores were reported for the AC (Ve river) basin when we used SPE datasets as inputs to the SWAT model; whereas the rain gauge-driven simulations exhibited *Good* to *Very Good* performances in daily streamflow simulation and monthly streamflow simulation (daily NSE for validation: 0.72, monthly NSE for validation: 0.88; see Appendix 7 and Appendix 8). We initially expected that when the SWAT model was recalibrated with satellite precipitation data, the problem of underestimation would be mitigated. However, since the underestimations of the SPE products were extremely large at this basin, the re-calibrated SWAT model did not perform well. This large underestimation can be seen in Figure 4. 13. We used violin plots to examine the distribution of monthly basin rainfall; monthly streamflow from SPE-driven simulations without re-calibration (i.e., using rain gauge calibration parameters); and monthly streamflow from SPE-driven simulations, with re-calibration from each SPE dataset. Although SPE products demonstrated similar distribution at low to medium rainfall (<500 mm. $month^{-1}$), a large discrepancy was found with high rainfall. The maximum rainfall per month, measured by the rain gauge, was up to 2250 mm. month^{-1}; while the figures from SPE datasets, ranged from only 800 to 1500 mm. month^{-1}. When we used the rain gauge's calibrated parameters for models using SPE rainfall inputs, the distributions of simulated streamflow were significantly different from that of observed streamflow (Figure 4. 13b). On the other hand, by using re-calibrated parameters in each SPE dataset, the distributions of simulated streamflow were more similar to observed streamflow. However, a large dissimilarity between high streamflow distribution from models and observed data has been identified (Figure 4. 13c). In short, from the simulation results at the AC basin, we suggest a re-evaluation for SPE datasets at regions that are heavily influenced by the tropical cyclone and monsoon systems. The simulated results of SPE-based models without re-calibrated parameters were even worse, compared to the models using re-calibration parameters, which is in line with previous studies (Alazzy et al., 2017; Li et al., 2018a).

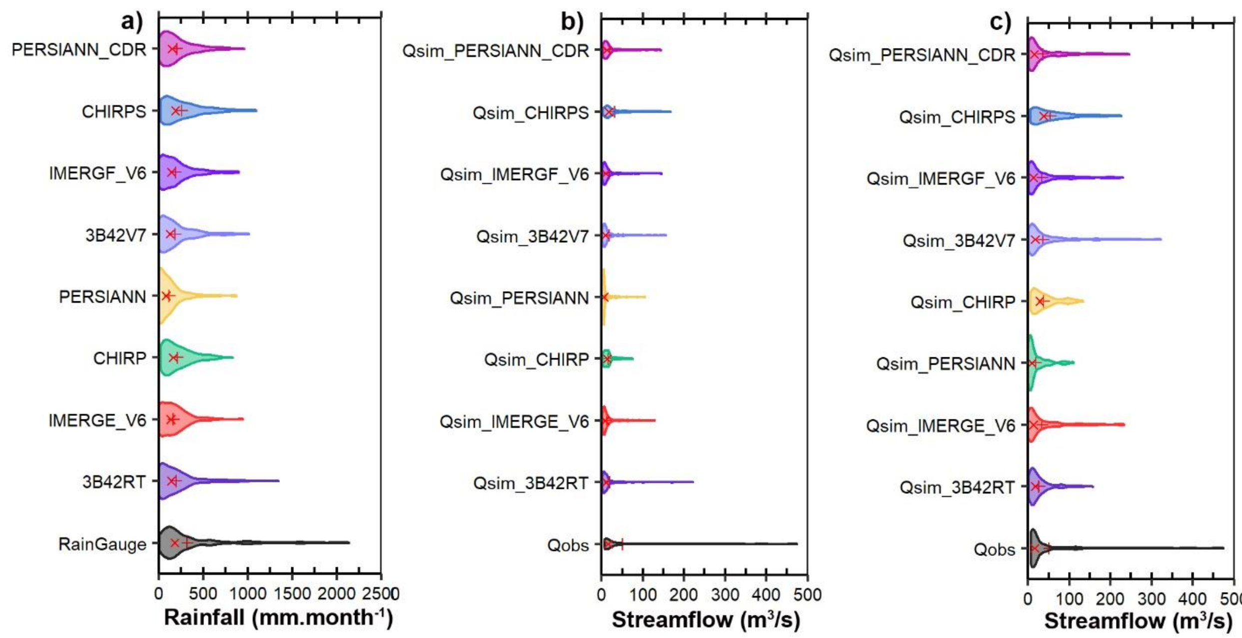

Figure 4. 13 Violin plots of a) monthly basin rainfall; b) streamflow simulation without re-calibration parameters (rain gauge parameters); c) streamflow simulation with re-calibration parameters using inputs from Satellite-derived Precipitation Estimation, at the AC basin. The cross sign indicates the median value; the plus sign indicates the mean value.

4.4.3. Gauge-corrected and Uncorrected SPE Products

Table 4. 4 presents the differences in the median between gauge-corrected and uncorrected versions of SPE datasets, in terms of precipitation and streamflow performance metrics. The gauge-corrected products incorporated five-day gauge data (CHIRPS) and monthly gauge data (3B42V7, IMERGF-V6, and PERSIANN-CDR) datasets. We expected that the late release of gauge-corrected products (often in several months' latency) would result in these products outperforming the uncorrected products. However, by using various precipitation metrics, we detected that the gauge-corrected products exhibited little improvement, or even worse performances (e.g., CHIRPS – CHIRP for POD: -0.254, PERSIANN-CDR-PERSIAN for RB: +0.230), in a daily time step. This suggests the necessity of incorporating daily gauge observations to improve precipitation performance at this time step. The monthly streamflow performance metrics indicated a considerable improvement on the NSE scores in both daily and monthly simulation (averaged +0.13 for daily simulation and +0.20 for monthly simulation), and a significant reduction in the PBIAS scores (-10.3% for daily simulation and -8.6%

for monthly simulation). This reflects that corrections provide more benefits to hydrological applications.

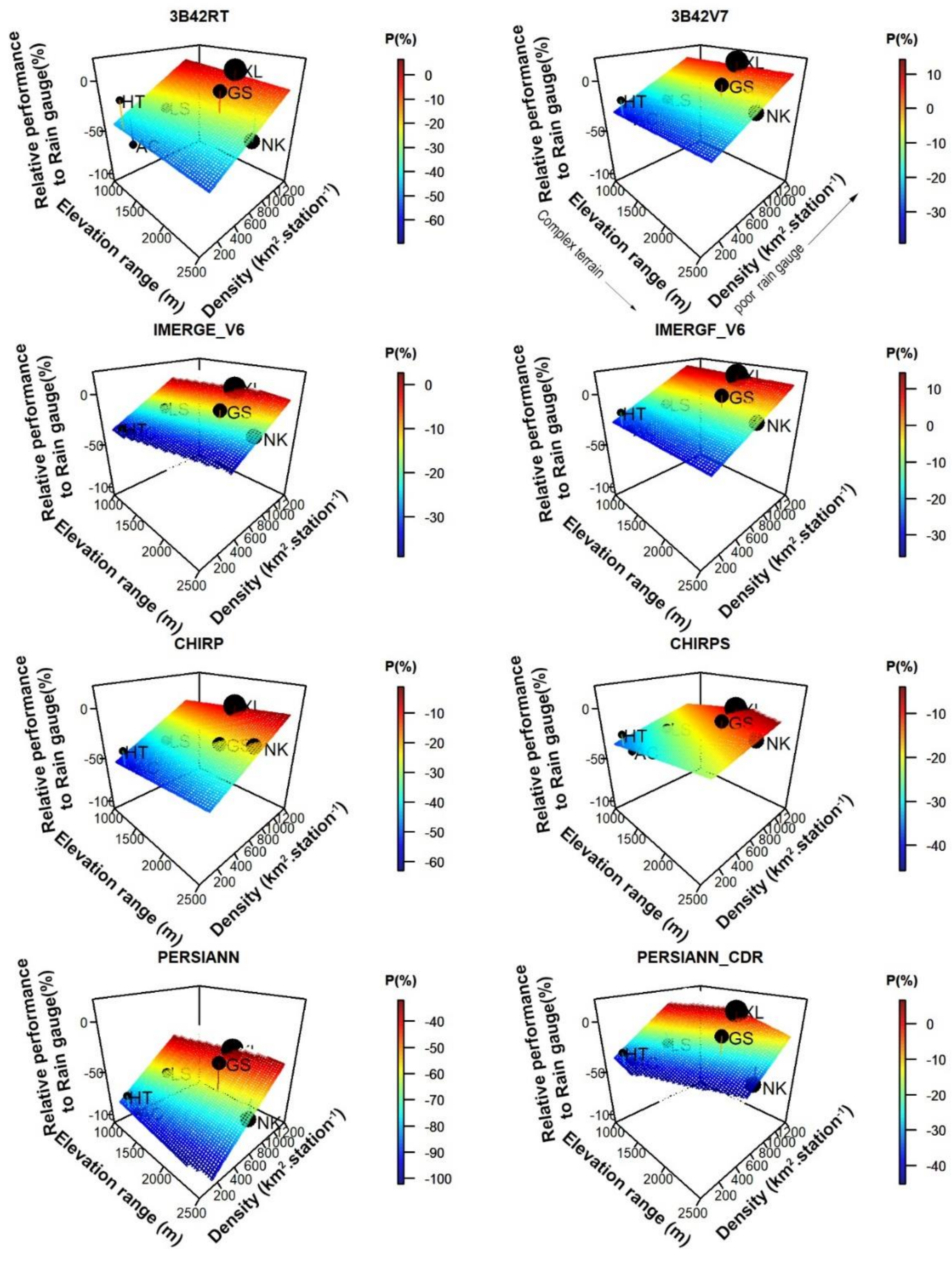

Figure 4. 14 Bivariate correlation analysis relative performance of SPE-driven simulations to rain gauge-driven simulation, elevation range, and rain gauge density. 3D surface denotes the performance's trend of SPE, compared to rain gauge (P%), as input for SWAT simulation. The black dot point indicates the relative size of the basin area.

Note that, in principle, higher spatial resolution is better. However, CHIRPS uses only infrared data, and, typically, this dataset did not capture well the variability in precipitation in space. Therefore, the theoretical higher spatial resolution might not provide any practical benefit. Previous studies comparing TMPA and CHIRPS performance (Luo et al., 2019; Wu et al., 2018) reached largely similar conclusions. PERSIANN precipitation datasets seem to not be comparable with other SPE products used in this study, probably because these datasets (1) also use infrared data as the CHIRPS dataset; (2) have a relative coarse spatial resolution.

4.4.4. The relative performance of SPE to rain gauge for SWAT simulation.

It is worth highlighting the rationale of "relative performance" when considering the gauge-based model as a benchmark to investigate the adequacy of SPE in driving hydrological modeling. We found evidence that the performances of SPE-based models relative to the rain gauge-based models ($P_{relative} = (NSE_{SPE}-NSE_{RG})/ NSE_{RG}x100$), were to some degree functions of elevation range and rain gauge network density (Figure 4. 14). Larger basins tended to be poorly gauged, and streamflow simulations imposed with SPE at large basins had comparable simulation results with those using precipitation from rain gauges. The 3D surface, fitted from elevation range, rain gauge density, and $P_{relative}$, suggested that high $P_{relative}$ values were observed at basins with a low rain-gauge density. On the other hand, several studies (Blöschl, 2013) indicated that hydrological simulations are performed better in large storage of watersheds. Because the relative variation in streamflow at these watersheds is small, it leads to better simulation results, compared to smaller watersheds.

4.4.5. Limitations and Further Study

In this study, we utilized the SPE products for monthly streamflow simulation, using their finest grid; however, we did not use the same grid size for different precipitation inputs. This is due to two factors. Firstly, Bai et al. (2018) revealed that the correlation of SPE with rain gauges, is different from various spatial resolutions. Secondly, the lack of advantage of GPM IMERG on streamflow simulation, compared to 3B42V7 at the Ganjiang River basin, might be due to the resampling of the grid size from 0.1° to 0.25° of GPM IMERG (Zhang et al., 2019).

SPE-driven simulations did not perform well in our simulations at a daily time step. Further study should apply a bias-correction scheme for the SPE products on this time step. The study would greatly benefit examination of extreme analysis and disaster management.

4.5. Conclusions

This study evaluated the performances of eight Satellite Precipitation Estimation (SPE) datasets, including uncorrected versions (IMERGE-V06, TMPA 3B42RT, CHIRP, and PERSIANN) and gauge-corrected versions (IMERGF-V6, TMPA 3B42V7, CHIRPS, and PERSIANN-CDR), regarding six sub-climate zones of Vietnam. The work consists of two parts: 1) comparisons of the SPE products to rain gauges, and 2) using hydrological SWAT models to simulate monthly streamflow at the six basins, representative of the six climate zones. Our findings can be summarized as follows:

(1) The SPE products exhibited a slightly better performance during the wet season, compared to the dry season, in terms of rainfall detection metric (POD, FAR, and CSI). However, the temporal dynamic performance (CC and RB) did not show any significant difference between the two seasons.
(2) IMERGF-V6 exhibited the best overall performance among SPE products, in comparison with rain gauges, and as inputs to the SWAT models for streamflow simulations. Our study is the first attempt to evaluate the performance of GPM IMERG in Vietnam, suggesting strong capability for this product in hydrological application purposes.

(3) CHIRPS achieved the smallest bias among SPE products, compared to rain gauge data, reflecting the aim of this product as a drought-warning system and for trend analysis.
(4) Gauge-corrected versions of SPE products exhibited slightly better over the uncorrected versions of SPE products, in terms of precipitation performance metrics. This suggests that the use of sub-monthly and monthly rain gauges did not significantly benefit SPE's improvement at the daily time step. However, the gauge-corrected SPE products performed better than their uncorrected counterparts in both daily and monthly streamflow simulation.
(5) SPE products can serve as alternative inputs to enhance the performance of hydrological models in basins, with a low rain-gauge network density.

This study determines the ability of SPE products to estimate rainfall, and produce input data for streamflow simulations in Vietnam. Our findings could be used as a guide to select which SPE products are suitable for hydrological applications. Although this study is specific for hydro-climatic conditions in the river basins of Vietnam, the methodology can be applied to watersheds in other regions of the world.

Chapter 5: Assimilation of SMAP Products for Improving Streamflow Simulations over Tropical Climate Region – Is Spatial Information more Important than Temporal Information?[4]

5.1. Introduction

In recent years, soil moisture (SM) has been increasingly investigated in hydrological research as it has a strong influence on the interaction between different components within the hydrological cycle (Ahmad et al., 2010; Grayson et al., 1997; Western et al., 2002). The SM content is a key variable that controls most of the land surface hydrological processes and thus is considered one of the most important parameters in land surface hydrology models (Sheikh et al., 2009). The increased need for satellite-based soil moisture information has led to the launch of many satellite missions to provide more accurate SM estimates at the global scale (Kim et al., 2018; Kim et al., 2019) that could be used to substitute in-situ SM observations that only cover a very limited portion of the land surface (Dorigo et al., 2021). These SM products include ASCAT (Advanced SCATterometer) (Bartalis et al., 2007), SMOS (Soil Moisture and Ocean Salinity) (Kerr et al., 2001), AMSR-E (Advanced Microwave Scanning Radiometer for the Earth Observing System onboard the Aqua satellite) (Kawanishi et al., 2003), AMSR-2 (Advanced Microwave Scanning Radiometer 2 onboard the Global Change Observation Mission – Water satellite) (Imaoka et al., 2010) and SMAP (Soil Moisture Active Passive) (Entekhabi et al., 2010). All of these SM data products are freely accessible, providing an opportunity to integrate SM information into hydrological models across the globe.

Owing to the release of the above-mentioned data products, assimilation of soil moisture (SM) in hydrological simulations has received much attention within the past decade. Specifically, of 150 studies conducted during the period of 2001–2021 on soil moisture assimilation in hydrology modelling, nearly ninety percent have been published since 2012 (see Appendix 9). A number of studies have assessed remotely-sensed SM assimilation in various hydrological applications, including flood prediction (Abbaszadeh et al., 2020; Patil and Ramsankaran, 2018), water balance estimation (Behera et al., 2019), and streamflow forecast (Patil and Ramsankaran, 2017; Sazib et al., 2020), along with agricultural monitoring and forecasting (Bolten et al., 2009; Mladenova et al., 2019). These studies have established a new frontier in hydrological research to take advantage of SM estimates from space to inform hydrological modeling.

However, satellite-based SM products also have several limitations, including shallow penetration depth (typically shallower than or equal to 5 cm) and relatively coarse spatial resolutions (larger than or equal to 9km) (Entekhabi et al., 2010). Therefore, the SM observed from space may often improve the top-soil layer estimation, unless carefully integrated into a soil moisture or hydrologic model through direct insertion or data assimilation. Although several studies (Laiolo et al., 2016) have shown that coarse spatial resolutions of remote sensing soil moisture could be useful in improving streamflow

[4] This chapter has been published as Le, M.H., Nguyen Q.B., Pham, H.T., Patil, A., Do H.X., Ramsankaran R., Bolten, J. D., & Lakshmi, V (2022). Assimilation of SMAP products in streamflow simulations – Is spatial information more important than temporal information. Remote Sensing, 14(7), 1607. https://doi.org/10.3390/rs14071607.

simulations, many studies have pointed out the limitations of low spatial resolutions of soil moisture in data assimilation, especially in small catchments (Matgen et al., 2012) or in flash flood forecasting (Han et al., 2012).

Table 5. 1 Summary of selected studies on remote sensing soil moisture data assimilation in hydrologic models. These studies were investigated in terms of climate region, number of studied catchments, used remotely sensed (RS) soil moisture (SM) datasets, data assimilation (DA) technique with hydrologic models.

	Climate Region	Catchments / RS SM Datasets	DA(*)/ Hydrological Models(**)	Main Findings
(Jadidoleslam et al., 2021)	Cold	131/ SMAP, SMOS	EnKF, EnKFV/ HLM	DA driven models reduce the peak error and could be useful for the application of satellite soil moisture for operational real-time streamflow forecasting.
(Abbaszadeh et al., 2020)	Temperate	4/ SMAP	EPFM/ WRF-Hydro	Assimilation of SM could improve streamflow simulation during flooding from hurricane Harvey in 2017, with a promising result from SM at 1km.
(Baguis and Roulin, 2017)	Temperate	1/ ASCAT	EnKF/ SCHEME	The DA algorithm could be a diagnostic tool to detect weakness in a model and to improve its performance.
(Patil and Ramsankaran , 2018)	Temperate	2/ SMOS, ASCAT	EnKF/ SWAT	A coupling Soil Moisture Analytical Relationship with EnKF could successfully update the sub-surface SM and streamflow components simulation.
(Laiolo et al., 2016)	Temperate	1/ EUMET-SAT H-SAF,	Nudging/ Continuum	Streamflow prediction for a small basin using a distributed hydrological model could be improved with the assimilation of soil moisture estimated from coarse spatial resolution remotely sensed products.
(Behera et al., 2019)	Tropical	1/ AMSR-E	Kalman Filter/ VIC	DA driven models could improve soil moisture in root zone and water balance estimation.
(Azimi et al., 2020)	Temperate	2/ SMAP, SACAT, CATSAR-	EnKF/ SWAT	Both active and passive-based SM driven simulation generally improved streamflow simulation. The impact of frequency of soil moisture observation on data assimilation performances in small catchments was discussed.
(Lü et al., 2016)	Arid	2/ ASCAT	EnKF/ HBV	A combined surface soil moisture and snow depth data assimilation into a hydrological model was proposed to improve streamflow estimation in cold and warm season headwater watersheds.
(Yang et al., 2021)	Temperate	3/ ESA CCI, SMAP	EnKF/ DDRM	Assimilation of soil moisture products in high spatial gridded modelling could increase DA performances in terms of simulating profile soil moisture.
(De Santis et al., 2021)	Cold, Temperate	775/ ESA CCI	EnKF/ MISDc-2L	An assessment of large-scale DA experiments in hydrological model streamflow simulation was carried out over Europe. This study also considered impacts of vegetation density, topographical complexity and basin area on the DA performances.
(Loizu et al., 2018)	Temperate	2/ ASCAT	EnKF/ MISDc, TOPLATS	This study examined the impacts of three different re-scaling techniques on SM data assimilation for two hydrological models. A careful evaluation for observation error and re-scaling technique is recommended for successful implementation of a data assimilation framework.

Note:

(*) Acronyms for data assimilation techniques: 'EnKF' Ensemble Kalman Filter, 'EnKFV' EnKF include time-varying error variances, 'EPFM' Evolutionary Particle Filter with Markov Chain Monte Carlo.

(**) Acronyms for hydrologic models: 'HLM' Hillslope Link Model, 'WRF-Hydro' Weather Research and Forecasting Hydrological model, 'SCHEME' SCHEldt-MEuse, from the names of the two major rivers of Belgium, 'SWAT' Soil and Water Assessment Tool, 'VIC' Variable Infiltration Capacity, 'HBV' Hydrologiska Byråns Vattenbalansavdelning, 'DDRM' Digital Elevation Model (DEM) based distributed rainfall-runoff model, 'MISDc-2L' Modello Idrologico Semi-Distribuito in continuo-2 layers, 'TOPLATS' TOPMODEL-Based Land Surface-Atmosphere Transfer Scheme.

To overcome the low spatial resolution of satellite-based SM products, several studies have proposed different downscaled algorithms to obtain a finer soil moisture dataset in space. These algorithms can be classified into three primary types, including (i) methods based on a satellite data combination of high and low resolution satellite data using active sensors (Narayan and Lakshmi, 2008; Narayan et al., 2006), and visible, infrared and thermal sensors (Fang et al., 2018b; Fang et al., 2013; Fang et al., 2020; Fang et al., 2019); (ii) methods based on the relationship between SM and other geophysical variables that exist at a finer spatial resolution (Busch et al., 2012; Ranney et al., 2015); (iii) methods based on mathematical modelling (e.g., land surface modelling) to simulate coarse resolution remotely sensed SM to a fine resolution model to update SM outputs (Bai et al., 2019; Yang et al., 2021).

On the other hand, compared to native resolution satellite-based products, downscaled satellite-based SM products are prone to having shorter data records, complicating typical data assimilation methodologies. For instance, with the first downscaling method mentioned above, a widely-used algorithm is a thermal inertia principle-based algorithm (Fang et al., 2022). This algorithm utilizes the universal relationship between land surface temperature (LST), vegetation index, soil wetness, and evapotranspiration to quantify SM as a function of LST and normalized different vegetation index (NDVI). However, the LST dataset, which is often retrieved from earth observations, often has large spatial and temporal gaps, resulting from atmospheric conditions (e.g., cloud and cloud shadows) (Li et al., 2018b). Consequently, these LST's gaps will cause gaps in space and time for downscaled SM product and result in an absence of temporal time series during the data assimilation process. Although efforts exist to fill the gaps from LST before the downscaling step (Fang et al., 2022; Pham et al., 2019), the challenge of supplementing temporally-downscaled SM data for assimilation still remains.

Investigation of the trade-offs between temporal and spatial resolution of remotely sensed SM products for constraining hydrologic models is an area of research that requires more attention. In a study of two catchments in Central Italy, Azimi et al. (2020) examined the benefit of having more frequent SM observations (temporal timescale) in streamflow simulation. The authors concluded that reduced temporal sampling from a remotely sensed soil moisture product could significantly reduce model performance, indicating that temporal resolution likely plays a more important role than spatial resolution in constraining the model. On the other hand, a study using SMAP soil moisture data assimilation in a community-based hydrologic model indicates that downscaled SMAP 1km would improve the accuracy of streamflow simulation (normal streamflow conditions), rather than the model using coarse resolution SMAP 9km data (Abbaszadeh et al., 2020).

In addition, the impact of the number, size, and nature of the hydrologic catchment requires further investigation—few studies have addressed the potential impacts of catchment characteristics on SM-based DA schemes. A majority of studies have examined the DA schemes in a focused area, and typically over relatively few catchments (e.g., < 4), making it difficult to make conclusive statements on the utility of such DA approaches (see Table 5. 1 Summary of selected studies on remote sensing soil moisture data assimilation in hydrologic models. These studies were investigated in terms of climate region, number of studied catchments, used remotely sensed (RS) soil moisture (SM) datasets, data assimilation (DA) technique with hydrologic models. and Appendix 10). Several studies that have included large samples of catchments concluded that a hydrological model with a SM-based DA framework may not significantly improve streamflow simulations, compared to the hydrological model without the DA (De Santis et al., 2021; Jadidoleslam et al., 2021).

Model complexity, and heterogeneous land surface characterization and meteorological forcing, can result in varying levels of uncertainty and model accuracy, issues not easily corrected through data assimilation. In fact, DA-driven hydrologic models often exhibit mixed results across climatic conditions. This is an active area of research, and more studies are encouraged. Currently, most studies focus on temperate regions (see Table 5. 1). In the tropical climate, streamflow is often of great variation, due to the impacts of large-scale phenomena such as ENSO on the seasonal and year-to-year variation in soil moisture, which results from the high variability in rainfall (Kumagai et al., 2009). Any technique such as DA that could enhance hydrological model performances in the tropical climate region is essential, but such studies have rarely been investigated (Fleischmann et al., 2021), owing to the difficulty of accessing streamflow records over these regions (Do et al., 2018).

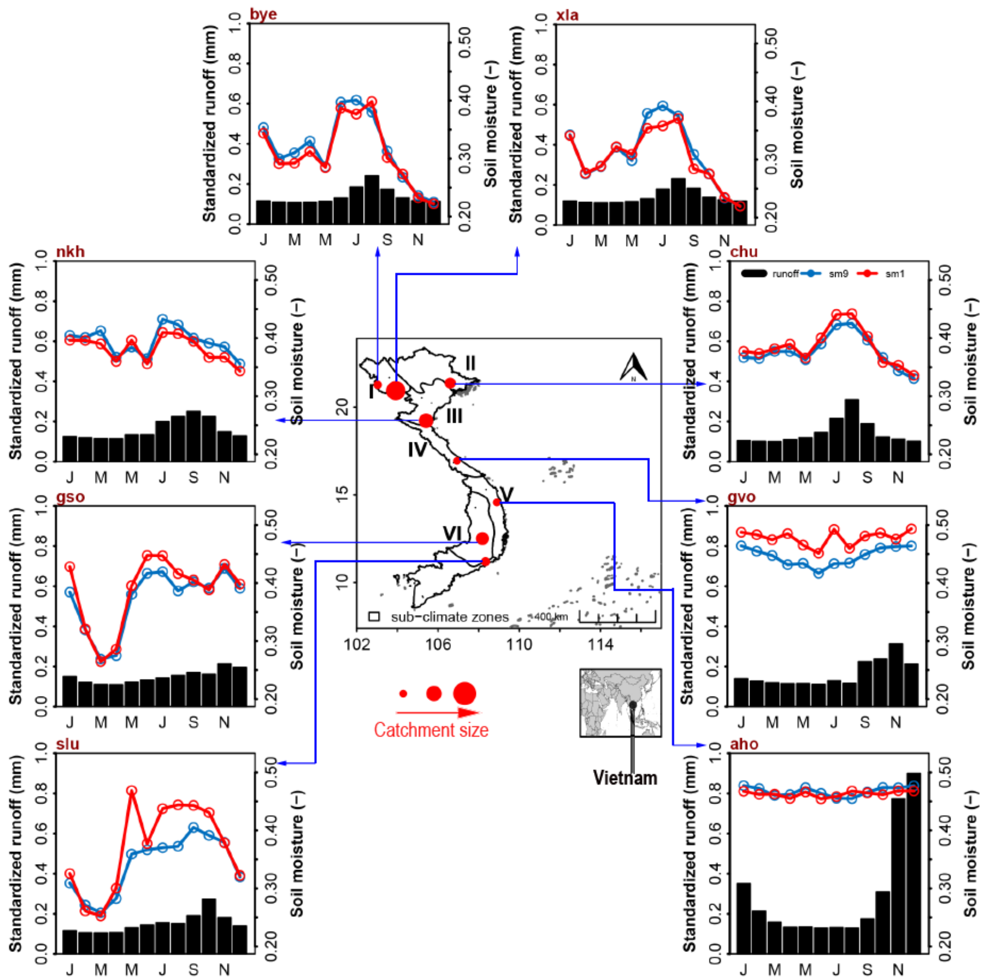

Figure 5. 1 Locations of eight catchments (red circle represents catchment centroid) in Vietnam, and their monthly averaged runoff (black bar), monthly averaged soil moisture estimated from SMAP 9km (SM9, blue line), and monthly averaged soil moisture estimated from SMAP 1km (SM1, red line). The runoff values were calculated based on the period of 2013–2019, while soil moisture values (volume soil moisture) were calculated based on the period of 2017–2019. A rescaling has been applied for the runoff time series to compare its variation across catchments. The circle size indicates relative size of the catchment. The Roman numerals indicate contrasting climate regions where the studied catchments located in. These regions are defined following (Nguyen and Nguyen, 2004).

Here, we build off of these previous studies and attempt to demonstrate the utility of satellite-based soil moisture for streamflow simulation, as well as assessing the impacts of temporal and spatial resolution on the model accuracy. We carefully investigate the application of two remotely sensed SM products (SMAP 9km and downscaled SMAP 1km) to examine whether spatial–temporal resolution has a substantial impact on the performance of the hydrological model to simulate streamflow through a data assimilation (DA) framework. We carried out the experiment over eight catchments across Vietnam—a tropical country that is under-represented in the literature. The hydrological Soil and

Water Assessment Tool (SWAT) model (Arnold et al., 1998) is selected as it performs well in numerous studies in the studied region (Ha et al., 2018; Le et al., 2020a; Nguyen, 2021; Tan et al., 2020; Vu et al., 2016), and there are several studies that have successfully implemented the DA framework in the SWAT model (Azimi et al., 2020; Liu et al., 2018). We selected the Ensemble Kalman Filter (EnKF) (Evensen, 2003) as the DA algorithm due to its popularity in many hydrological assimilation works (De Santis et al., 2021; Lü et al., 2015; Yang et al., 2021).

Table 5. 2 Description of hydrological stations used in this study. Average runoff characteristics in each catchment (min, median, mean, max) are based on time series 2013–2019. NDVI is the average NDVI value for each catchment during 2017–2019 extracted from MODIS MOD13Q1 250m product. SM9 and SM1 stand for the percentage of available SMAP 9km and downscaled SMAP 1km during the data assimilation period (2017–2019), respectively.

Full Name	Short Name	Long.	Lat.	Area	Min	Median	Mean	Max	NDVI	SM9	SM1
		(degree)	(degree)	(km²)	(mm/d)	(mm/d)	(mm/d)	(mm/d)	(-)	(%)	(%)
Giavong	gvo	106.93	16.93	267	0.09	0.91	2.49	136.56	0.801	42.37	9.68
Anhoa	aho	108.90	14.57	383	0.36	1.87	7.54	254.91	0.628	31.78	10.41
Banyen	bye	103.03	21.27	638	0.21	0.65	1.51	33.04	0.740	42.56	21.46
Songluy	slu	108.34	11.19	964	0.04	0.51	2.02	42.30	0.808	41.74	5.84
Chu	chu	106.60	21.37	2090	0.02	0.25	1.79	99.22	0.736	31.78	12.24
Giangson	gso	108.19	12.51	3100	0.18	1.28	1.95	28.71	0.753	31.78	11.6
Nghiakhanh	nkh	105.41	19.22	4024	0.32	1.16	2.39	92.11	0.770	31.78	14.52
Xala	xla	103.92	20.94	6430	0.13	0.89	1.64	24.72	0.686	34.16	16.62

Section 5.2 presents eight catchments together with the selected datasets while Section 5.3 provides a brief description of the hydrological SWAT model and data assimilation scheme that were used to conduct this study. Section 5.4 provides a comprehensive assessment of the findings, focusing on the discrepancies of model performance under different DA schemes. Section 5.5 concluded the study findings.

5.2. Materials and Methods

5.2.1. Catchment Sites and Its Streamflow Observations

We collected daily 2013–2019 streamflow time series from eight hydrological stations across Vietnam with their characteristics presented in Table 5. 2. The in-situ streamflow datasets have been used to calibrate the hydrological models for each catchment, and evaluate the performance of hydrological simulations with and without DA. These catchments were selected based on several study objectives. Firstly, they have a variety of catchment sizes so that we could examine the impacts of the spatial resolution of SMAP products on the data assimilation algorithm. Secondly, they are in contrasting climate conditions and geographic coordinates. Therefore, they have different runoff regimes and soil moisture patterns (Figure 5. 2), which are useful for drawing a general conclusion on our experiment. Lastly, all catchments have passed homogeneity time series testing, and have natural runoff conditions due to the lack of manmade structures (i.e., weirs, dams, etc.). These conditions enable us to isolate the impact of the DA methods by removing potential changes in streamflow dynamics due to human activities. Details on testing of homogeneity time series and checking of natural catchment conditions can be found in Do H et al. (2022).

5.2.2. Climatic Datasets

The climatic datasets forced into the hydrological model in this study are daily precipitation from GPM IMERG and daily maximum and minimum air temperature from NCEP CFSR V2. A detailed description of these datasets is given below.

5.2.2.1. GPM IMERG Precipitation

The half-hour 0.1 degree GPM IMERG Final run V6 (hereafter IMERG) (Hou et al., 2014) was downloaded from NASA Goddard Earth Science Data and Information Services Center (GES DISC, https://disc.gsfc.nasa.gov/). Daily precipitation totals were calculated by summing 24-h periods beginning at 19:00 UTC the day prior to the day of the record to match with the local daily rainfall collection time frame. Satellite precipitation has been shown to favorably compare with rain gages in various locations (Hashemi et al., 2017; Le et al., 2018; Mondal et al., 2018).

5.2.2.2. NCEP CFSR V2 Air Temperature

The 6-hour CFSR V2 for maximum and minimum air temperature (Saha et al., 2014) was downloaded from the National Center for Atmospheric Research (NCAR, https://rda.ucar.edu/) Data Archive. Depending on the parameters, the available resolution varies from 0.3 degrees to 2.5 degrees. In this study, we selected the finest resolution of 0.3 degrees. We obtained the maximum and minimum air temperature every 6 hours, and selected the maximum and minimum among these four periods per day to estimate the daily maximum and minimum air temperature, respectively.

5.2.3. Remotely Sensed Soil Moisture Datasets

We obtained two soil moisture (SM) products originating from Soil Moisture Active Passive (SMAP). These products have exhibited their potential use in water resources and hydrology in the studied region (Dandridge et al., 2020; Lakshmi et al., 2018), and are the data assimilation variables (i.e., state variables) which serve as the observed soil moisture to assimilate into the hydrological model.

5.2.3.1. Soil Moisture Active Passive

The 9km SMAP Level- 3 (hereafter SM9) was obtained from the National Snow and Ice Data Center (NSIDC DAAC, http://nsidc.org/data/smap). The SMAP provides, at approximately 06:00 and 18:00 local time (LT), soil moisture data in descending and ascending orbits, respectively. In this study, to match with daily simulation time in the study region, the SMAP ascending overpass time (18:00 LT) is selected as the observed soil moisture for a day. The accuracy for the SMAP data is designed with μRMSE of 0.04 m^3/m^3 (Kim et al., 2018).

5.2.3.2. Downscaled Soil Moisture Active Passive

Based on the assumption that daily soil moisture was negatively associated with the change in daily temperature under varying vegetation conditions, Fang et al., 2018 (Fang et al., 2018a); Fang et al., 2020 (Fang et al., 2020) proposed a linear regression model to estimate the daily soil moisture condition with known daily temperature and vegetation index. Using this linear regression model, we can create a finer spatial resolution for SM from high spatial resolutions of land surface temperature (reflecting the change in daily temperature) and of NDVI (reflecting the vegetation conditions). In this way, very high spatial soil moisture from SMAP —downscaled SMAP—has increased from 9-km to 1-km resolution (hereafter SM1). This SM1 product has been validated in CONUS (Fang et al., 2020), Australia (Fang et al., 2021), and at a global scale (Fang et al., 2022). In this study, we obtained SM1 from the global scale product (Fang et al., 2022), and extracted the 18:00 LT, similar to the SM9.

5.3. Methodology

5.3.1. Principle of the Hydrological SWAT Model in Streamflow Simulation

The Soil and Water Assessment Tool (SWAT) is a physically based, semi-distributed hydrologic model that simulates various hydrologic variables at time steps (i.e., daily, monthly, and yearly) at catchment scale. The Hydrologic Response Unit (HRU) is the basic spatial unit of the SWAT model. Runoff generation is estimated at the HRU level, and is then routed to sub-basins and, subsequently, to the entire basin (Neitsch et al., 2011). In the SWAT model, runoff generation is the sum of three components—surface runoff (Q_{surf}), lateral flow (Q_{lat}) and groundwater (Q_{gw}). The mathematical expression of these three components is described in the following.

Table 5. 3 Description of data used for SWAT and data assimilation framework in this study.

Attributes	Data Type	Description	Period(s)/ Resolution	Sources
Climatic data	Precipitation	IMERG Final Run V6	2011–2019/0.10°	(Hou et al., 2014)
	Max-, min- air temperature	CFSR vs2	2011–2019/0.25°	(Saha et al., 2014)
Catchment attributes	Land use land cover	MCD12Q1	2016/500m	(Friedl and Sulla-Menashe, 2019)
	Soil	HWSD	-/1km	(Nachtergaele et al., 2009)
	Digital Elevation Model	HydroSHEDS	-/90m (3sec)	(Lehner et al., 2008)
Data assimilation variable	Soil moisture	SMAP	2015–2019/9-km	(Entekhabi et al., 2010)
	Soil moisture	Downscaled SMAP	2015–2019/1-km	(Fang et al., 2022)
Ground data	Streamflow	Eight hydrological stations	2013–2019	VMHA*

**VMHA Vietnam Meteorological and Hydrological Administration*

The surface runoff process is a function of daily rainfall (R_{day}, unit in mm) and the retention parameter (S, unit in mm) based on the empirical formula using Soil Conservation Service (SCS) Curve Number (CN) method (SCS, 1972).

$$Q_{surf} = \frac{(R_{day} - 0.2 \cdot S)^2}{R_{day} + 0.8 \cdot S} \tag{5.1}$$

The retention parameter S is calculated as follows.

$$S = S_{max}\left(1 - \frac{SW}{SW + \exp\left(w_1 - w_2 \cdot SW\right)}\right) \tag{5.2}$$

Where S_{max} is the maximum value the retention parameter can obtain from any given day (mm). SW is the total soil moisture (in mm) of the entire profile excluding the amount of water held at the wilting point. w_1 and w_2 are shape coefficients.

The shape coefficients (w_1 and w_2) are calculated as follows:

$$w_1 = ln\left[\frac{FC}{1 - S_3 \cdot S_{max}^{-1}} - FC\right] + w_2 \cdot FC \tag{5.3}$$

$$w_2 = \frac{\left(ln\left[\frac{FC}{1 - S_3 \cdot S_{max}^{-1}} - FC\right] - ln\left[\frac{SAT}{1 - 2.54 \cdot S_{max}^{-1}} - SAT\right]\right)}{(SAT - FC)} \tag{5.4}$$

Where FC is field capacity, SAT is the amount of water when the soil profile is completely saturated (mm), and 2.54 is the retention parameter at the $CN = 99$. S_3 (mm) and S_{max} (mm) are retention parameters, calculated given CN_1 (dry condition) and CN_3 (normal condition) as follows.

$$S = 25.4 \cdot \left(\frac{1000}{CN} - 10\right) \tag{5.5}$$

Where $S_{max} = 25.4 \cdot \left(\frac{1000}{CN_1} - 10\right)$, and $S_3 = 25.4 \cdot \left(\frac{1000}{CN_3} - 10\right)$

The CN_1 and CN_3 are calculated given CN_2 value (given as SWAT model input) as follows:

$$CN_1 = CN_2 - \frac{20 \cdot (100 - CN_2)}{(100 - CN_2 + exp[2.533 - 0.0636 \cdot (100 - CN_2)])} \tag{5.6}$$

$$CN_3 = CN_2 \cdot exp[0.00673 \cdot (100 - CN_2)] \tag{5.7}$$

After the surface runoff is formed, the rest of water infiltrates the land to generate soil water inflow. Lateral flow (Q_{lat}, unit in mm) in each soil layer is given as follows:

$$Q_{lat} = 0.024 \cdot \left(\frac{2 \cdot SW_{ly.excess} \cdot K_{sat.ly} \cdot slp}{\varphi_d \cdot L_{hill}}\right) \tag{5.8}$$

Where $K_{sat.ly}$ is saturated hydraulic conductivity (mm/hr) at layer i (i =1, 2, 3), slp is the steepness of a slope (m/m), φ_d is the drainable porosity of the soil layer (mm/mm), and L_{hill} is the hillslope length (m). In addition, $SW_{ly.excess}$ is the amount of soil water that exceeds field capacity at layer i (i =1, 2, 3), is given as follows.

$$\begin{gathered} SW_{ly,excess} = SW_{ly} - FC_{ly} \; if \; SW_{ly} > FC_{ly} \\ SW_{ly,excess} = 0 \; if \; SW_{ly} \leq FC_{ly} \end{gathered} \tag{5.9}$$

Where SW_{ly} and FC_{ly} are the water content of the soil layer i (i =1, 2, 3), on a given day (mm) and at field capacity (mm).

The SW_{ly}, if it exists, also generates deep percolation ($Q_{perc,ly}$, unit in mm) (from one layer to the underlying layer) as follows:

$$Q_{perc,ly} = SW_{ly,excess}\left(1 - exp\left[\frac{-\Delta t \cdot K_{sat,ly}}{SAT_{ly} - FC_{ly}}\right]\right) \quad (5.10)$$

Where Δt is the time step (hr). The soil water at the third layer percolates to vadose zones and groundwater (shallow aquifer layer). We focus on assimilating the soil moisture dynamic but do not consider the 'revap' process—water may move from shallow aquifers to overlaying unsaturated zones.

5.3.2. Setup the Hydrological SWAT Model

To set up the SWAT model across various catchment size basins, we (i) defined the same threshold to create a river network (i.e., 30 km²) when using the DEM to delineate watersheds; (ii) set up a similar slope band setup (0-, 5-, 10-, 30-, and 50- degree).

For the climatic data inputs, using Thiessen polygon areal weighted average method (Thiessen, 1911), we calculated the mean areal precipitation for each sub-basin from gridded IMERG precipitation and the mean areal air temperature (i.e., maximum and minimum) for each sub-basin from gridded CFSR V2. Therefore, the precipitation and air temperature points as input for the SWAT models are equal to the total of the sub-basins.

To create HRU units, DEM, land use, and soil data are required. The 90-m void-filled digital elevation model (DEM) has been obtained from the hydrological data and maps based on SHuttle Elevation Derivatives at multiple Scales (HydroSHEDS, hydrosheds.org) (Lehner, 2012; Lehner et al., 2008). The HydroSHEDS DEM has provided a reliable watershed delineation for the given studied basins with the difference between the catchment area generated from HydroSHEDS DEM and metadata being within ± 15%. The 500-m land use land cover presented in this study is obtained from Collection 6 MODIS Land Cover (MCD12Q1 and MCD12C1) (Friedl and Sulla-Menashe, 2019) from the Land Processes Distributed Active Archive Center (LP DAAC, https://lpdaac.usgs.gov/products/mcd12q1v006/). The MODIS Land cover provides 17 different land cover types annually from 2001 to 2019. This study obtained 2016 land cover as representing the land use in the given studied areas. Furthermore, this study reclassified the original 17 land cover types to 10 land cover types to match with the SWAT format. This study used 1-km Harmonized World Soil Database (HWSD) version 1.2 maintained by the Food Agriculture Organization (FAO, http://www.fao.org) (Kansara and Lakshmi, 2021; Nachtergaele et al., 2009). To prepare soil inputs for SWAT, we reclassified the HWSD's soil mapping unit (SMU) to the FAO soil symbol, assigned soil properties for each soil layer using the HWSD database, and used soil water characteristics equations from Saxton and Rawls (2006) to create a proper user soil format for SWAT. Normally, two soil layers' profiles are created (i.e., 0–300mm, 300–1,000mm). However, SMAP can only measure soil moisture at the depth of 0–50 mm. Therefore, to have a realistic assimilation process, we re-classified the soil profile of SWAT from two layers to three layers (0–50 mm, 50–300mm, and 300–1000m) (Patil and Ramsankaran, 2017). All described spatial processing (watershed delineation and HRU creation) have been conducted in QGIS v2.6.1 and QSWAT v1.7 (Dile et al., 2016). Summarized descriptions of previously described datasets in Section 2 and DEM, soil, land use datasets for setup SWAT model are given in Table 5. 3. The detailed climatic conditions, catchment attributes and model setup information (sub-basins and HRUs) are provided in the Appendix 12.

With respect to the parameterization of the SWAT model, we selected the warm-up, calibration and validation periods as 2011–2012, 2013–2016, and 2017–2019, respectively. Thirteen different parameters (see Appendix 13), which impact surface runoff, evaporation, soil moisture, and channel routing in the SWAT model, have been chosen for the parameterization. The parameters' turning process was undertaken with the SUFI-2 algorithm that is built in to the SWAT-CUP software (Abbaspour, 2013). In the end, we optimized the best suitable parameters for each catchment for daily streamflow simulation. The SWAT driven simulation at this step is considered as a deterministic SWAT model.

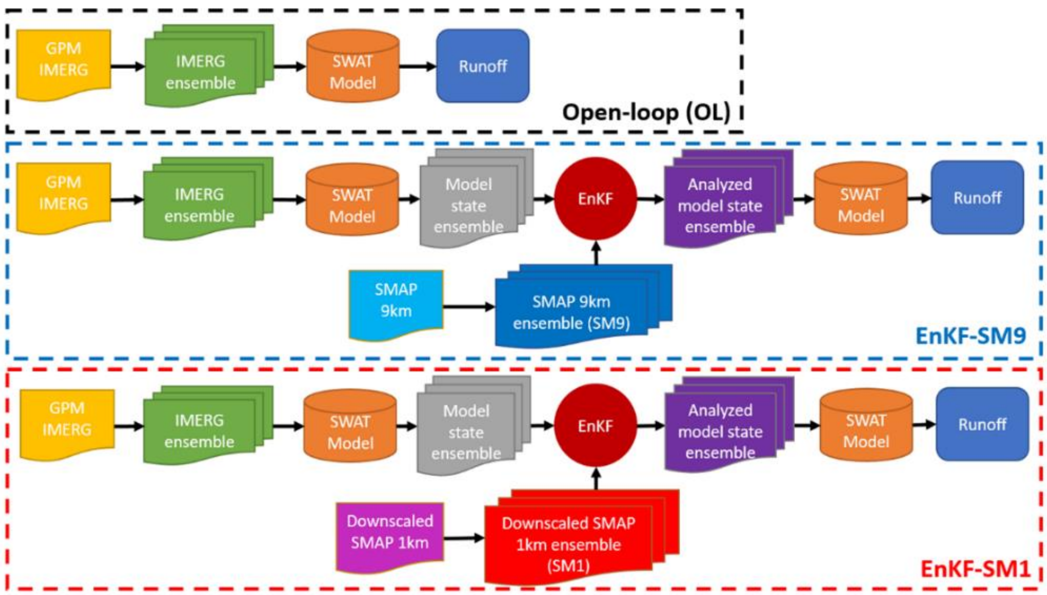

Figure 5. 2 Flow chart of this study. EnKF-SM9 and EnKF-SM1 stand for streamflow simulations using the SWAT model with the state variable of SM9 and EnKF technique, and streamflow simulations using the SWAT model with the state variable of downscaled SM1 and EnKF technique, respectively.

5.3.3. Data Assimilation - Ensemble Kalman Filter (EnKF)

5.3.3.1. Bias Correction of Observed SM and Ensembles Generation

The EnKF is a sequential data assimilation technique that is best applied using unbiased observations. To limit error covariance of the modeled and observed states in the EnKF, systematic errors between satellite SM retrievals and model states must be corrected before assimilation. It is assumed that long-term statistics of model states are consistent with those of in-situ SM (Lievens et al., 2015), thus the model simulated states are normally used to correct biases in the satellite SM retrievals. We first estimated observed SM (from SM9 and SM1) for the topsoil layer (0–50 mm) for each HRU by calculating average satellite-observed SM at each sub-basin using the areal weighted average method (Thiessen, 1911). The systematic differences between modelled (i.e., open loop) and remote sensing of soil moisture were then corrected using a mean-variance approach (Patil and Ramsankaran, 2017). From the mean-variance matching, both model simulated SM and observed SM were estimated on monthly timescale and HRU spatial scale. The bias corrected SM was then used for the next analysis.

We generated 100 ensembles using the Latin Hypercube sampling technique (Patil and Ramsankaran, 2017) and defined ranges of error variances used for generating ensemble of model forcing, soil field capacity and observed soil moisture states (see Appendix 14). Since we employed this EnKF data assimilation framework in multiple catchments with different climatic conditions, as well as with two different SM products, we assessed the error variances for each perturbed variable.

5.3.3.2. EnKF algorithm

The EnKF is a Monte Carlo approximation (i.e., ensemble) of the standard Kalman Filter for use in a non-linear model. It uses an ensemble of modelled states in a Bayesian-based auto-recursive analysis framework to optimally merge model estimates with state observations (i.e., SM). The EnKF was operated in two steps as follows.

Step 1—Uncertainties from the ensemble of modeled forecasts and ensemble of observations

During the soil water routing progress at any time step, at each HRU, the ensemble of model state (i.e., soil moisture) forecast is given as below.

$$x_{k+1}^{i-} = \boldsymbol{M}\left(x_k^{i+}, U_k^i\right) + w_{k+1} \tag{5.11}$$

Where $\boldsymbol{M}$ is a non-linear model, which is the hydrological SWAT model in this study. The superscript i represents a matrix of state ensembles with the forecast state (sign '-'), and analyzed state (sign '+'). The subscript k represents the time step. U_k^i is an ensemble of the model forcing. In this case, U is perturbed precipitation. w_{k+1} is Gaussian white noise representing the error due to uncertainties of forcing and model structure. Further, the ensemble of observations using the ensemble of states is calculated as follows.

$$\hat{z}_{k+1}^i = \boldsymbol{H}_k x_{k+1}^{i-} + v_{k+1} \tag{5.12}$$

Where $\hat{z}$ is the model predicted observation ensemble at time $k+1$. $\boldsymbol{H}$ is the observation operation to match the model states with the observations. Here, $\boldsymbol{H}$ is the areal weighted average soil moisture at HRU. v is the observation error, with separation of model errors and assumption of normally distributed with covariance $\sum_{k+1}^{z}$.

Step 2- Data assimilation progress

The model forecasts are updated towards observations using Kalman Gain matrix ($\boldsymbol{K}$) 's weights as,

$$x_{k+1}^{i+} = x_{k+1}^{i-} + \boldsymbol{K}\left(z_{k+1}^i - \hat{z}_{k+1}^i\right) \tag{5.13}$$

Where x_{k+1}^{i-}, x_{k+1}^{i+} represent an ensemble of model forecasts and of state after assimilation, respectively. z_{k+1}^i is an observation ensemble generated using the observation covariance matrix $\sum_{k+1}^{z}$.

The best linear unbiased estimation of x_{k+1}^{i+} when the Kalma gain is calculated as,

$$\boldsymbol{K} = \sum_{k+1}^{XZ} \left[\sum_{k+1}^{ZZ} + \sum_{k+1}^{Z} \right]^{-1} \tag{5.13}$$

Where $\sum_{k+1}^{ZZ}$ is the covariance of the model predicted observation ensemble obtained from $\boldsymbol{H}_k x_{k+1}^{i-}$. $\sum_{k+1}^{XZ}$ is the cross variance of the model forecast and observation prediction. After that, we resample the analyzed model state back into original layers at each HRU. The update retention parameters and soil moisture routing prior to the next step (t+1) are calculated as the equations (5.2) and (5.9), respectively.

Figure 5. 2 Flow chart of this study. EnKF-SM9 and EnKF-SM1 stand for streamflow simulations using the SWAT model with the state variable of SM9 and EnKF technique, and streamflow simulations using the SWAT model with the state variable of downscaled SM1 and EnKF technique, respectively. presents the flowchart of this study with detailed steps for each of the simulation scenarios: the open-loop model (hereafter OL); the assimilation of SM9 into the SWAT model with the EnKF technique (hereafter EnKF-SM9); and the assimilation of SM1 into the SWAT model with the EnKF technique (hereafter EnKF-SM1). The DA evaluation is in the period of 2017–2019 because this is the same as the validation period of the deterministic SWAT model.

5.3.4. Streamflow Performance Metrics

The modified Kling–Gupta efficiency (KGE, (Kling et al., 2012)) was used to evaluate streamflow simulations, with its formula as follows.

$$KGE = 1 - \sqrt{(r-1)^2 + (\beta-1)^2 + (\gamma-1)^2} \tag{5.14}$$

In which:

r is the Pearson correlation coefficient, reflecting the error in shape and timing between observed and simulated streamflow.

β is the bias term, evaluating the bias between observed and simulated streamflow.

γ is the ratio between coefficients of variation in observed and simulated streamflow, assessing the flow variability error with bias consideration.

We also calculated the benefit of the DA by using the Efficiency Index (Eff)(Massari et al., 2015), expressed as

$$Eff = 1 - \frac{\sum_{k=1}^{n}\left(Q_{da,k} - Q_{obs,k}\right)^2}{\sum_{k=1}^{n}\left(Q_{ol,k} - Q_{obs,k}\right)^2} \tag{5.15}$$

Where n represents the total time steps. $Q_{da,k}$, $Q_{ol,k}$, and $Q_{obs,k}$ denote the simulated streamflow with data assimilation, simulated streamflow without data assimilation (open loop), and observed streamflow at time step k, respectively. $Eff > 0$ denotes an improvement in streamflow simulation after implementing the DA scheme and vice versa for $Eff \leq 0$.

To focus on different aspects of flow time series, we transformed the flow time series before calculating KGE or Eff, as follows (Santos et al., 2018).

- Normal streamflow time series (hereafter Q_{nor}), to have more weights on high flow.
- Square root streamflow time series (hereafter Q_{sqr}), to have more weights on average flow.
- Inverse streamflow time series (hereafter Q_{inv}), to have more weights on low flow.

It is noted that with inverse streamflow transformation, to avoid zero flow, we added $1/100$ of mean observed flow before the transformation.

5.4. Results and Discussion

5.4.1. Characteristics of Soil Moisture SMAP Products

During the period of 2017–2019, apart from July, the average available data for SM9 across the studied catchments is approximately 35% in each month (Figure 5. 3). In July, a significant reduction in coverage of SM9 (below 25%) was observed. This is likely due to a large gap in July 2019 (see Appendix 15) because SMAP satellite was in a safe mode and did not provide the observed soil moisture information (O'Neill et al., 2020). The averaged coverage of SM1 was only one third of that of SM9 (approximately 11.5% in each month) and was 5% in July. The reason for SM1's low coverage in July is similar to that of SM9 as the SM1 is the downscaled product of SM9 and therefore inherits the gap from SM9.

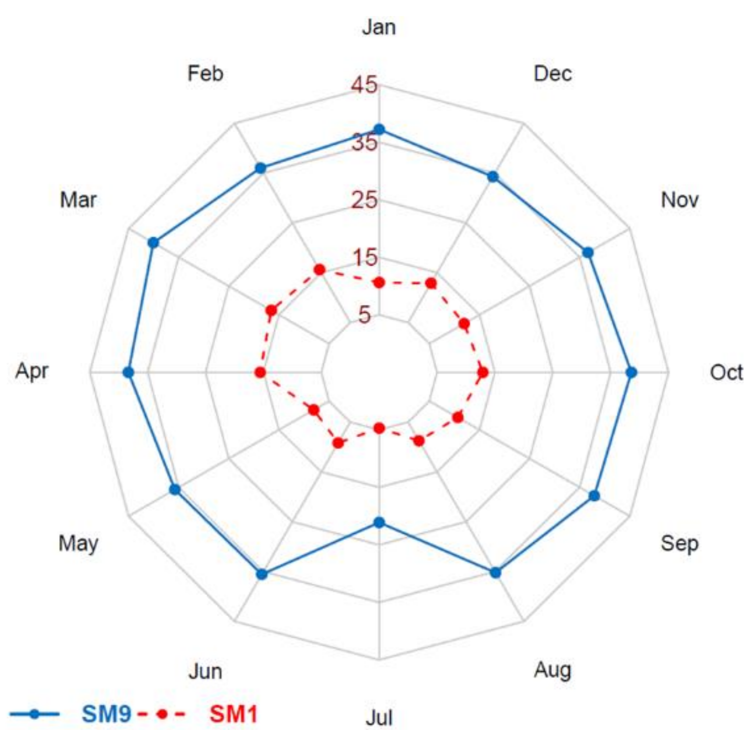

Figure 5. 3 Radar chart of average soil moisture available data (in percent) over 8 catchments in each month for SMAP 9km (SM9) and SMAP 1km (SM1) during 2017–2019.

The relationship between estimated SM value from SM9 and SM1 presented in Figure 5. 4. Two small catchments—gvo and aho (<500 km², Figure 5. 4a, b)—exhibited weak correlation between the two SM datasets as compared to the larger catchments. In these small catchments, the SM1 product seems to estimate higher SM value as higher density points are observed at the lower part of 1-1 line.

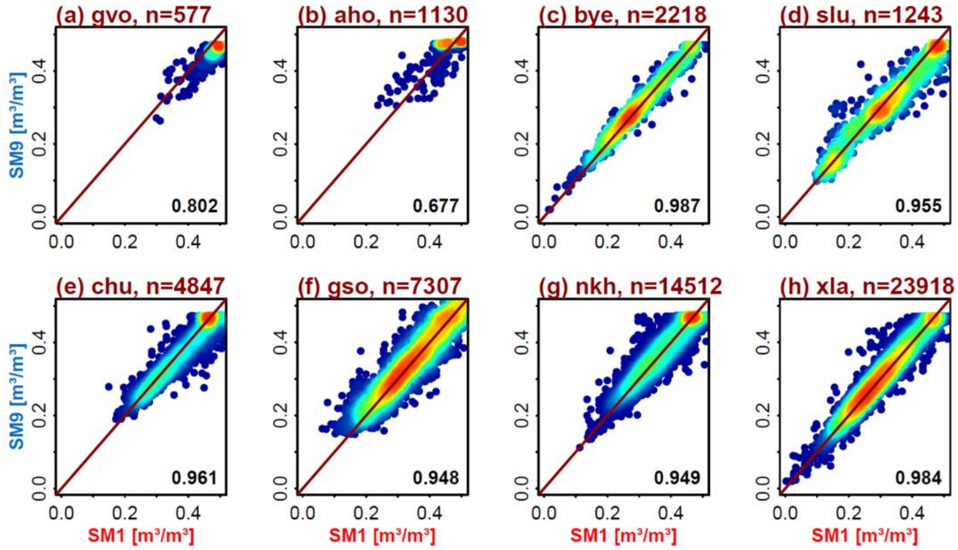

Figure 5. 4 Comparison between soil moisture volume metric estimated at sub-basins over eight catchments (a) gvo, (b) aho, (c) bye, (d) slu, (e) chu, (f) gso, (g) nkh, and (h) xla using SM9 and SM1. The points colors indicate points density, with more red meaning higher points density. The values in the bottom right indicate correlation values between the two soil moisture datasets. n is the total pair days which both SM9 and SM1 have values at a sub-basin.

Figure 5. 5 illustrates the proficiency of two SM products for reflecting a dry-down event in a medium-sized bye catchment. We used precipitation and SM to examine the drying of soil over time with respect to a rainfall event. After the rainfall event on April 4, 2018 (average 8.5 mm for the entire catchment), the catchment received less rainfall in subsequent days, and almost no rainfall after April 8. During the same period, we noted that both SM products exhibited similar dry down patterns. It is possible that SMAP observed the near-surface soil moisture conditions as they transitioned from saturated to dry conditions. Inter-comparison between these two SM products highlights the additional spatial patterns in soil moisture provided by each product. The SM1 dataset provides detailed variation in SM in space as compared to the SM9 dataset, demonstrated by its high standard deviation values (Figure 5. 5c). However, we also see the coverage of SM1 was not complete for the entire catchment. This is because of the limited coverage of this product due to its dependence on LST data, which is influenced by cloud cover.

5.4.2. Performances of Deterministic Hydrological SWAT Model in Simulating Streamflow

The statistical metrics for the SWAT model are presented in Table 5. 4, and optimized parameter sets of the SWAT model for each basin are provided in Appendix 11. The model performances for high flow (Q_{nor}) and average flow (Q_{sqr}) were satisfactory, with median KGE values of calibration/validation of 0.617/0.607 for high flow and 0.702/0.695 for average flow (Table 5. 4). The SWAT streamflow simulations are robust across the catchments (all KGE values were greater than 0.5), except for aho and slu catchments. It is likely that the rainfall patterns in these basins could be affected by topography (Le et al., 2020a; Trinh-Tuan et al., 2019a). The streamflow simulation for low flow (Q_{inv}) was relatively poor, with a median KGE of -0.263 and -0.086 for the calibration and validation periods, respectively. This poor performance for low flow has also been observed in previous studies (De Santis et al., 2021).

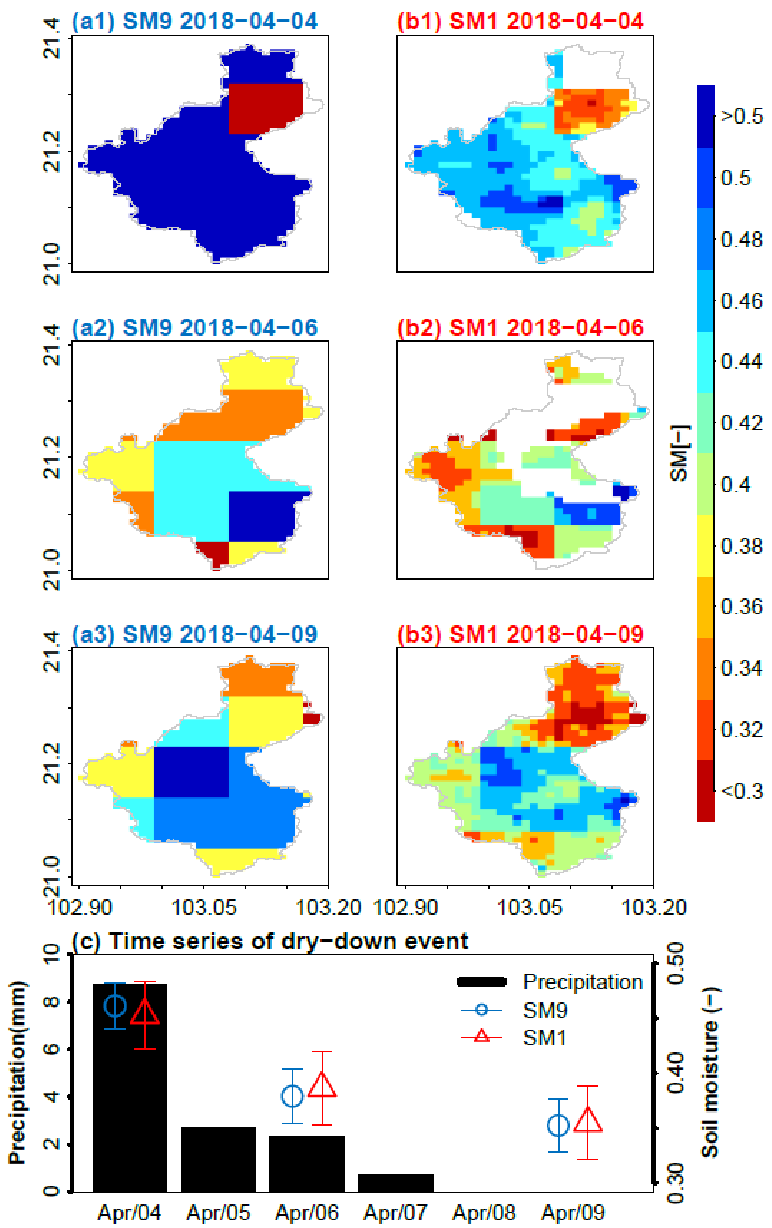

Figure 5. 5 Spatial variation in a dry-down event in bye catchment from April 4, 2018, to April 9, 2018, with soil moisture SMAP 9km (SM9, **a1**, **a2**, **a3**), soil moisture SMAP 1km (SM1, **b1**, **b2**, **b3**), and (**c**) time series of dry-down event at the same period from GPM IMERG (black bar) and SM9 (blue) and SM1(red). The error bars indicate standard deviation of SM variation in the catchment.

5.4.3. Temporal Variation for Open Loop, EnKF-SM9, and EnKF-SM1

Generally, soil moisture profiles across sub-basins in each catchment are mostly similar. For an illustrated purpose, we present here profiles of a sub-basin at xla river basin (>6,000 km²) in terms of precipitation, estimated SM from the open loop, EnKF-SM9, and EnKF-SM1 models for topsoil layer (0-50 mm), during the year of 2019 (Figure 5. 6). It is interesting that variation in topsoil SM does not exhibit strong correlation with variation in precipitation. This observation is different from another study in the tropical regions (Patil and Ramsankaran, 2017).

Table 5. 4 Statistical metrics for calibration and validation period with deterministic SWAT model. KGE_{nor}, KGE_{sqr}, and KGE_{inv} indicate performances with Q_{nor} (more weight on high flow), Q_{sqr} (more weight on average flow), and Q_{inv} (more weight on low flow), respectively.

Station Name	Calibration (2013–16)			Validation (2017–19)		
	KGE_nor	KGE_sqr	KGE_inv	KGE_nor	KGE_sqr	KGE_inv
gvo	0.623	0.703	0.413	0.670	0.686	0.674
aho	0.486	0.613	-0.984	0.417	0.462	-0.382
bye	0.786	0.864	0.176	0.575	0.796	0.259
slu	0.334	0.598	0.419	0.303	0.410	-0.089
chu	0.611	0.312	-2.708	0.694	0.470	-1.774
gso	0.757	0.718	-2.727	0.639	0.704	-0.977
nkh	0.542	0.700	-0.701	0.513	0.788	-0.082
xla	0.698	0.786	0.479	0.681	0.750	0.650
median	0.617	0.702	-0.263	0.607	0.695	-0.086

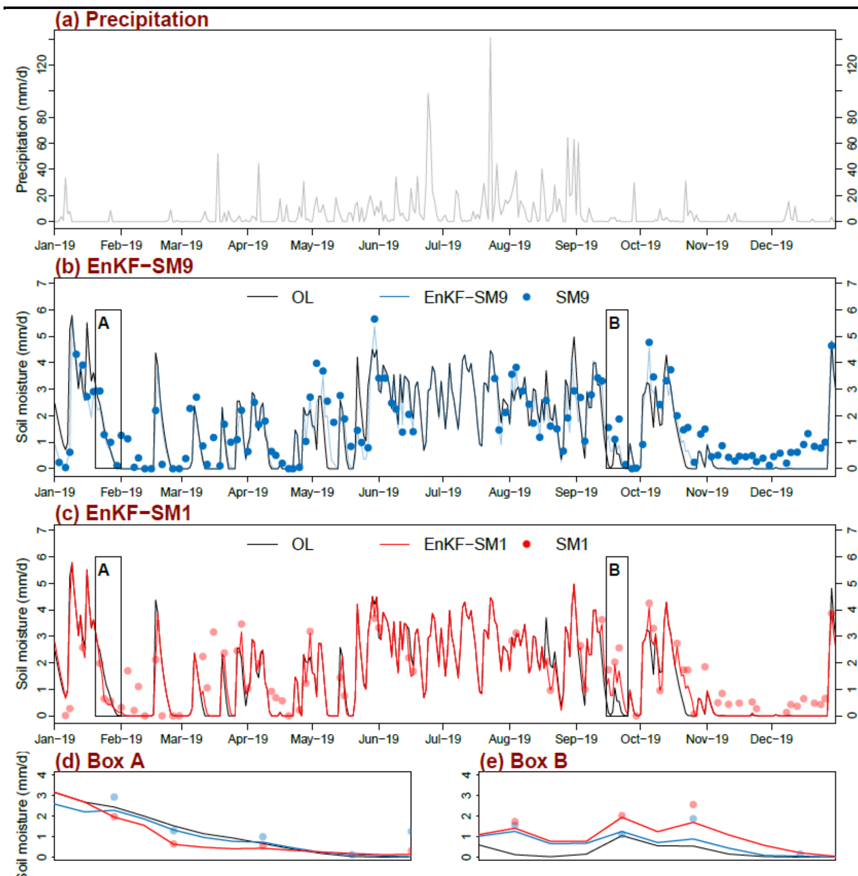

Figure 5. 6 Profile of a sub-basin of xla river basin during the year of 2019 for temporal variation in (**a**) areal precipitation; (**b**) soil moisture at the topsoil layer (0–5 mm) of OL, EnKF-SM9 model and observed SM9; (**c**)

soil moisture at the topsoil layer (0–50 mm) of OL, EnKF-SM1 model and observed SM1; (d) zoom of the last ten days in January 2019 (box A); (**e**) zoom of the last ten days in September 2019 (box B).

The relationship between topsoil SM and precipitation is even weaker when we examine it at smaller catchments (data not shown). Looking at details for typical 10-day periods in January 2019 (box A) and September 2019 (box B), we found the impacts of the DA framework on the SM simulations. Specifically, the SM simulations with the DA had drier down or more fluctuation as compared to simulations without DA, according to the variation in observed SM from SM9 and SM1. With respect to temporal simulated streamflow, the OL-based SWAT model produced results quite similar to the simulated time series from the deterministic SWAT model (Figure 5. 7a). On the other hand, the simulated streamflow from EnKF-SM9-SWAT and EnKF-SM1-SWAT are slightly better, with higher KGE_{sqr} values (Figure 5. 7a). When we examined the error density between the observed and simulated streamflow from different simulation scenarios, the error density from EnKF-SM1-SWAT had the peak closest to the zero-error vertical line (Figure 5. 7b).

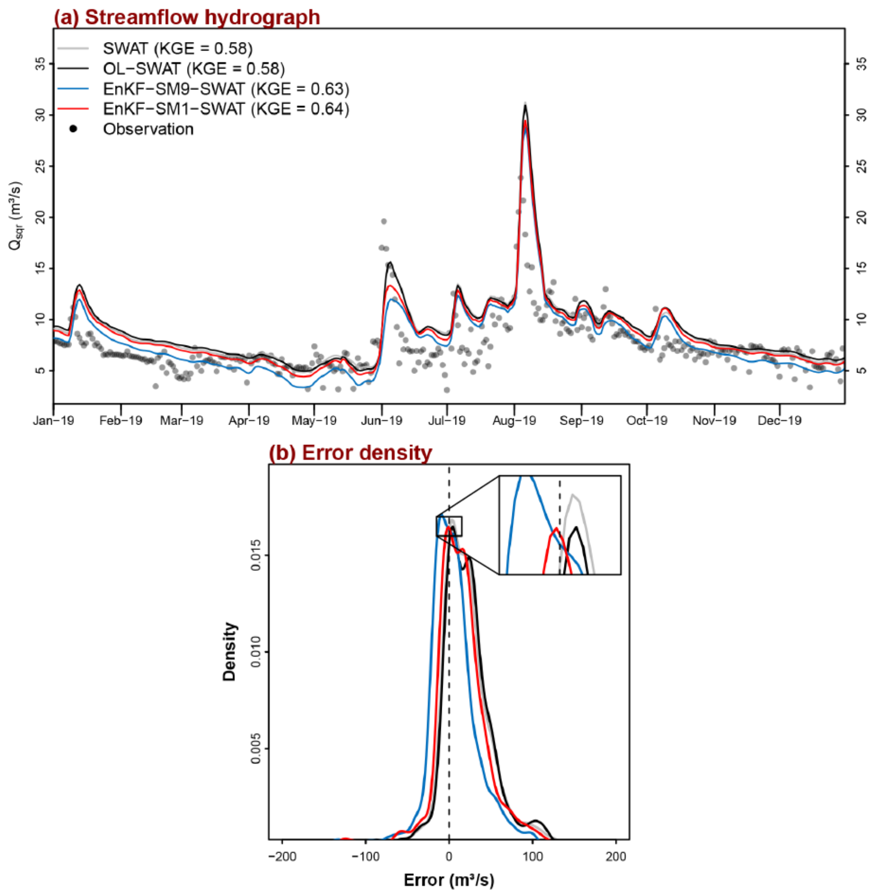

Figure 5. 7 (**a**) Streamflow hydrograph comparison, and (**b**) error density between observed and simulated streamflow from different hydrological SWAT simulation scenarios during the year of 2019 at xla river basin. The black dash line in (**b**) is the zero error vertical line. The inlet panel in (**b**) zooms in the peak error density from different simulation scenarios.

5.4.4. Statistical Performances for Data Assimilation with SM9 and SM1

Figure 5. 8 represents boxplots of streamflow simulations from the OL, EnKF-SM9, EnKF-SM1 models in two cases- all catchments (n=8) and catchments > 500 km² (n=6). The defined error values

for each basin for EnKF-SM9 and EnKF-SM1 are provided in Appendix 17 and Appendix 18, respectively. Overall, in the high flow assessment metric (Figure 5. 8a), the EnKF-SM1 model was slightly better than the OL model at either consideration of all catchments or catchments greater than 500 km². Meanwhile, the EnKF-SM9 model was only better than the OL model in the case of catchments greater than 500 km². We interpret this result as evidence that the high-spatial SM1 is robust in all types of catchments, while the SM9 is too-coarse for small watersheds. Furthermore, the assessment of average flow provided the same conclusion (Figure 5. 8b). This finding is similar to Abbaszadeh et al. (2020), as it implies the importance of spatial resolution over temporal resolution, but is in contrast to the work of Azimi et al. (2020).

On the other hand, low flow assessment (Figure 5. 8c) revealed that the EnKF-SM9 model had a higher median KGE score than the OL-model, either at all catchments or at catchments > 500 km². This may be because the OL model considers forecast error by perturbing rainfall forcing only, while the EnKF-SM9 model considers both forecast error and model error by perturbing rainfall forcing and soil moisture. The soil water content changes are more sensitive with changes in low flow in dry conditions than high flow in wet conditions or average flow.

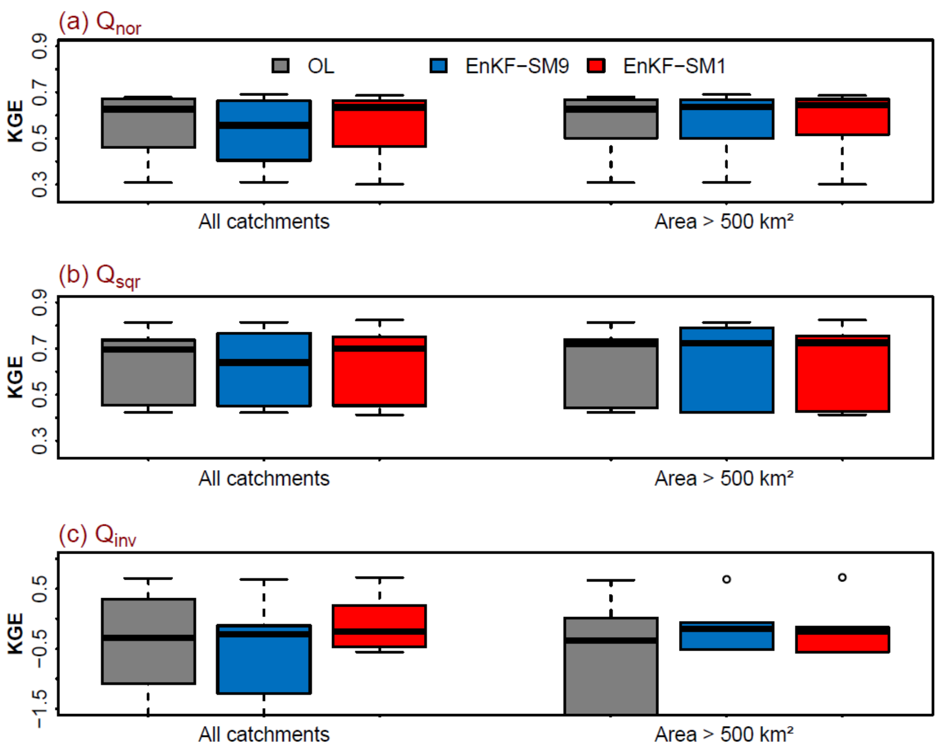

Figure 5. 8 Performance metrics in streamflow simulation in (a) normal-, (b) square root-, and (c) inverse-time series for open loop (OL)-, EnKF-SM9-, and EnKF-SM1-based SWAT model during the period 2017-2019. With respect to all catchments, total simulated catchments are 8. With respect to catchments having an area greater than 500 km², total simulated catchments are 6.

5.4.5. Assessment of Factors Impact on DA Performances

We examined the relationship between the Efficiency index (Eff) with the available SM for two DA models, EnKF-SM9 and EnKF-SM1 (Figure 5. 9). From all flow types (high, average, and low flow), the EnKF-SM1 models exhibited higher Eff scores than the EnKF-SM9 models. When we excluded small catchments (< 500 km²), higher Eff scores were observed for EnKF-SM models. Since SM1 has a shorter data record, our results suggest that spatial information plays a more important role than temporal information. We also found that the SM1 available day has a significant positive correlation with Eff scores, while this relationship for available SM9 is not significant (see Appendix 19), suggesting a potential approach for improving the high-spatial SM-based DA model that increases its temporal information.

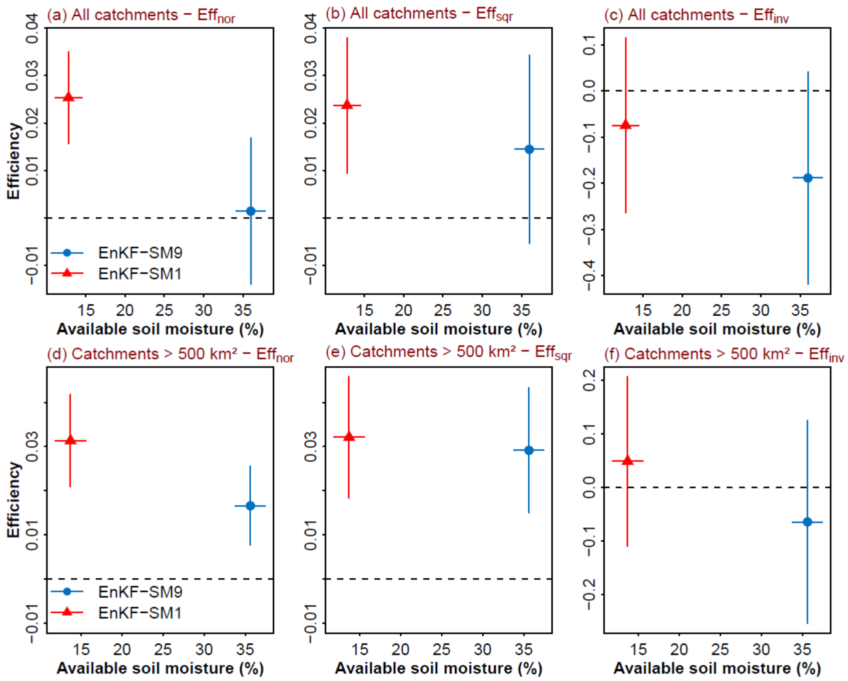

Figure 5. 9 Comparison between average efficiency index of streamflow simulation using assimilation of EnKF-SM9 model and assimilation of EnKF-SM1 model and OL-based model for all catchments (**a**, **b**, **c**) and catchments > 500 km² (**d, e**, **f**). Points above zero-dash line indicate an improvement in streamflow simulation after implementing the data assimilation framework as compared with the OL-based model simulation.

The relationships between the Eff and normalized different vegetation index (NDVI) for average flow, high flow, and low flow are given in Figure 5. 10a, b and c. Catchments with dense vegetation (higher NDVI values) seem to have lower Eff scores, reflecting the limitations of satellite-based SM to accurately capture soil water content at these dense vegetated catchments. This result is consistent with that of Azimi et al. (2020). However, our results provide new insight. When we compared the two SM-based models, the EnKF-SM1 seems to have less dependence with NDVI, demonstrated by its Eff not being significantly reduced when NDVI values were high, as compared to the departure of Eff of the EnKF-SM9 model.

5.5. Conclusions and Further Studies

As satellite-based remote sensing technology continues to advance, operational applications of satellite-based soil moisture products are becoming more routine. These valuable earth observations are proving to be a significant addition to several water resource management applications. However, there remain many unanswered questions regarding the most effective approach for integrating these data, as well as how temporal resolution, spatial resolution, and data record length affect their utility. The primary goal of this study was to address some of these questions and examine the trade-offs between optimal spatial vs optimal temporal resolution for two remotely sensed soil moisture (SM) products in a hydrologic data assimilation framework. Two remotely sensed SM datasets—downscaled SMAP 1km (SM1) and SMAP 9km (SM9)—were assimilated in the hydrological model (Soil and Water Assessment Tool, SWAT) using the Ensemble Kalman Filter (EnKF) algorithm. The effect of basin size was assessed by comparing simulated streamflow performance in eight catchments ranging in size from 267km² to 6,430 km² across tropical Vietnam.

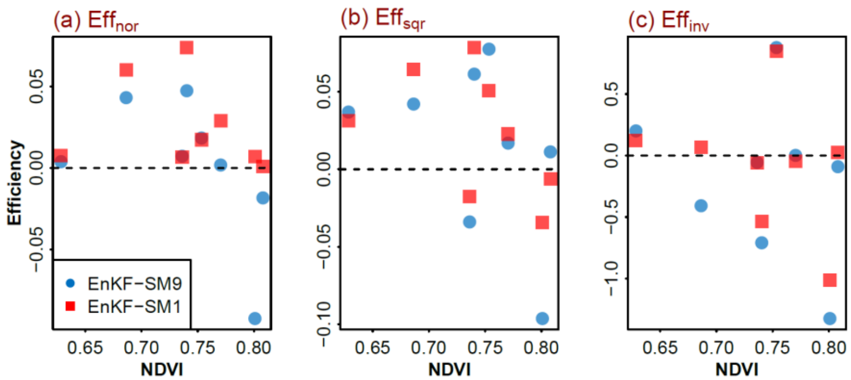

Figure 5. 10 Relationship between efficiency of data assimilation for (**a**) Eff_{nor}(high flow score); (**b**) Eff_{sqr}(average flow score); and (**c**) Eff_{inv}(low flow score) time series with average NDVI values over eight catchments.

Model fidelity was influenced by both temporal and spatial resolution, however, the DA-based models were slightly better than the open-loop models in three aspects of flow assessment with KGE metrics (low, average, and high flow). In addition, the EnKF-SM1 model was more pronounced, especially for small catchments. This indicates that the improvement in the streamflow simulation due to assimilated soil moisture is more significant in catchments where downscaled SMAP 1km has fewer missing observations. We also found that the vegetation effects on soil moisture are less significant in the EnKF-SM1 models compared to EnKF-SM9 models, further demonstrating the reduced uncertainty in streamflow from applying the finer spatial resolution soil moisture product. To this end, this study demonstrates the potential benefits of higher spatial resolution remotely sensed SM for improving hydrologic applications.

Overall, the results of this study provide useful information for developers of satellite-based SM product for improving their soil moisture retrieval algorithms at a global scale, especially in tropical regions. In addition, we conclude that optimal strategies for the integration of satellite-based soil moisture in hydrologic models must carefully consider basin size, climate, land cover, and, perhaps most importantly, the spatial and temporal resolution of the satellite-based products.

Chapter 6: Conclusions and further studies

6.1. Conclusions

As global datasets (observations from satellite-based remote sensing and outputs from land surface models) continue to advance, operational applications of global datasets-based products require increased scrutiny. These global datasets prove to be useful assets to support water resources management (WRM) at the local scale. However, there are still doubts on the reliability of global datasets across different regions in the globe, making it difficult for decision makers to confidently rely on information obtained from these data products. This dissertation fills this gap and provides large-scale validation of global datasets over an under-represented region for ground networks. The studies adopted a large sample approach to investigate the usefulness of different global datasets to support WRM across Vietnam. Table 6.1 provides a summary of investigated datasets, their utilities for WRM, and key findings obtained from this dissertation.

Several novel methodologies and frameworks to utilize global datasets in different WRM applications have been proposed in this dissertation. In Chapter 2, an empirical climatology-topography-based linear-scaling approach (CTLS) was developed to correct TMPA rainfall products. Specifically, a linear scaling approach with a set of 12 empirical multiple linear regression equations was formed based on the moderate correlation between climatological- and topographical- characteristics and correction factors. The CTLS can reduce TMPA's percentage bias (e.g., averaged |PBIAS| decreased by 15% in wet season for TMPA 3B42RT) and could be applied across the studied river basin even in areas without rain gauge. In Chapter 3, we characterize drought conditions derived from a re-analysis MERRA-2 dataset at a very high spatial resolution (1km), while previous studies often attempted drought conditions at a spatial resolution larger than or equal to 10km. The high spatial resolution dataset quantifies high spatial variation of drought conditions and brings the MERRA-2 dataset closer to the scale of WRM applications, which requires information over a few square kilometers. We proposed a study framework in Chapter 4 to select suitable gridded precipitation products to drive hydrological model streamflow simulations. A set of catchments (6 catchments) corresponding to six climate zones and 9 different precipitation products (rain gauge + 8 different gridded precipitation products) have been employed to form 54 different hydrologic models (6 x 9), where each model was separately calibrated to utilize each precipitation dataset input. With this intensive model experiment, this study exhibited that precipitation estimated from IMERG data could be an alternative forcing input to rain gauge (traditional forcing input) to drive hydrologic model streamflow simulation, especially for catchments with a low rain gauge density. In remotely sensed soil moisture data assimilation in a hydrologic model, there remains an unanswered question regarding how temporal and spatial resolution impact model performance. Therefore, we addressed this concern in Chapter 5 by examining the trade-offs between optimal spatial versus optimal temporal resolution for two remotely sensed soil moisture products in a hydrologic data assimilation framework. These products include SMAP 9km with low spatial resolution, but more temporal values, and its downscaled SMAP 1km that has high spatial resolution, but less temporal values. Additionally, we also employed the hydrologic data assimilation framework in a set of large sample catchments (8 catchments), while previous studies performed such evaluation over a few catchments.

Table 6. 1 Summary of four studies in this dissertation and their utilities for water resources management (WRM).

Variables	Global datasets*	Local datasets	Reference datasets	Key Findings	Utility for WRM
Precipitation[1]	3B42RT (P) 3B42V7 (P)	Rain gauge	Rain gauge	(1) TMPA's rainfall estimation in wet season is better than dry season. (2) TMPA's rainfall estimation can be improved using climatology-topography-based linear-scaling approach	Adjusted TMPA products can reliably estimate rainfall at areas where rain gauge is absence over the Red-Thai Binh River basin.
Drought indices[2]	MERRA-2 (P, T)	Rain gauge Meteorological stations	Official drought records	(1) Drought characteristics was sensitive to spatial resolutions. (2) Validation of MERRA-2 data showed reasonable results. (3) Drought exhibited contradictory trends in North and South Vietnam during 1989-2019.	Feasibility of using a model-based drought index in data-sparse areas for long-term trend drought analysis, and for practical applications of advanced re-analysis products in water resources management.
Streamflow[3]	3B42RT (P) CHIRP (P) PERSIANN (P) IMERGE-V6 (P) 3B42V7 (P) CHIRPS (P) PERSIANN-CDR (P) IMERGF-V6 (P)	Rain gauge	Rain gauge Observed streamflow	(1) IMERGF-V6 achieved the best overall performance among satellite-derived precipitation estimates (SPE) datasets. (2) There is a confidence for using SPE in determining monthly streamflow in large river basins.	This study could be a guide to determine the suitability of different SPE products for hydrological simulations. For example, IMERGF-V6 can be a suitable precipitation forcing product for hydrological model streamflow simulation. CHIRPS can be a reasonable product for drought analysis.
Streamflow[4]	IMERGF-V6 (P) SMAP 9km (SM) SMAP 1km (SM)		Observed streamflow	(1) High-spatial resolution of downscaled SMAP 1 km is more beneficial in the data assimilation framework in aiding the accuracy of streamflow simulation, as compared to that of SMAP 9 km, especially for the small catchments. (2) Improvement in the streamflow simulation with data assimilation is more significant at catchments where downscaled SMAP 1 km has fewer missing observations.	High spatio-temporal resolution of remotely sensed soil moisture could be useful in a data assimilation hydrologic model streamflow simulation framework in small catchments.

Note:
[1]Materials from chapter 2; [2]Materials from chapter 3; [3]Materials from chapter 4; [4]Materials from chapter 5.
** Acronym for global datasets.*
"3B42RT" The Tropical Rainfall Measurement Mission (TRMM) Multi-satellite Precipitation Analysis (TMPA) near real-time version "3B42V7" The Tropical Rainfall Measurement Mission (TRMM) Multi-satellite Precipitation Analysis (TMPA) research version
"MERRA-2" The Modern-Era Retrospective Analysis for Research and Applications, version 2 (MERRA-2)
"CHIRP" Climate Hazards group Infrared Precipitation
"PERSIANN" Precipitation Estimation from Remotely Sensed Information using Artificial Neural Networks
"IMERGE-V6" Global Precipitation Measurement (GPM) Integrated Multi-satellitE Retrievals for GPM (IMERG) Early Run V6 "CHIRPS" Climate Hazards group Infrared Precipitation with Stations
"PERSIANN-CDR" Precipitation Estimation from Remotely Sensed Information using Artificial Neural Networks-Climate Data Records
"IMERGF-V6" Global Precipitation Measurement (GPM) Integrated Multi-satellitE Retrievals for GPM (IMERG) Final Run V6
"SMAP 9km" Original Soil moisture Active and Passive
"SMAP 1km" Downscaled Soil moisture Active and Passive, extracted from Bin et al., 2022
"P" Precipitation; "T" Air temperature; "SM" Soil moisture

6.2. Further studies

Bias correction of near-real time satellite rainfall for the LMRB could be an interesting study. Such rainfall product could be beneficial to real-time operational water resources applications in the Lower Mekong River basin (LMRB), given a fact that in-situ monitoring network in the LMRB is limited due to restrictions in data-sharing between the riparian countries. The proposed near-real-time satellite rainfall product is IMERGE-V6 (0.1° in every half-hour with few hours latency). We proved that IMERGE-V6 driven hydrologic model could simulate streamflow comparably in Chapter 4. The proposal method will aim to provide corrected weights maps of IMERGE-V6 which are constraint by topography and seasonality. To build such maps, rain gauge across the basin should be collected to characterize rainfall error maps. Also, machine learning could be a potential model to make the corrected maps. Since long-term rain gauge records for the LMRB are rare, to utilize as many as possible the rain gauge dataset in the region, a smart training could be employed by training a machine learning model in selected years (normal year, high water year and low water year) in order to obtain a generalized weighted maps for all hydrologic conditions but using just a few years. The weighted maps will be validated by the years not included in the training period and the corrected IMERGE-V6 could be further validated by examining it as input to a hydrologic model to simulate streamflow.

Improvement of temporal data for high-spatial remotely sensed soil moisture could be another potential study. In Chapter 5, the performances of data assimilation hydrologic model streamflow simulation with downscaled SMAP 1km are significantly associated with the temporal available SMAP 1km. Specifically, when we have more available SMAP 1km data during the assimilation process, a better streamflow is observed. The reason of having less available SMAP 1km is that land surface temperature dataset obtained from MODIS that participate in the downscaled process, often has missing values due to cloud coverage. Therefore, if we could propose a method to increase the availability of land surface temperature dataset, we perhaps could increase the availability of downscaled SMAP 1km as well.

Appendix

Appendix 1 Original land cover dataset (30 m) and 1-km, 9-km, and 36-km agricultural land grid in the R3 region.

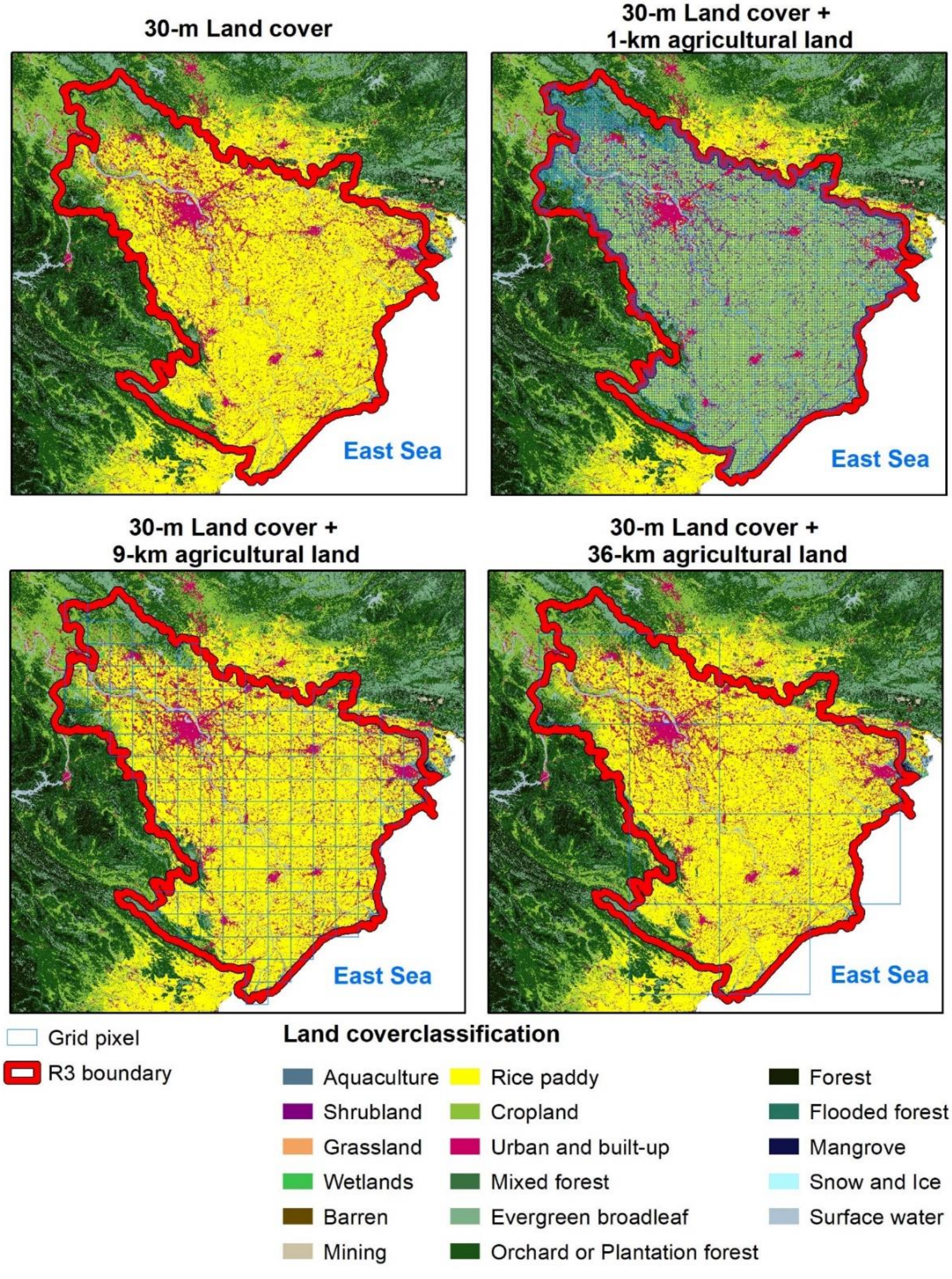

Appendix 2 Comparison between 9-km and 36-km MERRA-2 datasets with ground observation.

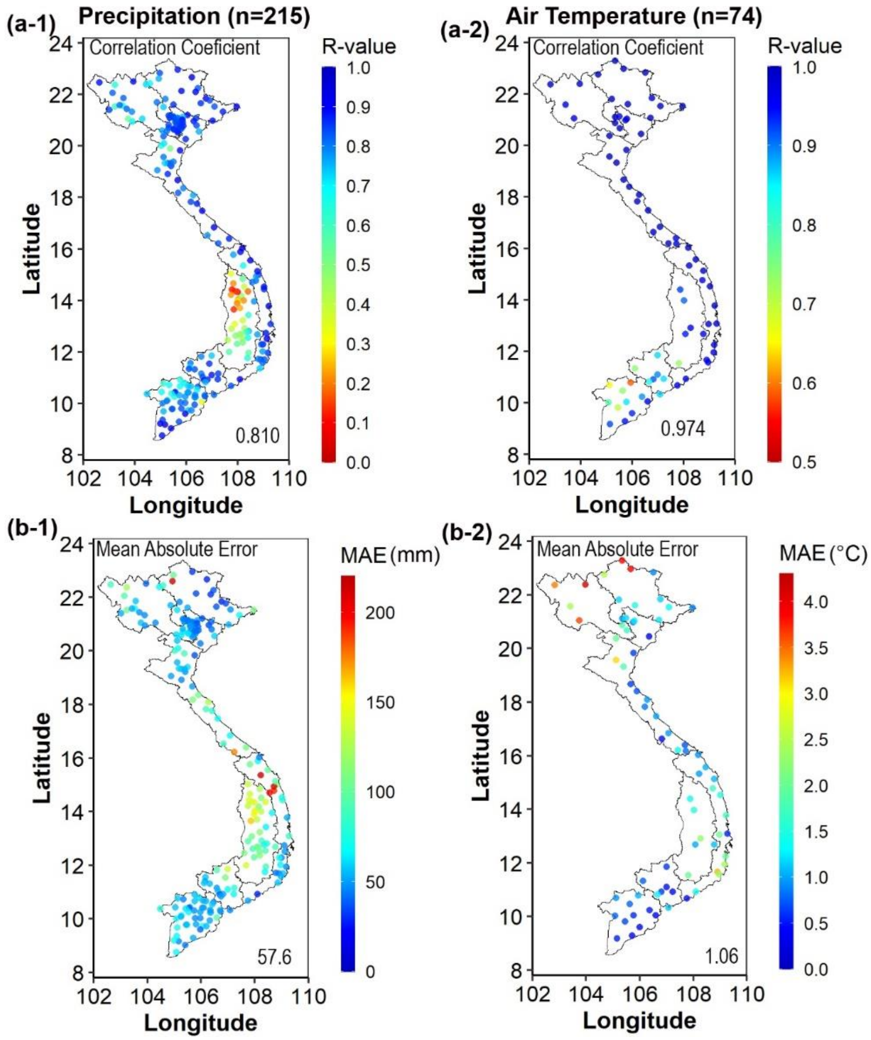

Figure S2.1. (a) Correlation coefficient and (b) Mean absolute error between 9-km MERRA-2 datasets and observed precipitation (right) and observed air temperature (left). Number inlets denote median values.

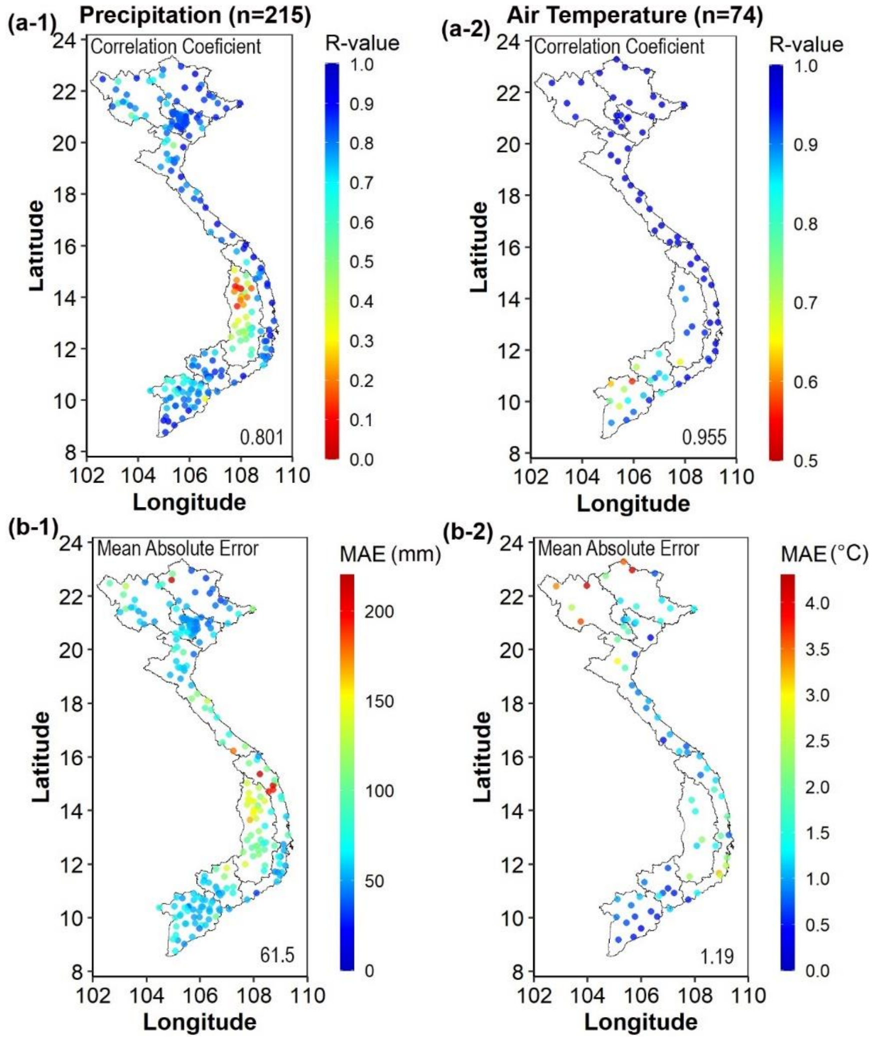

Figure S2.2. (a) Correlation coefficient and (b) Mean absolute error between 36-km MERRA-2 datasets and observed precipitation (right) and observed air temperature (left). Number inlets denote median values.

Appendix 3 Annual precipitation and temperature for each region based on MERRA-2 datasets (1-km, 9-km, 36-km).

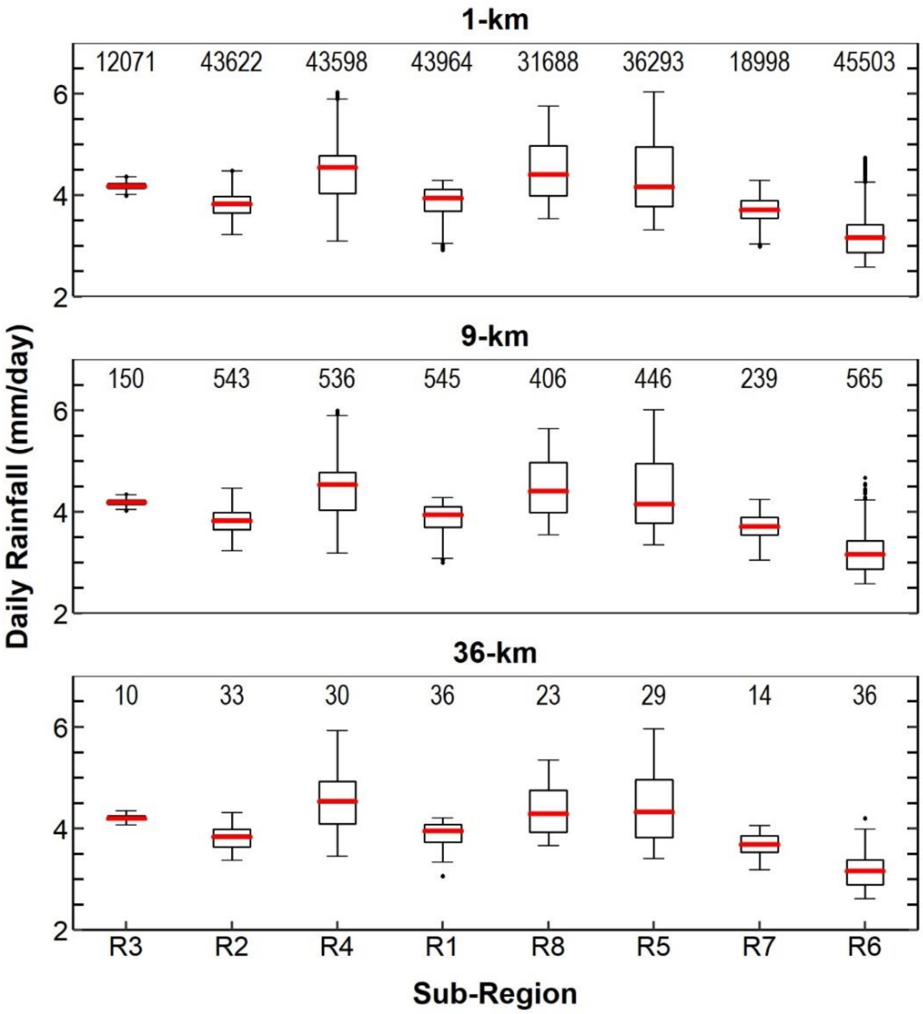

Figure S3.1 Boxplot of annual precipitation in each region in different spatial resolutions (1-km, 9-km, and 36-km).

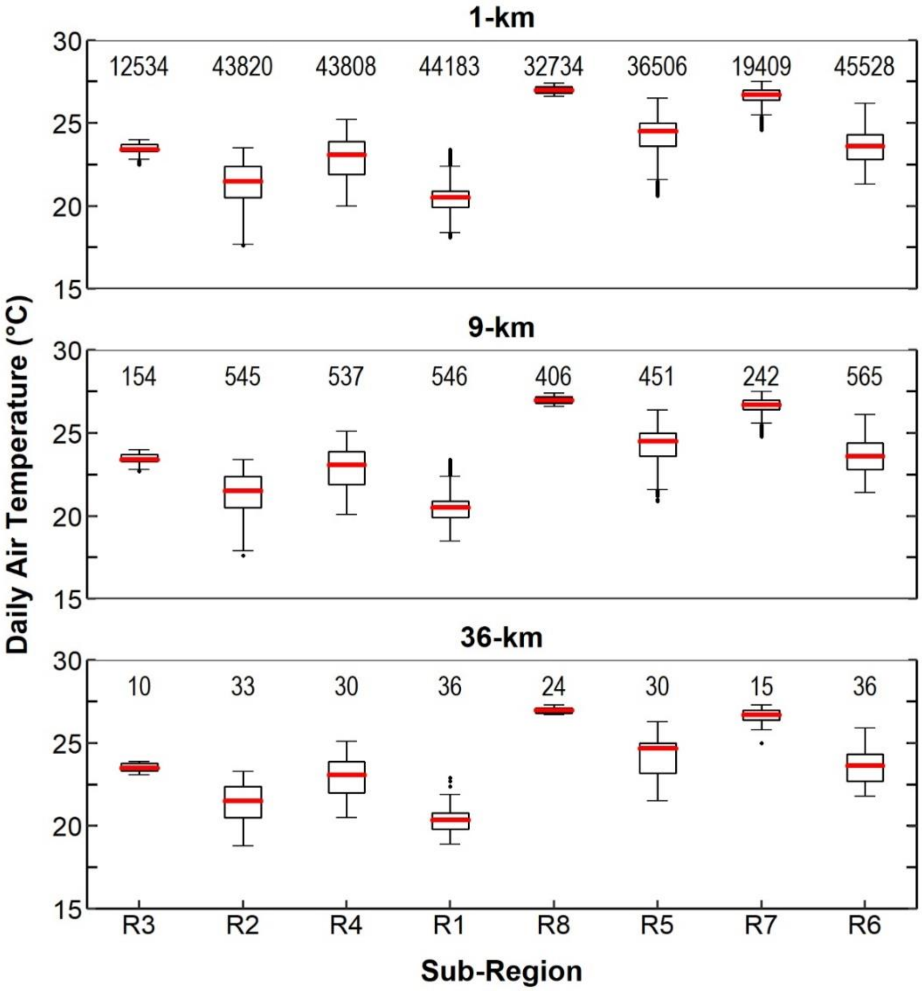

Figure S3.2 Boxplot of annual temperature in each region in different spatial resolutions (1-km, 9-km, and 36-km).

Appendix 4 List of rain gauges used in this study and their missing data during 2002-2017.

Station Name	Location	Lat.	Lon.	Missing (%)
a) XL (Ma River) basin				
Dienbien	Thanhxuong, Dienbien city, VN	21.37	103.00	1.9
Tuangiao	Tuangiao town, Dienbien, VN	21.58	103.42	0.0
Phadin	Toatinh, Tuangiao, Dienbien, VN	21.57	103.52	1.4
Songma	Songma town, Sonla, VN	21.05	103.75	3.8
Xala	Chiengkhuong, Songma, Sonla, VN	20.94	103.92	4.3
Muongang	Muongang,Tuangiao, Dienbien, VN	21.52	103.23	5.3
Thuanchau	Chiengly, Thuanchau, Sonla, VN	21.43	103.70	1.4
b) LS (Kycung River) basin				
Langson	Quanglac, Langson city, Langson, VN	21.83	106.77	0.0
Dinhlap	Dinhlap town, Langson, VN	21.53	107.10	0.0
Locbinh	Locbinh town, Langson, VN	21.77	106.92	0.9
c) HT (Boi River) basin				
Hoabinh	Tanthinh, Hoabinh city, VN	20.82	105.33	0.7
Kimboi	Bo town, Kimboi, Hoabinh, VN	20.67	105.53	0.7
Hungthi	Hungthi, Lacthuy, Hoabinh, VN	20.52	105.67	0.7
Bahangdoi	Thanhnong, Kimboi, Hoabinh, VN	20.58	105.69	0.6
Caophong	Bung Town, Kyson, Hoabinh, VN	20.70	105.32	1.0
Kimtien	Kimtien, Kimboi, Hoabinh, VN	20.63	105.52	0.6
d) NK (Hieu River) basin				
Tayhieu	Tayhieu, Nghiadan, Nghean, VN	19.32	105.40	0.0
Quychau	Quychau town, Quychau, Nghean, VN	19.57	105.12	0.0
Quyhop	Quyhop town, Quyhop, Nghean, VN	19.33	105.18	0.0
Nghiakhanh	Nghiakhanh, Nghiadan, Nghean, VN	19.22	105.41	0.0
NT1-5	Nghiabinh, Nghiadan, Nghean, VN	19.38	105.50	3.8
NT3-2	Minhhop, Quyhop, Nghean, VN	19.32	105.28	0.0
e) AC (Ve River) basin				
Bato	Bato town, Quangngai, VN	14.77	108.73	0.0

Anchi	Hanhphuoc, Nghiahanh, Quangngai, VN	14.99	108.81	0.0
Giavuc	Bavi, Bato, Quangngai, VN	14.70	108.57	0.0
Minhlong	Longhiep, Minhlong, Quangngai, VN	14.93	108.72	1.8
f) GS (Krong Ana River) basin				
Giangson	Hoahiep, Krongana, Daclac, VN	12.51	108.18	0.4
Buonmethuot	Buonmethuot City, Daclac, VN	12.68	108.08	0.3
Buonho	Buonho, Krongbuk, Daclac, VN	12.92	108.27	0.3
Mdrak	CuMTa,Mdrak, Daclac, VN	12.68	108.78	0.4
Krongbuk	Krongbuk, Krongpak, Daclac, VN	12.77	108.35	1.0

Appendix 5 Input description for the SWAT model used in this study.

	Data Description	Spatial, Resolution	XL Ma River	LS Kycung River	HT Boi River	NK Hieu River	AC Ve River	GS Krong Ana River
Zone			S1 North West	S2 North East	S3 North Delta	S4 North Central	S5 South Central	S6 Central Highland
Area (km²)			6430	1560	664	4024	854	3020
Dry Season/ Wet Season			XI-IV/V-X	XI-IV/V-X	XI-IV/V-X	XII-V/VI-XI	I-VIII/IX-XII	XII-IV/V-XI
Precipitation	Rain Gauge (stations)		7	3	6	6	4	5
	Uncorrected SPE / **Gauge-corrected SPE** TMPA 3B42RT/ TMPA 3B42V7 (grids) GPM IMERGE-V6/ GPM IMERGF-V6 (grids) CHIRP V2.0/ CHIRPS V2.0 (grids) PERSIANN/ PERSIANN-CDR (grids)	0.25° 0.1° 0.05° 0.25°	16 76 266 16	8 26 78 8	5 16 36 5	14 53 178 14	4 13 40 4	12 44 141 12
Air Temperature	Minimum Temp, Maximum Temp (stations)		2	2	1	3	1	2
Digital Elevation (DEM)	Shuttle Radar Topography Mission (SRTM)	30 m	Min:279 m Max:2184 m Mean:959 m	Min: 225 m Max: 1518 m Mean: 430 m	Min:8 m Max:1194 m Mean:254 m	Min: 29 m Max: 2417 m Mean: 397 m	Min: 3 m Max: 1126 m Mean: 350 m	Min: 387 m Max: 2424 m Mean: 659 m
Land use[1]	Land use in 2010 from SERVIR Mekong	30 m	FRST (67.4) GRAS (13.1) CRGR (9.8) FRSE (7.8)	CRGR (29.1) ORCD (23.2)	ORCD (39.3) FRST (38.1)	FRST (47.3) ORCD (25.6)	FRSE (36.9) ORCD (33.8)	FRST (33.2) FRSE (31.0)

				FRSD (22.1) FRSE (18.7)	CRGR (13.6) FRSE (8.4)	CRGR (13.2) FRSE (12.8)	FRST (24.5)	CRGR (27.9)
Soil[2]	Generated from vector layer of 1:1,000,000 soil map of Vietnam	30 m	ACu (51.1) ACf (45.5)	ACf (83.5) Cmd (6.5)	ACf (74.7) FRr (21.2)	ACf (82.8) FRr (8.0) ACu (5.6)	ACf (87.2) ACu (5.9) FLd (4.4)	ACf (41.4) FRr (20.8) ACu (18.7)
Sub-basins, HRUs	10% soil, 10% land use, 10% slope		145 sub-basins 735 HRUs	31 sub-basins 288 HRUs	17 sub-basins 149 HRUs	107 sub-basins 845 HRUs	15 sub-basins 98 HRUs	58 sub-basins 673 HRUs

Note:

[1] It presents the most dominant land use in the basin. The number in the blanket is the percentage of land use in a total. Symbol explanation: CRGR Cropland, FRSE Evergreen Forest, FRST Mixed Forest, GRAS Grassland, ORCD Orchard, and Plantation Forest.

[2] It presents the most dominant soils in the basin. The number in the blanket is the percentage of the soil type in a total. Symbol explanation: ACf Ferralic Acrisols, ACu Humic Acrisols, Cmd Dystric cambisols, FLd Eutric Fluvisols, FRr Rhodic Ferralsols.

Appendix 6 List of fifteen parameters considered for the calibration process, with their default values, calibrated range, and process. In SWAT-CUP, "r_", "v_", and "a_" refer to modify the default value by making a relative change to the default value, replacing the default value by the specific value and adding a specific value, respectively.

Parameter Name	Units	Description	Default	Range	Process
r__CN2	none	SCS runoff curve number	HRU specific	-0.1, +0.1	Surface Runoff
r__SOL_AWC	mm H_2O /mm soil	Available water capacity of the soil layer	Soil layer specific	-0.1, +0.1	Soil
r__SOL_K	mm/hr	Soil conductivity	Soil layer specific	-0.3, +0.3	Soil
r__SOL_Z	mm	Soil depth	300	-0.5, +0.5	Soil
v__ESCO	none	Soil evaporation compensation factor	0.95	0, +1.0	Evapotranspiration
v__SURLAG	none	Surface runoff lag coefficient	4	0, +25	Surface Runoff
v__QWHT	m	Initial groundwater height	1	0, +1.0	Groundwater
v__ALPHA_BF	1/days	Baseflow alpha factor	0.048	0, +1.0	Groundwater
a__GW_DELAY	days	Groundwater delay time	31	-1000, +1000	Groundwater
a__GWQMN	mm H_2O	Threshold depth of water in the shallow aquifer	1000	-1000, +5000	Groundwater
a__REVAPMN	mm H_2O	Percolation to the deep	750	-750, +750	Groundwater
v__GW_REVAP	none	Groundwater "revap" coefficient	0.02	+0.02, +0.1	Evapotranspiration
a__RCHRG_DP	none	Deep aquifer percolation fraction	0.05	-0.05, +0.05	Groundwater
a__CH_K2	mm/hr	Effective hydraulic conductivity	1	-0.01, +500	Channel
a__CH_N2	none	Manning coefficient for main channel	0.014	0.0, +0.3	Channel

Appendix 7 Performance measures (NSE and PBIAS) of daily streamflow SWAT simulations, driven by different precipitation input datasets over the six basins of Vietnam. The evaluation period: Cal. Calibration (2002-2009), Val. Validation (2010-2017).

Basin	Rainfall Input	NSE_cal	PBIAS_cal (%)	NSE_val	PBIAS_val (%)
XL	Rain Gauge	0.64	-1.7	0.69	7.4
	3B42RT	0.58	-1.5	0.55	-1.5
	IMERGE_V6	0.58	22.3	0.62	17.1
	CHIRP	0.54	8.7	0.58	13.1
	PERSIANN	0.3	27.2	0.11	48.3
	3B42V7	0.62	6.9	0.64	13.6
	IMERGF_V6	0.63	13	0.69	-9.2
	CHIRPS	0.47	3.2	0.56	10.5
	PERSIANN_CDR	0.52	-2.1	0.56	6.9
LS	Rain Gauge	0.62	6.4	0.64	-12
	3B42RT	0.34	-12.6	0.3	-22.4
	IMERGE_V6	0.55	14.3	0.50	27
	CHIRP	0.21	19.5	0.24	11.5
	PERSIANN	0.08	-5.3	0.13	9.1
	3B42V7	0.33	-2.1	0.37	-8.5
	IMERGF_V6	0.58	-6.5	0.59	-17.3
	CHIRPS	0.32	5.8	0.39	5.3
	PERSIANN_CDR	0.29	-14	0.32	9
HT	Rain Gauge	0.84	-13.4	0.78	-19.5
	3B42RT	0.33	-40.8	0.24	-37.1
	IMERGE_V6	0.50	-1.2	0.43	6.4
	CHIRP	0.27	-5.5	0.15	-28
	PERSIANN	0.06	-12	0.05	-24.9
	3B42V7	0.47	-5.4	0.28	-11.1
	IMERGF_V6	0.64	-3.7	0.52	-5.7
	CHIRPS	0.37	-3	0.38	-8.5
	PERSIANN_CDR	0.45	-24.6	0.28	-20.1
NK	RainGauge	0.72	19.6	0.76	17.3
	3B42RT	0.36	29.8	0.29	6.5
	IMERGE_V6	0.37	23.4	0.51	22.7
	CHIRP	0.38	23.2	0.38	21.8
	PERSIANN	0.1	39.3	0.01	53.6
	3B42V7	0.52	19.6	0.41	35
	IMERGF_V6	0.56	6.8	0.55	-12.6
	CHIRPS	0.44	8	0.51	0.9
	PERSIANN_CDR	0.15	25.8	0.15	21.9
AC	Rain Gauge	0.91	1.6	0.72	-48.9

Basin	Rainfall Input	NSE_cal	PBIAS_cal (%)	NSE_val	PBIAS_val (%)
	3B42RT	0.29	49.1	0.38	16.7
	IMERGE_V6	0.20	57.8	0.34	29.6
	CHIRP	0.19	46.1	0.14	14.9
	PERSIANN	-0.01	68.4	0.04	55.8
	3B42V7	0.21	49.9	0.22	29.9
	IMERGF_V6	0.44	51.6	0.5	22.5
	CHIRPS	0.29	21.5	0.2	-13.8
	PERSIANN_CDR	0.26	37.3	0.28	16.5
GS	Rain Gauge	0.72	2.9	0.65	18.1
	3B42RT	0.3	35.1	0.16	42.7
	IMERGE_V6	0.47	-3.1	0.47	20.1
	CHIRP	0.5	7.4	0.4	-5.4
	PERSIANN	0.3	21.8	0.19	45.3
	3B42V7	0.51	4.6	0.41	25.1
	IMERGF_V6	0.68	4.9	0.61	-0.2
	CHIRPS	0.41	-14.1	0.39	-15.8
	PERSIANN_CDR	0.45	-2	0.49	6.8

Appendix 8 Performance measures (NSE and PBIAS) of monthly streamflow SWAT simulations, driven by different precipitation input datasets over the six basins of Vietnam. The evaluation period: Cal. Calibration (2002-2009), Val. Validation (2010-2017).

Basin	Rainfall Input	NSE_cal	PBIAS_cal (%)	NSE_val	PBIAS_val (%)
XL	Rain Gauge	0.80	-9.6	0.74	25
	3B42RT	0.82	1.7	0.82	1.5
	IMERGE_V6	0.75	17.8	0.82	6.4
	CHIRP	0.73	8.5	0.78	13
	PERSIANN	0.53	10	0.50	31.2
	3B42V7	0.86	-1.8	0.89	9.3
	IMERGF_V6	0.84	2.9	0.91	4.3
	CHIRPS	0.70	-0.1	0.78	10.3
	PERSIANN_CDR	0.77	16.2	0.86	6.7
LS	Rain Gauge	0.87	2.8	0.87	-9.7
	3B42RT	0.55	-13.9	0.61	-7
	IMERGE_V6	0.74	1.9	0.66	15.1
	CHIRP	0.53	16.8	0.52	7.7
	PERSIANN	0.33	4.7	0.34	28.1
	3B42V7	0.61	-7.3	0.71	-12.4
	IMERGF_V6	0.73	-10.7	0.75	3.3
	CHIRPS	0.6	0.4	0.67	3
	PERSIANN_CDR	0.55	-14.8	0.7	-3.9
HT	Rain Gauge	0.9	-0.3	0.89	-8.3
	3B42RT	0.53	-18.9	0.39	-38.3
	IMERGE_V6	0.57	-12.5	0.67	-5.3
	CHIRP	0.53	21.8	0.55	-10.8
	PERSIANN	0.24	-24.5	0.21	-20.9
	3B42V7	0.78	7.3	0.72	-7.8
	IMERGF_V6	0.77	7.6	0.74	-3.5
	CHIRPS	0.66	17	0.71	-8.8
	PERSIANN_CDR	0.65	4.5	0.64	-20.3
NK	Rain Gauge	0.90	10.1	0.96	4.1
	3B42RT	0.54	-18.7	0.52	-39.1
	IMERGE_V6	0.61	13.3	0.77	12.5
	CHIRP	0.71	18.1	0.72	5.6
	PERSIANN	0.24	45.3	0.11	49.6
	3B42V7	0.80	11.2	0.74	-3.6
	IMERGF_V6	0.77	13.7	0.83	-4.9
	CHIRPS	0.74	14.6	0.80	8.40
	PERSIANN_CDR	0.47	22.20	0.55	17.7
AC	Rain Gauge	0.96	9.8	0.88	-42.5

Basin	Rainfall Input	NSE_cal	PBIAS_cal (%)	NSE_val	PBIAS_val (%)
	3B42RT	0.14	56.3	0.42	35.1
	IMERGE_V6	0.45	44	0.67	16.2
	CHIRP	0.34	41.6	0.33	-0.7
	PERSIANN	-0.1	71.9	0.07	53
	3B42V7	0.48	45.1	0.64	16.8
	IMERGF_V6	0.47	45.6	0.70	2.3
	CHIRPS	0.57	15	0.42	-40.5
	PERSIANN_CDR	0.45	37.10	0.6	18.8
GS	Rain Gauge	0.8	-3.8	0.76	17.8
	3B42RT	0.71	9	0.79	-5.5
	IMERGE_V6	0.69	9.9	0.73	4
	CHIRP	0.65	-4.5	0.49	-12.2
	PERSIANN	0.51	0.5	0.54	21.8
	3B42V7	0.74	-6.6	0.84	4.9
	IMERGF_V6	0.80	-11.9	0.82	-3.3
	CHIRPS	0.72	0.3	0.74	-0.6
	PERSIANN_CDR	0.65	-15.80	0.78	-6.5

Appendix 9 Publications (peer-reviewed articles) per year related to topic of soil moisture data assimilation in hydrological model. We obtained this result through Web of science searching engine (https://www.webofscience.com/). Keywords are "soil moisture" + "data assimilation" + "hydrological model". Subjects are constraint as water resources or geosciences multidisciplinary or environmental sciences or remote. We also consider peer-reviewed articles only.

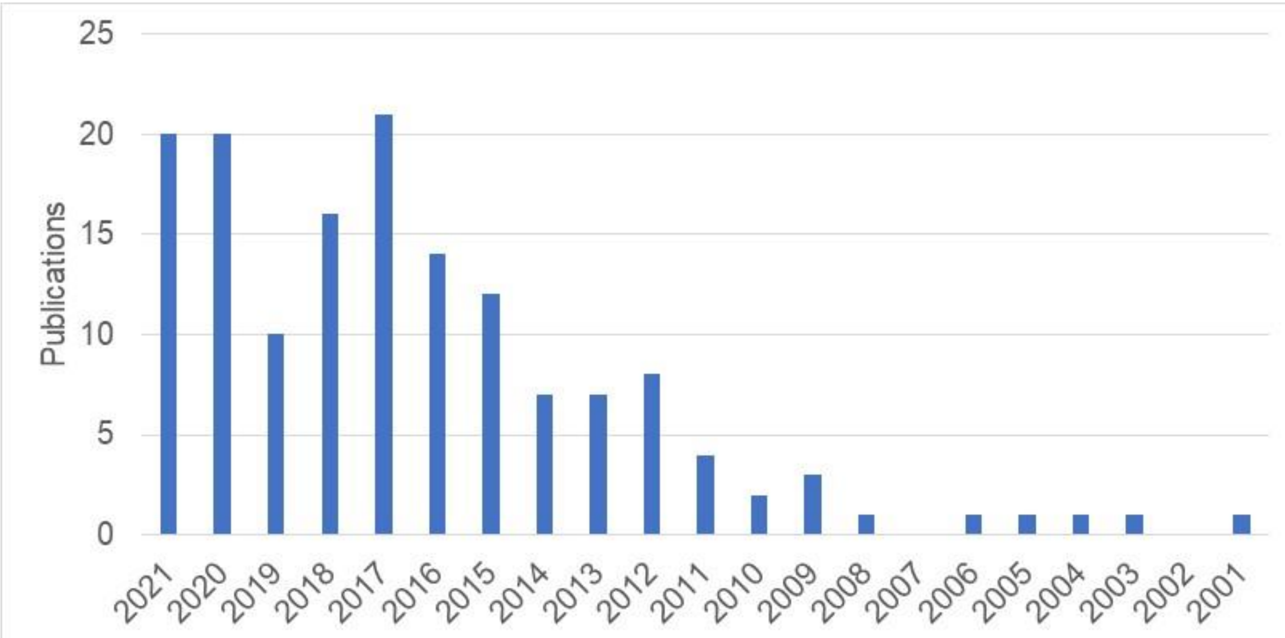

Appendix 10 The most currently studies (2015-present) on soil moisture data assimilation in hydrology using remotely sensed soil moisture as observed soil moisture in updating the model state variable. For studies that employed data assimilation framework for more than one catchment, approximately mean values of longitude and latitude is provided.

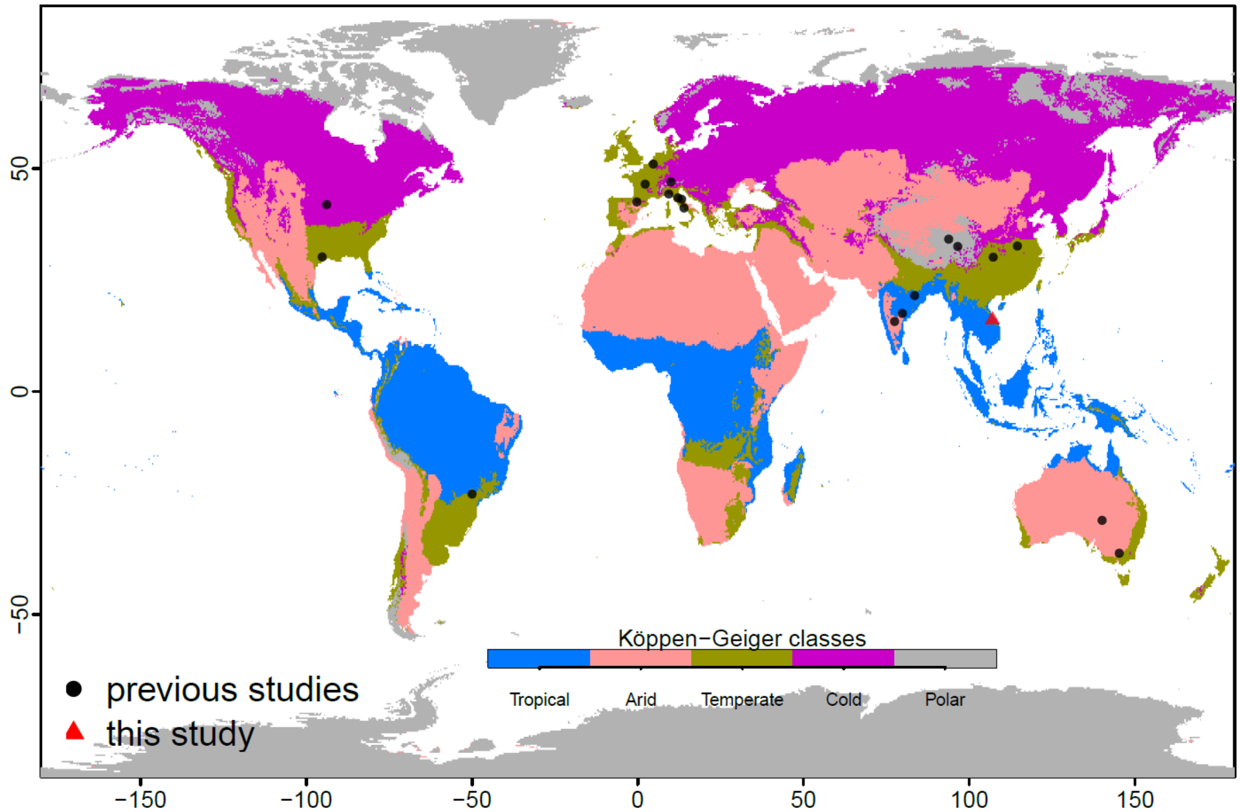

Appendix 11 Description of optimized SWAT model parameters for each basin.

Parameter Name	Default	gvo	aho	bye	slu	chu	gso	nka	xla
CN2.mgt	74	50	50	50	50	50	40	47	65
SURLAG.bsn	4	7.58	7.58	4	4	7.58	7	7	41.5
HRU_SLP.hru	0.217	0.212	0.215	0.21	0.217	0.217	0.025	0.217	0.096
GW_REVAP.gw	0.02	0.02	0.02	0.2	0.2	0.02	0.02	0.15	0.02
ESCO.hru	0.95	0.85	0.85	0.95	0.33	0.85	0.8	0.8	0.95
CH_N2.rte	0.014	0.1	0.1	0.1	0.1	0.1	0.1	0.1	0.28
CH_K2.rte	0	15	15	150	150	15	5	5	4.5
SOL_AWC(..).sol	0.1112	0.25	0.25	0.25	0.25	0.25	0.25	0.25	0.11
SOL_K(..).sol	7.113	7.1	7.1	7	7	7.1	7	7	6.83
ALPHA_BF.gw	0.048	0.9	0.95	0.95	0.95	0.9	0.9	0.9	0.56
GW_DELAY.gw	31	200	200	200	200	177	50	50	192
GWQMN.gw	1000	200	200	5000	5000	200	50	4000	1065
RCHRG_DP.gw	0.05	0.05	0.05	0.05	0.05	0.05	0.05	0.05	0.05

Appendix 12 Characteristics of climatic conditions and catchment attributes in eight studied catchments. The precipitation and potential evapotranspiration in each catchment are estimated from the calibrated SWAT model for the entire area of that catchment.

Types	Data Description	Spatial Resolution	gvo Benhai River	aho Trakhuc River	bye Namnua River	slu Luy River	chu LucNam River	gso Krong Ana River	nkh Hieu River	xla Ma River
Area (km²)			267	383	638	964	2,090	3,100	4,024	6,430
Dry Season/ Wet Season			I-VIII/ IX-XII	I-VIII/ IX-XII	XI-IV/ V-X	XI-IV/ V-X	XI-IV/ V-X	XII-IV/ V-XI	XII-V/ VI-XI	XI-IV/ V-X
Precipitation (unit in mm)	IMERG Final v6	~10km	1,911	2,165	1,644	1,577	1,807	1,798	1,755	1,629
Potential Evapotranspiration (unit in mm)	Hargreaves method with data from CFSR vs2	~25km	1,024	849	1,051	788	1,258	1,223	1,018	1,402
Digital Elevation (DEM) (unit in m)	HydroSHEDs	90m	Min: 10 Max: 1213 Mean: 215	Min: 19 Max: 1008 Mean: 366	Min: 470 Max: 1736 Mean: 945	Min: 25 Max: 1747 Mean: 451	Min: 7 Max: 1003 Mean: 248	Min: 407 Max: 2407 Mean: 658	Min: 33 Max: 2416 Mean: 396	Min: 282 Max: 2164 Mean: 958
Land use*	MODIS12Q1	500 m	FRSE (50.36) SHRB (47.18)	FRSE (67.10) SHRB (31.31)	FRSE (32.07) SHRB (63.75)	FRSE (46.15) CRGR (18.02) SHRB (16.97) FRSD (11.5)	SHRB (70.67) FRSE (27.84)	CRGR (41.10) SHRB (30.04) FRSE (26.51)	SHRB (45.94) FRSE (42.85)	SHRB (75.97) FRSE (18.44)
Soil**	HWSD	1km	Ao (100)	Ao (98.67)	Ao (100)	Ao (77.26) Lc (18.64)	Ao (92.95) Af (5.58)	Fr (39.62) Af (30.21) Ao (30.09)	Ao (98.85)	Ao (100)
Sub-basins, HRUs	10% soil, 10% land use, 10% slope		5 sub-basins 24 HRUs	9 sub-basins 50 HRUs	9 sub-basins 60 HRUs	17 sub-basins 116 HRUs	35 sub-basins 186 HRUs	59 sub-basins 314 HRUs	91 sub-basins 590 HRUs	125 sub-basins 579 HRUs

Note:

** Full name for land use- 'FRSE' Evergreen forests, 'FRSD' Deciduous forests, 'SHRB' shrubland, 'CRGR' cropland. Only major land use (>5% of total catchment area) or the first four major land use are listed. Values in blanket are percentage value over total catchment area.*

*** Full name for soil data- 'Ao' Orthic Acrisols, 'Af' Ferric Acrisols, 'Fr' Rhodic Ferralsols, 'Lc' Chromic Luvisol. Only major soil (>5% of total catchment area) or the first four major soil are listed. Values in blanket are percentage value over total catchment area.*

Appendix 13 Name, description, range and control processes of SWAT parameters. "r_", "v_", and "a_" refer to modify the default value by making a relative change to the default value, replacing the default value by the specific value and adding a specific value, respectively.

Parameter Name	Units	Description	Default	Range	Process
R_CN2.mgt	none	SCS runoff curve number	HRU specific	-0.25, +0.25	Surface Runoff
V_SURLAG.bsn	none	Surface runoff lag time	4	0.05, +24	Surface Runoff
R_HRU_SLP.hru	m/m	Average slope steepness	0.217	-0.25, +0.25	Surface Runoff
V_GW_REVAP.gw	none	Groundwater "revap" coefficient	0.02	0.02, +2	Evapotranspiration
V_ESCO.hru	none	Soil evaporation compensation factor	0.95	0, +1	Evapotranspiration
V_CH_N2.rte	none	Manning's "n" value for the main channel	0.014	0, +0.3	Channel
V_CH_K2.rte	mm/hr	Effective hydraulic conductivity in main channel alluvium	0	0, +500	Channel
R_SOL_AWC(..).sol	mm H_2O /mm soil	Available water capacity of the soil layer	0.1112	-0.25, +0.25	Soil
R_SOL_K(..).sol	mm/hr	Saturated hydraulic conductivity	7.113	-0.25, +0.25	Soil
V_ALPHA_BF.gw	days	Base flow alpha factor	0.048	0, +1	Groundwater
V_GW_DELAY.gw	days	Groundwater delay	31	0, +500	Groundwater
V_GWQMN.gw	mm H_2O	Threshold depth of water in the shallow aquifer required for return flow to occur	1000	0, +5000	Groundwater
V_RCHRG_DP.gw	None	Deep aquifer percolation fraction	0.05	0, +1	Groundwater

Appendix 14 Name, description and the range of perturbation defined errors of the EnKF data assimilation framework.

Perturbation variables	Description	Range
Observed soil moisture	Observed soil moisture coefficient	50–200
Precipitation	Precipitation error coefficient	0.1–1.0
Field capacity for soil layer 1	Field capacity for soil layer 1 coefficient	0.1-0.3
Field capacity for soil layer 2	Field capacity for soil layer 2 coefficient	0.05–0.2
Field capacity for soil layer 3	Field capacity for soil layer 3 coefficient	0.01–0.1
Soil moisture layer 1	Soil moisture error standard deviation for layer 1	0.01–0.1
Soil moisture layer 2	Soil moisture error standard deviation for layer 2	0.01–0.1
Soil moisture layer 3	Soil moisture error standard deviation for layer 3	0.01–0.1
Curve number	Curve number error standard	1–5

Appendix 15 Available soil moisture (grey rectangular) for SMAP 9km (SM9) and downscaled SMAP 1km (SM1) at each catchment during 2017–2019. The y-axis label is written as hydrological station name and soil moisture products. An available soil moisture day is counted as at least 30% of basin area has soil moisture pixels.

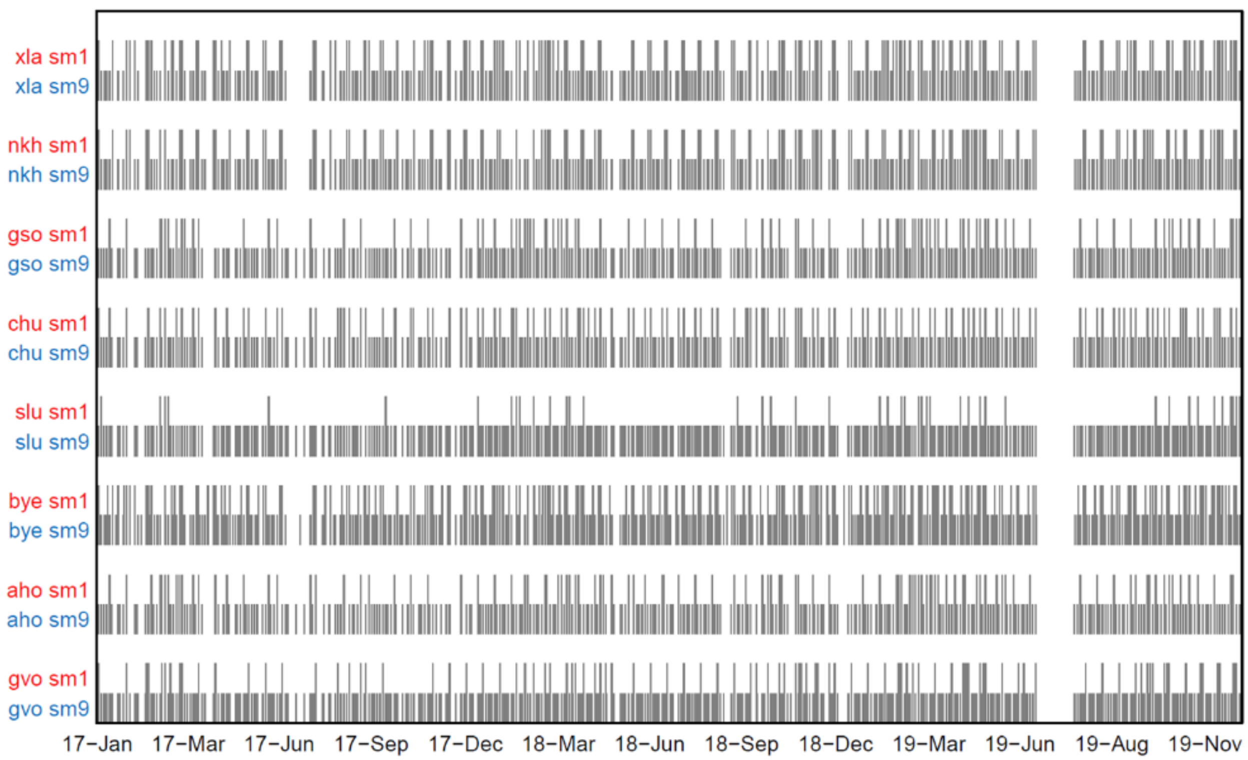

Appendix 16 Description of optimized SWAT model parameters for each basin.

Parameter Name	Default	gvo	aho	bye	slu	chu	gso	nka	xla
CN2.mgt	74	50	50	50	50	50	40	47	65
SURLAG.bsn	4	7.58	7.58	4	4	7.58	7	7	41.5
HRU_SLP.hru	0.217	0.212	0.215	0.21	0.217	0.217	0.025	0.217	0.096
GW_REVAP.gw	0.02	0.02	0.02	0.2	0.2	0.02	0.02	0.15	0.02
ESCO.hru	0.95	0.85	0.85	0.95	0.33	0.85	0.8	0.8	0.95
CH_N2.rte	0.014	0.1	0.1	0.1	0.1	0.1	0.1	0.1	0.28
CH_K2.rte	0	15	15	150	150	15	5	5	4.5
SOL_AWC(..).sol	0.1112	0.25	0.25	0.25	0.25	0.25	0.25	0.25	0.11
SOL_K(..).sol	7.113	7.1	7.1	7	7	7.1	7	7	6.83
ALPHA_BF.gw	0.048	0.9	0.95	0.95	0.95	0.9	0.9	0.9	0.56
GW_DELAY.gw	31	200	200	200	200	177	50	50	192
GWQMN.gw	1000	200	200	5000	5000	200	50	4000	1065
RCHRG_DP.gw	0.05	0.05	0.05	0.05	0.05	0.05	0.05	0.05	0.05

Appendix 17 Description of best guess error defined values for EnKF-SM9 model for each basin.

Error defined	gvo	aho	bye	slu	chu	gso	nkh	xla
Observed soil moisture coefficient	120	80	80	180	120	120	100	200
Precipitation error coefficient	1	1	1	1	0.2	0.5	0.1	1
Field capacity for soil layer 1 coefficient	0.45	0.3	0.3	0.45	0.45	0.3	0.45	0.3
Field capacity for soil layer 2 coefficient	0.1	0.1	0.1	0.1	0.1	0.1	0.1	0.1
Field capacity for soil layer 3 coefficient	0.05	0.05	0.05	0.05	0.05	0.05	0.05	0.05
Soil moisture error standard deviation for layer 1	0.02	0.02	0.02	0.02	0.02	0.02	0.02	0.02
Soil moisture error standard deviation for layer 2	0.02	0.02	0.02	0.02	0.02	0.02	0.02	0.02
Soil moisture error standard deviation for layer 3	0.02	0.02	0.02	0.02	0.02	0.02	0.02	0.02
Curve number error standard	1	1	1	3	1	1	1	1

Appendix 18 Description of best guess error defined values for EnKF-SM1 model for each basin.

Error defined	gvo	aho	bye	slu	chu	gso	nkh	xla
Observed soil moisture coefficient	30	50	120	180	200	120	80	200
Precipitation error coefficient	1	1	0.5	1	0.2	0.5	0.5	0.5
Field capacity for soil layer 1 coefficient	0.45	0.3	0.3	0.45	0.45	0.3	0.45	0.3
Field capacity for soil layer 2 coefficient	0.1	0.1	0.1	0.1	0.1	0.1	0.1	0.1
Field capacity for soil layer 3 coefficient	0.05	0.05	0.05	0.05	0.05	0.05	0.05	0.05
Soil moisture error standard deviation for layer 1	0.02	0.02	0.02	0.02	0.01	0.02	0.02	0.02
Soil moisture error standard deviation for layer 2	0.02	0.02	0.02	0.02	0.02	0.02	0.02	0.02
Soil moisture error standard deviation for layer 3	0.02	0.02	0.02	0.02	0.02	0.02	0.02	0.02
Curve number error standard	5	1	1	3	1	1	1	1

Appendix 19 Relationship between the efficiency index and available soil moisture with the Q_{nor} time series.

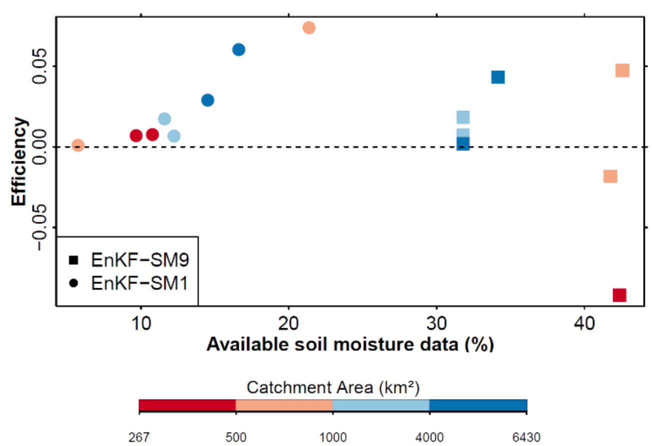

References

Abbaspour, K.C., 2013. SWAT-CUP 2012. SWAT Calibration and Uncertainty Program—A User Manual.

Abbaspour, K.C. et al., 2015. A continental-scale hydrology and water quality model for Europe: Calibration and uncertainty of a high-resolution large-scale SWAT model. Journal of Hydrology, 524: 733-752.

Abbaspour, K.C. et al., 2007. Modelling hydrology and water quality in the pre-alpine/alpine Thur watershed using SWAT. Journal of hydrology, 333(2-4): 413-430.

Abbaszadeh, P., Gavahi, K., Moradkhani, H., 2020. Multivariate remotely sensed and in-situ data assimilation for enhancing community WRF-Hydro model forecasting. Advances in Water Resources, 145: 103721.

Adjei, K.A., Ren, L., Appiah-Adjei, E.K., Odai, S.N., 2015. Application of satellite-derived rainfall for hydrological modelling in the data-scarce Black Volta trans-boundary basin. Hydrology Research, 46(5): 777-791.

Ahamed, A., Bolten, J.D., 2017. A MODIS-based automated flood monitoring system for southeast asia. International journal of applied earth observation and geoinformation, 61: 104-117.

Ahmad, S., Kalra, A., Stephen, H., 2010. Estimating soil moisture using remote sensing data: A machine learning approach. Advances in water resources, 33(1): 69-80.

Alazzy, A.A. et al., 2017. Evaluation of satellite precipitation products and their potential influence on hydrological modeling over the Ganzi river basin of the Tibetan Plateau. Advances in Meteorology, 2017.

Alijanian, M., Rakhshandehroo, G.R., Mishra, A.K., Dehghani, M., 2017. Evaluation of satellite rainfall climatology using CMORPH, PERSIANN-CDR, PERSIANN, TRMM, MSWEP over Iran. International Journal of Climatology, 37(14): 4896-4914.

Almazroui, M., 2011. Calibration of TRMM rainfall climatology over Saudi Arabia during 1998–2009. Atmospheric Research, 99(3-4): 400-414.

Arnold, J.G., Srinivasan, R., Muttiah, R.S., Williams, J.R., 1998. Large area hydrologic modeling and assessment part I: model development 1. JAWRA Journal of the American Water Resources Association, 34(1): 73-89.

Arsenault, K.R. et al., 2018. The Land surface Data Toolkit (LDT v7. 2)–a data fusion environment for land data assimilation systems. Geoscientific Model Development, 11(9): 3605-3621.

Arvor, D., Dubreuil, V., Ronchail, J., Simões, M., Funatsu, B.M., 2014. Spatial patterns of rainfall regimes related to levels of double cropping agriculture systems in Mato Grosso (Brazil). International Journal of Climatology, 34(8): 2622-2633.

Ashouri, H. et al., 2015. PERSIANN-CDR: Daily precipitation climate data record from multisatellite observations for hydrological and climate studies. Bulletin of the American Meteorological Society, 96(1): 69-83.

Azimi, S. et al., 2020. Assimilation of Sentinel 1 and SMAP–based satellite soil moisture retrievals into SWAT hydrological model: the impact of satellite revisit time and product spatial resolution on flood simulations in small basins. Journal of hydrology, 581: 124367.

Baguis, P., Roulin, E., 2017. Soil moisture data assimilation in a hydrological model: a case study in Belgium using large-scale satellite data. Remote Sensing, 9(8): 820.

Bai, J., Cui, Q., Zhang, W., Meng, L., 2019. An approach for downscaling SMAP soil moisture by combining Sentinel-1 SAR and MODIS data. Remote Sensing, 11(23): 2736.

Bai, L., Shi, C., Li, L., Yang, Y., Wu, J., 2018. Accuracy of CHIRPS satellite-rainfall products over mainland China. Remote Sensing, 10(3): 362.

Bartalis, Z. et al., 2007. Initial soil moisture retrievals from the METOP-A Advanced Scatterometer (ASCAT). Geophysical Research Letters, 34(20).

Beck, H.E. et al., 2018. Daily evaluation of 26 precipitation datasets using Stage-IV gauge-radar data for the CONUS. Hydrol. Earth Syst. Sci. Discuss.

Beck, H.E. et al., 2017a. MSWEP: 3-hourly 0.25 global gridded precipitation (1979-2015) by merging gauge, satellite, and reanalysis data. Hydrology and Earth System Sciences, 21(1): 589.
Beck, H.E. et al., 2017b. Global-scale evaluation of 22 precipitation datasets using gauge observations and hydrological modeling. Hydrology and Earth System Sciences, 21(12): 6201-6217.
Behera, S.S., Nikam, B.R., Babel, M.S., Garg, V., Aggarwal, S.P., 2019. The Assimilation of Remote Sensing-Derived Soil Moisture Data into a Hydrological Model for the Mahanadi Basin, India. Journal of the Indian Society of Remote Sensing, 47(8): 1357-1374.
Billah, M.M. et al., 2015. A methodology for evaluating evapotranspiration estimates at the watershed-scale using GRACE. Journal of Hydrology, 523: 574-586.
Blöschl, G., 2013. Runoff prediction in ungauged basins: synthesis across processes, places and scales. Cambridge University Press.
Bolten, J.D., Crow, W.T., Zhan, X., Jackson, T.J., Reynolds, C.A., 2009. Evaluating the utility of remotely sensed soil moisture retrievals for operational agricultural drought monitoring. IEEE Journal of Selected Topics in Applied Earth Observations and Remote Sensing, 3(1): 57-66.
Borgomeo, E. et al., 2018. The Water-Energy-Food Nexus in the Middle East and North Africa.
Brutsaert, W., 2005. Hydrology: an introduction. Cambridge University Press.
Busch, F.A., Niemann, J.D., Coleman, M., 2012. Evaluation of an empirical orthogonal function–based method to downscale soil moisture patterns based on topographical attributes. Hydrological Processes, 26(18): 2696-2709.
Cao, Y., Zhang, W., Wang, W., 2018. Evaluation of TRMM 3B43 data over the Yangtze River Delta of China. Scientific Reports, 8(1): 5290.
Cashion, J., Lakshmi, V., Bosch, D., Jackson, T.J., 2005. Microwave remote sensing of soil moisture: evaluation of the TRMM microwave imager (TMI) satellite for the Little River Watershed Tifton, Georgia. Journal of Hydrology, 307(1-4): 242-253.
Chen, H., Sun, J., 2015. Changes in Drought Characteristics over China Using the Standardized Precipitation Evapotranspiration Index. Journal of Climate, 28(13): 5430-5447. DOI:10.1175/jcli-d-14-00707.1
Curtarelli, M.P., Rennó, C.D., Alcântara, E.H., 2014. Evaluation of the Tropical Rainfall Measuring Mission 3B43 product over an inland area in Brazil and the effects of satellite boost on rainfall estimates. Journal of Applied Remote Sensing, 8(1): 083589.
Dai, A., 2011. Drought under global warming: a review. Wiley Interdisciplinary Reviews: Climate Change, 2(1): 45-65.
Dandridge, C., Fang, B., Lakshmi, V., 2020. Downscaling of SMAP Soil Moisture in the Lower Mekong River Basin. Water, 12(1): 56.
Dang Dinh Duc, 2017. Assessment current situation and possibility of exploting satellite rainfall for flood forecasting- an application for Chu River Basin. Journal of Climate Change Science (in Vietnamese).
De Santis, D. et al., 2021. Assimilation of Satellite Soil Moisture Products for River Flow Prediction: An Extensive Experiment in over 700 Catchments throughout Europe. Water Resources Research: e2021WR029643.
Diem, J.E., Ryan, S.J., Hartter, J., Palace, M.W., 2014. Satellite-based rainfall data reveal a recent drying trend in central equatorial Africa. Climatic Change, 126(1-2): 263-272.
Dile, Y.T., Daggupati, P., George, C., Srinivasan, R., Arnold, J., 2016. Introducing a new open source GIS user interface for the SWAT model. Environmental modelling & software, 85: 129-138.
Do H, X., Le -H, M., Pham H, T., Le H, T., Nguyen B, Q., 2022. Identifying hydrologic reference stations to understand changes in water resources across Vietnam - a data-driven approach. Vietnam Journal of Earth Sciences, 44(1): 145-165. DOI:10.15625/2615-9783/16980
Do, H.X., Gudmundsson, L., Leonard, M., Westra, S., 2018. The Global Streamflow Indices and Metadata Archive (GSIM)–Part 1: The production of a daily streamflow archive and metadata. Earth System Science Data, 10(2): 765-785.
Dorigo, W. et al., 2021. The International Soil Moisture Network: serving Earth system science for over a decade. Hydrology and Earth System Sciences Discussions: 1-83.
Drzik, J., Eide, E.B., Lehmann, A., 2015. The Global Risks 2015 The World Economic Forum.

Du, T.L.T. et al., 2020. Streamflow prediction in "geopolitically ungauged" basins using satellite observations and regionalization at subcontinental scale. Journal of Hydrology: 125016. DOI:https://doi.org/10.1016/j.jhydrol.2020.125016
Duan, Z. et al., 2018. Hydrological evaluation of open-access precipitation and air temperature datasets using SWAT in a poorly gauged basin in Ethiopia. Journal of Hydrology.
Ebert, E.E., Janowiak, J.E., Kidd, C., 2007. Comparison of near-real-time precipitation estimates from satellite observations and numerical models. Bulletin of the American Meteorological Society, 88(1): 47-64.
Emmanuel, I., Andrieu, H., Leblois, E., Flahaut, B., 2012. Temporal and spatial variability of rainfall at the urban hydrological scale. Journal of hydrology, 430: 162-172.
Entekhabi, D. et al., 2010. The soil moisture active passive (SMAP) mission. Proceedings of the IEEE, 98(5): 704-716.
Evensen, G., 2003. The ensemble Kalman filter: Theoretical formulation and practical implementation. Ocean dynamics, 53(4): 343-367.
Fang, B., Kansara, P., Dandridge, C., Lakshmi, V., 2021. Drought monitoring using high spatial resolution soil moisture data over Australia in 2015–2019. Journal of Hydrology, 594: 125960.
Fang, B., Lakshmi, V., Bindlish, R., Jackson, T.J., 2018a. AMSR2 soil moisture downscaling using temperature and vegetation data. Remote Sensing, 10(10): 1575.
Fang, B., Lakshmi, V., Bindlish, R., Jackson, T.J., 2018b. Downscaling of SMAP soil moisture using land surface temperature and vegetation data. Vadose Zone Journal, 17(1): 1-15.
Fang, B. et al., 2013. Passive microwave soil moisture downscaling using vegetation index and skin surface temperature. Vadose Zone Journal, 12(3).
Fang, B., Lakshmi, V., Bindlish, R., Jackson, T.J., Liu, P.-W., 2020. Evaluation and validation of a high spatial resolution satellite soil moisture product over the Continental United States. Journal of Hydrology, 588: 125043.
Fang, B. et al., 2022. A global 1-km downscaled SMAP soil moisture product based on thermal inertia theory. Vadose Zone Journal: e20182.
Fang, B., Lakshmi, V., Jackson, T.J., Bindlish, R., Colliander, A., 2019. Passive/active microwave soil moisture change disaggregation using SMAPVEX12 data. Journal of hydrology, 574: 1085-1098.
Fleischmann, A.S. et al., 2021. Synergistic Calibration of a Hydrological Model Using Discharge and Remotely Sensed Soil Moisture in the Paraná River Basin. Remote Sensing, 13(16): 3256.
Friedl, M., Sulla-Menashe, D., 2019. MCD12Q1 MODIS/Terra+Aqua Land Cover Type Yearly L3 Global 500m SIN Grid V006 [Data set]. In: DAAC., N.E.L.P. (Ed.).
Funk, C. et al., 2015. The climate hazards infrared precipitation with stations—a new environmental record for monitoring extremes. Scientific data, 2: 150066.
Funk, C.C. et al., 2014. A quasi-global precipitation time series for drought monitoring. US Geological Survey Data Series, 832(4).
Ganguli, P., Ganguly, A.R., 2016. Space-time trends in US meteorological droughts. Journal of Hydrology: Regional Studies, 8: 235-259.
García, L., Rodríguez, D., Wijnen, M., Pakulski, I., 2016. Earth observation for water resources management: current use and future opportunities for the water sector. World Bank Publications.
Gelaro, R. et al., 2017. The modern-era retrospective analysis for research and applications, version 2 (MERRA-2). Journal of Climate, 30(14): 5419-5454.
Gerlak, A.K., Lautze, J., Giordano, M., 2011. Water resources data and information exchange in transboundary water treaties. International Environmental Agreements: Politics, Law and Economics, 2(11).
Gocic, M., Trajkovic, S., 2014. Analysis of trends in reference evapotranspiration data in a humid climate. Hydrological Sciences Journal, 59(1): 165-180.
Golian, S., Javadian, M., Behrangi, A., 2019. On the use of satellite, gauge, and reanalysis precipitation products for drought studies. Environmental Research Letters, 14(7): 075005.
Grayson, R.B., Western, A.W., Chiew, F.H.S., Blöschl, G., 1997. Preferred states in spatial soil moisture patterns: Local and nonlocal controls. Water resources research, 33(12): 2897-2908.
Greve, P. et al., 2014. Global assessment of trends in wetting and drying over land. Nature geoscience, 7(10): 716-721.

Gupta, H.V., Sorooshian, S., Yapo, P.O., 1999. Status of automatic calibration for hydrologic models: Comparison with multilevel expert calibration. Journal of Hydrologic Engineering, 4(2): 135-143.
Ha, L.T., Bastiaanssen, W.G., Griensven, A.v., Van Dijk, A.I., Senay, G.B., 2018. Calibration of Spatially Distributed Hydrological Processes and Model Parameters in SWAT Using Remote Sensing Data and an Auto-Calibration Procedure: A Case Study in a Vietnamese River Basin. Water, 10(2): 212.
Ha, L.T., Bastiaanssen, W.G.M., van Griensven, A., van Dijk, A.I.J.M., Senay, G.B., 2017. SWAT-CUP for calibration of spatially distributed hydrological processes and ecosystem services in a Vietnamese river basin using remote sensing. Hydrology and Earth System Sciences Discussions: 1-35.
Han, X., Li, X., Hendricks Franssen, H.J., Vereecken, H., Montzka, C., 2012. Spatial horizontal correlation characteristics in the land data assimilation of soil moisture. Hydrology and Earth System Sciences, 16(5): 1349-1363.
Hargreaves, G.H., Samani, Z.A., 1982. Estimating potential evapotranspiration. Journal of the irrigation and Drainage Division, 108(3): 225-230.
Hashemi, H., Nordin, M., Lakshmi, V., Huffman, G.J., Knight, R., 2017. Bias Correction of Long-Term Satellite Monthly Precipitation Product (TRMM 3B43) over the Conterminous United States. Journal of Hydrometeorology, 18(9): 2491-2509.
He, Z. et al., 2017. Intercomparisons of Rainfall Estimates from TRMM and GPM Multisatellite Products over the Upper Mekong River Basin. Journal of Hydrometeorology, 18(2): 413-430.
Herold, N., Kala, J., Alexander, L., 2016. The influence of soil moisture deficits on Australian heatwaves. Environmental Research Letters, 11(6): 064003.
Hiep, N.H. et al., 2018. Hydrological model using ground-and satellite-based data for river flow simulation towards supporting water resource management in the Red River Basin, Vietnam. Journal of environmental management, 217: 346-355.
Hirsch, R.M., Slack, J.R., 1984. A nonparametric trend test for seasonal data with serial dependence. Water Resources Research, 20(6): 727-732.
Hoc, D., 2002. Drought and its mitigation measures. Agricultural Publishing House, Hanoi, Vietnam.
Hoerling, M. et al., 2012. On the increased frequency of Mediterranean drought. Journal of climate, 25(6): 2146-2161.
Hong, S., Lakshmi, V., Small, E.E., 2007. Relationship between vegetation biophysical properties and surface temperature using multisensor satellite data. Journal of climate, 20(22): 5593-5606.
Hong, Y., Adler, R.F., Huffman, G.J., Pierce, H., 2010. Applications of TRMM-based multi-satellite precipitation estimation for global runoff prediction: Prototyping a global flood modeling system, Satellite rainfall applications for surface hydrology. Springer, pp. 245-265.
Hou, A.Y. et al., 2014. The global precipitation measurement mission. Bulletin of the American Meteorological Society, 95(5): 701-722.
Hu, Q. et al., 2014. Multi-scale evaluation of six high-resolution satellite monthly rainfall estimates over a humid region in China with dense rain gauges. International Journal of Remote Sensing, 35(4): 1272-1294.
Huffman, G.J., 2016. The Transition in Multi-Satellite Products from TRMM to GPM (TMPA to IMERG), NASA/GSFC Code.
Huffman, G.J., Bolvin, D.T., 2013. TRMM and other data precipitation data set documentation. NASA, Greenbelt, USA, 28.
Huffman, G.J. et al., 2014. NASA global precipitation measurement (GPM) integrated multi-satellite retrievals for GPM (IMERG). Algorithm theoretical basis document, version, 4: 30.
Huffman, G.J., Bolvin, D.T., Nelkin, E.J., 2018. Integrated Multi-satellitE Retrievals for GPM (IMERG) technical documentation. NASA/GSFC Code, 612(2018): 47.
Huffman, G.J. et al., 2007. The TRMM multisatellite precipitation analysis (TMPA): Quasi-global, multiyear, combined-sensor precipitation estimates at fine scales. Journal of Hydrometeorology, 8(1): 38-55.
Hulton, G., 2012. Global costs and benefits of drinking-water supply and sanitation interventions to reach the MDG target and universal coverage, World Health Organization.
Imaoka, K. et al., 2010. Global Change Observation Mission (GCOM) for monitoring carbon, water cycles, and climate change. Proceedings of the IEEE, 98(5): 717-734.

Jadidoleslam, N., Mantilla, R., Krajewski, W.F., 2021. Data Assimilation of Satellite-Based Soil Moisture into a Distributed Hydrological Model for Streamflow Predictions. Hydrology, 8(1): 52.
Joshi, S., Garbrecht, J., Brown, D., 2019. Observed Spatiotemporal Trends in Intense Precipitation Events across United States: Applications for Stochastic Weather Generation. Climate, 7(3): 36.
Joyce, R.J., Janowiak, J.E., Arkin, P.A., Xie, P., 2004. CMORPH: A method that produces global precipitation estimates from passive microwave and infrared data at high spatial and temporal resolution. Journal of Hydrometeorology, 5(3): 487-503.
Jung, H.C. et al., 2017. Upper Blue Nile basin water budget from a multi-model perspective. Journal of hydrology, 555: 535-546.
Justice, C.O. et al., 1998. The Moderate Resolution Imaging Spectroradiometer (MODIS): Land remote sensing for global change research. IEEE transactions on geoscience and remote sensing, 36(4): 1228-1249.
Kansara, P., Lakshmi, V., 2021. Estimation of land-cover linkage to trends in hydrological variables of river basins in the Indian sub-continent using satellite observation and model outputs. Journal of Hydrology, 603: 126997.
Kawanishi, T. et al., 2003. The Advanced Microwave Scanning Radiometer for the Earth Observing System (AMSR-E), NASDA's contribution to the EOS for global energy and water cycle studies. IEEE Transactions on Geoscience and Remote Sensing, 41(2): 184-194.
Kawase, H. et al., 2010. Physical mechanism of long-term drying trend over tropical North Africa. Geophysical research letters, 37(9).
Kendall, M.G., 1938. A new measure of rank correlation. Biometrika, 30(1/2): 81-93.
Kerr, Y.H. et al., 2001. Soil moisture retrieval from space: The Soil Moisture and Ocean Salinity (SMOS) mission. IEEE transactions on Geoscience and remote sensing, 39(8): 1729-1735.
Kha, D.D., Nhu, N.Y., Long, V.V., Van, D.T.H., 2020. Utility of GSMaP precipitation and point scale in gauge measurements for stream flow modelling–a case study in Lam River Basin, Vietnam. Journal of Ecological Engineering, 21(2).
Khan, S.I. et al., 2014. Evaluation of three high-resolution satellite precipitation estimates: Potential for monsoon monitoring over Pakistan. Advances in Space Research, 54(4): 670-684.
Kidd, C., 2001. Satellite rainfall climatology: A review. International Journal of Climatology, 21(9): 1041-1066.
Kim, H., Lakshmi, V., 2018. Use of Cyclone Global Navigation Satellite System (CYGNSS) observations for estimation of soil moisture. Geophysical Research Letters, 45(16): 8272-8282.
Kim, H. et al., 2018. Global-scale assessment and combination of SMAP with ASCAT (active) and AMSR2 (passive) soil moisture products. Remote Sensing of Environment, 204: 260-275.
Kim, K., Park, J., Baik, J., Choi, M., 2017. Evaluation of topographical and seasonal feature using GPM IMERG and TRMM 3B42 over Far-East Asia. Atmospheric Research, 187: 95-105.
Kim, S., Zhang, R., Pham, H., Sharma, A., 2019. A Review of Satellite-Derived Soil Moisture and Its Usage for Flood Estimation. Remote Sensing in Earth Systems Sciences: 1-22.
Kling, H., Fuchs, M., Paulin, M., 2012. Runoff conditions in the upper Danube basin under an ensemble of climate change scenarios. Journal of Hydrology, 424: 264-277.
Kneis, D., Chatterjee, C., Singh, R., 2014. Evaluation of TRMM rainfall estimates over a large Indian river basin (Mahanadi). Hydrology and Earth System Sciences, 18(7): 2493-2502.
Krishnan, R. et al., 2016. Deciphering the desiccation trend of the South Asian monsoon hydroclimate in a warming world. Climate Dynamics, 47(3-4): 1007-1027.
Kumagai, T.o., Yoshifuji, N., Tanaka, N., Suzuki, M., Kume, T., 2009. Comparison of soil moisture dynamics between a tropical rain forest and a tropical seasonal forest in Southeast Asia: Impact of seasonal and year-to-year variations in rainfall. Water Resources Research, 45(4).
Kumar, B., Lakshmi, V., 2018. Accessing the capability of TRMM 3B42 V7 to simulate streamflow during extreme rain events: Case study for a Himalayan River Basin. Journal of Earth System Science, 127(2): 27.
Kumar, S.V. et al., 2006. Land information system: An interoperable framework for high resolution land surface modeling. Environmental modelling & software, 21(10): 1402-1415.

Laiolo, P. et al., 2016. Impact of different satellite soil moisture products on the predictions of a continuous distributed hydrological model. International Journal of Applied Earth Observation and Geoinformation, 48: 131-145.
Lakshmi, V., 2013. Remote sensing of soil moisture. ISRN Soil Science, 2013.
Lakshmi, V., Fayne, J., Bolten, J., 2018. A comparative study of available water in the major river basins of the world. Journal of Hydrology, 567: 510-532.
Lakshmi, V., Hong, S., Small, E.E., Chen, F., 2011. The influence of the land surface on hydrometeorology and ecology: new advances from modeling and satellite remote sensing. Hydrology Research, 42(2-3): 95-112.
Le, A., Pricope, N., 2017. Increasing the Accuracy of Runoff and Streamflow Simulation in the Nzoia Basin, Western Kenya, through the Incorporation of Satellite-Derived CHIRPS Data. Water, 9(2): 114.
Le, H., Sutton, J., Bui, D., Bolten, J., Lakshmi, V., 2018. Comparison and Bias Correction of TMPA Precipitation Products over the Lower Part of Red–Thai Binh River Basin of Vietnam. Remote Sensing, 10(10): 1582.
Le, H.M. et al., 2019a. A Comparison of Spatial–Temporal Scale Between Multiscalar Drought Indices in the South Central Region of Vietnam, Spatiotemporal Analysis of Extreme Hydrological Events. Elsevier, pp. 143-169.
Le, M.-H., Lakshmi, V., Bolten, J., Bui, D.D., 2020a. Adequacy of Satellite-derived Precipitation Estimate for Hydrological Modeling in Vietnam Basins. Journal of Hydrology, 586: 124820. DOI:https://doi.org/10.1016/j.jhydrol.2020.124820
Le, M.-H., Lakshmi, V., Bolten, J., Du Bui, D., 2020b. Adequacy of Satellite-derived Precipitation Estimate for Hydrological modeling in Vietnam Basins. Journal of Hydrology: 124820.
Le, P.V., Phan-Van, T., Mai, K.V., Tran, D.Q., 2019b. Space–time variability of drought over Vietnam. International Journal of Climatology, 39(14): 5437-5451.
Legates, D.R., McCabe, G.J., 1999. Evaluating the use of "goodness-of-fit" measures in hydrologic and hydroclimatic model validation. Water Resources Research, 35(1): 233-241.
Lehner, B., 2012. Derivation of watershed boundaries for GRDC gauging stations based on the HydroSHEDS drainage network (GRDC Report Series- report 41).
Lehner, B., Verdin, K., Jarvis, A., 2008. New global hydrography derived from spaceborne elevation data. Eos, Transactions American Geophysical Union, 89(10): 93-94.
Lenderink, G., Buishand, A., Deursen, W.v., 2007. Estimates of future discharges of the river Rhine using two scenario methodologies: direct versus delta approach. Hydrology and Earth System Sciences, 11(3): 1145-1159.
Lettenmaier, D.P. et al., 2015. Inroads of remote sensing into hydrologic science during the WRR era. Water Resources Research, 51(9): 7309-7342.
Li, D., Christakos, G., Ding, X., Wu, J., 2018a. Adequacy of TRMM satellite rainfall data in driving the SWAT modeling of Tiaoxi catchment (Taihu lake basin, China). Journal of hydrology, 556: 1139-1152.
Li, X., Zhou, Y., Asrar, G.R., Zhu, Z., 2018b. Creating a seamless 1 km resolution daily land surface temperature dataset for urban and surrounding areas in the conterminous United States. Remote Sensing of Environment, 206: 84-97.
Li, Y. et al., 2019. Evaluation of Three Satellite-Based Precipitation Products Over the Lower Mekong River Basin Using Rain Gauge Observations and Hydrological Modeling. IEEE Journal of Selected Topics in Applied Earth Observations and Remote Sensing.
Li, Z. et al., 2015. Multiscale hydrologic applications of the latest satellite precipitation products in the Yangtze River Basin using a distributed hydrologic model. Journal of Hydrometeorology, 16(1): 407-426.
Lievens, H. et al., 2015. SMOS soil moisture assimilation for improved hydrologic simulation in the Murray Darling Basin, Australia. Remote Sensing of Environment, 168: 146-162.
Liu, X., Yang, T., Hsu, K., Liu, C., Sorooshian, S., 2017. Evaluating the streamflow simulation capability of PERSIANN-CDR daily rainfall products in two river basins on the Tibetan Plateau. Hydrology and Earth System Sciences, 21(1): 169.
Liu, Y., Wang, W., Liu, Y., 2018. ESA CCI soil moisture assimilation in SWAT for improved hydrological simulation in upper Huai river basin. Advances in Meteorology, 2018.

Lobligeois, F., Andréassian, V., Perrin, C., Tabary, P., Loumagne, C., 2014. When does higher spatial resolution rainfall information improve streamflow simulation? An evaluation using 3620 flood events. Hydrology and Earth System Sciences, 18(2): p. 575-p. 594.
Loizu, J. et al., 2018. On the assimilation set-up of ASCAT soil moisture data for improving streamflow catchment simulation. Advances in Water Resources, 111: 86-104.
López-Moreno, J.I. et al., 2013. Hydrological response to climate variability at different time scales: A study in the Ebro basin. Journal of Hydrology, 477: 175-188. DOI:https://doi.org/10.1016/j.jhydrol.2012.11.028
Lorenz, C., Kunstmann, H., 2012. The hydrological cycle in three state-of-the-art reanalyses: Intercomparison and performance analysis. Journal of Hydrometeorology, 13(5): 1397-1420.
Lü, H., Crow, W.T., Zhu, Y., Ouyang, F., Su, J., 2016. Improving streamflow prediction using remotely-sensed soil moisture and snow depth. Remote sensing, 8(6): 503.
Lü, H., Crow, W.T., Zhu, Y., Yu, Z., Sun, J., 2015. The impact of assumed error variances on surface soil moisture and snow depth hydrologic data assimilation. IEEE Journal of Selected Topics in Applied Earth Observations and Remote Sensing, 8(11): 5116-5129.
Luo, X., Wu, W., He, D., Li, Y., Ji, X., 2019. Hydrological Simulation Using TRMM and CHIRPS Precipitation Estimates in the Lower Lancang-Mekong River Basin. Chinese Geographical Science, 29(1): 13-25.
Mann, H.B., 1945. Nonparametric tests against trend. Econometrica: Journal of the Econometric Society: 245-259.
Massari, C., Brocca, L., Tarpanelli, A., Moramarco, T., 2015. Data assimilation of satellite soil moisture into rainfall-runoff modelling: A complex recipe? Remote Sensing, 7(9): 11403-11433.
Matgen, P. et al., 2012. Can ASCAT-derived soil wetness indices reduce predictive uncertainty in well-gauged areas? A comparison with in situ observed soil moisture in an assimilation application. Advances in Water Resources, 44: 49-65.
Mazdiyasni, O., AghaKouchak, A., 2015. Substantial increase in concurrent droughts and heatwaves in the United States. Proceedings of the National Academy of Sciences, 112(37): 11484-11489.
McCabe, M.F. et al., 2017. The future of Earth observation in hydrology. Hydrology and earth system sciences, 21(7): 3879.
McCarty, W. et al., 2016. MERRA-2 input observations: Summary and assessment. NASA Tech. Rep. Series on Global Modeling and Data Assimilation, NASA/TM-2016-104606, 46: 64.
McNally, A. et al., 2017. A land data assimilation system for sub-Saharan Africa food and water security applications. Scientific data, 4(1): 1-19.
Michaelides, S. et al., 2009. Precipitation: Measurement, remote sensing, climatology and modeling. Atmospheric Research, 94(4): 512-533.
Miralles, D.G., Gentine, P., Seneviratne, S.I., Teuling, A.J., 2019. Land–atmospheric feedbacks during droughts and heatwaves: state of the science and current challenges. Annals of the New York Academy of Sciences, 1436(1): 19.
Mladenova, I.E. et al., 2019. Evaluating the operational application of SMAP for global agricultural drought monitoring. IEEE Journal of Selected Topics in Applied Earth Observations and Remote Sensing, 12(9): 3387-3397.
Moazami, S., Golian, S., Kavianpour, M.R., Hong, Y., 2013. Comparison of PERSIANN and V7 TRMM Multi-satellite Precipitation Analysis (TMPA) products with rain gauge data over Iran. International Journal of Remote Sensing, 34(22): 8156-8171.
Mohammed, I.N., Bolten, J.D., Souter, N.J., Shaad, K., Vollmer, D., 2022. Diagnosing challenges and setting priorities for sustainable water resource management under climate change. Scientific reports, 12(1): 1-15.
Mohammed, I.N., Bolten, J.D., Srinivasan, R., Lakshmi, V., 2018. Improved Hydrological Decision Support System for the Lower Mekong River Basin Using Satellite-Based Earth Observations. Remote sensing, 10(6).
Mondal, A., Khare, D., Kundu, S., 2015. Spatial and temporal analysis of rainfall and temperature trend of India. Theoretical and applied climatology, 122(1-2): 143-158.

Mondal, A., Lakshmi, V., Hashemi, H., 2018. Intercomparison of trend analysis of multisatellite monthly precipitation products and gauge measurements for river basins of India. Journal of Hydrology, 565: 779-790.

MONRE, 2012. Circular on national technical standard of meteorological monitoring, 25/2012/TT-BTNMT.

Moriasi, D.N. et al., 2007. Model evaluation guidelines for systematic quantification of accuracy in watershed simulations. Transactions of the ASABE, 50(3): 885-900.

Moriasi, D.N., Gitau, M.W., Pai, N., Daggupati, P., 2015. Hydrologic and water quality models: Performance measures and evaluation criteria. Transactions of the ASABE, 58(6): 1763-1785.

Mu, Q., Zhao, M., Running, S.W., 2011. Improvements to a MODIS global terrestrial evapotranspiration algorithm. Remote Sensing of Environment, 115(8): 1781-1800.

Munia, H. et al., 2016. Water stress in global transboundary river basins: significance of upstream water use on downstream stress. Environmental Research Letters, 11(1): 014002.

Munia, H.A. et al., 2020. Future transboundary water stress and its drivers under climate change: A global study. Earth's Future, 8(7): e2019EF001321.

Muñoz-Sabater, J. et al., 2021. ERA5-Land: A state-of-the-art global reanalysis dataset for land applications. Earth System Science Data, 13(9): 4349-4383.

Nachtergaele, F., Velthuizen, H.v., Verelst, L., 2009. Harmonized World Soil Database, FAO, IIASA, ISRIC, ISSCAS, JRC.

Narayan, U., Lakshmi, V., 2008. Characterizing subpixel variability of low resolution radiometer derived soil moisture using high resolution radar data. Water resources research, 44(6).

Narayan, U., Lakshmi, V., Jackson, T.J., 2006. High-resolution change estimation of soil moisture using L-band radiometer and radar observations made during the SMEX02 experiments. IEEE Transactions on Geoscience and Remote Sensing, 44(6): 1545-1554.

Nash, J.E., Sutcliffe, J.V., 1970. River flow forecasting through conceptual models part I—A discussion of principles. Journal of Hydrology, 10(3): 282-290.

National Institute for Soils and Fertilizers, 2002. The basic information of main soil units of Vietnam. The Gioi Publishers, Hanoi, Vietnam.

NAWAPI, 2017a. Red-Thai Binh River Basin Water Resources Planning, Main Report (in Vietnamese), Ministry of Natural Resources and Environment, Hanoi.

NAWAPI, 2017b. Red-Thai Binh River Basin Water Resources Planning, Term of Reference (in Vietnamese), Ministry of Natural Resources and Environment, Hanoi.

NAWAPI, 2018. Bang Giang - Ky Cung Water Resources Planning Project, Water Resources Assessment Report (in Vietnamese), Ministry of Natural Resources and Environment, Hanoi.

NCHMF, 2000. Rainfall classification of Vietnam, Hanoi.

Neitsch, S.L., Arnold, J.G., Kiniry, J.R., Williams, J.R., 2011. Soil and water assessment tool theoretical documentation version 2009, Texas Water Resources Institute.

Nerini, D. et al., 2015. A comparative analysis of TRMM–rain gauge data merging techniques at the daily time scale for distributed rainfall–runoff modeling applications. Journal of Hydrometeorology, 16(5): 2153-2168.

Ngo, V.Q. et al., 2020. Water Resources Engineering (in Vietnamese). Hanoi: Bach Khoa Publishing House - Hanoi.

Nguyen-Le, D., Matsumoto, J., Ngo-Duc, T., 2015. Onset of the rainy seasons in the eastern Indochina Peninsula. Journal of Climate, 28(14): 5645-5666.

Nguyen-Xuan, T. et al., 2016. The Vietnam Gridded Precipitation (VnGP) Dataset: Construction and Validation. SOLA, 12: 291-296.

Nguyen, C.N., Bui, D.D., 2016. Overview of transboundary waters in Vietnam.

Nguyen, D.N., Nguyen, T.H., 2004. Climate and Climate Resources in Vietnam (in Vietnamese). Agricultural Publishing House, Hanoi, Vietnam.

Nguyen, D.Q., Renwick, J., McGregor, J., 2014. Variations of surface temperature and rainfall in Vietnam from 1971 to 2010. International Journal of Climatology, 34(1): 249-264.

Nguyen, H., Shaw, R., 2011. Chapter 8 Drought Risk Management in Vietnam. Droughts in Asian Monsoon Region; Emerald Group Publishing Limited: Bingley, UK: 141-161.

Nguyen, L.B., 2021. Accuracy of Integrated Multi-SatelliE Retrievals for GPM Satellite Rainfall Product over North Vietnam. Polish Journal of Environmental Studies, 30(6): 5657-5667.
Nguyen, P. et al., 2019. The CHRS Data Portal, an easily accessible public repository for PERSIANN global satellite precipitation data. Scientific data, 6: 180296.
Nguyen, T.H., Masih, I., Mohamed, Y.A., van der Zaag, P., 2018. Validating Rainfall-Runoff Modelling Using Satellite-Based and Reanalysis Precipitation Products in the Sre Pok Catchment, the Mekong River Basin. Geosciences, 8(5): 164.
Njoku, E.G., Entekhabi, D., 1996. Passive microwave remote sensing of soil moisture. Journal of hydrology, 184(1-2): 101-129.
O'Neill, P.E. et al., 2020. SMAP Enhanced L3 Radiometer Global Daily 9 km EASE-Grid Soil Moisture, Version 4, NASA National Snow and Ice Data Center Distributed Active Archive Center, Boulder, Colorado USA.
Ochoa-Sánchez, A., Pineda Ordonez, L.E., Crespo, P., Willems, P., 2014. Evaluation of TRMM 3B42 precipitation estimates and WRF retrospective precipitation simulation over the Pacific-Andean region of Ecuador and Peru. Hydrology and Earth System Sciences, 18: 3179-3193.
Orlowsky, B., Seneviratne, S.I., 2013. Elusive drought: uncertainty in observed trends and short-andlong-term CMIP5 projections. Hydrology and Earth System Sciences, 17(5): 1765-1781.
Ott, R.L., Longnecker, M.T., 2015. An introduction to statistical methods and data analysis. Nelson Education.
Patil, A., Ramsankaran, R., 2017. Improving streamflow simulations and forecasting performance of SWAT model by assimilating remotely sensed soil moisture observations. Journal of Hydrology, 555: 683-696.
Patil, A., Ramsankaran, R., 2018. Improved streamflow simulations by coupling soil moisture analytical relationship in EnKF based hydrological data assimilation framework. Advances in Water Resources, 121: 173-188.
Pham, H.T., Kim, S., Marshall, L., Johnson, F., 2019. Using 3D robust smoothing to fill land surface temperature gaps at the continental scale. International Journal of Applied Earth Observation and Geoinformation, 82: 101879.
Pham, H.T., Marshall, L., Johnson, F., 2021. Daily time series of river water levels derived from a seasonal linear model using multisource satellite products under uncertainty. Journal of Hydrology, 602: 126783.
Phan, V.-T., Ngo-Duc, T., 2009. Seasonal and interannual variations of surface climate elements over Vietnam. Climate Research, 40(1): 49-60.
Plengsaeng, B., Wehn, U., van der Zaag, P., 2014. Data-sharing bottlenecks in transboundary integrated water resources management: a case study of the Mekong River Commission's procedures for data sharing in the Thai context. Water international, 39(7): 933-951.
Poortinga, A. et al., 2017. A Self-Calibrating Runoff and Streamflow Remote Sensing Model for Ungauged Basins Using Open-Access Earth Observation Data. Remote Sensing, 9(1): 86.
Rana, S., McGregor, J., Renwick, J., 2015. Precipitation seasonality over the Indian subcontinent: An evaluation of gauge, reanalyses, and satellite retrievals. Journal of Hydrometeorology, 16(2): 631-651.
Ranney, K.J., Niemann, J.D., Lehman, B.M., Green, T.R., Jones, A.S., 2015. A method to downscale soil moisture to fine resolutions using topographic, vegetation, and soil data. Advances in Water Resources, 76: 81-96.
Raziei, T., Bordi, I., Pereira, L.S., 2013. Regional drought modes in Iran using the SPI: the effect of time scale and spatial resolution. Water resources management, 27(6): 1661-1674.
Ren, P., Li, J., Feng, P., Guo, Y., Ma, Q., 2018. Evaluation of Multiple Satellite Precipitation Products and Their Use in Hydrological Modelling over the Luanhe River Basin, China. Water, 10(6): 677.
Rodell, M. et al., 2018. Emerging trends in global freshwater availability. Nature, 557(7707): 651-659.
Rodell, M. et al., 2004. The global land data assimilation system. Bulletin of the American Meteorological Society, 85(3): 381-394.
Rojas, O., Vrieling, A., Rembold, F., 2011. Assessing drought probability for agricultural areas in Africa with coarse resolution remote sensing imagery. Remote sensing of Environment, 115(2): 343-352.
Rutten, M., van Dijk, M., van Rooij, W., Hilderink, H., 2014. Land Use Dynamics, Climate Change, and Food Security in Vietnam: A Global-to-local Modeling Approach. World Development, 59: 29-46. DOI:10.1016/j.worlddev.2014.01.020

Saha, S. et al., 2010. The NCEP climate forecast system reanalysis. Bulletin of the American Meteorological Society, 91(8): 1015-1058.
Saha, S. et al., 2014. The NCEP climate forecast system version 2. Journal of climate, 27(6): 2185-2208.
Sahoo, A.K., Sheffield, J., Pan, M., Wood, E.F., 2015. Evaluation of the tropical rainfall measuring mission multi-satellite precipitation analysis (TMPA) for assessment of large-scale meteorological drought. Remote Sensing of Environment, 159: 181-193.
Sangati, M., Borga, M., 2009. Influence of rainfall spatial resolution on flash flood modelling. Natural Hazards and Earth System Sciences, 9(2): 575-584.
Santos, L., Thirel, G., Perrin, C., 2018. Pitfalls in using log-transformed flows within the KGE criterion. Hydrology and Earth System Sciences, 22(8): 4583-4591.
Saxton, K.E., Rawls, W.J., 2006. Soil water characteristic estimates by texture and organic matter for hydrologic solutions. Soil science society of America Journal, 70(5): 1569-1578.
Sazib, N., Bolten, J., Mladenova, I., 2020. Exploring Spatiotemporal Relations between Soil Moisture, Precipitation, and Streamflow for a Large Set of Watersheds Using Google Earth Engine. Water, 12(5): 1371.
Schaefer, J.T., 1990. The critical success index as an indicator of warning skill. Weather and Forecasting, 5(4): 570-575.
Sen, P.K., 1968. Estimates of the regression coefficient based on Kendall's tau. Journal of the American statistical association, 63(324): 1379-1389.
Sharma, S., Mujumdar, P., 2017. Increasing frequency and spatial extent of concurrent meteorological droughts and heatwaves in India. Scientific reports, 7(1): 1-9.
Sheffield, J., Wood, E.F., 2008. Global trends and variability in soil moisture and drought characteristics, 1950–2000, from observation-driven simulations of the terrestrial hydrologic cycle. Journal of Climate, 21(3): 432-458.
Sheffield, J. et al., 2018. Satellite Remote Sensing for Water Resources Management: Potential for Supporting Sustainable Development in Data-Poor Regions. Water Resources Research, 54(12): 9724-9758.
Sheffield, J., Wood, E.F., Roderick, M.L., 2012. Little change in global drought over the past 60 years. Nature, 491(7424): 435-438.
Sheikh, V., Visser, S., Stroosnijder, L., 2009. A simple model to predict soil moisture: Bridging Event and Continuous Hydrological (BEACH) modelling. Environmental Modelling & Software, 24(4): 542-556.
Simons, G. et al., 2016. Integrating global satellite-derived data products as a pre-analysis for hydrological modelling studies: A case study for the Red River Basin. Remote Sensing, 8(4): 279.
Simpson, E.H., 1949. Measurement of diversity. nature, 163(4148): 688-688.
Sorooshian, S. et al., 2000. Evaluation of PERSIANN system satellite-based estimates of tropical rainfall. Bulletin of the American Meteorological Society, 81(9): 2035-2046.
Sun, Q. et al., 2018. A review of global precipitation data sets: Data sources, estimation, and intercomparisons. Reviews of Geophysics.
Svoboda, M., Hayes, M., Wood, D., 2012. Standardized precipitation index user guide. World Meteorological Organization Geneva, Switzerland.
Tan, M.L., Duan, Z., 2017. Assessment of GPM and TRMM precipitation products over Singapore. Remote Sensing, 9(7): 720.
Tan, M.L., Gassman, P., Yang, X., Haywood, J., 2020. A review of SWAT applications, performance and future needs for simulation of hydro-climatic extremes. Advances in Water Resources: 103662.
Teutschbein, C., Seibert, J., 2012. Bias correction of regional climate model simulations for hydrological climate-change impact studies: Review and evaluation of different methods. Journal of Hydrology, 456: 12-29.
Thiessen, A.H., 1911. Precipitation averages for large areas. Monthly weather review, 39(7): 1082-1089.
Thorndahl, S. et al., 2017. Weather radar rainfall data in urban hydrology. Hydrology and Earth System Sciences, 21(3): 1359-1380.
Thornthwaite, C.W., 1948. An approach toward a rational classification of climate. Geographical review, 38(1): 55-94.
Tong, K., Su, F., Yang, D., Hao, Z., 2014. Evaluation of satellite precipitation retrievals and their potential utilities in hydrologic modeling over the Tibetan Plateau. Journal of Hydrology, 519: 423-437.

Tran Thanh Xuan, Hoang Minh Tuyen, Tran Hong Thai, Nguyen Kien Dung, 2012. Water resources on Vietnam's river system (in Vietnamese). Science and Technology Publisher, Hanoi.

Tran, T.X., 2006. Hydrology and Water Resources Characteristics of Vietnam (in Vietnamese). Agricultural Publisher, Hanoi.

Trinh-Tuan, L., Matsumoto, J., Ngo-Duc, T., Nodzu, M.I., Inoue, T., 2019a. Evaluation of satellite precipitation products over Central Vietnam. Progress in Earth and Planetary Science, 6(1): 54.

Trinh-Tuan, L. et al., 2019b. Application of Quantile Mapping Bias Correction for Mid-future Precipitation Projections over Vietnam. SOLA.

Tuan, B.M., 2019. Extratropical Forcing of Submonthly Variations of Rainfall in Vietnam. Journal of Climate, 32(8): 2329-2348.

Tuo, Y., Duan, Z., Disse, M., Chiogna, G., 2016. Evaluation of precipitation input for SWAT modeling in Alpine catchment: A case study in the Adige river basin (Italy). Science of The Total Environment, 573: 66-82.

UN-Water, 2013. Transboundary Waters (http://unwater.org/topics/transboundary-waters/en/).

UNU-INWEH, 2013. Water security & the global water agenda: a UN-Water analytical brief. United Nations University (UNU).

USDA Soil Conservation Service, 1972. National Engineering Handbook Section 4 Hydrology, Chapters 4-10.

Ushio, T. et al., 2009. A Kalman filter approach to the Global Satellite Mapping of Precipitation (GSMaP) from combined passive microwave and infrared radiometric data. Journal of the Meteorological Society of Japan. Ser. II, 87: 137-151.

Valdes-Abellan, J., Pardo, M., Tenza-Abril, A.J., 2017. Observed precipitation trend changes in the western Mediterranean region. International Journal of Climatology, 37: 1285-1296.

Van Der Linden, R., Fink, A.H., Phan-Van, T., Trinh-Tuan, L., 2016. Synoptic-dynamic analysis of early dry-season rainfall events in the Vietnamese central highlands. Monthly Weather Review, 144(4): 1509-1527.

Van Dijk, A., Renzullo, L.J., 2011. Water resource monitoring systems and the role of satellite observations. Hydrology and Earth System Sciences, 15(1): 39-55.

Van Loon, A.F. et al., 2016. Drought in a human-modified world: reframing drought definitions, understanding, and analysis approaches.

Velpuri, N., Senay, G., 2013. Analysis of long-term trends (1950–2009) in precipitation, runoff and runoff coefficient in major urban watersheds in the United States. Environmental Research Letters, 8(2): 024020.

Vermote, E., 2015. MOD09A1 MODIS/terra surface reflectance 8-day L3 global 500m SIN grid V006. NASA EOSDIS Land Processes DAAC, 10.

Vicente-Serrano, S.M., Beguería, S., López-Moreno, J.I., 2010. A multiscalar drought index sensitive to global warming: the standardized precipitation evapotranspiration index. Journal of climate, 23(7): 1696-1718.

Viglione, A., Borga, M., Balabanis, P., Blöschl, G., 2010. Barriers to the exchange of hydrometeorological data in Europe: Results from a survey and implications for data policy. Journal of Hydrology, 394(1-2): 63-77.

Vu-Thanh, H., Ngo-Duc, T., Phan-Van, T., 2014. Evolution of meteorological drought characteristics in Vietnam during the 1961–2007 period. Theoretical and applied climatology, 118(3): 367-375.

Vu, M., Raghavan, S., Liong, S.-Y., 2016. Use of Regional Climate Models for Proxy Data over Transboundary Regions. Journal of Hydrologic Engineering, 21(6): 05016010.

Vu, M., Raghavan, S.V., Liong, S.Y., 2012. SWAT use of gridded observations for simulating runoff–a Vietnam river basin study. Hydrology and Earth System Sciences, 16(8): 2801-2811.

Vu, T., Mishra, A., 2016. Spatial and temporal variability of standardized precipitation index over Indochina peninsula. Cuadernos de Investigación Geográfica, 42(1): 221-232.

Vu, T.M., Raghavan, S.V., Liong, S.Y., Mishra, A.K., 2018. Uncertainties of gridded precipitation observations in characterizing spatio-temporal drought and wetness over Vietnam. International Journal of Climatology, 38(4): 2067-2081.

Vu, T.T., Dao, N.K., Do, Q.L., 2017. Using gridded rainfall products in simulating streamflow in a tropical catchment–A case study of the Srepok River Catchment, Vietnam. Journal of Hydrology and Hydromechanics, 65(1): 18-25.

Wang, F., Wang, Z., Yang, H., Zhao, Y., 2018. Study of the temporal and spatial patterns of drought in the Yellow River basin based on SPEI. Science China Earth Sciences, 61(8): 1098-1111. DOI:10.1007/s11430-017-9198-2

Wang, W., Lu, H., 2016. Evaluation and comparison of newest GPM and TRMM products over Mekong River Basin at daily scale. IEEE, pp. 613-616.

Wang, W. et al., 2016. Modelling hydrologic processes in the Mekong River Basin using a distributed model driven by satellite precipitation and rain gauge observations. PloS one, 11(3): e0152229.

Western, A.W., Grayson, R.B., Blöschl, G., 2002. Scaling of soil moisture: A hydrologic perspective. Annual Review of Earth and Planetary Sciences, 30(1): 149-180.

Wilks, D.S., 2006. Statistical Methods in the Atmospheric Sciences (International Geophysics Series; V. 91). Academic Press.

Williams, J.R., 1969. Flood routing with variable travel time or variable storage coefficients. Transactions of the ASAE, 12(1): 100-0103.

Winkler, K., Gessner, U., Hochschild, V., 2017. Identifying droughts affecting agriculture in Africa based on remote sensing time series between 2000–2016: rainfall anomalies and vegetation condition in the context of ENSO. Remote Sensing, 9(8): 831.

WMO, 1994. Guide to hydrological Practices: Data Acquisition and Processing, Analysis, Forecasting and other Applications.

Wu, Z. et al., 2018. Hydrologic Evaluation of Multi-Source Satellite Precipitation Products for the Upper Huaihe River Basin, China. Remote Sensing, 10(6): 840.

Xie, P., Arkin, P.A., 1996. Analyses of global monthly precipitation using gauge observations, satellite estimates, and numerical model predictions. Journal of climate, 9(4): 840-858.

Xu, R. et al., 2017. Ground validation of GPM IMERG and TRMM 3B42V7 rainfall products over southern Tibetan Plateau based on a high-density rain gauge network. Journal of Geophysical Research: Atmospheres, 122(2): 910-924.

Xue, X. et al., 2013. Statistical and hydrological evaluation of TRMM-based Multi-satellite Precipitation Analysis over the Wangchu Basin of Bhutan: Are the latest satellite precipitation products 3B42V7 ready for use in ungauged basins? Journal of Hydrology, 499: 91-99.

Yang, H., Xiong, L., Liu, D., Cheng, L., Chen, J., 2021. High spatial resolution simulation of profile soil moisture by assimilating multi-source remote-sensed information into a distributed hydrological model. Journal of Hydrology, 597: 126311.

Yilmaz, K.K. et al., 2005. Intercomparison of rain gauge, radar, and satellite-based precipitation estimates with emphasis on hydrologic forecasting. Journal of Hydrometeorology, 6(4): 497-517.

Yuan, F. et al., 2017. Assessment of GPM and TRMM Multi-Satellite Precipitation Products in Streamflow Simulations in a Data-Sparse Mountainous Watershed in Myanmar. Remote Sensing, 9(3): 302.

Yuan, X. et al., 2019. Anthropogenic shift towards higher risk of flash drought over China. Nature communications, 10(1): 1-8.

Yue, S., Pilon, P., Phinney, B., Cavadias, G., 2002. The influence of autocorrelation on the ability to detect trend in hydrological series. Hydrological processes, 16(9): 1807-1829.

Zad, M., Najja, S., Zulkafli, Z., Muharram, F.M., 2018. Satellite Rainfall (TRMM 3B42-V7) Performance Assessment and Adjustment over Pahang River Basin, Malaysia. Remote Sensing, 10(3).

Zhang, A., Jia, G., 2013. Monitoring meteorological drought in semiarid regions using multi-sensor microwave remote sensing data. Remote Sensing of Environment, 134: 12-23.

Zhang, X. et al., 2013. Enhanced poleward moisture transport and amplified northern high-latitude wetting trend. Nature Climate Change, 3(1): 47-51.

Zhang, Y., Liu, W., Zhao, M., 2020. The drag effect of water resources on China's regional economic growth: analysis based on the temporal and spatial dimensions. Water, 12(1): 266.

Zhang, Z. et al., 2019. Hydrologic Evaluation of TRMM and GPM IMERG Satellite-Based Precipitation in a Humid Basin of China. Remote Sensing, 11(4): 431.

Zhao, F., Zhang, L., Chiew, F.H., Vaze, J., Cheng, L., 2013. The effect of spatial rainfall variability on water balance modelling for south-eastern Australian catchments. Journal of hydrology, 493: 16-29.
Zhu, Y., Wang, W., Singh, V.P., Liu, Y., 2016. Combined use of meteorological drought indices at multi-time scales for improving hydrological drought detection. Science of the Total Environment, 571: 1058-1068.
Zuo, D. et al., 2018. Spatiotemporal patterns of drought at various time scales in Shandong Province of Eastern China. Theoretical and applied climatology, 131(1-2): 271-284.